MODELING OF HUMAN BRAIN TISSUES AND HEAD INJURIES INDUCED BY BLAST AND BALLISTIC IMPACT

A Dissertation

by

SAHIL KULKARNI

Submitted to the Office of Graduate and Professional Studies of
Texas A&M University
in partial fulfillment of the requirements for the degree of

DOCTOR OF PHILOSOPHY

Chair of Committee,	Xin-Lin Gao
Co-Chair of Committee,	Miladin Radovic
Committee Members,	Ibrahim Karaman Bruce Wang
Head of Department,	Andreas Polycarpou

December 2013

Major Subject: Mechanical Engineering

ABSTRACT

The use of body armor and combat helmets has reduced fatalities from explosions and ballistic attacks. However, frequent use of improvised explosive devices and continuing efforts to reduce the weight of each combat helmet have increased the risk of ballistic-impact and blast-induced traumatic brain injuries among soldiers. The objective of this dissertation research project is to develop predictive constitutive and computational models to be used in head injury diagnosis and to aid in the development of new combat helmets that can mitigate non-penetrating head injuries.

A transversely isotropic visco-hyperelastic constitutive model is provided for soft tissues, which accounts for large deformations, high strain rates, and short-memory effects. The presented model is tested for a range of strain rates and for multiple loading scenarios based on available experimental data for porcine and human brain tissues.

Using this constitutive relation, a finite element model of a helmet/head assembly is developed to study non-penetrating TBI. The effects of constitutive models and blast directions on finite elements simulations of blast induced TBI are investigated. Further, the effectiveness of combat helmets against non-penetrating TBI induced by blast and ballistic impacts is studied. Two types of combat helmets are considered: the *advanced combat helmet (ACH)* and the *enhanced combat helmet (ECH)*. Spatial distributions and temporal variations of the intracranial pressure and stress components obtained in the simulations reveal significant differences in brain tissue responses to different constitutive models and blast directions. It is found that these combat helmets provide

some level of protection against non-penetrating TBI and that the level of protection is higher for the ECH than the ACH.

DEDICATION

Dedicated to my family and God

ACKNOWLEDGEMENTS

First and foremost, I would like to express my gratitude to the chair of my dissertation committee, Dr. Xin-Lin Gao for his patience and guidance throughout the duration of my study. His constant support has been a driving force in the course of this work.

I am thankful to the members of my dissertation committee, Dr. Miladin Radovic, Dr. Ibrahim Karaman, and Dr. Bruce Wang for their time, insightful questions, and valuable ideas which have contributed to the scientific discourse presented in this dissertation.

I am grateful to Dr. David Schmueser – University Business Development Manager at Altair Inc. for providing me access to Hypermesh Suite. All the simulations reported in this dissertation were carried out using Texas A&M Supercomputing Facility *EOS IBM iDataplex Cluster* under the guidance Mr. Ping Luo and Mr. Marinus Pennings. I would like to thank Mr. Luo and Mr. Pennings for providing crucial technical assistance essential to the completion of my studies. I am thankful to the US Army – Soldier Equipment Program that partly supported the work presented in this dissertation. I am also indebted to Dr. Hongbing Lu from the University of Texas at Dallas for providing me access to his computing cluster.

Last, but not least, I would like to thank my family members for their encouragement, patience and prayers I so desperately needed during the final years of my degree.

NOMENCLATURE

PASGT	Personal Armor System for Ground Troops Combat Helmet
ACH	Advanced Combat Helmet
ECH	Enhanced Combat Helmet
MICH	Modular Integrated Communications Helmet
LWH	Lightweight Helmet
TBI	Traumatic Brain Injury
BTBI	Blast Induced Traumatic Brain Injury
BABT	Behind Armor Blunt Trauma
BFD	Back Face Deformation

TABLE OF CONTENTS

Page

LIST OF FIGURES

LIST OF TABLES

CHAPTER I

INTRODUCTION

1.1 Background

Helmets have been used for head protection for centuries. The French Adrian helmet was the first modern steel combat helmet. Steel helmets similar to the French Adrian helmet were soon adopted by other warring nations. The original World War I French and British helmet designs were adapted by the U.S. Army to form the Hadfield steel helmet. The Hadfield helmet was eventually re-designed for lower weight, better comfort, and higher protection to produce the famous World War II M1 steel helmet (Walsh et al., 2005). In the early 1960s, the U.S. Army embarked on a program to replace the M1 steel helmet design with a single-walled, lighter, and more protective configuration. After considerable research and development efforts, the improved Personnel Armor System for Ground Troops (PASGT) combat helmet (made using Kevlar® fibers) replaced the steel M1 helmet. Since the PASGT helmet, the U.S. Army has introduced two more kinds of combat helmets. The first is the Advanced Combat Helmet (ACH), and the second is the lightweight helmet (LWH) of the U.S. Marine Corps (see Fig. 1). These modern-era helmets have saved many lives and received great praise. Since their successful implementation, the trend for helmet development has been mainly towards weight reduction, and the concept of “a soldier as effective as a tank” (e.g., Carey et al., 2000) has become appealing to the Army. It has been envisioned that an advanced helmet should have a remote sight, a night vision device, a GPS, and a laser range finder to make an individual soldier a more effective fighter. Incorporating all these desired features in the helmet would require a radical change in the functionality and helmet design.

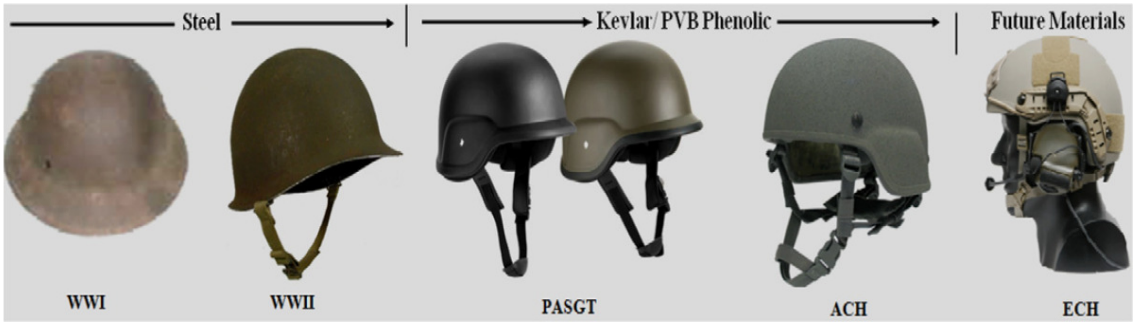

Figure 1. Changing designs and materials of the U.S. Army helmet from World War I to the latest headgear system (Walsh et al., 2006).

Traumatic brain injury (TBI), also known as intra-cranial injury, is damage to the brain induced by external mechanical forces, resulting in permanent or temporary impairment of the brain functions. Because of its high economic impact on the society and families of the affected, TBI is also an important social problem. Brain injuries can result from direct impact on the skull, leading to skull fracture and subsequent damage to the brain tissue. Such injuries are penetrating TBIs, which are mainly caused by motor vehicle accidents, sports and work related accidents, and falls. TBI can also be induced by sudden indirect motion applied to the skull or passage of shockwaves into the intracranial cavity. Such brain injuries may not be accompanied by visible damage to the skull and are therefore non-penetrating TBIs. Ballistic protection has been the primary function of a combat helmet. The performance of a combat helmet has always been measured in terms of its ability to defeat a bullet travelling at certain velocity, thus preventing penetrating trauma to the user. Modern combat helmets have been quite successful in preventing penetrating traumatic brain injuries.

However, frequent use of improvised explosive devices, increase in available energy of bullets, and reduction in weight of a combat helmet have exacerbated occurrence of non-penetrating TBIs. Blast induced traumatic brain injury is one such non-penetrating TBI caused by ingress and reflection of blast-induced shock-waves in the intra-cranial cavity (Cernak and Haeusslein, 2010). Ballistic impact induced behind helmet blunt trauma (Cannon, 2001; Prat et al., 2012) is another type of non-penetrating injury resulting from projectile impacts on combat helmets. Although the combat helmet may stop the projectile, part of the energy of the projectile absorbed by the helmet shell is transferred to the skull and intracranial cavity because of rapid deformations of the helmet shell. If this energy transferred to the brain tissue is sufficiently large enough it may lead to non-penetrating type of TBI's. Fig. 2 outlines the various causes and biological symptoms of TBI.

1.2 Motivation

Numerous experimental and computational studies have been conducted to determine brain responses to blast events and ballistic impacts (e.g., El Sayed et al., 2008; Moore et al., 2009; Grujicic et al., 2009; Chafi et al., 2009; Nyein et al., 2010; Ganpule et al., 2010, 2011). Several causes have been identified for blast-induced traumatic brain injury. Regarding the effectiveness of the current helmets against blast waves, the limited studies available in the literature present contradictory results. There has been no consensus about whether the current helmet designs are effective for preventing blast induced TBI. The existing studies on ballistic impacts mainly focus on evaluating the helmet shell response. The coupling between the head-helmet and the intracranial response to a ballistic impact is not studied in detail. In addition, the material models used in the published TBI simulations tend to be overly simplified. The suitability of available constitutive relations for representing experimentally observed brain tissue behaviors has not been verified. Any constitutive model developed to capture brain tissue responses in blast/ballistic events should be able to represent different mechanical behaviors (and loading regimes) in one general framework and should be validated for large strains and high strain rates.

1.3 Organization

The rest of the dissertation is organized as follows.

In Chapter II, a comprehensive review and a comparative study of various issues involved in TBI and combat helmet design is presented.

In Chapter III, a transversely isotropic visco-hyperelastic constitutive model is developed for brain tissues based on continuum mechanics.

In Chapter IV, a computational model for predicting blast induced traumatic brain injury is provided.

In Chapter V, the effectiveness of combat helmets in mitigating TBI induced by blast and ballistic impacts is investigated.

In Chapter VI, a summary is given and some conclusions are drawn based on the studies reported in Chapters II – V.

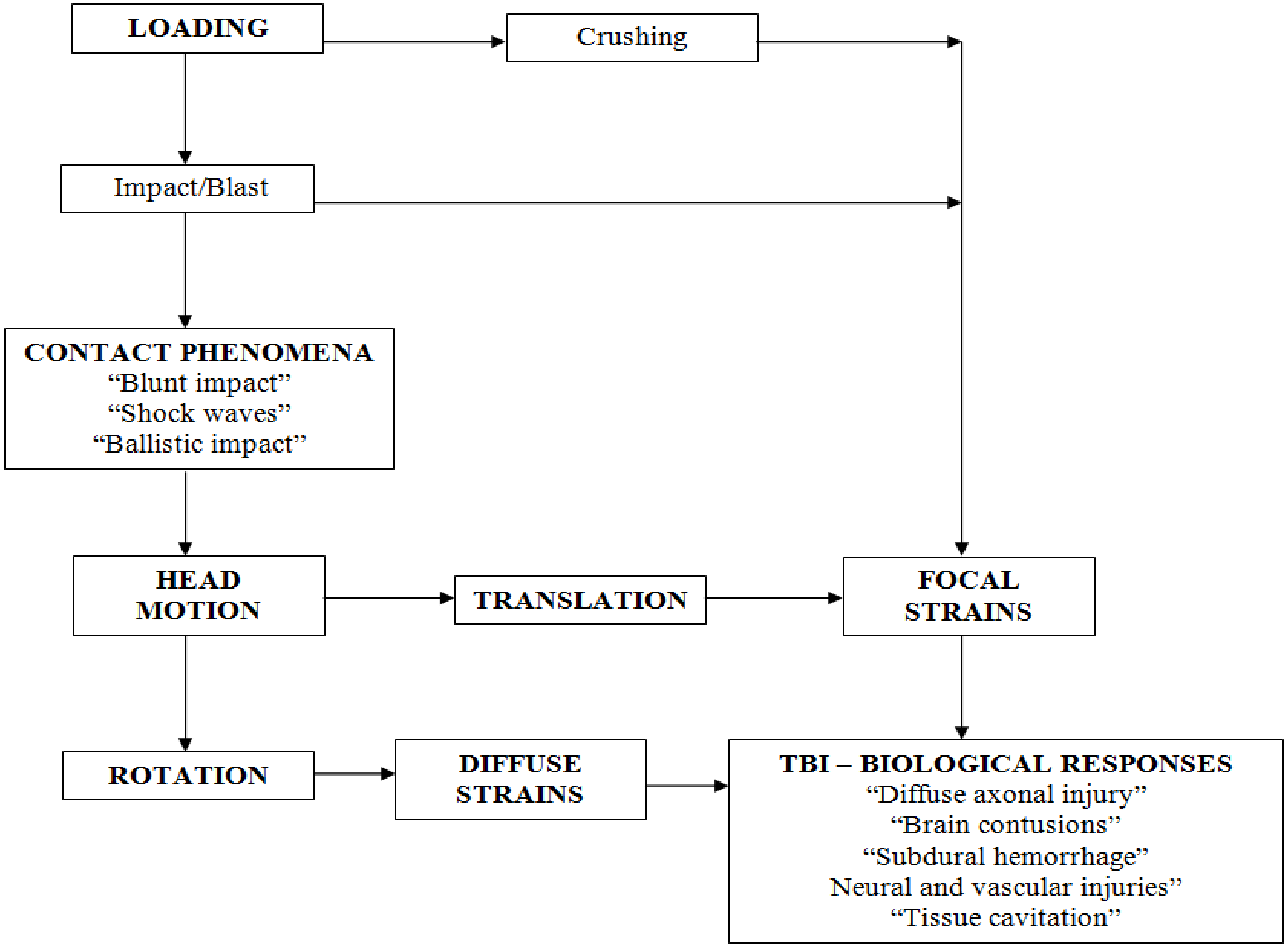

Figure 2. Causes of TBI.

CHAPTER II

BALLISTIC HELMETS – THEIR DESIGN, MATERIALS, AND PERFORMANCE AGAINST TRAUMATIC BRAIN INJURY

2.1 Introduction

This Chapter provides a comparative study on the design, materials, and ballistic and blast performance of the combat helmets used by the U.S. Army based on a comprehensive and critical review of existing studies. Mechanisms of ballistic energy absorption, effects of helmet curvatures on ballistic performance, and performance measures of helmets are discussed. Properties of current helmet materials (including Kevlar® K29, K129 fibers and thermoset resins) and future candidate materials for helmets (such as nano-composites and thermoplastic polymers) are elaborated. Also, available experimental and computational studies on blast-induced TBI are examined, and constitutive models developed for brain tissues are reviewed.

2.2 Ballistic Helmets

2.2.1 Mechanisms of Ballistic Energy Absorption

The basic function of a combat helmet is to provide protection against shrapnel and ballistic threats. The ballistic performance of a material can be measured using the ballistic limit (e.g., David et al., 2009a). For a given projectile, the ballistic limit is defined as the projectile velocity at which the projectile is expected to penetrate the armor/helmet 50% of the time. Also, when a bullet strikes a helmet, a cone is formed on the back face of the helmet. The depth of this back-face signature (a conical bulge) is required not to exceed a critical value. If the depth exceeds this value, the helmet shell can strike the skull, resulting in behind armor blunt trauma (BABT) (e.g., Carroll and Soderstrom, 1978; Sarron, et al., 2000; Cannon, 2001; Hisley et al., 2011; Prat et al., 2012).

Impact events are of three types (e.g., Naik and Shrirao, 2004): lower velocity impact, high velocity impact, and hyper-velocity impact. Low velocity impact is defined as an impact event where the time for the projectile in contact with the helmet exceeds the period of the lowest vibrational mode. In a low velocity impact event, the boundary conditions of the structural component are important in order to accurately describe the impact response. In a high velocity impact (ballistic or blast impact) event, the local material behavior in the impacted zone governs the impact response of the structure. In a hyper-velocity impact event, the locally impacted material behaves like a fluid and very high stresses are induced.

The PASGT and the ACH are made from ballistic fabrics (Kevlar®). Most ballistic fabrics exhibit a weave pattern formed by warp and weft yarns (e.g., Gao and Mall, 2000; David et al., 2009a; Nilakantan et al., 2011). When a woven fabric is impacted by a projectile, transverse and longitudinal waves are generated (e.g., Bazhenov, 1997). These longitudinal and transverse waves travel along the yarns until they encounter an obstacle like a fabric edge or a fiber cross-over point. The waves are reflected at the obstacles and collide with the outward travelling waves. The kinetic energy carried by these stress waves is dissipated through a number of mechanisms, including cone formation on the helmet back face, deformation of secondary yarns, primary yarn breakage, inter-yarn friction, and friction between the projectile and the fabric (e.g., Gogineni et al., 2012). Shear plugging has also been observed as one energy dissipating mechanism (Naik and Shrirao, 2004). As the strain within a fiber exceeds a critical value (called the dynamic tensile strain), the fiber fails. Each successive fabric layer absorbs the un-dissipated energy until the projectile is defeated. Failure of all fabric layers results in complete perforation. If the projectile velocity becomes zero before complete penetration, then the projectile has been successfully defeated.

2.3 Conventional Material Systems

2.3.1 Personal Armor System for Ground Troops

The first combat helmet was the French Adrian steel helmet. This was adopted by other nations including the U.S. to form the Hadfield helmet, which was used during the First World War. The Hadfield helmet was re-designed for better comfort and protection to produce the M1 helmet. The M1 helmet was the longest serving helmet. The M1 helmet could defeat a pistol shot fired at a certain velocity, as required by the ballistic criterion imposed then (Carey et al., 2000). However, the M1 helmet was manufactured in only one size (e.g., Laible, 1980). In addition, it retained heat, did not protect the temporal area, and had to be removed before using tele-communication devices. To mitigate these difficulties, the New Helmet Design Program was initiated in 1972. Composites had already been developed by that time, with the Kevlar® fibers developed in 1965. This program led to the development of the new Kevlar® fiber-based Personal Armor System for Ground Troops (PASGT) helmet (Walsh et al., 2005), which overcame the drawbacks of the M1 helmet and replaced the M1 steel helmet in the 1980s. The PASGT helmet was manufactured in four sizes, had improved ventilation, and covered a larger part of the head. The shell was made of layers of Kevlar® K29 fibers and offered protection against 0.22 caliber, Type 2 fragment simulating projectile. The V50 ballistic limit for the PASGT helmet was required to be not less than 610 m/s (Tham et al., 2007). The PASGT helmet was in service for 20 years and demonstrated great field durability. However, with its standard 9 mm thickness shell, it barely met the operational needs. The PASGT helmet also had fitting problems.

2.3.2 Modular Integrated Communications Helmet and Advanced Combat Helmet

With an aim to reduce the weight of the PASGT helmet, the U.S. Army launched a new helmet development program. Two new helmets were introduced, namely the Modular Integrated Communications Helmet (MICH) and the Advanced Combat Helmet (ACH).

The MICH utilizes Kevlar® fibers and provides less coverage than the PASGT helmet. However, this causes less vision obstruction for the wearer and combines well with the interceptor body armor. For the PASGT helmet, the high collar of the interceptor body armor pushed the helmet forward, thus obstructing vision in prone position.

The ACH, derived from the MICH, is made from the Kevlar® K129 fiber. The Kevlar® K129 fiber has an areal density of around 185 g/m^2 compared to 270 g/m^2 for the Kevlar® K29 fiber, but has a strength which is 40% higher than that of the Kevlar® K29 fiber (used for the PASGT helmet). The Kevlar® K129 fiber also has a higher energy absorption capacity than the Kevlar® K29 fiber (Bilisik and Turhan, 2009). The ACH thus has a higher ballistic and impact protection capability than the PASGT helmet at a smaller weight.

The ACH also has a pad system inside the helmet, replacing the nylon cord suspension system used in the PASGT helmet. This provides a better fit to the wearer and can give a higher protection against blunt trauma in case of ballistic impact (e.g., Aare and Kleiven, 2005; Moss et al., 2009). Recently, a survey on soldiers' satisfaction with ballistic helmets was conducted by Ivins et al. (2007). The survey indicated a strong preference of the soldiers for the ACH over the PASGT helmet. The survey also identified some problems with the ACH. Table 1 lists a brief summary of the survey.

Table 1 Comparison of the ACH helmet with the PASGT helmet (Ivins et al., 2007)

Problem Type	Percentage of all ACH users (n = 535)	Percentage of all PASGT users (n = 570)
Loose Screws	11	1.8
Loose/Broken Straps	5.8	3.7
Hard/Loose pads	4.1	No padding
Heat Retention	1.5	0.9
Poor Fit	0.6	4
Falls from Head	0.6	0.7
Weight Satisfaction	84.7	6.4
Other	1.1	1.8

2.4 Modern Material Systems

2.4.1 Polymers

There are many factors that control the response of a material to ballistic impact. However, the main source of kinetic energy absorption is the straining and breakage of primary and secondary fibers. Therefore, the stress-strain curve and the fiber tensile strength play a major role in predicting the impact response of a ballistic fiber. Table 2 shows the tensile properties for various armor-grade fibers. Kevlar® fibers, variants of a rigid rod liquid crystalline synthetic polymer fiber developed by DuPont in 1965, have been used in most modern body armor systems. The PASGT helmet uses the Kevlar® K29 fiber. The ACH, which was fielded in 2003 to replace the PASGT helmet, uses the Kevlar® K129 fiber and provides an improvement in ballistic performance and user interface. The new padding system inside the ACH affords better comfort and higher protection. Like the PASGT helmet, the ACH utilizes a thermoset resin shell (as the matrix material) bonded to Kevlar® K129 fibers.

Thermoplastic resin shells have been considered as an alternative to thermoset resin shells. Thermoplastic resins are sufficiently tough and chemical resistant. Thermoplastics are also melt-processable. It has been shown that the elasticity of a matrix greatly affects the energy absorption capacity of a composite. A rigid matrix reduces the ballistic performance as compared to a flexible matrix (Faur-Csukat, 2006). However, thermoplastics have lower tensile strength than thermoset resins. This has an adverse effect on the structural stability and the transient deformation characteristics of the helmet. Thermoplastics (as matrix materials) are therefore used with fibers having a higher tensile modulus than the Kevlar® fibers to augment the matrix stiffness.

Table 2 Tensile properties for various fibers (Bilisik and Turhan, 2009; David et al., 2009a; Song, 1986)

Material	**Properties**			
	Density (g/cm^3)	**Breaking Strain (%)**	**Tensile Strength (MPa)**	**Tensile Modulus (GPa)**
Nylon 66	1.14	18.2	1006	5
Kevlar® K29	1.44	3.5	2794	67
Kevlar® K129	1.44	3.3	3429	96
PBO	1.58	3.8	7386	195
Spectra 1000	0.97	2.7	2995	172
Dyneema®	0.97	3.8	2500	120

Thermoplastics for ballistic applications have been studied extensively (Bilisik and Turhan, 2009; Walsh et al., 2005; Walsh et al., 2006). Both manufacturing and design aspects of thermoplastics were investigated in Walsh et al. (2005, 2006), where various Kevlar® fiber-thermoplastic matrix systems were explored. The weight was the primary consideration in preparing the samples. An increase in ballistic resistance was obtained at a much lower weight. However, the depth of the back-face signature increased considerably compared to that for a thermoset resin based helmet, thus increasing the possibility of blunt trauma injury. A detailed study of thermoplastics for ballistic applications was conducted in Song (1986), where semi-crystalline and amorphous polymer matrices were examined. The materials used for the samples were Kevlar® K29 fiber/nylon 66 matrix laminates, Kevlar® K29 fiber/polyetheretherketone (PEEK) matrix laminates, Kevlar® K29 fiber/polycarbonate matrix laminates, Kevlar® K29 fiber/polysulfone matrix laminates, Kevlar® KM2 fiber/polysulfone matrix laminates, and Kevlar® KM2 fiber/linear low-density polyethylene (LLDPE) matrix laminates. The effects of processing temperature, cooling rate, polymer morphology, fiber-wetting characteristics, reinforcing fabric configuration, and composite stiffness on the ballistic impact resistance of thermoplastic-based composites were investigated in Song (1986). The main energy absorbing mechanisms identified for the laminated composites were fiber failure in tension, matrix cracking, and delamination. Processing temperature had a significant effect on the ballistic performance of amorphous and low crystalline polymer composites. Increasing processing temperature improved the wet-ability, leading to dense packing of the matrix molecules. This resulted in a stiffer matrix, diminishing the energy absorption capacity. For semi-crystalline polymer composites, processing temperature changes the nature of the crystals formed. However, this was found to have very little effects on ballistic properties.

Fabric configuration also has a significant influence on ballistic properties (e.g., Cheng and Chen, 2010; David et al., 2009a).

The Enhanced Combat Helmet (ECH), which has been under development since 2007 for the U.S. Marine Corps and U.S. Army, makes use of the Dyneema® HB80 unidirectional composite material, which consists of a matrix of ultra high molecular weight polyethylene (UHMWPE) reinforced by carbon fibers (e.g., Xiong, 2004). The values of the ballistic limit for UHMWPE and several other materials are shown in Fig. 3.

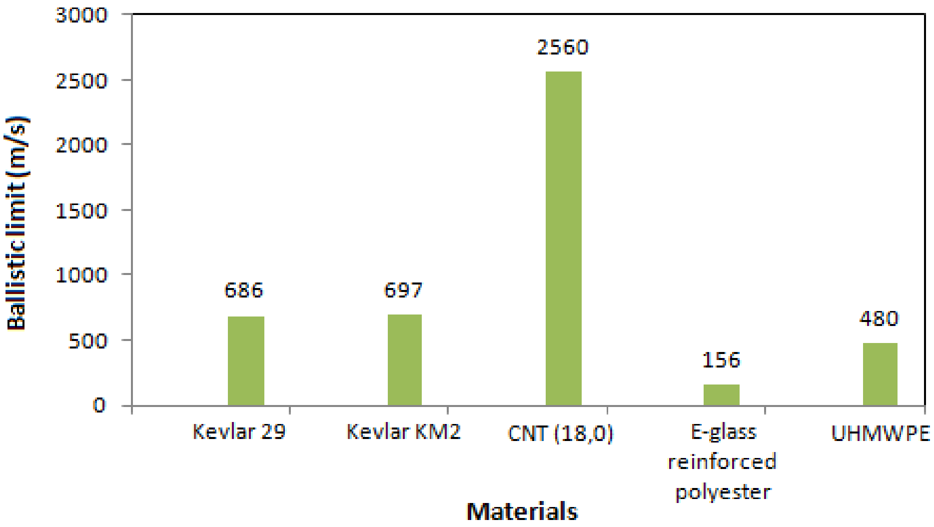

Figure 3. Ballistic limits for various materials (e.g., Song, 1986; David et al., 2009a). The value for the CNT was based on molecular dynamics simulations (Mylvaganam and Zhang, 2007).

2.5 Traumatic Brain Injury

2.5.1 Numerical Simulations

A number of injury models have been proposed to capture brain responses to blast waves. Finite element methods have been widely used to model the damage to the body induced by blast waves. To model the motion and response of the body and its internal elements, the simulations usually begin with generating geometric models of varying complexity.

Three-dimensional (3-D) imaging data obtained from magnetic resonance imaging (MRI) or computed tomography (CT) techniques can be utilized to generate geometric models of various parts of a human head. In such image-based geometric modeling, suitably smooth surfaces representing brain tissues can be extracted from 3-D MRI or CT imaging data. Once the geometric model is created, standard tetrahedral or hexahedral meshing algorithms can be implemented for finite element (FE) mesh generation. Image based geometric modeling has been used by Ganpule et al. (2010) for generating geometric models of skull, facial bones, neck bones, and brain tissues needed in their study on blast induced TBI.

Another popular approach is voxel meshing (Keyak et al., 1990). This method combines the surface detection and mesh creation stages in one process. In this approach, volumetric pixels (voxels) are divided into different regions using various segmentation techniques. These regions are then exported as hex elements. This algorithm is easy to implement, produces all hex mesh, and leads to conformity of mesh at interfaces. A 3-D FE human head model for studying brain trauma was proposed in Chen and Ostoja–Starzewski (2010) using the voxel meshing technique. The FE mesh of their head model, consisting entirely of hexahedral elements, was developed from MRI data sets using a custom developed C++ code. Five different tissue types – scalp, skull, CSF, grey mater, and white mater – were identified from the MRI imaging data using a segmentation procedure. Voxel meshing was also employed by Taylor and Ford (2009) to construct a head model based on the segmentation of high resolution photographic data using a pattern recognition algorithm.

A few commercial software packages that provide image based meshing capabilities are currently available, which include *Amira* (Mercury Systems, MA, USA), *Mimics* (Materialise, NJ, USA), *Simpleware* (Simpleware Ltd., UK), and *Scan23D* (Dassault Systèmes Solidworks Corp, Velizy, France). *Mimics* was used by El Sayed et al. (2008) to reconstruct FE mesh from MRI data. The resulting mesh consisted of 9 components – skull without facial bones, cerebrospinal fluid (CSF) in the form of a 3-mm thick layer, gray matter, white matter, cerebellum, corpus callosum, telencephalic nuclei, brain stem, and ventricles.

The effect of primary blast waves on the skull has been studied by Moore et al. (2009). The Bowen curve (Bowen et al., 1968) was used to obtain a threshold of 5.2 atm for lung injury, a lethal dose of 18.6 atm for 50% lung injury was adopted, and the upper and lower bounds for survivable blast brain injury were established. In Nyein et al. (2010), a FE model for an unprotected head was proposed using a mesh containing 808,766 elements (see Fig 4). The computational model distinguished different parts of the head: ventricle, glia, white matter, gray matter, eyes, venous sinus, cerebrospinal fluid (CSF), air sinus, muscle, skin and fat. The volumetric response of the brain tissue was described by the Tait equation of state, the deviatoric response by the neo-Hookean elasticity model, and the skull response by the Mie-Gruneisen/Hugoniot equation of state. Significantly different strain distributions were observed in different parts of the tissue material and brain. Based on the maximum compressive/tensile stress and von Mises stress in the brain, it was concluded that the blast intensity corresponding to 50% of the lethal lung injury caused mild traumatic brain injury (mTBI). In addition, direct blast propagation into the brain occurred with the skull absorbing very little or no pressure intensity.

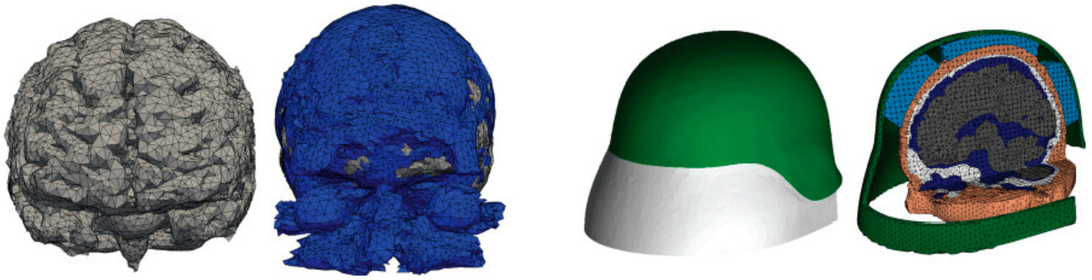

Figure 4. A detailed head model (Nyein et al., 2010).

A similar study was carried out by Grujicic et al. (2009). The comparison of the von Mises stress for three blast intensities showed that the stress values were not high enough to cause mTBI. However, direct passage of longitudinal and transverse pressure waves within the intra cranial cavity could lead to mTBI.

The effectiveness of the skull in protecting the brain from blast waves was studied by Teland (2010). A pig head model consisting of the skull, brain, and CSF was used. The material was assumed to be linearly elastic. It was found that the hard skull does not protect the brain from the blast waves. The pressure waves were not absorbed by the skull material but traveled through the skull to the brain.

Comparisons of brain responses to front and lateral impacts (see Fig. 5) have been studied by El Sayed et al. (2008). In their study, the load on the head was applied as a pressure wave rather than a direct blast. The pressure was applied as a semi-sinusoidal time distribution for six milliseconds (ms), with a peak magnitude of 7.90 kN. For the frontal impact, peak positive pressures were observed beneath the impact site, while negative pressures were observed in the area opposite to the impact site. Irreversible cavitation damage was also observed. However, no permanent shear damage was found.

For the lateral impact simulations, the magnitudes of the coup and countercoup pressures developed were much higher. In addition, the magnitude of the shear stress developed was ten times higher than that in the frontal impact case, causing shear yielding. This showed that a lateral impact had a more damaging effect on the brain than a direct frontal impact.

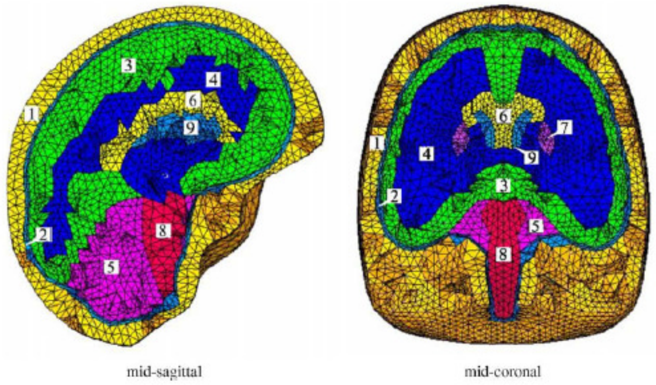

mid-sagittal
mid-coronal

Figure 5. Head model used by El-Sayed et al. (2008).

A detailed head model was used in Chafi et al. (2009) to predict the pressure distribution, shear stress distribution, and principal strain distribution in a brain subjected to a blast wave. The isotropic Mooney-Rivlin model was used to describe the hyper-elastic constitutive relation of the brain tissue material. The viscoelastic response is represented in terms of a convolution integral, and the relaxation modulus is described by a standard Prony series. The Jones-Wilkins-Lee equation of state (EOS) was used to model explosives, and the material parameters used in the EOS were those of trinitrotoluene (TNT). Three blast intensities corresponding to 0.0838, 0.205, and 0.5 lbs of TNT were used at a fixed standoff distance. In the simulations, no uniform pressure gradient was observed across the brain tissue. In addition, the classical coup and countercoup pattern was not observed (unlike in other studies). Both positive and negative pressures were observed at the impact site as well as at the opposite side. Based on the Ward criterion (Ward et al., 1980), for the blast scenarios generated by 0.205 lb and 0.5 lb TNT, the average peak positive pressure exceeded the established thresholds. The brainstem, white matter, and corpus callosum experienced maximum shear stresses. At early stages of impact, the pressure intensities were higher than shear stress magnitudes. However, the stress magnitudes elevated after these early stages. The maximum principle strains were observed in the brainstem. According to the criterion of Bain and Meaney (1998), for a blast scenario of 0.5 lb explosive, the principal strain values exceeded the established threshold.

2.5.2 Ballistic Helmet and Traumatic Brain Injury

Traditionally, combat helmet design has been focused on providing protection against ballistic impact from projectiles. The Advanced Combat Helmet (ACH) made from the Kevlar® fibers was designed to protect against shrapnel, fragmentation, and 9 mm bullet shots (see Fig. 6).

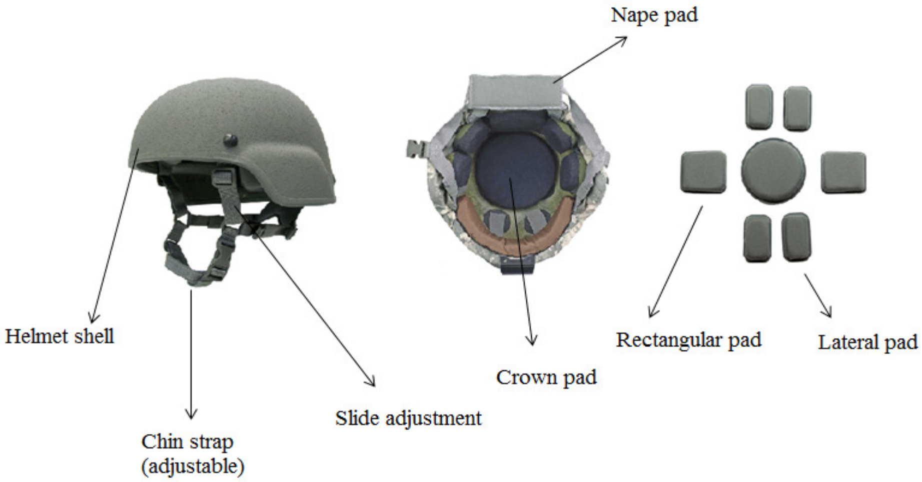

Figure 6. ACH and its parts.

The response of a Kevlar® helmet to ballistic impacts was studied in Tham et al. (2007). It was found that a Kevlar® helmet could defeat a high-velocity 9 mm bullet and a 1.1 gram fragment-simulating projectile (FSP).

There has been a recent interest in testing the effectiveness of the helmet against blast events and blunt trauma injuries. The response of a combat helmet to blast waves was studied by Moss et al. (2009) by modeling the skull as a hollow elastic ellipsoid containing viscoelastic CSF and using a simplified face, neck and body system with no lower jaw. The head was subjected to a shock wave with an overpressure of one bar over the ambient pressure and a 450m/s blast wind. For an unprotected head, the skull wall deforms and collides with the brain. This develops large positive and negative pressure spikes in the cranial cavity. It also creates damaging shear strains. For a head protected with a helmet, the 1.3 cm gap between the helmet and the head creates an "underwash" effect. The gap allows the blast wave to wash in between the helmet and the head. This causes more pressure on the skull than in an unprotected head. For a helmet with padding, the helmet is coupled to the head and the underwash effect is mitigated. It should be mentioned that without including lower jaw and anatomical details (such as skull thickness variations, grey or white matter, and ventricles), the model adopted by Moss et al. (2009) is overly simplified and needs to be validated, as also noted in Nyein et al. (2010).

In a recent study (Ganpule et al., 2010, 2011), it was observed that tight foam pads between a head and a helmet can eliminate the underwash effect and thus provide a better protection from blast.

The effect of an ACH and a conceptual face shield on stress wave propagation within the brain tissue following a blast has been studied in Nyein et al. (2010). A human head model was used along with a model of the ACH provided by the Natick Soldier Research Development and Engineering Center. The material models were the same as those used earlier in Moore et al. (2009). Simulations were carried out for an unprotected head, a head with a helmet, and a head with a helmet and a face shield. It was found that the main transmission pathway of the blast waves to the brain was through the soft tissues of the face. Tissue cavitation was also observed as a possible mechanism of brain damage. The simulation of a helmeted head with the current variant of the ACH showed that the helmet provides no mitigation of blast effects on the brain tissue, as it does not protect the face. The third simulation was carried out for a head with the ACH and with a conceptual face shield attached to it. It was observed that the presence of the face shield significantly contributed to reducing the stress intensity in the brain.

A similar study was carried out in Grujicic et al. (2009). The blast intensity and material models were taken to be the same as those used in Moore et al. (2009). Their simulations revealed that the blast wave propagates through the skull. It travels faster in the intra cranial cavity, and multiple reflections occur. Maximum compressive stresses were found on the impacted side, while the maximum tensile stresses were seen on the side opposite to the point of impact. Intra cranial shear stress values were substantially lower than those of the principle stresses. The maximum shear stresses were located in the brain stem. For both 5.2 atm and 18.6 atm blast intensities, no shear-induced mTBI was observed, while there was a possibility of contusion type TBI. For a head protected by a helmet, the findings obtained by Grujicic et al. (2010a) were contradictory to those reported in Moore et al. (2009) and Nyein et al. (2010). For the helmeted head, the load transfer path to the skull was found to be different. The underwash effect observed in other simulations was also seen. However, for the helmeted head a 40% reduction in the maximum principal stress magnitude and an 8% reduction in the maximum shear stress magnitude were obtained. No mention was made regarding the propagation of blast waves through the soft tissue of the face. This is in contrast to the simulations reported by others (e.g., Moore et al., 2009; Ganpule et al., 2011), where the helmet either produced an increase in the pressure intensity on the skull or produced no significant reduction.

A comparative study on the blast wave mitigation capability of suspension pad materials has been conducted by Grujicic et al. (2010b). The effects of blast waves on an unprotected head and a head protected with an ACH with polyurea as the suspension pad material were studied. In the absence of information about the currently used suspension pad material in the ACH, Ethylene-Vinyl-Acetate (EVA) was chosen as a second material (other than polyurea). The material models and the pressure intensities were taken to be the same as those used in their earlier study (Grujicic et al., 2010a). High peak axial stresses and peak particle velocities were chosen as parameters for comparison. It was found that polyurea lowered the peak stresses and peak velocities transferred to the skull (and hence to the brain). Because these two are primary TBI causing mechanisms, it was concluded that polyurea was a better suspension pad material than EVA.

The Department of Defense’s blast injury research program (Stuhmiller, 2008) and the non-lethal weapons human effects program under the guidance of the Air Force Research Laboratory (Simonds, 2008) were initiated to conduct biomedical research in order to improve the current understanding of blast injuries. The goal of these programs is to characterize the complete hazard caused by the blast waves. The thoracic human body models used to study ballistic impact of armor and the human head models employed to investigate the physical effects of blast were combined to form the Advanced Total Body Model (Simonds, 2008; Stuhmiller, 2008). An integrated finite element model consisting of head, neck, thorax, and abdominal regions was employed to understand the mechanisms for BTBI.

A study on the effect of facial protective devices on injury mitigation in BTBI was conducted by Jason (2010). The head and material models employed in this study were the same as the ones used in Nyein et al. (2010), and simulations were carried out for both the ACH and the ECH. The blast wave was generated by an explosion of 3.16 g of TNT in a free air explosion at a 0.12 m standoff distance. The model validation was carried out by comparing the simulated results for a side blast explosion with the experimental results obtained at the Naval Sea Systems Command Warfare Center (with experiments carried out on a series of mannequins) (Nyein et al., 2010). In order to reduce the effect of the blast waves travelling through the soft tissues of the face into the intra cranial cavity, a face shield (see Fig. 7) was added to the helmet. The material of the face shield was the same as that of the helmet shell. The following simulations were carried out on: a) an ACH with a face shield, b) an ECH with a face shield, c) an ACH with a pair of ski goggles, and d) an ECH with a pair of ski goggles. The material model of the goggles was the same as that of the helmet shell. It was observed that the face shield prevents the direct transmission of the negative and positive pressure waves through the soft tissue of the face to the brain. The transfer of the pressure waves occurs through the foam padding. An undesirable effect of the face shield was also observed. There is a late increase in the pressure imposed on the surface of the face because of the air trapped between the face shield and the face. It was also observed that the unprotected region in the rear of the head causes an increase in the pressure exerted on the soft tissues of the face. It was proposed to extend the helmet shell to cover the neck. For the simulation with the goggles, it was observed that the goggles protect the soft tissue of the face. However, physical interaction between the goggles and the head offers a new pathway for pressure transmission. It was also observed that this secondary pathway reduces the pressure transmitted to the head through the padding, i.e., it reduces the underwash effect. For the ECH, similar phenomena were observed.

The use of sandwich structures in helmet liners of the ACH for pressure wave attenuation was studied by Goel (2011). The author proposed to drill channels in the helmet liners, and fill these channels with an incompressible material, either fluid or solid, as shown in Fig. 8. Experimental and computational analyses were carried out on specially prepared samples but not on an actual helmet. Both solid (glass beads, aerogel, or solid foam) and liquid (glycerin, water, or AgileZorb) filler materials were tested. Glycerin was found to have the highest pressure attenuation ability among all filler materials tested. It was revealed that lower-porosity materials (such as glycerin and glass beads) showed lower energy transmission than high-density materials (such as aerogel). The use of glycerin resulted in a 50% reduction in the peak pressure. However, the use of glycerin led to a considerable increase in the weight of the liners.

Figure 7. Face shield and goggles suggested to improve blast mitigation capabilities of combat helmets (Jason, 2010).

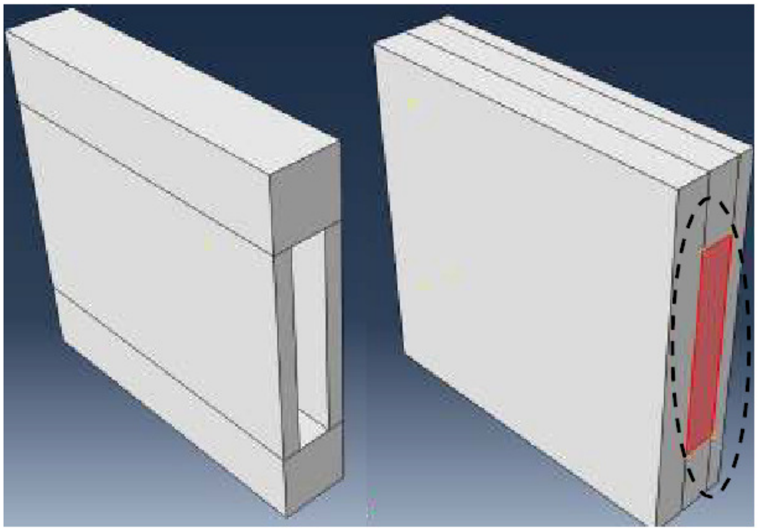

Figure 8. Drilling channels in the liner of an ACH filled with an incompressible material (Goel, 2011).

2.5.3 Damage Criteria for Brain

Damage criteria are useful for predicting the probability of TBI under mechanical loading. The currently used injury criterion is the head injury criterion (HIC) adopted by the National Highway Traffic Safety Administration (NHTSA) based on the work of Gadd (1966). The HIC is an empirical criterion mainly used in the automobile industry and is based on the probability of injury due to a global translational head acceleration. While the HIC is useful for predicting injury in automobile accidents, it may not be applicable for predicting blast induced TBI. This is because the HIC is based on global kinematics data to predict injury, whereas the blast-induced TBI is caused by intra cranial mechanical responses. Further, the HIC is based on experimental data, for which only external impact loading is applied. In addition, rotational head accelerations have not been taken into account in developing the HIC. In order to overcome these drawbacks, Newman proposed the Head Impact Power (HIP) criterion (Newman et al., 2000). This criterion is based on angular and linear accelerations. However, both these criteria are proposed for impact loading rather than blast loading. The two main known causes of BTBI are penetration of pressure waves into the skull and rotational acceleration.

In the past decade, many 3-D finite element head models have been used to develop injury criteria for the brain. The Wayne State University (WSU) head model (e.g., Zhang et al., 2009), MIT DVBIC head model (Nyein et al., 2010), SIMon head model (Takhounts et al., 2003a), and University of Louis Pasteur (ULP) head model (Willinger and Baumgartner, 2001) are some of the popular 3-D head models used in finite element analyses. Recent experimental validation (Marjoux et al., 2006) has shown that the SIMon head model gives rather inaccurate results for predicting TBI compared to the ULP model. This has been attributed to the fact that the head model used in the ULP criterion is closer to the real anatomy of a human head than the SIMon model.

Various injury criteria based on stress, strain, strain rate, intra-cranial pressure gradient, and type of explosives are summarized in Table 3. Except for the criterion reported in Chafi et al. (2009), none of the criteria listed in Table 3 have been developed for blast events. All the criteria have been developed for direct impact loading, which is minimal for blast events.

Even though a lot of efforts have been made to understand the mechanisms of TBI, injury thresholds for BTBI remain undetermined. Protective equipment designed using the existing injury criteria may be inadequate. The environment created by a shock wave is quite complex. In addition, pressure waves are initiated inside the intra cranial cavity. The intensity of a blast, nature of explosives used, and standoff distance all affect the brain tissue's response to loading. Superimposing tolerance curves for each kind of head injury and defining the lowest curve as a head injury tolerance criterion might be one way of going forward.

Table 3 Various local injury criteria based on pressure gradients, strains, stresses and strain rates

Criterion	Threshold	Location of Injury	Probability	Application	Reference
Stress					
von Mises	6-11 kPa	Corpus Callosum	50%	Rat brain/Car crash injuries	Shreiber et al. (1997)
	8.4 kPa	Corpus Callosum	50%	Footballers (FEM)	Kleiven (2008)
	> 30 kPa	Brain Neurological Lesions	100%	Motorcyclists/ Footballers	Willinger and Baumgartner (2001)
	> 16 kPa	Brain Neurological Lesions	50%	Motorcyclists/ Footballers (FEM)	
Shear	8-16 kPa	Diffuse Axonal Injuries	100%	Sheep Brain	Anderson et al. (1999)
	11-16.5 kPa	Diffuse Axonal Injuries	100%	Motorcycle Accidents	Claessens et al. (1997)
	> 10 kPa	Mild TBI	80%	Footballers (FEM)	Zhang et al. (2004)

Table 3 Continued

Criterion	**Threshold**	**Location of Injury**	**Probability**	**Application**	**Reference**
Strain					
$\varepsilon\dot{\varepsilon}$	30/s	Gray Matter	50%	Multiple specimens	Viano and Lovsund (1999)
$\varepsilon\dot{\varepsilon}$	10.1/s	Gray Matter	50%	Footballers (FEM)	Kleiven (2008)
$\varepsilon, \dot{\varepsilon}$	$\varepsilon > 0.2$ $\dot{\varepsilon} > 10/s$	White Matter	100%	Tissue culture	Morrison et al. (2003)
Shear Strain	> 0.24	Mild TBI	80%	Footballers (FEM)	Zhang et al. (2004)
Lagrangian Principal Strain	> 0.21 > 0.181	Morphological injury Electrophysiological Impairment	50%	Guinea Pigs	Bain and Meaney (1998)
Cumulative Strain	≥ 0.55	White Matter	50%	FEM	Takhounts et al. (2003a)
Intra Cranial Pressure (ICP)					
ICP	< 173 kPa > 235 kPa	Concussion	0% 100%	Animal/Human Cadavers (FEM)	Ward et al. (1980)
	> 90 kPa > −76 kPa	Injury (coup side) Injury (counter coup side)	50%	Footballers (FEM)	Zhang et al. (2004)
Amount of Explosives					
0.205 lb TNT (Standoff distance 160 cm)	ICP > 235 kPa	Coup/Counter Coup side	100%	FEM	Chafi et al. (2009)
	Shear stress > 16.5 kPa	Brain stem			
	Principal strain > 0.22				

2.6 Constitutive Modeling

As has been mentioned, experiments for studying blast-induced traumatic brain injury are mainly carried out on specially prepared models of human skulls and tissues, mannequins or dolls, and different animals. Numerical simulations are performed on geometrical models of skull and other brain components, with or without a helmet. All these experiments and simulations require constitutive modeling in order to assign appropriate properties to the constructed models to obtain accurate results.

In an experimental study on human brain tissues, Donnelly and Medige (1997) investigated shear properties at different strain rates. Brain tissues were obtained from fresh human cadavers. The brain specimens consisted of samples cut from brain cerebrum. The majority of the tests were performed at strain rates of 0, 30, 60, and 90/s, with some additional tests performed at 120 and 180/s. Thirty tests were performed at each strain rate, and all the samples were tested up to a shear strain of 100%. The stress-strain curves were fitted with a two-parameter power-law function of the form $\sigma = A\varepsilon^B$. A common value of 1.28 was used for the exponent B, while the amplitude of A varied with the strain rate. It was found that rate effects were predominant between 0 to 60/s, while no rate effect was observed beyond 60/s. Shafieian et al. (2011) performed shear deformation tests on bovine brain tissues at strain rates of 100~750/s. The average shear modulus varied from 11.17 kPa at 100/s to 22.44 kPa at 750/s. These results validated the hypothesis of Donnelly and Medige (1997) that the response of a brain tissue in shear at strain rates higher than 100/s is independent of the strain rate.

Table 4 Properties of Some Materials Used for the U.S. Army Helmets (e.g., Song, 1986; Hearle, 2001; Bilisik and Turhan, 2009; Czechowski et al., 2012)

Helmet	**Material (Shell/Fabric)**	**Properties**	**Shell (Matrix)**	**Fiber (Reinforcement)**
Hadfield	Steel	Tensile Strength (MPa)	250	-
		Tensile Modulus (GPa)	183	-
		Breaking Strain (%)	10	-
PASGT	Thermoset resin/ Kevlar® K29 composite	Tensile Strength (MPa)	7,386	2,794
		Tensile Modulus (GPa)	195	67
		Breaking Strain (%)	3.8	3.5
ACH	Thermoset resin/ Kevlar® K129 composite	Tensile Strength (MPa)	7,386	3,429
		Tensile Modulus (GPa)	195	96
		Breaking Strain (%)	3.8	3.3
ECH	Dyneema® HB80 composite	Tensile Strength (MPa)	Not available	2,500
		Tensile Modulus (GPa)	Not available	120
		Breaking Strain (%)	Not available	3.5~3.7

More discussions on mechanical testing of brain tissues can be found in a comprehensive review paper by Chatelin et al. (2010). The material properties for the helmet are standard, depending upon the helmet type. The properties of some materials used for helmets are given in Table 4.

Development of material models for biological brain tissues is an area of on-going research (e.g., Hrapko et al., 2009; Clayton et al., 2012). From the biomechanical perspective, brain is a very complex organ involving many sub-structures including brain stem, cerebral cortex, and thalamus. Understanding how the loading and kinematic boundary conditions applied to the skull/organ translate into the stress-strain relation of the brain tissue is challenging because of the interplay among a number of factors such as non-linear visco-elasticity, anisotropy, rate dependency, hysteresis behavior in cyclic tension-compression tests, and sensitivity. Many biomechanical, experimental, and numerical studies have been carried out to develop constitutive models for the brain material. The constitutive models developed can be divided into three main categories, as listed below.

2.6.1 Linear Viscoelastic Models

Linear viscoelastic models (e.g., Gefen et al., 2003; Nicolle et al., 2004) describe the creep and relaxation responses. Standard viscoelastic models or some variants of them are used to model tissue responses. The number of material constants needed in such a model depends on how many springs and dashpots are used (e.g., David et al., 2009b, 2010, 2011, 2012). However, linear viscoelastic models are suitable only over a small strain regime and are not adequate to describe tissue responses under blast loading.

2.6.2 Large Strain Hyper-Elastic Models

The Helmholtz free energy function is ordinarily used to define a hyper-elastic material or Green elastic material. Fung (Fung, 1967) proposed such a function, called a pseudo-strain energy function, to describe a particular aspect of an inelastic material. One approach in hyper-elastic modeling is to use polynomial strain energy functions to describe the material response (Fung, 1967; Velardi et al., 2006). The material parameters used in a polynomial function are numerous and may not have any physical meaning. These models tend to be numerically unstable at high strains (Balzani et al., 2006), and may violate convexity conditions. Another approach is to use the invariants of the deformation gradient tensor (e.g., Holzapfel et al., 2000; Merodio and Ogden, 2003; Dorfmann et al., 2007). This approach can be used to describe the anisotropic behavior of soft tissues by decoupling a strain energy density function into contributions from fiber and matrix phases. This is the most often used approach. However, hyper-elastic models represent only elastic or quasi-static deformations. These models alone cannot capture the complexities of the tissue response such as permanent deformations and memory effects. In the decoupled framework, the energy contribution from the matrix depends on the first and second invariants of the Cauchy-Green strain tensor, while the fibers are considered as non-linear springs with the energy contribution depending on the fourth invariant of the Cauchy-Green strain tensor. An extensive literature review has shown that almost all current phenomenological models use this approach (e.g., Wright and Ramesh, 2012; Chatelin et al., 2012). However, a strain energy density function depending only on the fourth invariant is inadequate to describe the brain tissue behavior at medium to high strains, especially for shear loading. This is particularly important for simulating blast injuries, as shearing failures (such as diffuse axonal injuries) are a primary cause of TBI. In addition, the bulk modulus of the brain tissue is considerably higher than the shear modulus (Stalnaker, 1969; McElhaney et al., 1976). Therefore, it is necessary that a constitutive model developed to simulate TBI mechanisms accurately characterize the shear as well as the tension/compression behavior of the brain tissue.

2.6.3 Large Strain Hyper-Viscoelastic Models

Hyper-viscoelastic constitutive modeling combines the methodologies of linear viscoelasticity and hyper-elasticity.

The Mooney-Rivlin hyper-elastic model and the Neo-Hookean material model are the most commonly used constitutive equations to represent quasi-static responses of brain tissues. For example, Mendis (1992) used hyper-viscoelastic modeling to characterize large deformations of brain tissues. The quasi-static deformation (hyper-elastic part) was represented by an incompressible two parameter Mooney-Rivlin model. The material parameters for the viscoelastic model were determined by fitting with experimental data from rate-dependent compression tests. Wang and Wineman (1972) constructed a continuum mechanics model for the probe test of Fallenstein and Hulce (1969) by treating the brain tissue as a homogenous, isotropic, linear, viscoelastic material. They assumed that the skull is entirely filled by the brain and the skull is rigid with zero deformation. Also, the shear effects at the brain-skull interface are ignored in their model. A numerical method was implemented to solve for the shear stress relaxation functions in terms of measured displacements and forces by the probe.

Darvish and Crandall (2001) proposed a third-order non-linear Green-Rivlin viscoelastic model and compared it with a third-order quasi-linear viscoelastic model. For both the models, the elastic response was represented by a second-order Rivlin strain energy density function. They also tested bovine brain tissues in simple shear using forced vibrations from 0.5 to 200 Hz up to a Lagrangian shear strain of 20%. The third-order non-linear properties were characterized by applying simple, double, and triple harmonic inputs. The fully non-linear Green–Rivlin model also contains inter-modular distortions: frequency combinations of the fundamental frequencies and their integer harmonics. This study was continued by Takhounts et al. (2003b), where bovine and human brain tissues were compared. A linear viscoelastic shear strain limit of 17.5% was established for the brain tissues. The quasi-linear viscoelastic model was found to be suitable up to a strain value of 50%, while the Green-Rivlin non-linear model was seen to work for any shear strain range.

Hyper-viscoelastic models also use a decoupled representation of the Helmholtz free energy function. One way is to decompose the total deformation gradient tensor into an elastic part and a viscoelastic part. El Sayed et al. (2008) and Prevost et al. (2011) developed two non-linear models based on this decomposition technique. El Sayed et al. (2008) proposed a generalized framework where a number of Maxwell-type relaxation viscoelastic networks were considered in parallel with viscoplastic networks. The number of material constants adopted varied with the number of networks used. By utilizing this model, they were able to capture the hysteretic and dissipative characteristics of soft tissues in tension up to a strain of 50%. Prevost et al. (2011) used an elastic network to represent instantaneous deformations and a viscoelastic network for dissipative responses. Hrapko et al. (2008) used a Mooney-Rivlin viscoelastic network along with a non-linear hyper-elastic spring to model shear and compressive responses up to a strain rate of 1/s. This methodology of decomposing the deformation gradient tensor into an elastic part and a viscoelastic part is based on the theory developed by Lee (1969). However, this decomposition is built upon the assumptions that the body is isotropic in the reference configuration and the origin in the stress space always lies inside the body (Green and Naghdi, 1971). Therefore, this method cannot be extended to model the anisotropic response of a soft tissue. Another way of implementing hyper-viscoelastic models is to decompose the deformation gradient tensor into a dilatational part and a volume-preserving part. This method, unlike the one by Lee (1969), is not restricted to isotropy. This volume preserving and volume changing decomposition technique has been used to develop constitutive models for knee ligaments and tendons (Pioletti, 1997), musculoaponeurotic system and facial skin tissue (Rubin and Bodner, 2001), bovine liver tissue (Roan and Vemaganti, 2010), porcine brain tissue (Hrapko et al., 2008), arteries (Holzapfel and Gasser, 2000), and caterpillar muscle (Dorfmann et al., 2007). All these models have been developed to capture tissue responses in a uniaxial tension and have been validated for a limited range of loading regimes and low strain rates. Several studies have been conducted to determine the range of strains and strain rates associated with TBI. Strains greater than 10% and strain rates greater than 10/s have been observed to cause severe damage to brain tissues (Rashid et al., 2012).

CHAPTER III

A TRANSVERSELY ISOTROPIC VISCO-HYPERELASTIC CONSTITUTIVE MODEL FOR SOFT TISSUES

3.1 Introduction

Soft tissues represent body tissues that envelope, bind, connect and support other body parts. Mechanical behavior of a soft tissue can be characterized by non-linear elastic deformations, strain rate sensitivity, hysteresis, viscoelastic responses (relaxation and creep), and permanent strains. Soft tissues have been extensively studied using continuum mechanics and non-linear elasticity (e.g., Humphrey, 2003; Holzapfel and Ogden, 2010).

Brain tissues (e.g., Prange and Margulies, 2002; Velardi et al., 2006; Ning et al., 2006; Pervin and Chen, 2010), spinal cord tissues (e.g., Sacks and Sun, 2003; Peng et al., 2006), and ligaments (e.g., Zhurov et al., 2007) have been found to be transversely isotropic. Body tissues exhibiting orthotropic material symmetry include cardiac tissues (e.g., Dokos et al., 2002; Holzapfel and Ogden, 2009) and arteries (e.g., Holzapfel and Ogden, 2010). The current study is focused on the constitutive modeling of transversely isotropic soft tissues, which can be treated as hyperelastic or visco-hyperelastic materials.

For a hyperelastic or Green elastic material, a strain energy density function can be used to determine all stress components. One approach is to use a polynomial strain energy density function to describe the material response (e.g., Vaishnav et al., 1972;

Fung et al., 1979). The material parameters involved in such a polynomial function are numerous and often do not have any physical meaning. These models tend to be numerically unstable at high strains and violate convexity conditions (e.g., Holzapfel et al., 2000). Another approach is to work with a strain energy density function that contains two terms – one for the matrix and the other for the reinforcing fibers (e.g.,Holzapfel et al., 2000; Ciarletta et al., 2010). The matrix is often modeled as a neo-Hookean material, a compressible Blatz-Ko material, or a Mooney-Rivlin solid. The most commonly used reinforcing model is the "standard reinforcing model" (e.g., Horgan and Saccomandi, 2005; Holzapfel and Ogden, 2010). In this model, the strain energy density function for the isotropic matrix is augmented by a term for the reinforcing fibers, which is a function (usually exponential or power) of a fourth invariant of the right Cauchy-Green deformation tensor. It is assumed that the fibers have no influence on the mechanical behavior of a soft tissue in compression, for its along-fiber shear deformation, or when it is stretched perpendicular to the fiber orientation.

Constitutive modeling of soft tissues as hyperelastic materials can also be conducted by using separate strain energy density functions for the matrix, fibers, and fiber-matrix interaction zone (e.g., Wu and Yao, 1976; Criscione et al., 2001; Lu et al., 2012). This additive decomposition of the total strain energy into three separateterms is based on the experimental finding that intralamellar fiber-fiber and fiber-matrix interactions make a significant contribution to soft tissue stiffness. To describe the interaction energy, Criscione et al. (2001) proposed five physically based invariants. A phenomenological model was developed by Peng et al. (2006) for human annulus fibrosus by providing a new strain energy density function to account for the fiber-matrix shearing interaction. Guo et al. (2006) explained the shear interaction based on mechanics of composites, which was also verified numerically (Guo et al., 2007).

The effect of strain rate on soft tissues is important, particularly for blast-induced traumatic brain injuries. Experiments have demonstrated that brain tissues are sensitive to the time scale of loading. A brain tissue responds immediately to loading, is sensitive to load variations, and remembers the history of loading (e.g., Prevost et al., 2011). It has been experimentally observed that shear responses of human brain tissues are rate-dependent (Shuck and Advani, 1972; Hrapko et al., 2008; Donnelly and Medige, 1997). Changes in strain rate generate additional amounts of stress in the soft tissue. Tensile/compressive responses of brain tissues are also found to be rate-dependent (Tamura et al., 2007, 2008). Brain tissue responses under tension/compression loading stiffen considerably as the rate of loading increases (Rashid et al., 2012). Unlike shear responses, tensile/compressive responses are explicitly more sensitive at higher strain rates (Tamura et al., 2007, 2008). This is of particular importance in modeling traumatic brain injuries(TBI)induced by blast events, where the duration of impact is on the order of milliseconds· Explicit modeling of strain rate responses will help characterize tissue properties near impact sites (particularly useful in modeling TBI) over the expected range of loading rate.

In this Chapter, a new strain energy density function is proposed for soft tissues by modeling a soft tissue as a transversely isotropic composite consisting of a matrix (base) material and reinforcing fibers. The matrix (elastin is regarded as isotropic and described by using the neo-Hookean strain energy density function. Another function is used to represent the contributions from both fiber stretching and fiber-matrix interaction. The rest of this paper is organized as follows. In section 3.2, elements of continuum mechanics essential for the formulation are presented. In section 3.3, a new strain energy density function for describing quasi-static responses of soft tissues is proposed and examined, and its predictions are compared with those by a standard reinforcing model. Relevant issues on the polyconvexity of the strain energy density function and the ellipticity of the elasticity tensor are also briefly addressed. In section 3.4, a viscous potential is proposed for simulating rate-dependent responses of soft tissues (treating as transversely isotropic visco-hyperelastic materials). In addition, explicit expressions for the fourth-order elasticity and viscosity tensors are provided in general forms for transversely isotropic visco-hyperelastic materials, which can be implemented infinite element models for soft tissues.

3.2 Elements of Continuum Mechanics

3.2.1 Kinematics

Let **X** be the position vector of a material point in the undeformed (reference) configuration, and **x** be the corresponding position vector in the deformed configuration. The latter is related to the former through the equation of motion:

$$\mathbf{x} = \chi(\mathbf{X}, t), \tag{3.1}$$

where χ is a function describing the motion. The deformation gradient tensor, $\boldsymbol{F}$, is given by

$$\mathbf{F} = \frac{\partial \mathbf{x}}{\partial \mathbf{X}}, \tag{3.2}$$

which is a two-point tensor mapping the vector d**X** in the reference configuration to the vector d**x** in the deformed configuration (i.e., d**x** = **F**d**X**). It is required that **F** satisfy

$$J = \det \mathbf{F} > 0, \tag{3.3}$$

where J is the Jacobian representing the ratio of the deformed volume dv to the undeformed volume dV (i.e., dv = JdV).

The right and left Cauchy-Green deformation tensors are, respectively, given by

$$\mathbf{C} = \mathbf{F}^T\mathbf{F}, \ \mathbf{B} = \mathbf{F}\mathbf{F}^T, \tag{3.4a,b}$$

where the superscript T denotes the transpose of the tensor.

The three principal invariants of **C** are defined as

$$I_1 = tr\mathbf{C}, \ I_2 = \frac{1}{2}\left[(tr\mathbf{C})^2 - tr(\mathbf{C}^2)\right], \ I_3 = \det \mathbf{C}, \tag{3.5}$$

which are the identical to those of **B**. For an incompressible material, $I_3 = J^2 = 1$. For an isotropic hyperelastic material, the strain energy density function can be constructed using these three invariants, which forms an integrity basis (e.g., Spencer, 1971; Boehler, 1987; Zheng et al., 1994).

For a transversely isotropic hyperelastic material with a preferred direction described by the unit vector $\boldsymbol{a}_0$ in the reference configuration, two additional invariants defined by

$$I_4 = \boldsymbol{a}_0 \bullet \mathbf{C}\boldsymbol{a}_0, \quad I_5 = \boldsymbol{a}_0 \bullet \mathbf{C}^2\boldsymbol{a}_0 \tag{3.6}$$

are needed in the invariant formulation of the constitutive equations (Spencer, 1972). If the reinforcing fibers are considered inextensible, then $I_4 = 1$.

It should be mentioned that the number of invariants (i.e., five) required in the invariant formulation corresponds to the number of independent stiffness or compliance constants needed for characterizing a transversely isotropic linearly elastic material (e.g., Ding et al., 2006; Gao and Mao, 2013).A general discussion on the link between the invariant formulation and the linearized elastic moduli of a transversely isotropic material has been provided by Schröder and Neff (2003).

Note that among the five invariants defined in Eqs. (3.5) and (3.6) only I_3 and I_4 can be physically interpreted, with $\sqrt{I_3}$ and $\sqrt{I_4}$ being, respectively, the volume ratio and the stretch in the fiber direction $\boldsymbol{a}_0$. This motivated the efforts in developing physically-based invariants, as alternatives to I_1~I_5 defined in Eqs. (3.5) and (3.6),for describing mechanical responses of transversely isotropic hyperelastic materials (e.g., Criscione at al., 2001; Lu and Zhang, 2005; Shariff, 2008).

The rate of deformation tensor is given by

$$\mathbf{D} = \frac{1}{2}\left(\mathbf{L} + \mathbf{L}^T\right), \tag{3.7}$$

where $\mathbf{L} = \nabla\mathbf{v}$ is the velocity gradient. It can be readily shown that

$$\mathbf{L} = \dot{\mathbf{F}}\mathbf{F}^{-1}, \tag{3.8}$$

where the overhead dot represents the total time derivative, and the superscript "–" denotes the inverse. It follows from Eqs. (3.4a), (3.7) and (3.8) that the total material derivative of $\mathbf{C}$ is given by

$$\dot{\mathbf{C}} \equiv \frac{D\mathbf{C}}{Dt} = 2\mathbf{F}^T\mathbf{D}\mathbf{F}. \tag{3.9}$$

3.2.1 Stress Tensors

For hyperelastic materials, the use of the principle of material frame indifference and the first and second laws of thermodynamics gives

$$\mathbf{S} = 2\frac{\partial W}{\partial \mathbf{C}}, \tag{3.10}$$

where **S** is the second Piola-Kirchhoff (P-K) stress tensor (measuring the force per unit undeformed area), and W (= $W(\mathbf{C})$) is the strain energy density function (measuring the strain energy per unit undeformed volume). The Cauchy stress (measuring the force per unit deformed area) can be computed from **S** in Eq. (3.10) as

$$\boldsymbol{\sigma} = 2J^{-1}\mathbf{F}\frac{\partial W}{\partial \mathbf{C}}\mathbf{F}^T. \tag{3.11}$$

Equations (3.10) and (3.11) are compressible materials.

For incompressible materials with $J = 1$, Eqs. (3.10) and (3.11) become

$$\mathbf{S} = 2\frac{\partial W}{\partial \mathbf{C}} - p\mathbf{C}^{-1}, \quad \boldsymbol{\sigma} = 2\mathbf{F}\frac{\partial W}{\partial \mathbf{C}}\mathbf{F}^T - p\mathbf{I}, \tag{3.12a,b}$$

where p is the hydrostatic pressure acting as a Lagrange multiplier (associated with the kinematic constraint $\det\mathbf{C} = 1$), and **I** is the second-order identity tensor.

For a transversely isotropic hyperelastic material, the strain energy density function can be constructed using the five invariants $I_1 - I_5$ (Spencer, 1972), i.e.,

$$W = W(I_1, I_2, I_3, I_4, I_5), \tag{3.13}$$

where I_i ($i \in \{1, 2, 3, 4, 5\}$) are functions of **C** defined in Eqs. (3.4) and (3.5). It then follows from Eqs. (3.12a) and (3.13), with the help of the chain rule, that

$$\boldsymbol{S} = 2\sum_{j=1}^{5} \frac{\partial W}{\partial I_j} \frac{\partial I_j}{\partial \boldsymbol{C}} - p\mathbf{C}^{-1}, \tag{3.14}$$

where

$$\frac{\partial I_1}{\partial \mathbf{C}} = \mathbf{I},\ \frac{\partial I_2}{\partial \mathbf{C}} = I_1\mathbf{I} - \mathbf{C},\ \frac{\partial I_3}{\partial \mathbf{C}} = I_3\mathbf{C}^{-1},\ \frac{\partial I_4}{\partial \mathbf{C}} = \mathbf{a}_0 \otimes \mathbf{a}_0,\ \frac{\partial I_5}{\partial \mathbf{C}} = \mathbf{a}_0 \otimes \mathbf{C}\mathbf{a}_0 + \mathbf{C}^T\mathbf{a}_0 \otimes \mathbf{a}_0, \tag{3.15}$$

which are directly obtained from Eqs. (3.5) and (3.6).

Using Eq. (3.15) in Eq. (3.14) gives the second Piola-Kirchhoff stress as

$$\begin{aligned}\mathbf{S} = 2\left[\left(\frac{\partial W}{\partial I_1} + I_1\frac{\partial W}{\partial I_2}\right)\mathbf{I} - \frac{\partial W}{\partial I_2}\mathbf{C} + \frac{\partial W}{\partial I_4}\mathbf{a}_0 \otimes \mathbf{a}_0 + \frac{\partial W}{\partial I_5}\left(\mathbf{a}_0 \otimes \mathbf{C}\mathbf{a}_0 + \mathbf{C}^T\mathbf{a}_0 \otimes \mathbf{a}_0\right)\right] \\ - p\mathbf{C}^{-1},\end{aligned} \tag{3.16}$$

Similarly, substituting Eqs. (3.13) and (3.15) into Eq. (3.12b) results in, with the help of the Cayley-Hamilton theorem,

$$\boldsymbol{\sigma} = 2\left[\frac{\partial W}{\partial I_1}\mathbf{B} - \frac{\partial W}{\partial I_2}\mathbf{B}^{-1} + I_4\frac{\partial W}{\partial I_4}\mathbf{a} \otimes \mathbf{a} + I_4\frac{\partial W}{\partial I_5}\left(\mathbf{a} \otimes \mathbf{B}\mathbf{a} + \mathbf{B}^T\mathbf{a} \otimes \mathbf{a}\right)\right] - p\mathbf{I} \tag{3.17}$$

as the Cauchy stress, where the $\partial W/\partial I_3$term and one term containing $\partial W/\partial I_2$ have been consolidated with the hydrostatic pressure term.

3.2.1 Constitutive Laws

A constitutive law is required to describe the stress-strain relation of a material. Any constitutive law must satisfy the principle of determinism, the principle of local action, and the principle of material frame indifference (Truesdell et al., 2004). It has been shown that the following constitutive law satisfies all these three principles (e.g., Pioletti and Rakotomanana, 2000):

$$\mathbf{S}(t) = \mathbf{S}_e(\mathbf{C}(t)) + \Im_{s=0}^{\infty}[\mathbf{G}(t-s); \mathbf{C}(t)], \tag{3.18}$$

where **S** is the second Piola-Kirchhoff stress tensor, $\mathbf{S}_\mathrm{e}(\mathbf{C}(t))$ is an equilibrium term representing the elastic response, **C** is the right Cauchy-Green deformation tensor, t is the present time, s is the elapsed time, and $\Im$ is a functional describing the history of $\mathbf{G}(t - s) = \mathbf{C}(t - s) - \mathbf{C}(t)$.

Equation (3.18) gives a general constitutive equation for a simple material. It says that the stress at the present time t depends on the values of the right Cauchy-Green deformation tensor at all times $s \geq 0$. It may happen that only a small part of the deformation history has an influence on the stress. That is, only values of **C** at s close to zero affect the value of **S**. Hence, **C** may be approximated by a Taylor series near $s = 0$ up to some order. As a result, the stress depends only on a finite number of time derivatives of **C**. Such a material is called a material of differential type (Truesdell et al., 2004). In particular, if only the first time derivative is considered as $s \rightarrow 0$, Eq. (3.18) can be rewritten as

$$\begin{aligned} \mathbf{S}(t) &= \mathbf{S}_e(\mathbf{C}(t)) + \Im_{s=0}^{\delta}[\mathbf{G}(t-s); \mathbf{C}(t)] + \Im_{s=\delta}^{\infty}[\mathbf{G}(t-s); \mathbf{C}(t)] \\ &= \mathbf{S}_e(\mathbf{C}(t)) + \mathbf{S}_v(\dot{\mathbf{C}}(t); \mathbf{C}(t)) + \Im_{s=\delta}^{\infty}[\mathbf{G}(t-s); \mathbf{C}(t)], \end{aligned} \tag{3.19}$$

where $\delta \rightarrow 0^+$. Note that the response functional $\Im$ in Eq. (3.19) can be expressed in terms of an integral to obtain

$$\mathbf{S}(t) = \underbrace{\mathbf{S}_e(\mathbf{C}(t))}_{\substack{\textit{Equilibrium}\\ \textit{response}}} + \underbrace{\mathrm{S}_v(\dot{\mathbf{C}}(t);\mathbf{C}(t))}_{\substack{\textit{Short-term}\\ \textit{memory response}}} + \underbrace{\int_{\delta}^{\infty} \Sigma(\mathbf{G}(t-s), s; \mathbf{C}(t))ds}_{\substack{\textit{Long-term}\\ \textit{memory response}}}. \tag{3.20}$$

Equation (3.20) is a general constitutive law for a material of integral type.

When only short term effects is included, Eq. (3.20) reduces to

$$\mathbf{S}(t) = \mathbf{S}_e(\mathbf{C}(t)) + \mathbf{S}_v(\dot{\mathbf{C}}(t);\mathbf{C}(t)), \tag{3.21}$$

where the first term is the elastic (equilibrium state) stress, and the second term is the rate-dependent viscous (non-equilibrium state)stress.

3.3 Quasi-static Response

A quasi-static response represents an equilibrium response of a soft tissue as $t \rightarrow \infty$.

For transversely isotropic hyperelastic materials, it has been shown (Spencer, 1972) that in addition to the principal invariants I_1, I_2, I_3 for isotropic materials, two quasi-invariants I_4 and I_5 are required to fully describe the material response, which are defined in Eqs. (3.6). Note that the invariant I_4 is directly linked to the fiber stretch, and the invariant I_5 is related to the fiber stretch and registers the fiber matrix shear interaction.

The invariant I_4 has been extensively used to model soft tissues (e.g., Holzapfel et al., 2000; Horgan and Saccomandi, 2004; Holzapfel and Ogden, 2010; Chatelin et al., 2012; Wright and Ramesh, 2012). As an example, a strain energy density function of the following decoupled form has been proposed:

$$W\left(I_1, I_2, I_4\right) = W_{matrix}\left(I_1, I_2\right) + W_{fiber}\left(I_4\right), \tag{3.22}$$

where $W_{fiber}(I_4)$, called the *standard reinforcing model*, is a convex function of I_4 (e.g., Holzapfel et al., 2000; Dorfmann et al., 2007).

However, the invariant I_5 has rarely been used due to a lack of understanding of the energy contribution from the fiber-matrix interaction. By analogy with Eq. (3.22), a strain energy function involving I_5 can be defined to have the form:

$$W\left(I_1, I_2, I_5\right) = W_{matrix}\left(I_1, I_2\right) + W_{fiber}\left(I_5\right). \tag{3.23}$$

Merodio and Ogden (2002, 2003, 2004) studied models involving the invariant I_5 and compared the resulting predictions with those by models containing the invariant I_4. They found that the constitutive models employing the strain energy density function of the form in Eq. (3.23) are considerably stiffer than those models based on the strain energy density function of the form in Eq. (3.22). They also showed that the models based on Eq. (3.23) are numerically unstable, as I_5 can have multiple minima with respect to $\mathbf{C}$.

Schröder and Neff (2003) proposed a variety of strain energy density functions for modeling transversely isotropic soft tissues based on the five invariants I_1~I_5defined in Eqs. (3.5) and (3.6). Some of their functions are summarized in Table 5 along with several other commonly used invariants for modeling transversely isotropic materials.

Balzani et al. (2006) suggested a strain energy density function for biological soft tissues by using the mixed invariant K_3 listed in Table 5, which contains three or more material parameters and has been used to fit experimental data obtained under uniaxial tensile loading.

Table 5 Invariant terms for transversely isotropic soft tissues

Invariant term	**Shortening (compressive loading)**	**Elongation (tensile loading)**	**Suitability for modeling soft tissues**
$I_1, I_1^2, \frac{I_1}{I_3^{1/3}}, \frac{I_1^2}{I_3^{1/3}}$	Increase	Increase	Isotropic invariants. Suitable for modeling isotropic non-collagenous matrix
$I_2, I_2^2, \frac{I_2}{I_3^{1/3}}, \frac{I_2^2}{I_2^{1/3}}$	Increase	Increase	
$I_4, I_4^2, I_1 I_4$	Decrease	Increase	Suitable for embedded collagen fibers
I_5	Increase or decrease	Increase or decrease	Not Polyconvex
$K_1 = I_2 + I_5 - I_1 I_4$	Increase	Decrease	Unsuitable for collagen fibers
$K_2 = I_1 - I_4$	Increase	Increase	Unsuitable for collagen fibers.
$K_3 = I_1 I_4 - I_5$	Decrease	Increase	Suitable for collagen fibers
$I_1^2 + I_1 I_4$	Increase	Increase	Unsuitable for collagen fibers
$3I_1^2 - I_1 I_4$	Increase	Increase	Unsuitable for collagen fibers
$3I_1 - 2I_4$	Increase	Decrease	Unsuitable for collagen fibers
$2I_2^2 + I_2 I_5 - I_1 I_2 I_4$	Increase	Increase	Unsuitable for collagen fibers
$2I_2^2 + I_1 I_2 I_4 - I_2 I_5$	Increase	Increase	Unsuitable for collagen fibers
$K_4 = I_2 - 2I_5 + 2I_1 I_4$	Decrease	Increase	Suitable for collagen fibers

Following the studies of Schröder and Neff (2003) and Balzani et al. (2006) and based on the observations that fibers have negligible compression stiffness (thereby not contributing to the strain energy when under contraction) and the fiber-matrix interaction affects the mechanical response of a soft tissue, two strain energy density functions listed in Table 6 are proposed in the current study, each of which contains only two material parameters.

Table 6 The strain energy density functions proposed in the current study

Strain Energy Density Function	Model No.
$W_e^I = \frac{\mu}{2}(I_1 - 3) - \frac{\mu_1}{2} J_m \ln\left[1 - \frac{(I_4 - 1)^n}{J_m}\right]$	I
$W_e^{II} = \frac{\mu}{2}(I_1 - 3) + \mu_1 (K_4 - 7)^q,$ $K_4 = I_2 + 2I_1 I_4 - 2I_5$	II

In Table 6, μ is the shear modulus for infinitesimal deformations, μ_1 is a material constant, n and q are two constants, and J_m is the limiting value of $(I_1 - 3)$ accounting for the polymeric chain extensibility (Horgan and Saccomandi, 2005). Model I in Table 6 is a generalized version of one strain energy density function considered by Horgan and Saccomandi (2005) and can be identified as a standard reinforcing model (see Eq. (3.22)). On the other hand, Model II in Table 6 is newly proposed and has not been used before for constitutive modeling. It makes use of the mixed invariant K_4 provided in Shroder and Neff (2003) and listed in Table 5. The feasibility of Model II for describing constitutive behavior of soft tissues will be studied for various loading conditions along with that of Model I in the remaining part of this section.

It is required that the strain energy density function and the second P-K stress be zero-valued in the reference configuration, where there is no deformation such that **F** = **I**, **C** = **I**, $I_1 = 3$, $I_2 = 3$, $I_3 = 1$, $I_4 = 1$, and $I_5 = 1$. Upon using Eqs. (3.13)-(3.15), these requirements become

$$
\begin{aligned}
&W\big|_{I_1=3,I_2=3,I_3=1,I_4=1,I_5=1} = 0,\\
&(W_1+2W_2)\big|_{I_1=3,I_2=3,I_3=1,I_4=1,I_5=1} = \frac{p_0}{2},\\
&(W_4+2W_5)\big|_{I_1=3,I_2=3,I_3=1,I_4=1,I_5=1} = 0,
\end{aligned} \tag{3.24}
$$

where $W_j \equiv \partial W/\partial I_j$ (j = 1,2,3,4,5), and p_0 is the value of the hydrostatic pressure in the reference configuration. It can be readily shown that Eq. (3.24) can be identically satisfied by both W_e^I and W_e^{II} listed in Table 6 as long as $\mu = p_0$. That is, the two strain energy density functions W_e^I and W_e^{II} satisfy the vanishing stress and energy conditions in the reference configuration.

Also, W_e^I and W_e^{II} can be shown to be polyconvex for $\mu > 0$, $\mu_1 > 0$, $n > 1$, $I_4 < J_m^{1/n}+1$ and $\mu > 0$, $\mu_1 > 0$, $q > 1$, respectively, since I_1, I_4 and K_4 involved are polyconvex (Shroder and Neff, 2003; Steigmann, 2003). The polyconvexity of each of these two strain energy density functions ensures the ellipticity of the corresponding acoustic tensor for all deformations (Shroder and Neff, 2003; Shroder, 2010), thereby leading to numerically stable constitutive models.

In order to be physically admissible, the strain energy density functions W_e^I and W_e^{II} will be further tested below by fitting the experimental stress-strain curves obtained under different loading conditions.

3.2.1 Uniaxial Loading

The stress responses to uniaxial loading along the X_1-direction predicted using W_e^I and W_e^{II} are examined here. The reinforcing fibers are oriented at an angle θ relative to the X_1 axis, as shown in Fig. 9.

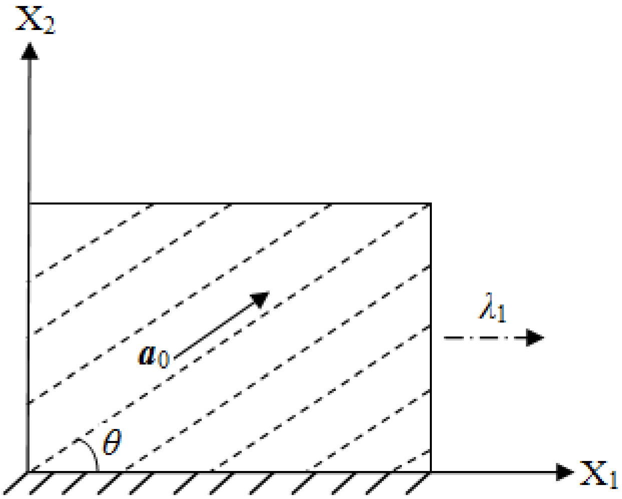

Figure 9. Uniaxial tension of a composite specimen with fibers making an angle θ relative to the X_1 axis.

For uniaxial loading in the X_1-direction, the deformation gradient tensor **F**, the left Cauchy-Green deformation tensor **B**, and the inverse of **B** are given by

$$\left[F_{ij}\right]=\begin{bmatrix}\lambda_1 & 0 & 0\\ 0 & \lambda_2 & 0\\ 0 & 0 & \lambda_3\end{bmatrix},\quad \left[B_{ij}\right]=\begin{bmatrix}\lambda^2{}_1 & 0 & 0\\ 0 & \lambda^2{}_2 & 0\\ 0 & 0 & \lambda^2{}_3\end{bmatrix},$$

$$\left[B^{-1}_{ij}\right]=\begin{bmatrix}1/\lambda^2{}_1 & 0 & 0\\ 0 & 1/\lambda^2{}_2 & 0\\ 0 & 0 & 1/\lambda^2{}_3\end{bmatrix}, \qquad (3.25\text{a-c})$$

where λ_1, λ_2 and λ_3, satisfying the incompressibility condition $\lambda_1\lambda_2\lambda_3 = 1$, are the principal stretches along the X_1-, X_2 and X_3-directions, respectively.

The unit vector representing the fiber orientation in the reference and deformed configurations reads

$$\boldsymbol{a}_0 = \cos\theta \mathbf{e}_1 + \sin\theta \mathbf{e}_2, \quad \boldsymbol{a} = \lambda_1 \cos\theta \mathbf{e}_1 + \lambda_2 \sin\theta \mathbf{e}_2. \tag{3.26a,b}$$

It then follows from Eqs. (3.5), (3.6), (3.25a-c) and (3.26a,b) that the five invariants in this case are

$$\begin{gathered} I_1 = \lambda_1^2 + \lambda_2^2 + \lambda_3^2, \ I_2 = \lambda_1^2\lambda_2^2 + \lambda_2^2\lambda_3^2 + \lambda_1^2\lambda_3^2, \ I_3 = 1, \\ I_4 = \lambda_1^2 \cos^2\theta + \lambda_2^2 \sin^2\theta, \ I_5 = \lambda_1^4 \cos^2\theta + \lambda_2^4 \sin^2\theta. \end{gathered} \tag{3.27}$$

For the strain energy density functions W_e^I and W_e^{II} presented in Table 6, Eq. (3.17) gives

$$\begin{aligned} \sigma_{11e}^I &= \mu B_{11} + \frac{2\mu_0 (I_4 - 1)^{n-1}}{1 - \frac{(I_4-1)^n}{J_m}} (\mathbf{a} \otimes \mathbf{a})_{11} - p^I, \\ \sigma_{11e}^{II} &= 2\left[\frac{\mu}{2} + 2\mu_1 n I_4 (K_4 - 7)^{n-1}\right] B_{11} - 2\mu_1 n (K_4 - 7)^{n-1} B_{11}^{-1} \\ &\quad + 4\mu_1 n I_1 (K_4 - 7)^{n-1} (\mathbf{a} \otimes \mathbf{a})_{11} \\ &\quad - 4\mu_1 n (K_4 - 7)^{n-1} \left(\mathbf{a} \otimes \mathbf{Ba} + \mathbf{B}^T \mathbf{a} \otimes \mathbf{a}\right)_{11} - p^{II}. \end{aligned} \tag{3.28}$$

The deformation defined in Eq. (3.25a-c) is homogeneous. Hence, the equilibrium equations in the absence of body forces will be satisfied if the hydrostatic pressure p is a constant.

For uniaxial loading along the X_1 direction, $\sigma_{33} = 0$. This gives, from W_e^I and W_e^{II} in Table 6 and Eqs. (3.17) and (3.26b),

$$\begin{aligned} p^I &= \mu B_{33}, \\ p^{II} &= \left[\mu + 4\mu_1 n I_4 (K_4 - 7)^{n-1}\right] B_{33} - 2\mu_1 n (K_4 - 7)^{n-1} B_{33}^{-1}. \end{aligned} \tag{3.29}$$

Using Eqs. (3.29), (3.25b,c) and (3.26b) in Eq. (3.28) then yields

$$\frac{\sigma_{11e}^{I}}{\mu}=\lambda_1^2-\lambda_3^2+\frac{\gamma_0(I_4-1)^{n-1}}{1-\frac{(I_4-1)^n}{J_m}}\lambda_1^2\cos^2\theta,$$

$$\frac{\sigma_{11e}^{II}}{\mu}=2\left[\frac{1}{2}+\gamma n I_4(K_4-7)^{n-1}\right](\lambda_1^2-\lambda_3^2)-\gamma n(K_4-7)^{n-1}(\lambda_1^{-2}-\lambda_3^{-2}) \qquad (3.30)$$
$$+2\gamma n I_1(K_4-7)^{n-1}\lambda_1^2\cos^2\theta-4\gamma n(K_4-7)^{n-1}\lambda_1^4\cos^2\theta,$$

where

$$\gamma_0=\frac{2\mu_0}{\mu},\quad \gamma=\frac{2\mu_1}{\mu} \qquad (3.31)$$

is a dimensionless parameter.

For uniaxial loading along the fiber direction with $\theta = 0$ and $\lambda_2 = \lambda_3$, Eq. (3.27) and Table 6 give

$$I_1=\lambda_1^2+\frac{2}{\lambda_1},\ I_2=2\lambda_1+\frac{1}{\lambda_1^2},\ I_3=1,\ I_4=\lambda_1^2,\ I_5=\lambda_1^4,\ K_4=6\lambda_1+\frac{1}{\lambda_1^2}. \qquad (3.32)$$

The normal stress in the X_1-direction, σ_{11e}^{I}, induced by the uniaxial tensile loading in the fiber direction (with $\theta = 0$ and $\lambda_2 = \lambda_3$) is plotted in Figs. 10 and 11. The numerical values of σ_{11e}^{I} and σ_{11e}^{II} shown in Figs. 10 and 11 are obtained from Eqs. (3.30) and (3.32). For illustration purposes, in the calculations, n in W_e^I and q in W_e^{II} vary from 1.5 to 5. Also, J_m in W_e^I is selected to be 4.3. This value has been used by Destrade et al. (2008) to study soft tissues and is based on fitting experimental data for porcine brainstems (Ning et al., 2006).

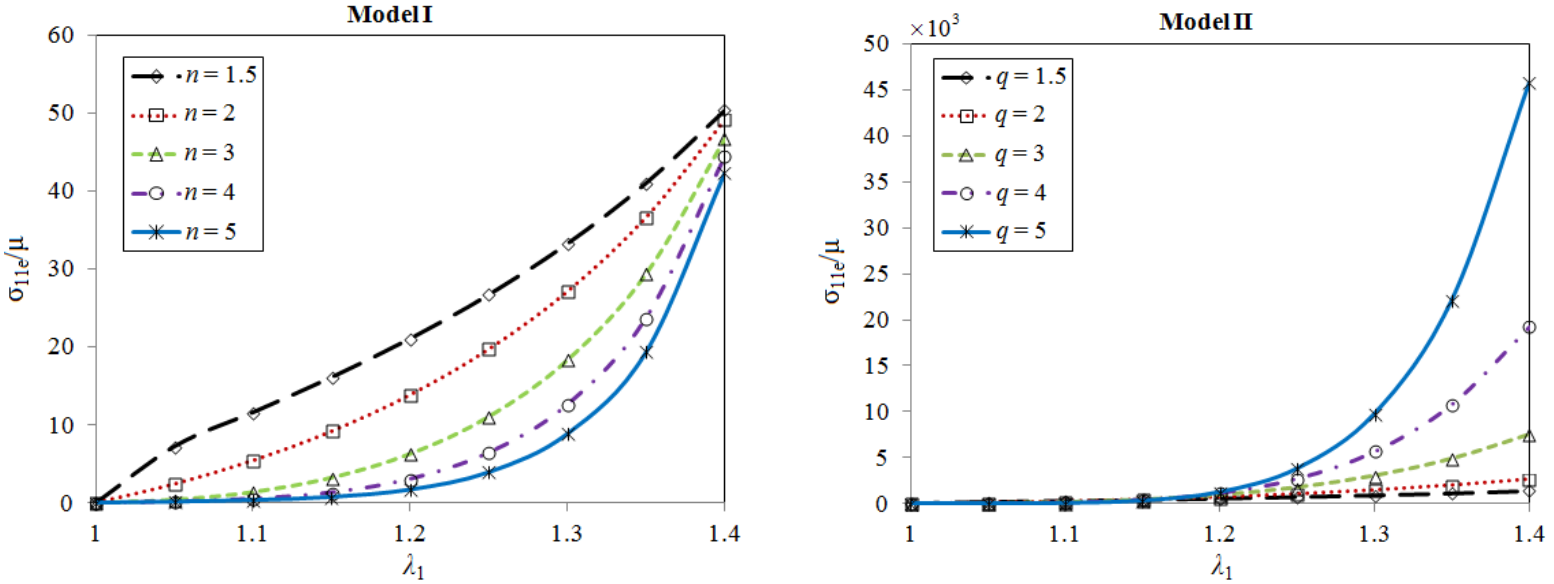

(a) (b)

Figure 10. σ_{11e}/μ vs. λ_1 in the fiber direction: (a) Model I with $J_m = 4.3$, $\gamma_0 = 10$; (b) Model II with $\gamma = 10$.

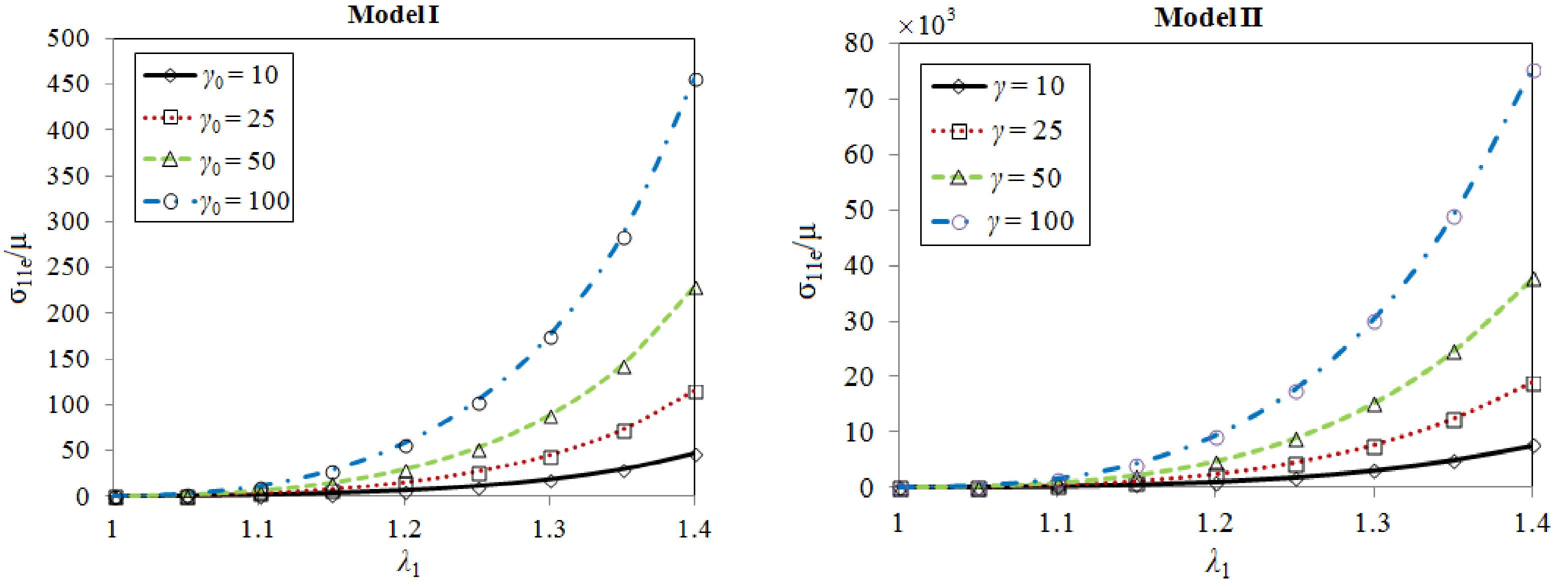

(a) (b)

Figure 11. σ_{11e}/μ vs. λ_1 in the fiber direction: (a) Model I with $\gamma_0 = 10, 25, 50, 100$, $J_m = 4.3$, $n = 3$; (b) Model II with $\gamma = 10, 25, 50, 100$, $q = 3$.

Figures 10(a) and 10(b) illustrate the influence of the parameters n and q, respectively. Clearly, increasing the value of n in Model I reduces the stress contribution from the reinforcing fibers (see Fig. 10(a)), while increasing the value of q in Model II increases the stress contribution from the reinforcing fibers (see Fig. 10(b)). Also, it is seen that the effect of the parameter q is significant only when λ_1 is large. For small extensions, the curves with different values of n (for $n > 3$) or q are almost coincident. In particular, the stress response stiffens considerably at higher values of q.

Figures 11(a) and 11(b) show the effect of the parameters γ_0 and γ, respectively, on the stress response predicted by the two models. It is observed that the stress $\sigma_{11\mathrm{e}}$ is a monotonically increasing function of the stretch for any value of γ_0 or γ considered.

To illustrate the efficacy of the two models, the stress-stretch responses predicted by the two models are compared with the experimental data of porcine brain tissues obtained in the uniaxial tensile tests by Tamura et al. (2008), as shown in Figs. (12a) and (12b). The values of the optimized data fitting parameters are listed in Table 7. It is seen from Figs. (12a) and (12b) and Table 7 that the predictions by the two models agree well with the experimental data.

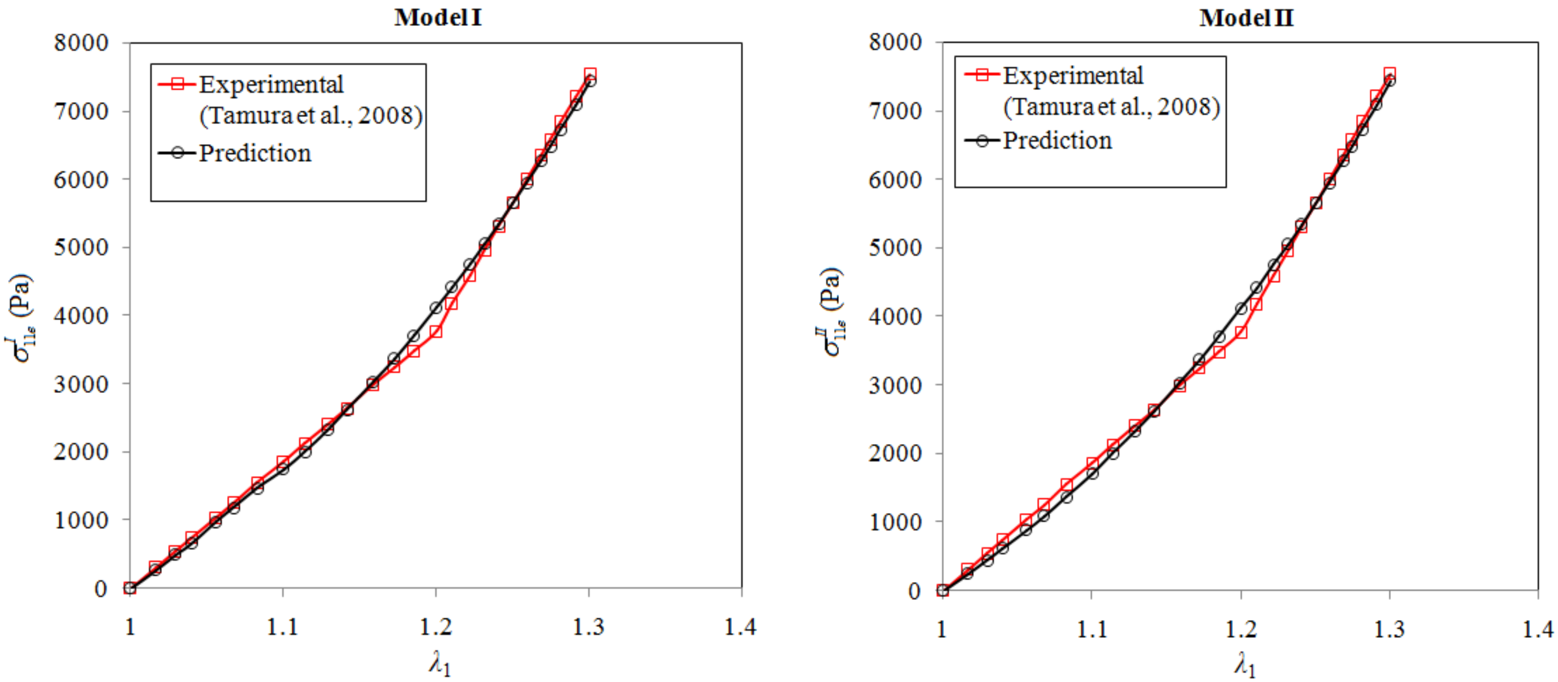

(a) (b)

Figure 12. Comparison of the current predictions with the experimental data of Tamura et al. (2008) at strain rate of 25/s : a) predictions by Model I for $n = 3.63$, $\gamma_0 = 0.6349$, $\mu = 5640.176$ Pa, $\mu_0 = 1790.57$ Pa, $J_m = 4.3$; b) predictions by Model II for $q = 4.5$, $\gamma = 0.008$, $\mu = 2944.66$ Pa, $\mu_1 = 11.694$ Pa

Table 7 Data fitting parameters for the Models I and II under uniaxial tensile loading.

Data	**Strain rate**	**Model No.**	**First Order Optimality Measure**	**Error (Infinity norm)**
Tamura et al. (2008)	25/s	I	6.773e-4	0.02745
		II	0.10753	0.02704

3.2.2 Bi-axial Loading

For a planar bi-axial deformation (see Fig. 9), the deformation gradient tensor **F** and the left Cauchy-Green deformation tensor **B** are given by

$$\left[F_{ij}\right]=\begin{bmatrix} F_{11} & F_{12} & 0 \\ F_{21} & F_{22} & 0 \\ 0 & 0 & F_{33} \end{bmatrix}, \quad \left[B_{ij}\right]=\begin{bmatrix} F_{11}^2+F_{12}^2 & F_{11}F_{21}+F_{22}F_{12} & 0 \\ F_{11}F_{21}+F_{22}F_{12} & F_{21}^2+F_{22}^2 & 0 \\ 0 & 0 & F_{33}^2 \end{bmatrix}, \quad (3.33)$$

where

$$F_{33}=\frac{1}{\left(F_{11}F_{22}-F_{12}F_{21}\right)}=\lambda_3. \quad (3.34)$$

It then follows from Eqs. (3.5), (3.6) and Eq. (3.34) that the fiber direction in the deformed configuration and the five invariants are

$$\begin{aligned} &\mathbf{a}=\mathbf{F}\mathbf{a}_0=(F_{11}\cos\theta+F_{12}\sin\theta)\mathbf{e}_1+(F_{21}\cos\theta+F_{22}\sin\theta)\mathbf{e}_2, \\ &I_1=B_{11}+B_{22}+B_{33}, \; I_2=B_{11}B_{22}+B_{11}B_{33}+B_{22}B_{33}-B_{12}^2, \; I_3=1 \\ &I_4=a_1^2+a_2^2, \; I_5=B_{11}a_1^2+2B_{12}a_1a_2+B_{22}a_2^2. \end{aligned} \quad (3.35)$$

Note that in reaching the first expression in Eq. (3.35) it has been assumed that the fibers are inextensible.

Upon using the plane stress approximation (σ_{33} = 0), the expression for the hydrostatic pressure p can be obtained from Eq. (3.17) as, with I_4 = 1 for inextensible fibers,

$$p = 2\frac{\partial W}{\partial I_1}B_{33} - 2\frac{\partial W}{\partial I_2}B_{33}^{-1} + 2\frac{\partial W}{\partial I_4}\left(\mathbf{a}\otimes\mathbf{a}\right)_{33} + 2\frac{\partial W}{\partial I_5}\left(\mathbf{a}\otimes\mathbf{Ba}+\mathbf{B}^T\mathbf{a}\otimes\mathbf{a}\right)_{33}. \quad (3.36)$$

Using Eq. (3.36) in Eq. (3.17) gives the non-zero components of the Cauchy stress $\boldsymbol{\sigma}$ as

$$\begin{aligned}
\sigma_{11e} &= 2\frac{\partial W}{\partial I_1}\left(B_{11}-B_{33}\right) + 2\frac{\partial W}{\partial I_2}\left(B_{33}^{-1}-B_{11}^{-1}\right) + 2\frac{\partial W}{\partial I_4}\left[\left(\mathbf{a}\otimes\mathbf{a}\right)_{11} - \left(\mathbf{a}\otimes\mathbf{a}\right)_{33}\right] \\
&\quad + 2\frac{\partial W}{\partial I_5}\left[\left(\mathbf{a}\otimes\mathbf{Ba}+\mathbf{B}^T\mathbf{a}\otimes\mathbf{a}\right)_{11} - \left(\mathbf{a}\otimes\mathbf{Ba}+\mathbf{B}^T\mathbf{a}\otimes\mathbf{a}\right)_{33}\right], \\
\sigma_{22e} &= 2\frac{\partial W}{\partial I_1}\left(B_{22}-B_{33}\right) + 2\frac{\partial W}{\partial I_2}\left(B_{33}^{-1}-B_{22}^{-1}\right) + 2\frac{\partial W}{\partial I_4}\left[\left(\mathbf{a}\otimes\mathbf{a}\right)_{22} - \left(\mathbf{a}\otimes\mathbf{a}\right)_{33}\right] \qquad (3.37\text{a-c}) \\
&\quad + 2\frac{\partial W}{\partial I_5}\left[\left(\mathbf{a}\otimes\mathbf{Ba}+\mathbf{B}^T\mathbf{a}\otimes\mathbf{a}\right)_{22} - \left(\mathbf{a}\otimes\mathbf{Ba}+\mathbf{B}^T\mathbf{a}\otimes\mathbf{a}\right)_{33}\right], \\
\sigma_{12e} &= 2\frac{\partial W}{\partial I_1}B_{12} - 2\frac{\partial W}{\partial I_2}B_{12}^{-1} + 2\frac{\partial W}{\partial I_4}\left(\mathbf{a}\otimes\mathbf{a}\right)_{12} + 2\frac{\partial W}{\partial I_5}\left(\mathbf{a}\otimes\mathbf{Ba}+\mathbf{B}^T\mathbf{a}\otimes\mathbf{a}\right)_{12},
\end{aligned}$$

where

$$\begin{aligned}
\left[\left(\mathbf{a}\otimes\mathbf{a}\right)_{ij}\right] &= \begin{bmatrix} a_1^2 & a_1a_2 & 0 \\ a_2a_1 & a_2^2 & 0 \\ 0 & 0 & 0 \end{bmatrix}, \\
\left[\left(\mathbf{a}\otimes\mathbf{Ba}\right)_{ij}\right] &= \begin{bmatrix} a_1\left(B_{11}a_1+B_{12}a_2\right) & a_1\left(B_{12}a_1+B_{22}a_2\right) & 0 \\ a_2\left(B_{11}a_1+B_{12}a_2\right) & a_2\left(B_{12}a_1+B_{22}a_2\right) & 0 \\ 0 & 0 & 0 \end{bmatrix}, \qquad (3.38) \\
\left[\left(\mathbf{B}^T\mathbf{a}\otimes\mathbf{a}\right)_{ij}\right] &= \begin{bmatrix} a_1\left(B_{11}a_1+B_{12}a_2\right) & a_2\left(B_{12}a_1+B_{22}a_2\right) & 0 \\ a_1\left(B_{11}a_1+B_{12}a_2\right) & a_2\left(B_{12}a_1+B_{22}a_2\right) & 0 \\ 0 & 0 & 0 \end{bmatrix}.
\end{aligned}$$

If there is no shear, then the deformation gradient tensor is a diagonal matrix of the form diag [λ_1 λ_2 λ_3], with $\lambda_3 = 1/\lambda_1\lambda_2$ (due to incompressibility). For this special case, W is a function of only two independent stretches, λ_1 and λ_2, in addition to the fiber angle θ. However, if the symmetry axis of the transversely isotropic material is not aligned with one loading direction, then a shear stress is required to maintain a homogeneous deformation in the specimen. In such a case the deformation gradient tensor will have the form given in Eq. (3.33).

Figures 13 and 14 show the tensile stress-stretch curves for σ_{11e} and σ_{22e} in a specimen with the fiber direction along the X_1 axis subjected to equi-biaxial tension (with zero shear), which are obtained from Eqs. (3.37a,b) with $\theta = 0$ (i.e., the fiber orientation in this case is taken to be along the X_1 axis.

It is seen from Figs. 13(a) and 13(b) that the axial normal stress-stretch curves predicted by both models for the biaxial loading are similar to those predicted for uniaxial loading (see Figs 10(a) and 10(b)).

However, the transverse-direction normal stress responses predicted by Model I are significantly different from those predicted by Model II, as shown in Figs. (14a) and (14b). Model II predicts σ_{22e}–λ_1 curves exhibiting stiffening behavior (similar to those exhibited by the σ_{11e}–λ_1 curves (see Figs. (13b) and (14b)), which is typical of the strain-hardening behavior experimentally displayed by soft tissues (e.g., Velardi et al., 2006). On the other hand, Model I predicts an increasing extensibility with increasing stress, with no stiffening effect observed (see Fig 14(a)).

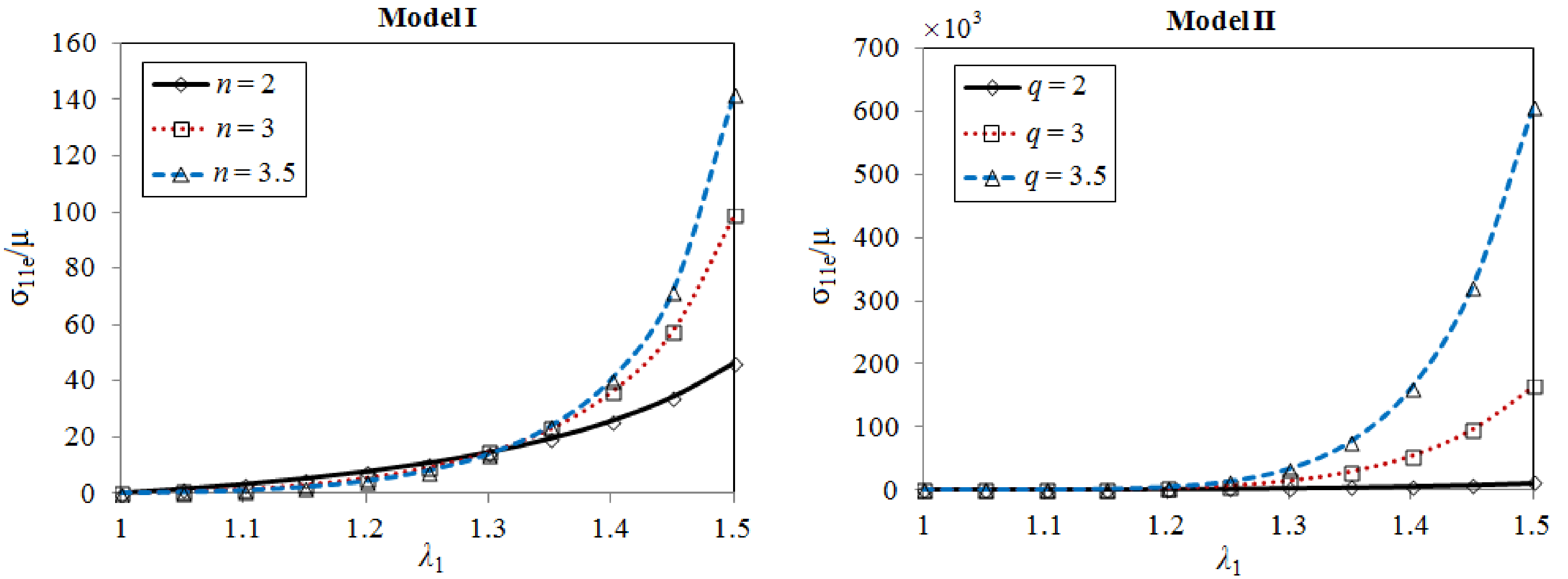

(a) (b)

Figure 13. σ_{11e} vs. λ_1 in a specimen with the fiber direction along the X_1 axis subjected to equi-biaxial tension: (a) Predictions by Model I with $J_m = 4.3$, $\gamma_0 = 10$; (b) Predictions by Model II with $\gamma = 10$.

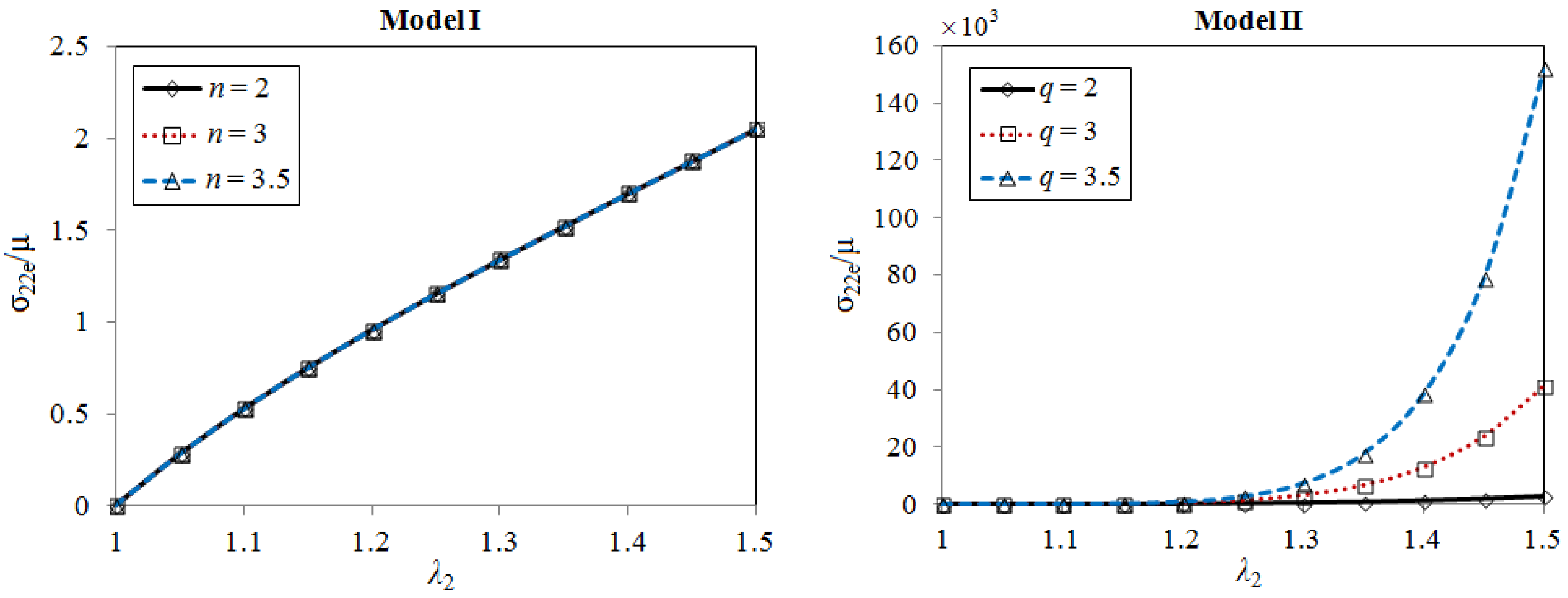

(a) (b)

Figure 14. σ_{22e}/μ vs. λ_2 ($=\lambda_1$) in a specimen with the fiber direction along the X_1 axis subjected to equi-biaxial tension: (a) Predictions by Model I with $J_m = 4.3$, $\gamma_0 = 10$; (b) Predictions by Model II with $\gamma = 10$.

What is shown in Fig. 14(a) can be explained as follows. For the fiber orientation along the x_1 axis, $\theta = 0$ and $F_{12} = F_{21} = 0$. It then follows from Eqs. (3.33) and (3.35) that for the equi-biaxial deformation considered,

$$\begin{aligned}
&\left[F_{ij}\right]=\begin{bmatrix}\lambda_1 & 0 & 0\\ 0 & \lambda_2 & 0\\ 0 & 0 & \lambda_1^{-1}\lambda_2^{-1}\end{bmatrix},\quad \left[B_{ij}\right]=\begin{bmatrix}\lambda_1^2 & 0 & 0\\ 0 & \lambda_2^2 & 0\\ 0 & 0 & \lambda_1^{-2}\lambda_2^{-2}\end{bmatrix},\\
&\mathbf{a}=\lambda_1\mathbf{e}_1,\\
&I_1=\lambda_1^2+\lambda_2^2+\lambda_1^{-2}\lambda_2^{-2},\ I_2=\lambda_1^2\lambda_2^2+\lambda_2^{-2}+\lambda_1^{-2},\ I_3=1,\ I_4=\lambda_1^2,\ I_5=\lambda_1^4.
\end{aligned} \tag{3.39}$$

Using Eq. (3.39) and the expressions of W_e^I and W_e^{II} (see Table 6) in Eqs. (3.37b) yields

$$\begin{aligned}
&\sigma_{22e}^{I}=\mu\left(B_{22}-B_{33}\right),\\
&\sigma_{22e}^{II}=2\left[\frac{\mu}{2}+2\mu_1 n I_4(K_4-7)^{n-1}\right]\left(B_{22}-B_{33}\right)+2\mu_1 n(K_4-7)^{n-1}\left(B_{33}^{-1}-B_{22}^{-1}\right).
\end{aligned} \tag{3.40a,b}$$

It can be seen from Eq. (3.40a) that σ_{22e} predicted by Model I contains no contribution from the reinforcing fibers (represented by $W_{\text{fiber}}(I_4)$), unlike that predicted by Model II (see Eq. (3.40b)). Therefore, the σ_{22e}–λ_1 curves in Fig. 14(a) are essentially those of a neo – Hookean solid based on Eq. (3.40a) that is derived from the first (neo-Hookean) term of term of W_e^I given in Table 6.

Next, the predictions by both Model I and Model II are tested by comparing with the experimental data obtained by Zemanek et al. (2009) for equi-biaxial testing of soft tissues of artery. It has been shown (Sacks and Sun, 2003; Bass et al., 2004) that material parameters determined only from uniaxial tension tests may not correctly describe biaxial deformation responses. Hence, the experimental data of Zemanek et al. (2009) from equi-biaxial tensile tests are simultaneously fitted to σ_{11e} and σ_{22e} predicted by

Model I and Model II, respectively. The predicted and experimental σ_{11e}–λ_1 and σ_{22e}–λ_1 curves are shown in Figs. 15(a) and 15(b) (for Model I) and Figs. 16(a) and 16(b) (for Model II). It is seen from Figs. 16(a) and 16(b) that there is an excellent agreement between the predictions by Model II and the experimental data. In contrast, the predictions by Model I do not agree very well with the experimental data, as shown in Figs. 15(a) and 15(b).

For a general biaxial deformation with the deformation gradient tensor given in Eq. (3.33), the non-zero components of the Cauchy stress are σ_{11e}, σ_{22e}, σ_{33e}, σ_{12e}, and σ_{21e} ($=\sigma_{12e}$). Using a thin sheet approximation for soft tissues allows σ_{33e} to be set to zero, which then leads to the determination of the hydrostatic pressure p from Eq. (3.36). For Model II, the resulting three expressions for the non-zero stress components σ_{11e}, σ_{22e} and σ_{12e} ($=\sigma_{21e}$) involve four independent constitutive functions, namely, $\partial W/\partial I_1$, $\partial W/\partial I_2$, $\partial W/\partial I_4$, and $\partial W/\partial I_5$, for the incompressible material (see Eqs. (3.37a-c)). In order to fully characterize the transversely isotropic material properties, the minimum experimental tests required include: (a) planar biaxial tests with in-plane shear, and (b) through thickness shear tests. However, for membrane tissues (like brain tissues) where thin sections can be prepared, planar biaxial tests with an in-plane shear stress component would be sufficient for full characterization of the material properties. To the best of our knowledge, the current multi-axial experimental data available for transversely isotopic soft tissues are limited to equi-biaxial tests only.

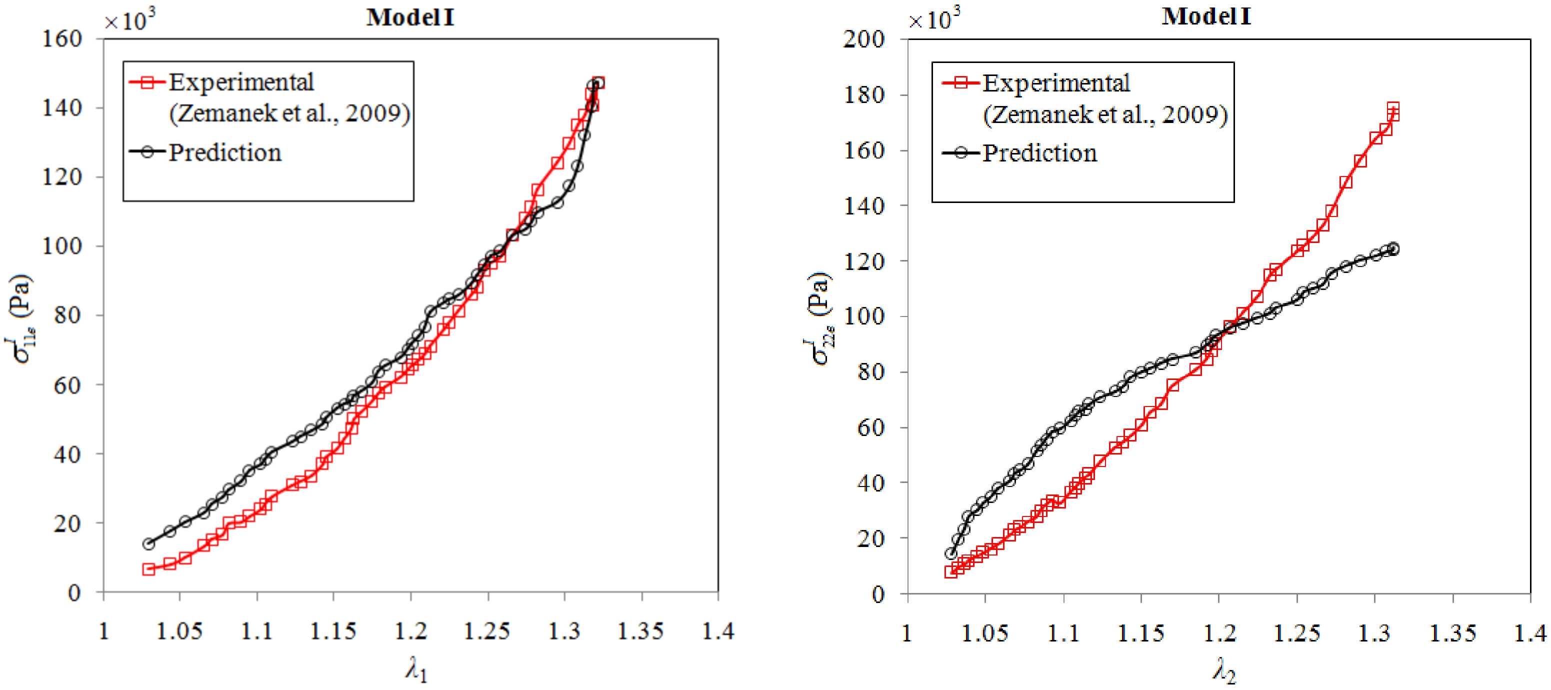

(a) (b)

Figure 15. Comparison of the predictions by Model I with the equi-biaxial tension test data of Zemanek et al. (2009) for arterial wall tissues: (a) σ_{11e}; (b) σ_{22e}. The parameter values used are n =15.35, γ_0 = 10.3985, μ = 87939.09 Pa, μ_0 = 457220.08 Pa, J_m = 4.3.

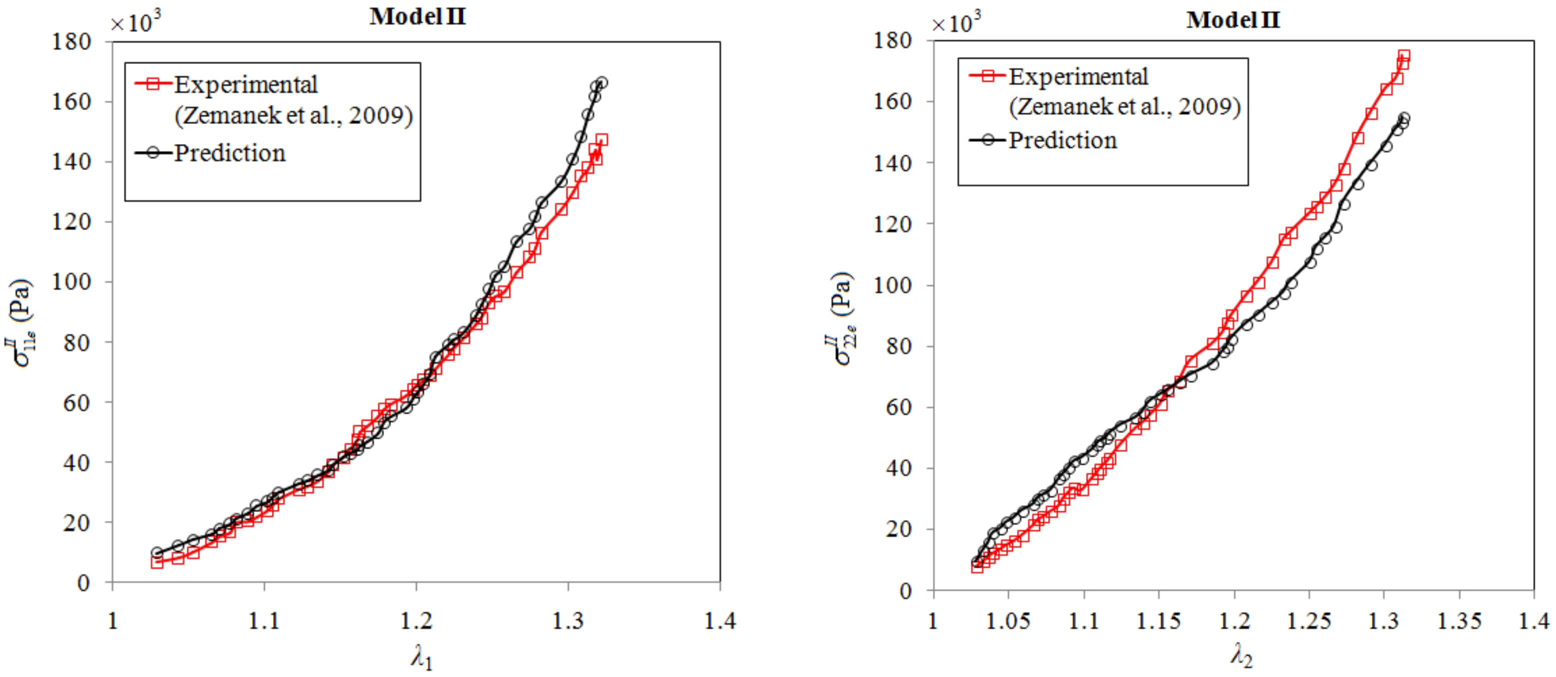

(a) (b)

Figure 16. Comparison of the predictions by Model II with the equi-biaxial tension test data of Zemanek et al. (2009) for arterial wall tissues: (a) σ_{11e}; (b) σ_{22e}. The parameter values used are $q = 2.256$, $\gamma = 0.018734$, $\mu = 26978.84$ Pa, $\mu_1 = 252.72$ Pa.

3.2.3 Shearing Deformation

Consider a simple shear deformation. When the simple shear of the amount k is applied in the X_1-direction, as shown in Fig. 17, the deformation gradient tensor **F**, the left Cauchy-Green deformation tensor **B**, and the inverse of **B** are given by

$$\left[F_{ij}\right]=\begin{bmatrix}1 & k & 0\\ 0 & 1 & 0\\ 0 & 0 & 1\end{bmatrix},\quad \left[B_{ij}\right]=\begin{bmatrix}1+k^2 & k & 0\\ k & 1 & 0\\ 0 & 0 & 1\end{bmatrix},\quad \left[B_{ij}^{-1}\right]=\begin{bmatrix}1 & -k & 0\\ -k & 1+k^2 & 0\\ 0 & 0 & 1\end{bmatrix}. \tag{3.41}$$

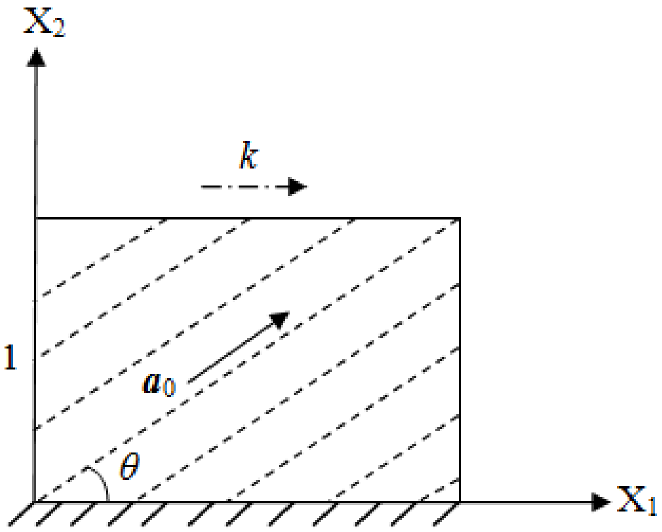

Figure 17. Simple shearing deformation.

It follows from Eqs. (3.5), (3.6) and (3.41) that

$$\begin{aligned}&I_1=I_2=3+k^2,\ I_3=1\\ &I_4=1+k^2\sin^2\theta+2k\cos\theta\sin\theta,\\ &I_5=3k^2\sin^2\theta+4k\cos\theta\sin\theta+k^2(\cos\theta+k\sin\theta)^2+1.\end{aligned} \tag{3.42}$$

Using Eq. (3.42) and the expressions of W_e^I and W_e^{II} given in Table 6 in Eq. (3.17) then gives

$$\frac{\sigma_{12e}^{I}}{\mu} = k + \frac{\gamma_0 \left(I_4 - 1\right)^{n-1} \sin\theta(\cos\theta + k\sin\theta)}{1 - \dfrac{\left(I_4 - 1\right)^{n}}{J_m}},$$

$$\begin{aligned} \frac{\sigma_{12e}^{II}}{\mu} = &\left[1 + 2\gamma n I_4 \left(K_4 - 1\right)^{n-1}\right] k + \gamma n \left(K_4 - 7\right)^{n-1} k \\ &+ 2\gamma n I_1 \left(K_4 - 7\right)^{n-1} \sin\theta(\cos\theta + k\sin\theta) \\ &- 2\gamma n \left(K_4 - 7\right)^{n-1} \left\{(\cos\theta + k\sin\theta)\left[k(\cos\theta + k\sin\theta) + \left(2 + k^2\right)\sin\theta\right] + k\sin^2\theta\right\}. \end{aligned} \tag{3.43}$$

It follows from Eq. (3.42) that for the shear loading along the fiber direction (i.e., $\theta = 0$), $I_4 = 1$ and $K_4 = k^2 + 7$, and for the shear loading perpendicular to the fiber direction (i.e., $\theta = \pi/2$), $I_4 = k^2 + 1$ and $K_4 = 3k^2 + 7$. When $\theta = 0$, $I_4 = 1$ and from Eq. (3.42) and Model I reduces to the neo-Hookean model, while Model II contains the second term depending on the shear strain k. For all other fiber directions (with $\theta \neq 0$ or $\pi/2$), K_4 can be obtained from Eq. (3.42) as $K_4 = 7 + k^2(1 + 2\sin^2\theta) + 4k\cos\theta\sin\theta$.

Table 8 shows the values of the strain energy density functions of the two models for shear deformations. The values in column two are determined from the experimental stress-strain curves of Hrapko et al. (2008) and Donnelly and Medige (1997) (for simple shear loading). It can be seen from Table 8 that there is a very good agreement between W_e^{II} and the experimental data. Therefore, even though the fibers are not stretched, the fiber-matrix and fiber-fiber interactions contribute to the tissue response. This may be the reason for the stiffer behavior predicted by Model II.

Table 8 Strain energy density function values for shear loading along the fiber direction at different loading rates.

Strain Rate (/s)	Trapezoidal Integration (J/m^3)	Strain energy function for *model I* (J/m^3)			Strain energy function for *model II* (J/m^3)		
	W_{tot}	W_{fiber}	W_{matrix}	W_{tot}	W_{fiber}	W_{matrix}	W_{tot}
0.01	4.15	0	3.92	3.92	0	3.92	3.92
0.1	5.72	0	5.49	5.49	0	5.49	5.49
1	7.92	0	7.56	7.56	0	7.56	7.56
15	648.5	0	682.9	682.9	100.32	556.8	657.1
60	1274.6	0	1310.9	1310.9	106.58	1178	1284.6
90	1444.2	0	1508.2	1508.2	173.1	1282.1	1455.3

For simple shear in a direction ϕ relative to the X_1 axis in the X_1X_2 plane, the coordinate system with the following base vectors:

$$\mathbf{e}_1 = \cos\phi\mathbf{i}_1 + \sin\phi\mathbf{i}_2,\ \mathbf{e}_2 = -\sin\phi\mathbf{i}_1 + \cos\phi\mathbf{i}_2,\ \mathbf{e}_3 = \mathbf{i}_3 \tag{3.44}$$

is adopted such that the shear loading is along the $\mathbf{e}_1$ direction. In Eq. (3.44), $\mathbf{i}_1$, $\mathbf{i}_2$ and $\mathbf{i}_3$ are the base vectors associated with the coordinate system (X_1, X_2, X_3). The deformation gradient tensor is then given by

$$\begin{aligned}\mathbf{F} = \mathbf{I} + k\mathbf{e}_1 \otimes \mathbf{e}_2 = \mathbf{F} = \mathbf{I} + k\mathbf{e}_1 \otimes \mathbf{e}_2 &= \left(1 - k\sin\phi\cos\phi\right)\mathbf{i}_1 \otimes \mathbf{i}_1 \\ &+ \left(k\cos^2\phi\right)\mathbf{i}_1 \otimes \mathbf{i}_2 - \left(k\sin^2\phi\right)\mathbf{i}_2 \otimes \mathbf{i}_1 \\ &+ \left(1 + k\sin\phi\cos\phi\right)\mathbf{i}_2 \otimes \mathbf{i}_2 + \mathbf{i}_3 \otimes \mathbf{i}_3.\end{aligned} \tag{3.45}$$

The corresponding components of right Cauchy Green tensor are,

$$\boldsymbol{C}_{ij} = \begin{bmatrix} 1 - k\sin 2\phi + k^2\sin^2\phi & k\cos 2\phi - \frac{k^2}{2}\sin 2\phi & 0 \\ k\cos 2\phi - \frac{k^2}{2}\sin 2\phi & 1 + k\sin 2\phi + k^2\cos^2\phi & 0 \\ 0 & 0 & 1 \end{bmatrix} \tag{3.46}$$

It follows from Eqs. (3.5), (3.6), and (3.46) that

$$\begin{aligned} I_1 &= 3+k^2 \\ I_2 &= 3+k^2 \\ I_4 &= 1-k\sin(2\phi)+k^2\sin^2\phi, \\ I_5 &= 1+k^2+\left(2+k^2\right)\left[-k\sin(2\phi)+k^2\sin^2\phi\right], \\ \boldsymbol{a} &= \left(1-k\sin\phi\cos\phi\right)\mathbf{i}_1-k\sin^2\phi\mathbf{i}_2. \end{aligned} \tag{3.47}$$

Also, for the fibers along the X_1-direction in the reference configuration (i.e., $\boldsymbol{a}_0 = \mathbf{i}_1$) and being inextensible,

$$\boldsymbol{a} = \mathbf{F}\boldsymbol{a}_0 = \left(1-k\sin\phi\cos\phi\right)\mathbf{i}_1-k(\sin^2\phi)\mathbf{i}_2, \tag{3.48}$$

where use has been made of Eq. (3.45).

Figures 18, 19 and 20 show the variation of σ_{12}/μ with k predicted by both the models. Figures (18a), (19a) and (20a) are for Model I, and Figs. (18b), (19b) and (20b) are for Model II. From Figs. (18a) and (19a), it is seen that for Model I (as a *standard reinforcing model*) predicts unstable stress-strain behavior (decreasing stress for increasing strain) at higher strains, while Model II predicts the stress-strain response that is commonly observed in soft tissues under shear loading (e.g., Donnelly and Medige, 1997; Dokos et al., 2000).

According to Model II, the shear stress acting on planes parallel and perpendicular to the shearing direction has the form:

$$\sigma_{12s}^{II} = k+\frac{\gamma}{2}q\left(k^2+2k^2\sin^2\phi-2k\sin 2\phi\right)^{q-1}\left(2k+4k\sin^2\phi-2\sin 2\phi\right) \tag{3.49}$$

The shear stress given in Eq. (3.49) is plotted in Figs. 21 and 22. A similar analysis based on a standard reinforcing model was conducted in Qiu and Pence (1997). It can be seen from Figs 21(a), 21(b), 22(a), and 22(b) that model II exhibits monotonically increasing stress at higher strains unlike a standard reinforcing model (Qiu and Pence,1997). To test the efficacy of the two models in fitting experimental data, the predicted shear stress-strain curves are compared with the experimental curves provided in Donnelly and Medige (1997) for human brain tissues and Hrapko et al. (2008) for porcine brain tissues, as shown in Figs. 23 and 24. Both sets of data are for the shear loading along the fiber direction at different strain rates. Clearly, the predicted curves by Model II better capture the experimental curves for the brain tissues at both the strain rates.

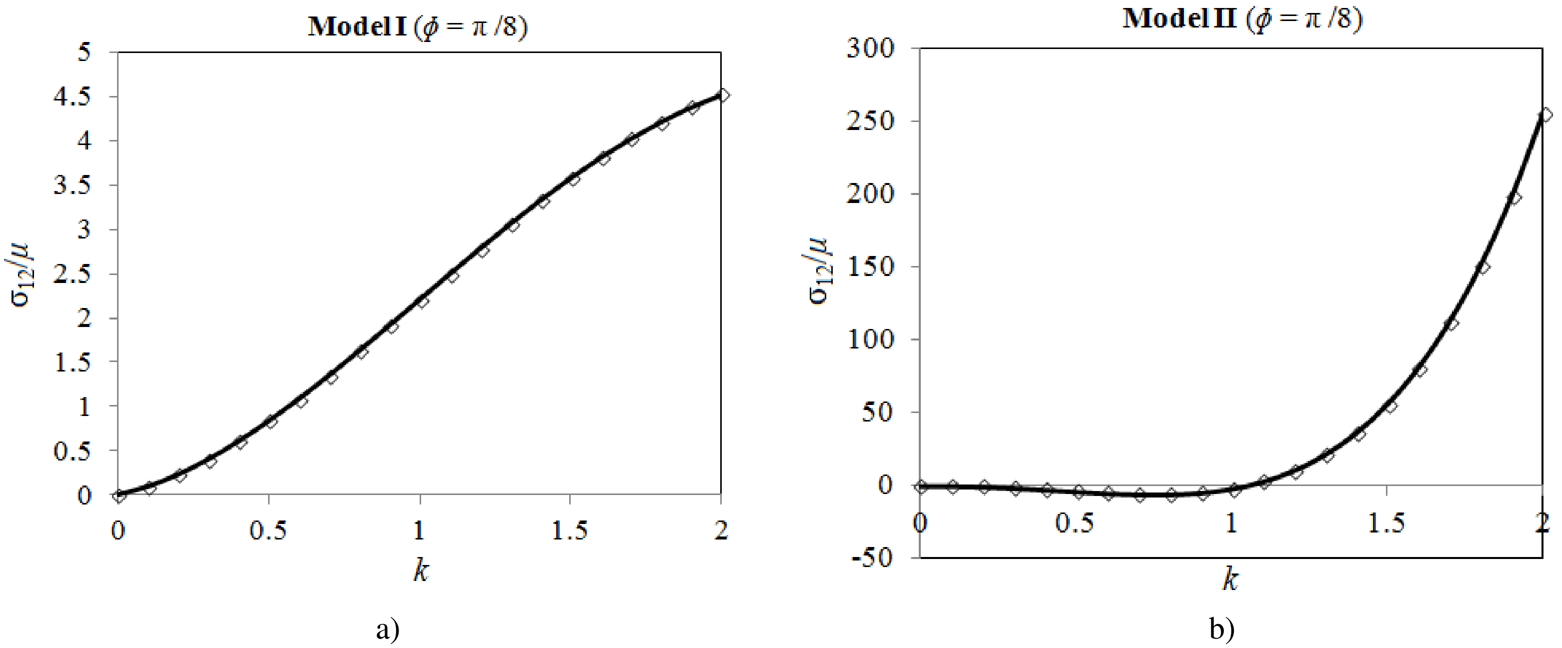

Figure 18. σ_{12}/μ versus k for $\phi = \pi/8$, and $\gamma_0 = \gamma = 20$, $n = 2$, $q = 2$, $J_m = 4.3$:a)Model I; b)Model II

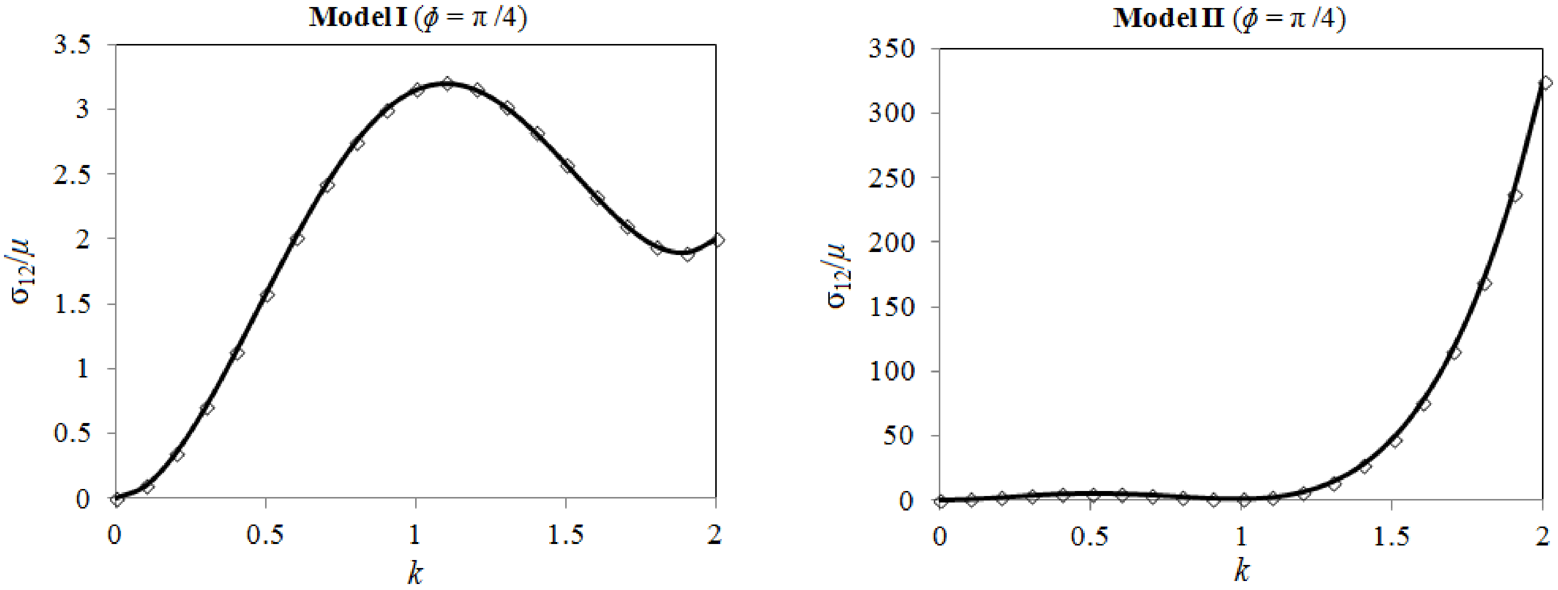

(a) (b)

Figure 19. σ_{12}/μ versus k for $\phi = \pi/4$, and $\gamma_0 = \gamma = 20$, $n = 2$, $q = 2$, $J_m = 4.3$:a)Model I; b)Model II

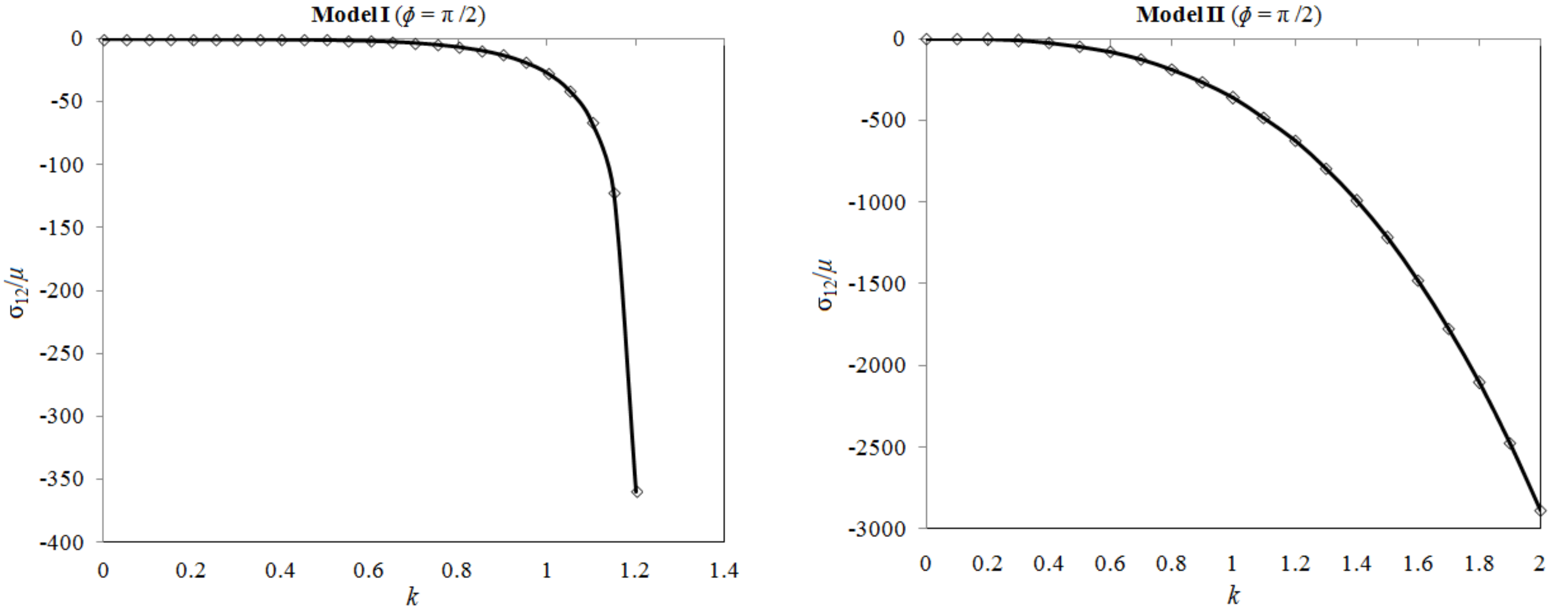

(a) (b)

Figure 20. σ_{12}/μ versus k for $\phi = \pi/2$, and $\gamma_0 = \gamma = 20$, $n = 2$, $q = 2$, $J_m = 4.3$:a)Model I; b)Model II

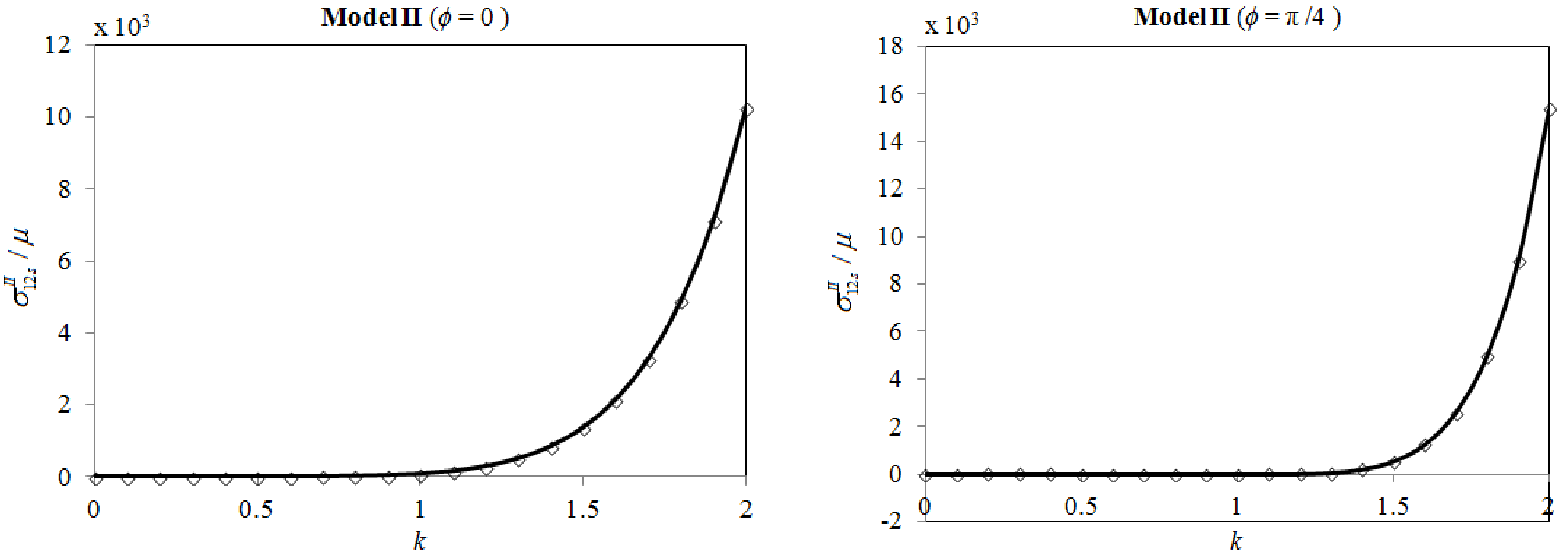

(a) (b)

Figure 21. σ^{II}_{12s}/μ versus the shear strain for $\phi = 0$ [a)], π/4 [b)], and $\gamma = 20$, $q = 4$.

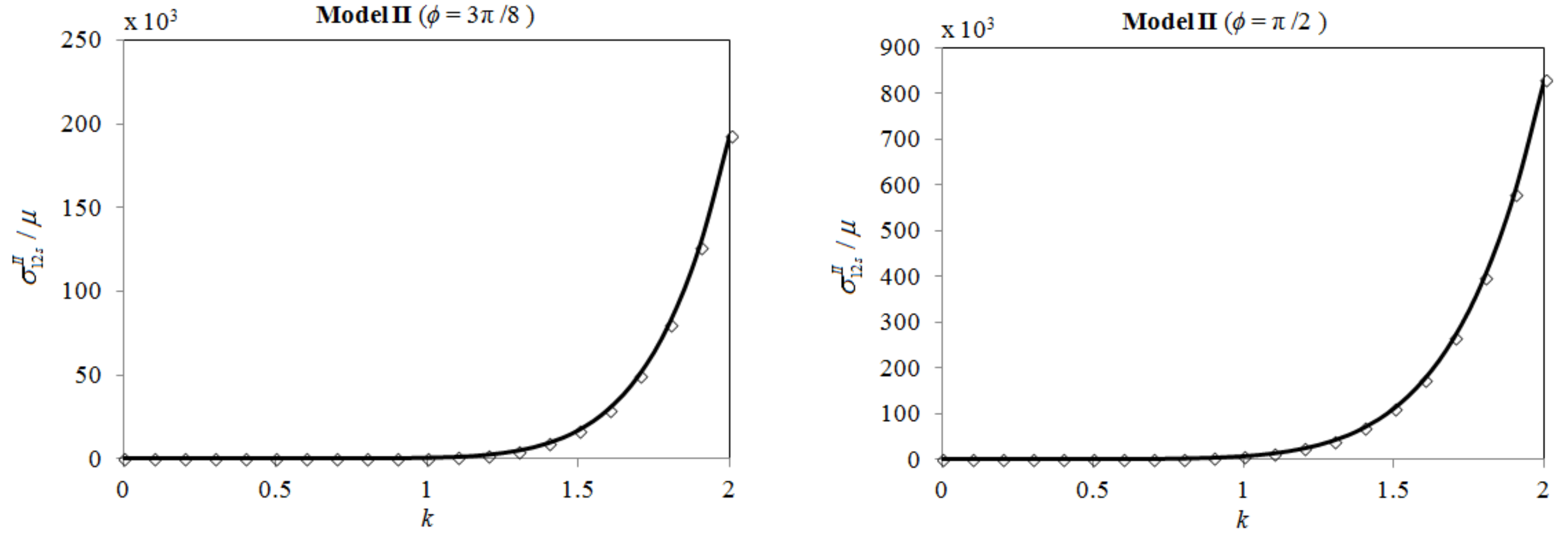

(a) (b)

Figure 22. σ_{12s}^{II}/μ versus the shear strain for $\phi = 3\pi/8$ [a)], $\pi/2$ [b)], and $\gamma = 20$, $q = 4$.

In this section, the two models are proposed and compared for various homogenous deformations. It is seen that Model II better describes the experimentally observed behavior of soft tissues than Model I (a standard reinforcing model).

Experiments on soft tissues are generally restricted to uniaxial extension/compression or simple shear. There is no testing data available for general plane shear or general plane deformations, which can help characterize the nature of the interaction energy between fibers and matrix. In the absence of such data, it is difficult to prove that any particular functional form of W accurately represents the interaction. The newly proposed strain energy density function in Model II contains the mixed invariant K_4, which can represent the fiber stretch and fiber-matrix interaction, in addition to a neo-Hookean term that can describe the incompressible matrix. Hence, it is selected to be a new strain energy density function.

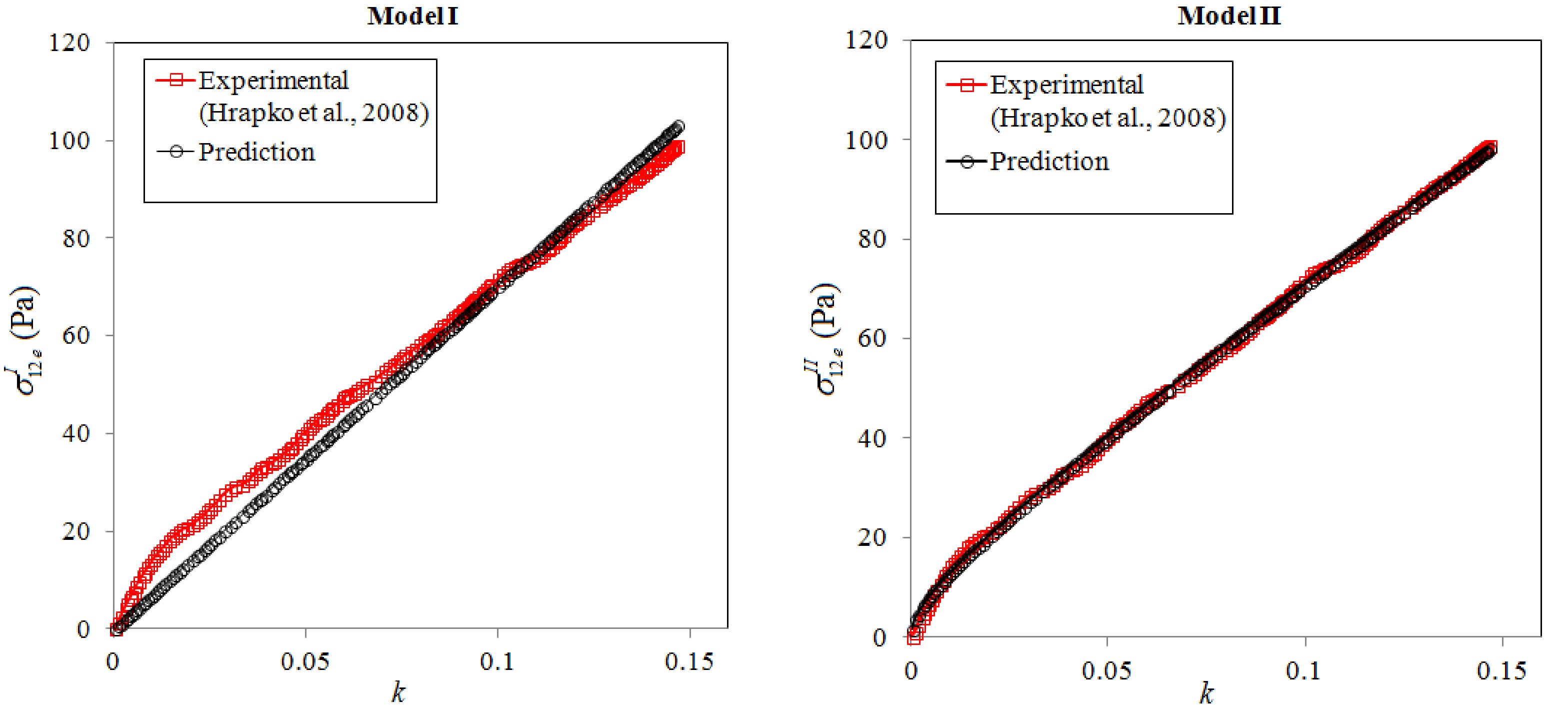

(a) (b)

Figure 23. Comparison of the predictions by Models I and II with the experimental data of Hrapko et al. (2008) at the strain rate of 1/s: (a) Model I for $n = 1$, $\gamma_0 = 0.0283$, $\mu = 704.80$ Pa, $\mu_0 = 10$ Pa; b) Model II for $q = 0.6892$, $\gamma = 8.1008$, $\mu = 524.61$ Pa, $\mu_1 = 32.38$ Pa.

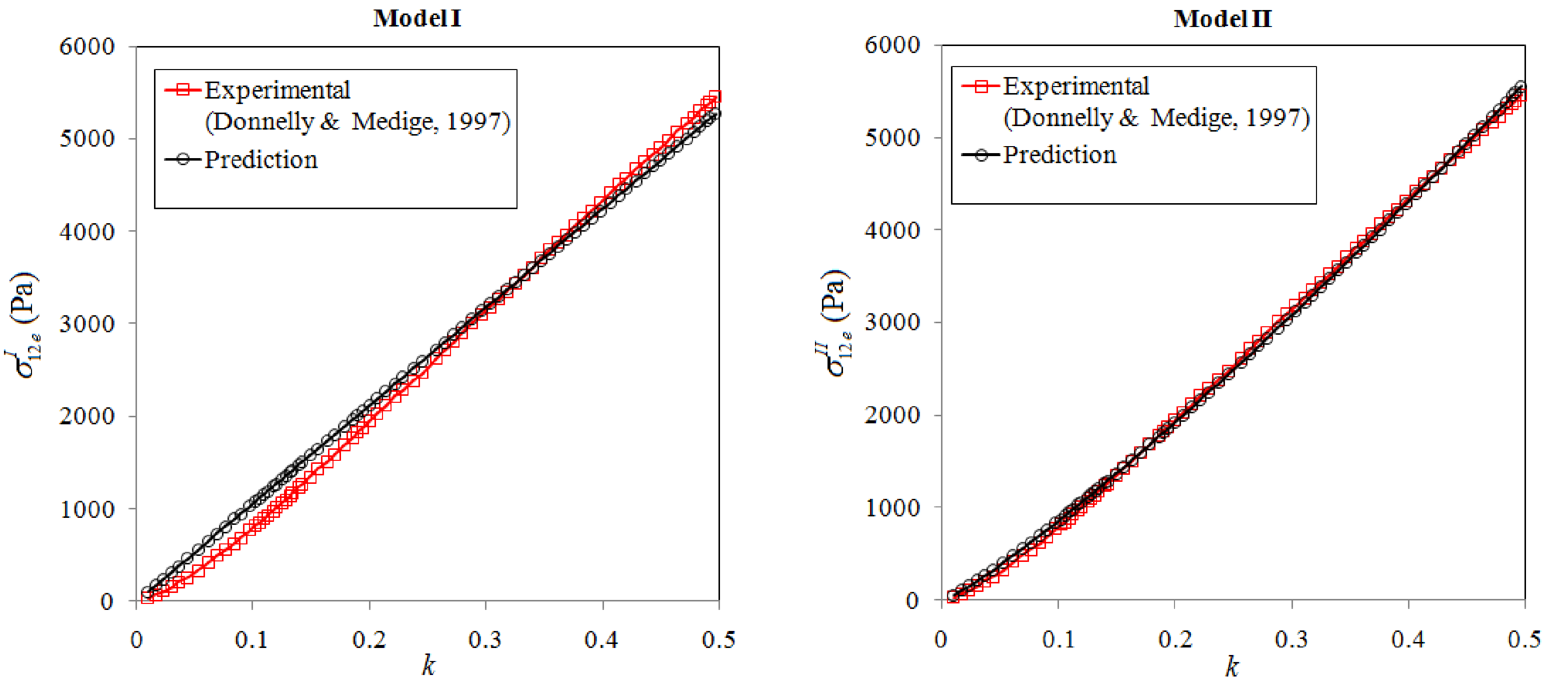

(a) (b)

Figure 24. Comparison of the predictions by Models I and II with the experimental data of Donnelly and Medige (1997) at the strain rate of 60/s: (a) Model I for $n = 1$, $\gamma_0 = 0.00283$, $\mu = 10623.8$ Pa, $\mu_0 = 10$ Pa; (b) Model II for $q = 1.1$, $\gamma = 9.5870$, $\mu = 2001.71$ Pa, $\mu_1 = 4796.9181$ Pa.

3.4 Rate-dependent Materials

Hyper-viscoelastic constitutive modeling combines the methodologies of viscoelasticity and hyperelasticity. One approach is to multiplicatively decompose the total deformation gradient tensor into an elastic part and a viscoelastic part (e.g., Prevost et al., 2011) following the work of Lee (1969). The decomposition method of Lee (1969) is based on the assumption that the body is isotropic in the reference configuration, and the origin in the stress-temperature space always lies inside the loading surface (Green and Naghdi, 1971). As a result, this approach cannot be directly used to model anisotropic responses of soft tissues. Another approach to implementing hyper-viscoelastic models is to decompose the deformation gradient tensor into a dilatational part and a volume-preserving part. This alternative approach is not restricted to any particular configuration.

For an isothermal deformation, the Clausius-Duhem inequality has the form (e.g., Coleman and Noll, 1963; Limbert and Middleton, 2004; Gurtin et al., 2010):

$$D_{\text{int}} = \frac{1}{2}\boldsymbol{S} : \dot{\boldsymbol{C}} - \dot{W}_e \geq 0 \tag{3.50}$$

where D_{int} is the internal dissipation, $\boldsymbol{S}$ is 2nd P-K stress, $\dot{\mathbf{C}}$ is the total material derivative of $\mathbf{C}$ defined in Eq. (3.9) and W_e is a hyperelastic strain energy and $\dot{W}_e$ is the total time derivative of W_e. For $W_\text{e} = W_\text{e}(\mathbf{C})$, equation (3.50) can be written as,

$$D_{\text{int}} = \frac{1}{2}\left(\boldsymbol{S} - 2\frac{\partial W_e}{\partial \boldsymbol{C}} \right) : \dot{\boldsymbol{C}} \geq 0 \tag{3.51}$$

for any **C** and $\dot{\mathbf{C}}$.

For hyperelastic materials, the satisfaction of Eq. (51) for any $\dot{\mathbf{C}}$ requires that

$$\boldsymbol{S} = 2\frac{\partial W_e}{\partial \boldsymbol{C}} \tag{3.52}$$

For materials with only the short-term memory effect, the second P-K stress **S** has the form given in Eq. (3.21). In order to account for the rate-dependent viscous effects observed in soft tissues, a viscous (or dissipative) potential of the following form can be introduced (e.g., Pioletti and Rakotomanana, 2000; Limbert and Middleton, 2004):

$$W_v = W_v(\dot{\boldsymbol{C}};\boldsymbol{C}), \tag{3.53}$$

where $\dot{\mathbf{C}}$ is the variable and **C** is acting as a parameter. Since both **C** and $\dot{\mathbf{C}}$ are objective, Eq. (3.53) satisfies the material frame indifference principle. From Eq. (3.53), the internal dissipation D_{int} due to the viscous effects can be computed as

$$D_{int} = \frac{\partial W_v}{\partial \dot{\mathbf{C}}} : \dot{\mathbf{C}} \equiv \frac{1}{2}\mathbf{S}_v : \dot{\mathbf{C}} \tag{3.54}$$

for any **C** and $\dot{\mathbf{C}}$.

Combining Eqs. (3.51), (3.52) and (3.54) yields

$$\mathbf{S} = \mathbf{S}_e + \mathbf{S}_v, \tag{3.55}$$

where $\mathbf{S}_e$, as the elastic part of the second Piola-Kirchhoff stress **S,** is given in Eq. (3.52), and

$$\mathbf{S}_v = 2\frac{\partial W_v}{\partial \dot{\mathbf{C}}}, \tag{3.56}$$

is the viscous part of **S**.

For incompressible materials, Eq. (3.55) can be modified to give

$$\mathbf{S} = 2\frac{\partial W_e}{\partial \mathbf{C}} + 2\frac{\partial W_v}{\partial \dot{\mathbf{C}}} - p\mathbf{C}^{-1}, \tag{3.57}$$

where p is a hydrostatic pressure. Equation (3.57) provides a visco-hyperelastic constitutive law for incompressible materials with short term memory effects.

In order to describe the short-term memory response of brain tissues, the following viscous potential is proposed:

$$W_v = \frac{1}{2}\mu_3 J_2 (I_1 - 3)^{n_1} + \mu_4 J_5 (K_4 - 7)^{n_2}, \tag{3.58}$$

where μ_3 and μ_4 are material constants, n_3 and n_4 are fitting exponents, and

$$J_2 = \frac{1}{2} tr\left(\dot{\mathbf{C}}^2\right), \quad J_5 = (\boldsymbol{a}_0 \otimes \boldsymbol{a}_0) : \dot{\mathbf{C}}^2 \tag{3.59}$$

are two invariants of $\dot{\mathbf{C}}$ (Boehler, 1987; Limbert and Middleton, 2004).

Using Eq. (3.58) in Eq. (3.56) gives

$$\mathbf{S}_v = \mu_2 \dot{\mathbf{C}}(I_1 - 3)^{n_1} + 2\mu_3 \left[\mathbf{a}_0 \otimes \dot{\mathbf{C}}\mathbf{a}_0 + \dot{\mathbf{C}}\mathbf{a}_0 \otimes \mathbf{a}_0 \right] (K_4 - 7)^{n_2}. \tag{3.60}$$

It is clear from Eq. (3.60) that $\mathbf{S}_v = 0$ in the reference configuration where $\mathbf{F} = \mathbf{I}$ and $\dot{\mathbf{C}} = \mathbf{0}$ for any values of μ_3 and μ_4. Also, it follows from Eq. (3.60) that

$$\mathbf{S}_v = \mu_2 (I_1 - 3)^{n_1} \dot{\mathbf{C}} : \dot{\mathbf{C}} + 2\mu_3 (K_4 - 7)^{n_2} \left[\mathbf{a}_0 \otimes \dot{\mathbf{C}}\mathbf{a}_0 + \dot{\mathbf{C}}\mathbf{a}_0 \otimes \mathbf{a}_0 \right] : \dot{\mathbf{C}} \geq 0. \tag{3.61}$$

for any $\mu_2 \geq 0$ and $\mu_3 \geq 0$. That is, the viscous potential in Eq. (3.58) is thermodynamically admissible if $\mu_2 \geq 0$ and $\mu_3 \geq 0$.

To evaluate the newly proposed viscous potential, predictions based on Eq. (3.60) (for $\mathbf{S}_v$) along with Model II given in Table 6 (for $\mathbf{S}_e$) are compared with the rate-dependent experimental data of Donnelly and Medige (1997), Tamura et al. (2008), Shafieian and Darvish (2009), and Prevost et al. (2011). The material constants for Model II (describing the quasi-static response) are listed in Table 9. The rate-dependent viscous stress $\mathbf{S}_v$ computed using Eq. (3.60) is added to the quasi-static stress $\mathbf{S}_e = 2\partial W_e^{II} / \partial \mathbf{C} - p\mathbf{C}^{-1}$ (see Eq. (3.12a)) to obtain the total stress $\mathbf{S} = \mathbf{S}_e + \mathbf{S}_v$ in the material. The parameters involved in Eq. (3.60) and used for computing $\mathbf{S}_v$ are listed in Tables 10 and 11.

Table 9 Fitting parameters in Model II for quasi-static responses in tension and shear

Parameters	**Tensile response**	**Shear response**
μ	279.41 Pa	359.74 Pa
μ_1	0.3315 Pa	0 Pa
q	6.7	1

Figures 25 and 26 shows the material response to uniaxial tensile loading at strain rates ranging from 0.1/s to 25/s. Figures 27, 28, 29 and 30 displays the response to simple shear loading at strain rates between 0.1/s and 90/s. The error in data fitting and success of minimization as indicated by the first order optimality measure are displayed in Table 10 (for tensile loading) and Table 11 (for shear loading).

Table 10 Values of the parameters in W_v for computing the viscous stress at different strain rates: uniaxial tension.

Strain rate (/s)	μ_2 (Pa·s^2)	μ_3 (Pa·s^2)	n_1	n_2	First order optimality measure	Error	Data
0.1	4676.07	15.665	1	4.85	0.00121	0.0278	Prevost et al. (2011)
1	4367.78	119.665	1	0.30	0.04273	0.0262	
4.3	0	95.29	1	0.823	0.1955	0.0597	Tamura et al. (2008)
25	0	30.45	1	0.95	0.03202	0.04507	

Table 11 Values of the parameters in W_v for computing the viscous stress at different strain rates: along-fiber simple shear.

Strain rate (/s)	μ_2 (Pa·s^2)	μ_3 (Pa·s^2)	n_1	n_2	First order optimality measure	Maximum Error	Data
0.1	19.971	170.79	1	0.19	2.667e-7	0.0201	Hrapko et al. (2008)
1	302.72	50.7275	1	0.25	8.10e-6	0.0235	
15	0	209.46	1	0.52	0.00869	0.0472	Donnelly and Medige (1997)
30	0	146.37	1	0.55	0.04608	0.0388	
45	0	125.85	1	0.55	2.065	0.0662	
60	0	57.585	1	0.43	0.54419	0.0581	
90	0	46.05	1	0.463	0.3086	0.04980	
100	0	49.249	1	0.40	0.0172	0.03262	Shafieian and Darvish (2009)

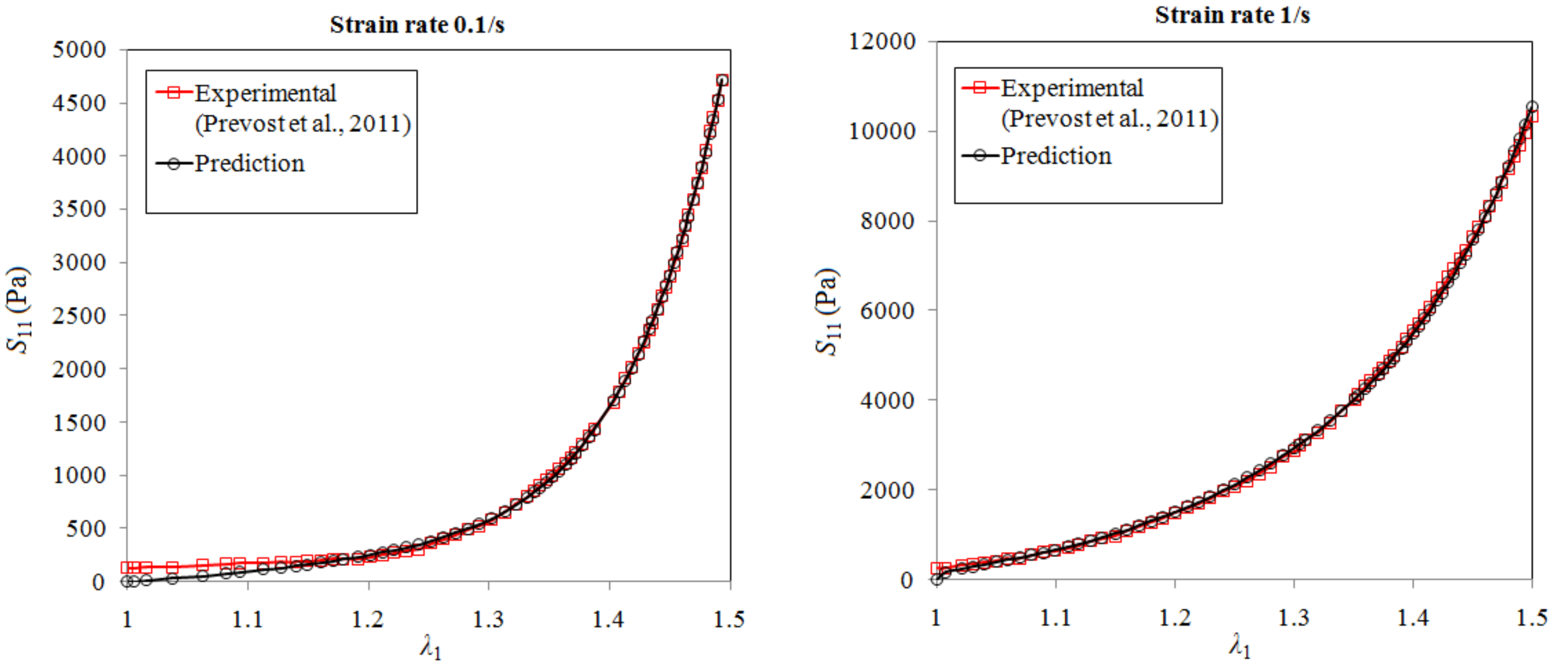

(a) (b)

Figure 25. S_{11} ($=S_{11e} + S_{11v}$) vs. λ_1: a) for 0.1/s loading rate b) 1/s loading rate

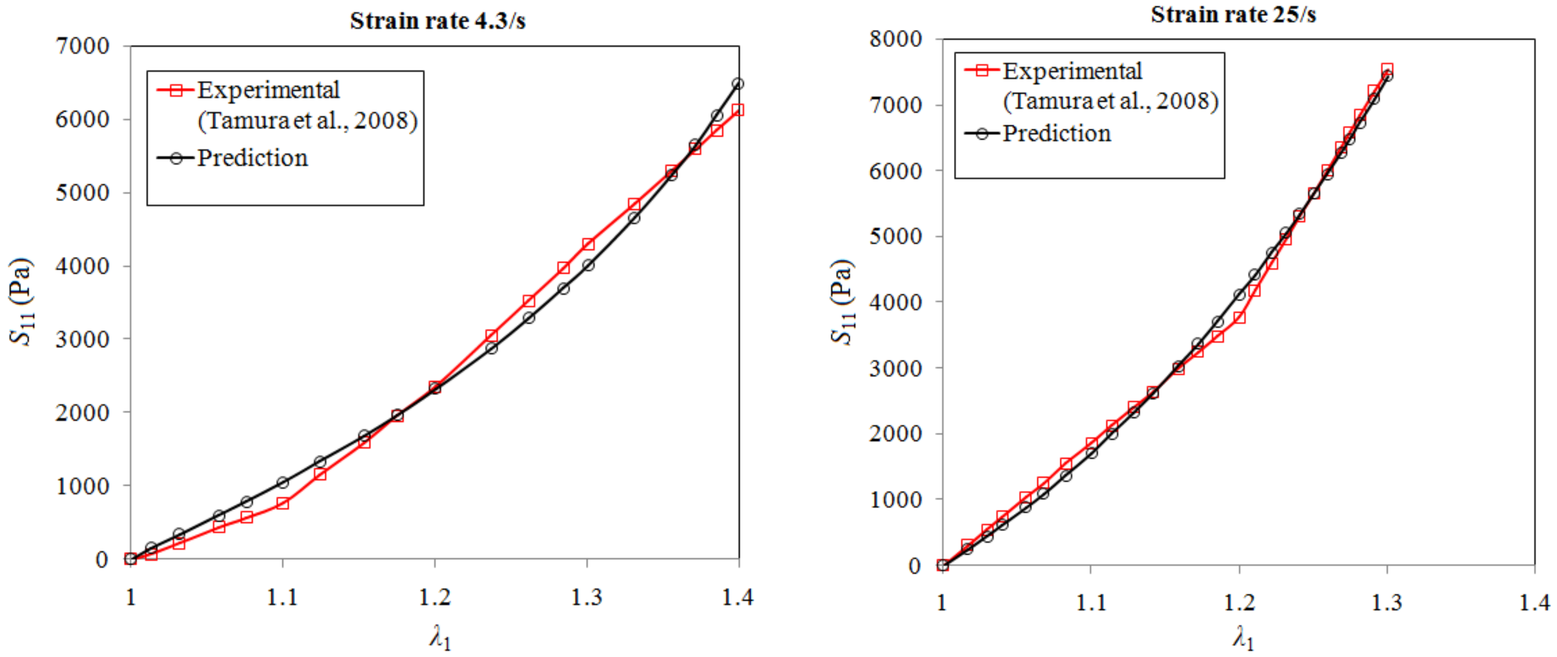

(a) (b)

Figure 26. S_{11} $(=S_{11e}+S_{11v})$ vs. λ_1: a) for 4.3/s loading rate b) 25/s loading rate

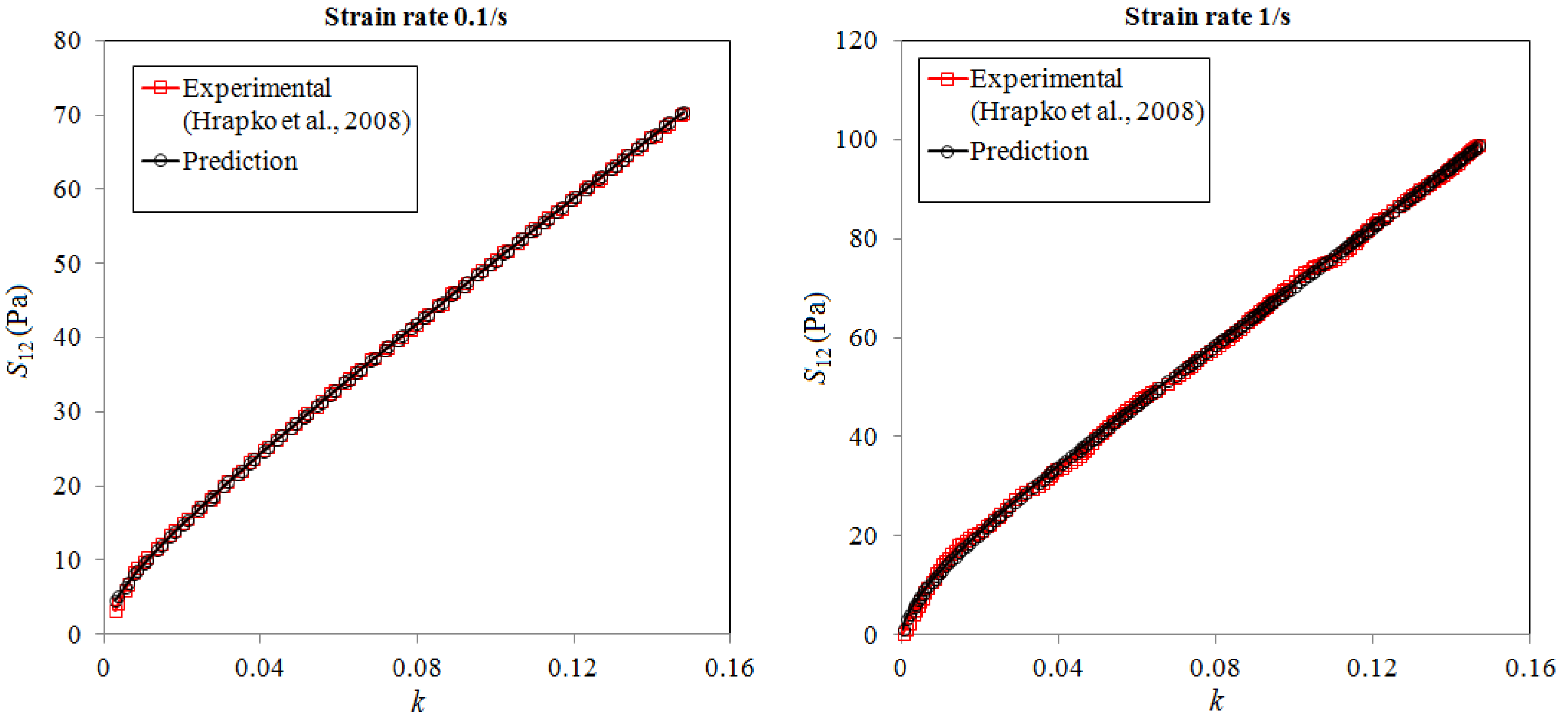

(a) (b)

Figure 27. S_{12} (=S_{12e} + S_{12v}) vs. k for porcine brain tissues under simple shear loading at different strain rates: a) 0.1/s b) 1/s

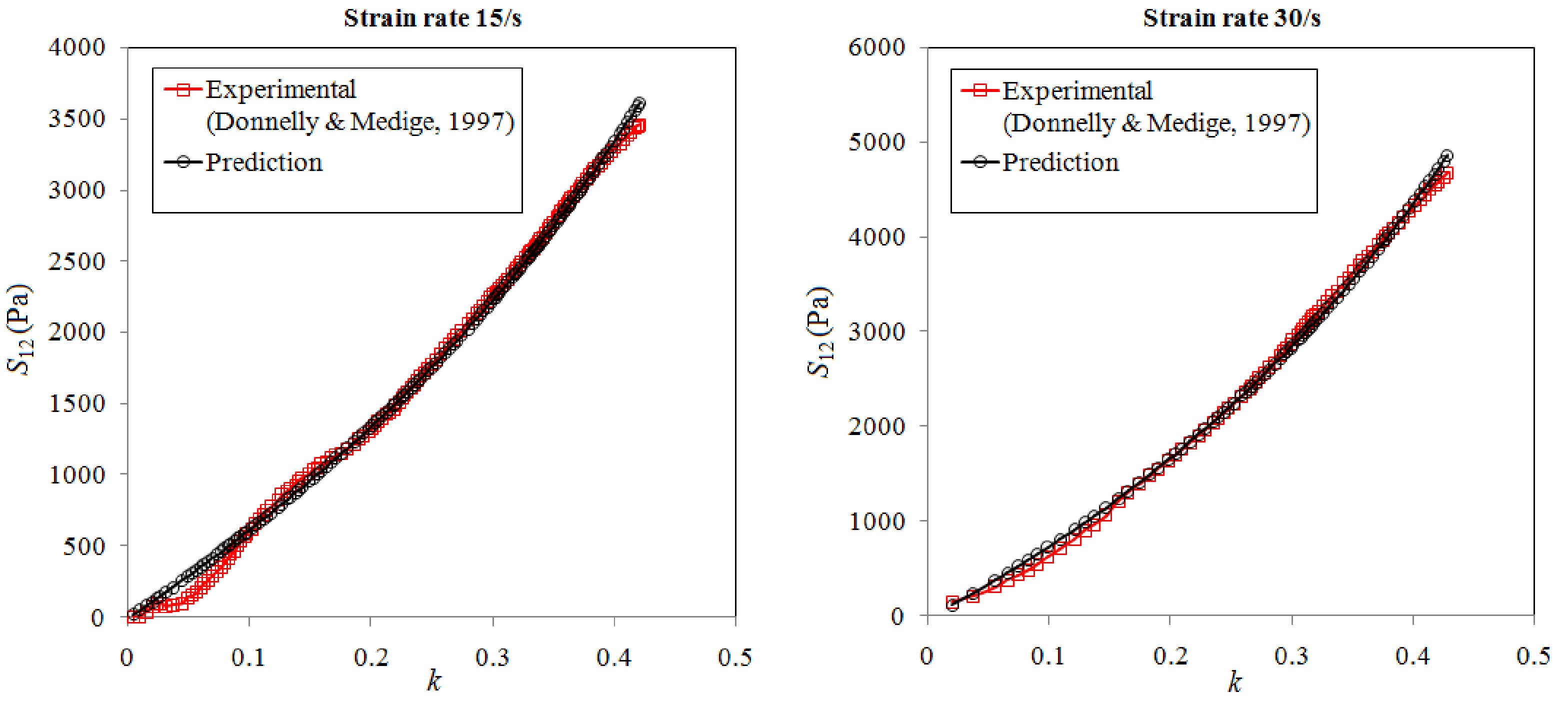

(a) (b)

Figure 28. S_{12} (=S_{12e} + S_{12v}) vs. k for human brain tissues under simple shear loading at high strain rates: a) 15/s b) 30/s

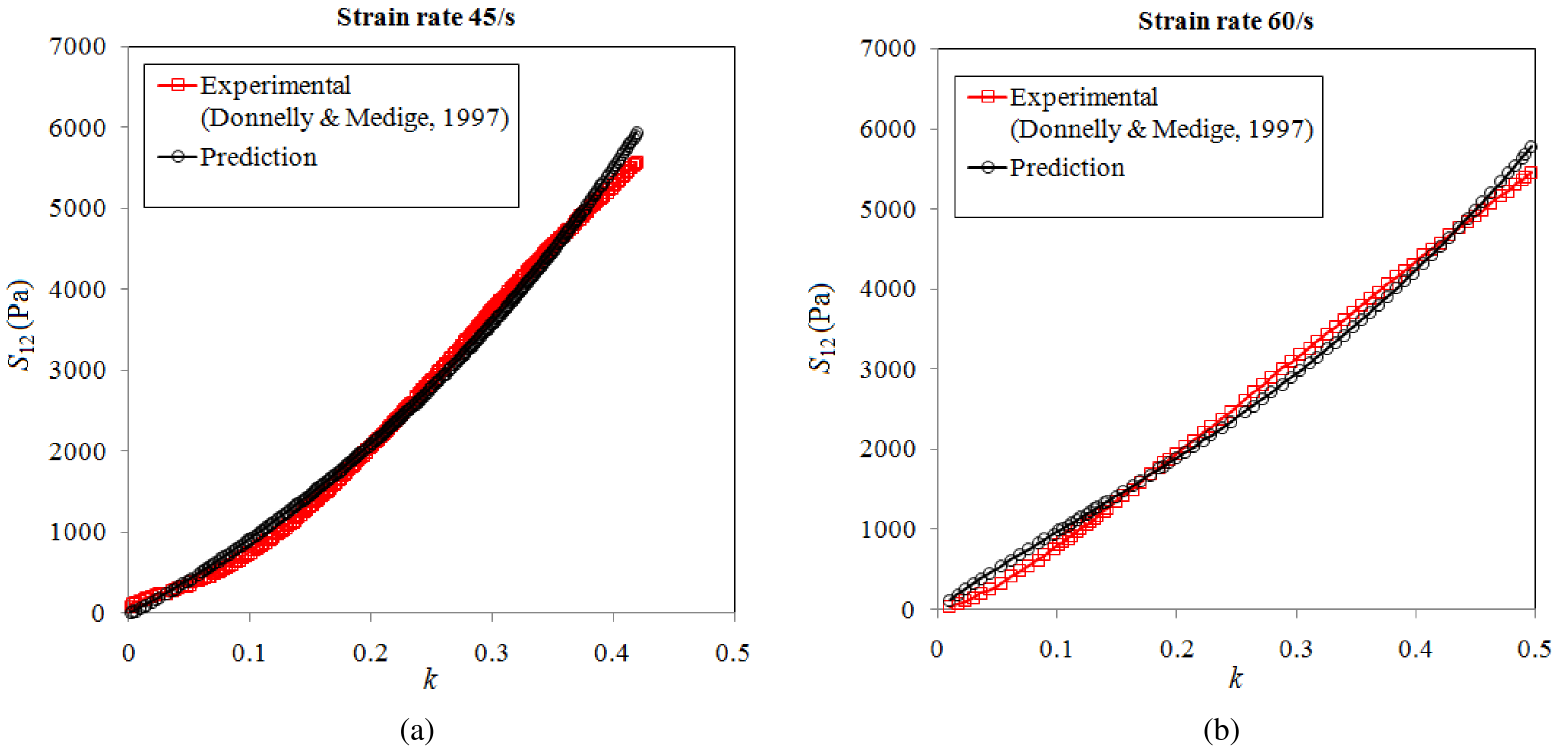

(a) (b)

Figure 29. S_{12} ($=S_{12e} + S_{12v}$) vs. k for human brain tissues under simple shear loading at strain rates of: a) 45/s b) 60/s

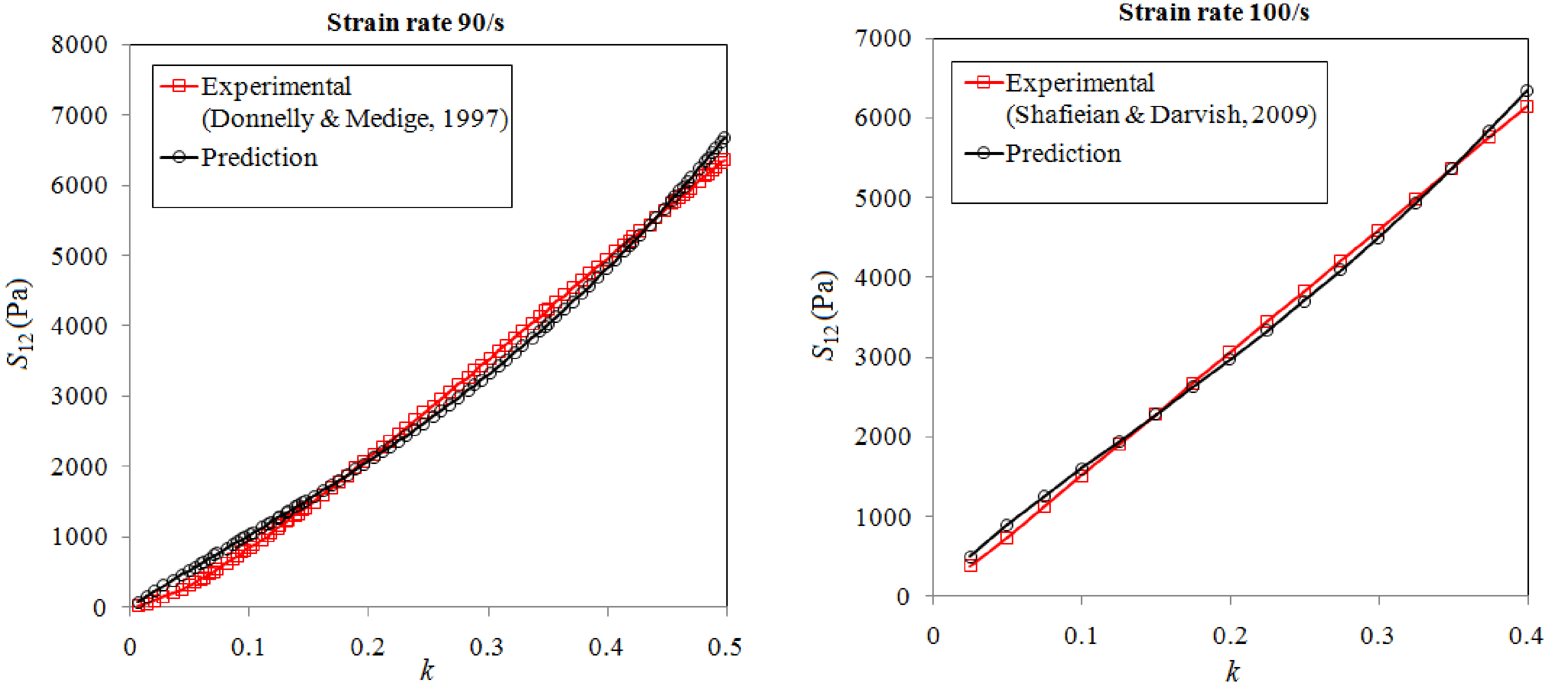

(a) (b)

Figure 30. S_{12} ($=S_{12e}+S_{12v}$) vs. k for human brain tissues under simple shear loading at strain rates of: a) 90/s b) 100/s

Clearly, Figs. 25-30 show that the normal and shear stresses predicted by the current visco-hyperelastic model agree well with the experimental data available for the uniaxial and simple shear loading.

3.4.1 Elasticity and Viscosity Tensors

Elasticity tensors, which are also known as linearized tangent moduli, are fundamental for finite element implementation of any material model.

Note that from Eq. (3.55) that the second Piola-Kirchhoff stress **S** is a function of $\mathbf{C}$ and $\dot{\mathbf{C}}$. One can then write (e.g., Limbert and Middleton, 2004)

$$\mathbf{S} = \mathbf{E}_e : \mathbf{C} + \mathbf{E}_v : \dot{\mathbf{C}}, \tag{3.62}$$

where

$$\mathbf{E}_e \equiv 2\frac{\partial \mathbf{S}_e}{\partial \mathbf{C}}, \quad \mathbf{E}_v \equiv 2\frac{\partial \mathbf{S}_v}{\partial \dot{\mathbf{C}}}, \tag{3.63a,b}$$

are the fourth-order elastic and viscous, parts, respectively. Using Eqs. (3.52) and (3.56) in Eqs. (3.63a,b) gives

$$\mathbf{E}_e = 4\frac{\partial W_e}{\partial \mathbf{C}\partial \mathbf{C}}, \quad \mathbf{E}_v = 4\frac{\partial W_v}{\partial \dot{\mathbf{C}}\partial \dot{\mathbf{C}}}. \tag{3.64a,b}$$

For transversely isotropic materials, $W_e(\mathbf{C}) = W_e(I_1,I_2,I_3,I_4,I_5)$ (Spencer, 1972). Using Eq. (3.64a) then gives the elasticity tensor as

$$
\begin{aligned}
\mathbf{E}_e = {} & 4\left(\frac{\partial^2 W_e}{\partial I_1 \partial I_1} + 2I_1 \frac{\partial^2 W_e}{\partial I_1 \partial I_2} + \frac{\partial W_e}{\partial I_2} + I_1^2 \frac{\partial^2 W_e}{\partial I_2 \partial I_2}\right)\mathbf{I}\otimes\mathbf{I} - 4\left(\frac{\partial^2 W_e}{\partial I_1 \partial I_2} + I_1 \frac{\partial^2 W_e}{\partial I_2 \partial I_2}\right)(\mathbf{I}\otimes\mathbf{C} + \mathbf{C}\otimes\mathbf{I}) \\
& + 4\frac{\partial^2 W_e}{\partial I_2 \partial I_2}(\mathbf{C}\otimes\mathbf{C}) - 4\frac{\partial W_e}{\partial I_2}\mathbf{I}_4 + 4\left(\frac{\partial^2 W_e}{\partial I_1 \partial I_4} + I_1 \frac{\partial^2 W_e}{\partial I_2 \partial I_4}\right)[\mathbf{I}\otimes(\mathbf{a_0}\otimes\mathbf{a_0}) + (\mathbf{a_0}\otimes\mathbf{a_0})\otimes\mathbf{I}] \\
& - 4\frac{\partial^2 W_e}{\partial I_2 \partial I_4}[\mathbf{C}\otimes(\mathbf{a_0}\otimes\mathbf{a_0}) + (\mathbf{a_0}\otimes\mathbf{a_0})\otimes\mathbf{C}] + 4\frac{\partial^2 W_e}{\partial I_4 \partial I_4}\left(\mathbf{a_0}\otimes\mathbf{a_0}\otimes\mathbf{a_0}\otimes\mathbf{a_0}\right) \\
& + 4\left(\frac{\partial^2 W_e}{\partial I_1 \partial I_5} + I_1 \frac{\partial^2 W_e}{\partial I_2 \partial I_5}\right)\left[\mathbf{I}\otimes\left(\mathbf{a_0}\otimes\mathbf{Ca_0} + \mathbf{Ca_0}\otimes\mathbf{a_0}\right) + \left(\mathbf{a_0}\otimes\mathbf{Ca_0} + \mathbf{Ca_0}\otimes\mathbf{a_0}\right)\otimes\mathbf{I}\right] \\
& - 4\frac{\partial^2 W_e}{\partial I_2 \partial I_5}\left[\mathbf{C}\otimes\left(\mathbf{a_0}\otimes\mathbf{Ca_0} + \mathbf{Ca_0}\otimes\mathbf{a_0}\right) + \left(\mathbf{a_0}\otimes\mathbf{Ca_0} + \mathbf{Ca_0}\otimes\mathbf{a_0}\right)\otimes\mathbf{C}\right] \\
& + 4\frac{\partial^2 W_e}{\partial I_5 \partial I_5}\left[\left(\mathbf{a_0}\otimes\mathbf{Ca_0} + \mathbf{Ca_0}\otimes\mathbf{a_0}\right)\otimes\left(\mathbf{a_0}\otimes\mathbf{Ca_0} + \mathbf{Ca_0}\otimes\mathbf{a_0}\right)\right] \\
& + 4\frac{\partial^2 W_e}{\partial I_4 \partial I_5}\left[(\mathbf{a_0}\otimes\mathbf{a_0})\otimes\left(\mathbf{a_0}\otimes\mathbf{Ca_0} + \mathbf{Ca_0}\otimes\mathbf{a_0}\right) + \left(\mathbf{a_0}\otimes\mathbf{Ca_0} + \mathbf{Ca_0}\otimes\mathbf{a_0}\right)\otimes(\mathbf{a_0}\otimes\mathbf{a_0})\right] \\
& + 4\frac{\partial W_e}{\partial I_5}\frac{\partial^2 I_5}{\partial\mathbf{C}\partial\mathbf{C}} + 4\left(I_3 \frac{\partial^2 W_e}{\partial I_1 \partial I_3} + I_1 I_3 \frac{\partial^2 W_e}{\partial I_2 \partial I_3}\right)(\mathbf{I}\otimes\mathbf{C}^{-1} + \mathbf{C}^{-1}\otimes\mathbf{I}) \\
& - 4I_3 \frac{\partial^2 W_e}{\partial I_2 \partial I_3}(\mathbf{C}\otimes\mathbf{C}^{-1} + \mathbf{C}^{-1}\otimes\mathbf{C}) + 4\left(I_3 \frac{\partial W_e}{\partial I_3} + I_3^2 \frac{\partial^2 W_e}{\partial I_3 \partial I_3}\right)(\mathbf{C}^{-1}\otimes\mathbf{C}^{-1}) \\
& + 4I_3 \frac{\partial^2 W_e}{\partial I_3 \partial I_4}\left[(\mathbf{a_0}\otimes\mathbf{a_0})\otimes\mathbf{C}^{-1} + \mathbf{C}^{-1}\otimes(\mathbf{a_0}\otimes\mathbf{a_0})\right] \\
& + 4I_3 \frac{\partial^2 W_e}{\partial I_3 \partial I_5}\left[(\mathbf{a_0}\otimes\mathbf{Ca_0} + \mathbf{Ca_0}\otimes\mathbf{a_0})\otimes\mathbf{C}^{-1} + \mathbf{C}^{-1}\otimes(\mathbf{a_0}\otimes\mathbf{Ca_0} + \mathbf{Ca_0}\otimes\mathbf{a_0})\right] \\
& + 4I_3 \frac{\partial W_e}{\partial I_3}\frac{\partial\mathbf{C}^{-1}}{\partial\mathbf{C}},
\end{aligned}
\tag{3.65}
$$

where $\mathbf{I}_4$ is the fourth-order identity tensor and use has been made of Eq. (3.15). For incompressible materials, the dependence of W_e on I_3 is suppressed, and Eq. (3.65) reduces to that provided in Weiss et al. (1996) (without the last 10 tensorial terms).

For transversely isotropic materials, $W_v\ (\dot{\mathbf{C}}) = W_v(J_1,J_2,J_3,J_4,J_5,J_6,J_7,J_8,J_9,J_{10},J_{11},J_{12})$ (Boehler, 1987; Limbert and Middleton, 2004), where J_2 and J_5 are defined in Eq. (3.59), and the other 10 invariants are given by

$$\begin{aligned}
&J_1 = tr\left(\dot{\mathbf{C}}\right),\quad J_3 = \det\left(\dot{\mathbf{C}}\right),\quad J_4 = (\boldsymbol{a}_0 \otimes \boldsymbol{a}_0) : \dot{\mathbf{C}},\\
&J_6 = tr\left(\mathbf{C}\dot{\mathbf{C}}\right),\quad J_7 = tr\left(\mathbf{C}\dot{\mathbf{C}}^{\mathbf{2}}\right),\quad J_8 = tr\left(\mathbf{C}^{\mathbf{2}}\dot{\mathbf{C}}\right),\\
&J_9 = tr\left(\mathbf{C}^{\mathbf{2}}\dot{\mathbf{C}}^{\mathbf{2}}\right),\quad J_{10} = tr\left[(\boldsymbol{a}_0 \otimes \boldsymbol{a}_0)\mathbf{C}\dot{\mathbf{C}}\right],\quad J_{11} = tr\left[(\boldsymbol{a}_0 \otimes \boldsymbol{a}_0)\mathbf{C}\dot{\mathbf{C}}^{\mathbf{2}}\right],\\
&J_{12} = tr\left[(\boldsymbol{a}_0 \otimes \boldsymbol{a}_0)\mathbf{C}^{\mathbf{2}}\dot{\mathbf{C}}\right].
\end{aligned} \tag{3.66}$$

It then follows from Eq. (3.56), (3.59) and (3.66) that

$$\begin{aligned}
\mathbf{S}_v = {} & 2\frac{\partial W_v}{\partial J_1}\mathbf{I} + 2\frac{\partial W_v}{\partial J_2}\dot{\mathbf{C}} + 2J_3\frac{\partial W_v}{\partial J_3}\dot{\mathbf{C}}^{-1} + 2\frac{\partial W_v}{\partial J_4}\mathbf{a}_0 \otimes \mathbf{a}_0 + 2\frac{\partial W_v}{\partial J_5}\left(\mathbf{a}_0 \otimes \dot{\mathbf{C}}\mathbf{a}_0 + \dot{\mathbf{C}}\mathbf{a}_0 \otimes \mathbf{a}_0\right)\\
& + 2\frac{\partial W_v}{\partial J_6}\mathbf{C} + 2\frac{\partial W_v}{\partial J_7}\left(\mathbf{C}\dot{\mathbf{C}} + \dot{\mathbf{C}}\mathbf{C}\right) + 2\frac{\partial W_v}{\partial J_8}\mathbf{C}^2 + 2\frac{\partial W_v}{\partial J_9}\left(\mathbf{C}^2\dot{\mathbf{C}} + \dot{\mathbf{C}}\mathbf{C}^2\right) + 2\frac{\partial W_v}{\partial J_{10}}\mathbf{C}\left(\mathbf{a}_0 \otimes \mathbf{a}_0\right)\\
& + 2\frac{\partial W_v}{\partial J_{11}}\left[\mathbf{C}\mathbf{a}_0 \otimes \dot{\mathbf{C}}\mathbf{a}_0 + \dot{\mathbf{C}}\mathbf{C}\left(\mathbf{a}_0 \otimes \mathbf{a}_0\right)\right] + 2\frac{\partial W_v}{\partial J_{12}}\mathbf{C}^2\left(\mathbf{a}_0 \otimes \mathbf{a}_0\right),
\end{aligned} \tag{3.67}$$

where use has been made of the following results:

$$\begin{aligned}
&\frac{\partial J_1}{\partial \dot{\mathbf{C}}} = \mathbf{I},\quad \frac{\partial J_2}{\partial \dot{\mathbf{C}}} = \dot{\mathbf{C}},\quad \frac{\partial J_3}{\partial \dot{\mathbf{C}}} = J_3\dot{\mathbf{C}}^{-1},\quad \frac{\partial J_4}{\partial \dot{\mathbf{C}}} = \boldsymbol{a}_0 \otimes \boldsymbol{a}_0,\\
&\frac{\partial J_5}{\partial \dot{\mathbf{C}}} = \boldsymbol{a}_0 \otimes \dot{\mathbf{C}}\boldsymbol{a}_0 + \dot{\mathbf{C}}\boldsymbol{a}_0 \otimes \boldsymbol{a}_0,\quad \frac{\partial J_6}{\partial \dot{\mathbf{C}}} = \mathbf{C},\\
&\frac{\partial J_7}{\partial \dot{\mathbf{C}}} = \mathbf{C}\dot{\mathbf{C}} + \dot{\mathbf{C}}\mathbf{C},\quad \frac{\partial J_8}{\partial \dot{\mathbf{C}}} = \mathbf{C}^2,\quad \frac{\partial J_9}{\partial \dot{\mathbf{C}}} = \mathbf{C}^2\dot{\mathbf{C}} + \dot{\mathbf{C}}\mathbf{C}^2,\quad \frac{\partial J_{10}}{\partial \dot{\mathbf{C}}} = \mathbf{C}(\boldsymbol{a}_0 \otimes \boldsymbol{a}_0),\\
&\frac{\partial J_{11}}{\partial \dot{\mathbf{C}}} = \mathbf{C}\boldsymbol{a}_0 \otimes \dot{\mathbf{C}}\boldsymbol{a}_0 + \dot{\mathbf{C}}\mathbf{C}(\boldsymbol{a}_0 \otimes \boldsymbol{a}_0),\quad \frac{\partial J_{12}}{\partial \dot{\mathbf{C}}} = \mathbf{C}^2(\boldsymbol{a}_0 \otimes \boldsymbol{a}_0).
\end{aligned} \tag{3.68}$$

Substituting Eq. (3.67) into Eq. (3.63b) will lead to the general expression of the viscosity tensor involving all 12 invariants J_1~J_{12}. This expression would be very long. A compact form for the viscosity tensor was provided in Limbert and Middleton (2004) using a different notation.

When only the first five invariants of $\dot{\mathbf{C}}$ are considered in the viscous potential W_v, i.e., $W_v = W_v(J_1,J_2,J_3,J_4,J_5)$, which includes the viscous potential proposed in the current study (see Eq. (3.58)) as a special case, the viscosity tensor can be explicitly obtained from Eq. (3.64b), (3.59), (3.66) and (3.68) as

$$\begin{aligned}
\mathbf{E}_v = {} & 4\frac{\partial^2 W_v}{\partial J_1 \partial J_1}\mathbf{I}\otimes\mathbf{I} + 4\frac{\partial^2 W_v}{\partial J_1 \partial J_2}(\mathbf{I}\otimes\dot{\mathbf{C}} + \dot{\mathbf{C}}\otimes\mathbf{I}) + 4J_3\frac{\partial^2 W_v}{\partial J_1 \partial J_3}(\mathbf{I}\otimes\dot{\mathbf{C}}^{-1} + \dot{\mathbf{C}}^{-1}\otimes\mathbf{I}) \\
& + 4\frac{\partial^2 W_v}{\partial J_1 \partial J_4}\left[\mathbf{I}\otimes(\mathbf{a_0}\otimes\mathbf{a_0}) + (\mathbf{a_0}\otimes\mathbf{a_0})\otimes\mathbf{I}\right] \\
& + 4\frac{\partial^2 W_v}{\partial J_1 \partial J_5}\left[\mathbf{I}\otimes(\mathbf{a_0}\otimes\dot{\mathbf{C}}\mathbf{a_0} + \dot{\mathbf{C}}\mathbf{a_0}\otimes\mathbf{a_0}) + (\mathbf{a_0}\otimes\dot{\mathbf{C}}\mathbf{a_0} + \dot{\mathbf{C}}\mathbf{a_0}\otimes\mathbf{a_0})\otimes\mathbf{I}\right] \\
& + 4\frac{\partial^2 W_v}{\partial J_2 \partial J_2}(\dot{\mathbf{C}}\otimes\dot{\mathbf{C}}) + 4J_3\frac{\partial^2 W_v}{\partial J_2 \partial J_3}(\dot{\mathbf{C}}\otimes\dot{\mathbf{C}}^{-1} + \dot{\mathbf{C}}^{-1}\otimes\dot{\mathbf{C}}) \\
& + 4\frac{\partial^2 W_v}{\partial J_2 \partial J_4}[\dot{\mathbf{C}}\otimes(\mathbf{a_0}\otimes\mathbf{a_0}) + (\mathbf{a_0}\otimes\mathbf{a_0})\otimes\dot{\mathbf{C}}] \\
& + 4\frac{\partial^2 W_v}{\partial J_2 \partial J_5}[\dot{\mathbf{C}}\otimes(\mathbf{a_0}\otimes\dot{\mathbf{C}}\mathbf{a_0} + \dot{\mathbf{C}}\mathbf{a_0}\otimes\mathbf{a_0}) + (\mathbf{a_0}\otimes\dot{\mathbf{C}}\mathbf{a_0} + \dot{\mathbf{C}}\mathbf{a_0}\otimes\mathbf{a_0})\otimes\dot{\mathbf{C}}] \\
& + 4\frac{\partial W_v}{\partial J_2}\mathbf{I_4} + 4J_3\left(\frac{\partial W_v}{\partial J_3} + J_3\frac{\partial^2 W_v}{\partial J_3 \partial J_3}\right)\dot{\mathbf{C}}^{-1}\otimes\dot{\mathbf{C}}^{-1} \\
& + 4J_3\frac{\partial^2 W_v}{\partial J_3 \partial J_4}[(\mathbf{a_0}\otimes\mathbf{a_0})\otimes\dot{\mathbf{C}}^{-1} + \dot{\mathbf{C}}^{-1}\otimes(\mathbf{a_0}\otimes\mathbf{a_0})] \\
& + 4J_3\frac{\partial^2 W_v}{\partial J_3 \partial J_5}[(\mathbf{a_0}\otimes\dot{\mathbf{C}}\mathbf{a_0} + \dot{\mathbf{C}}\mathbf{a_0}\otimes\mathbf{a_0})\otimes\dot{\mathbf{C}}^{-1} + \dot{\mathbf{C}}^{-1}\otimes(\mathbf{a_0}\otimes\dot{\mathbf{C}}\mathbf{a_0} + \dot{\mathbf{C}}\mathbf{a_0}\otimes\mathbf{a_0})]
\end{aligned}$$

$$
\begin{aligned}
&+4J_3\frac{\partial W_v}{\partial J_3}\frac{\partial \dot{\mathbf{C}}^{-1}}{\partial \dot{\mathbf{C}}}+4\frac{\partial^2 W_v}{\partial J_4 \partial J_4}\left(\mathbf{a_0}\otimes\mathbf{a_0}\otimes\mathbf{a_0}\otimes\mathbf{a_0}\right)\\
&+4\frac{\partial^2 W_v}{\partial J_4 \partial J_5}[(\mathbf{a_0}\otimes\mathbf{a_0})\otimes(\mathbf{a_0}\otimes\dot{\mathbf{C}}\mathbf{a_0}+\dot{\mathbf{C}}\mathbf{a_0}\otimes\mathbf{a_0})+(\mathbf{a_0}\otimes\dot{\mathbf{C}}\mathbf{a_0}+\dot{\mathbf{C}}\mathbf{a_0}\otimes\mathbf{a_0})\otimes(\mathbf{a_0}\otimes\mathbf{a_0})]\\
&+4\frac{\partial^2 W_v}{\partial J_5 \partial J_5}(\mathbf{a_0}\otimes\dot{\mathbf{C}}\mathbf{a_0}+\dot{\mathbf{C}}\mathbf{a_0}\otimes\mathbf{a_0})\otimes(\mathbf{a_0}\otimes\dot{\mathbf{C}}\mathbf{a_0}+\dot{\mathbf{C}}\mathbf{a_0}\otimes\mathbf{a_0})+4\frac{\partial W_v}{\partial J_5}\frac{\partial^2 J_5}{\partial \dot{\mathbf{C}}\partial \dot{\mathbf{C}}}.
\end{aligned}
\tag{3.69}
$$

Note that Eqs. (3.65) and (3.69) are in the material description. The elasticity tensor $\mathbf{E}_e$ and viscosity tensor $\mathbf{E}_v$ in the spatial description can be respectively obtained from the Piola transformation of the corresponding tensor in the material description (e.g., Holzapfel, 2000).

For the strain energy density function W_e^{II} (see Table 6) and the viscous potential function W_v (see Eq. (3.58)) proposed in the current study, the elasticity tensor $\mathbf{E}_e$ and the viscosity tensor $\mathbf{E}_v$ can be obtained by directly using Eqs. (3.65) and (3.69).

CHAPTER IV

MODELING OF BLAST-INDUCED TRAUMATIC BRAIN INJURY: EFFECTS OF THE BRAIN TISSUE CONSTITUTIVE RELATION AND BLAST DIRECTION

4.1 Introduction

Traumatic brain injury (TBI) can result from external mechanical loading such as blunt impact, sudden accelerations, ballistic impact, and blast loading. Injuries to the brain tend to have a greater long term- effect than injuries to extremities.

A review of literature shows that impact – induced TBI has been extensively studied (Zhang et al., 2001; Brands, 2002; Kleiven and Hardy, 2002; Hardy et al., 2007; El Sayed et al., 2008; Chen and Ostoja-Starzewski, 2010). Finite element (FE) modeling is widely used in such kind of studies. The internal dynamics of the human head under direct impact or impulse loading has been well understood, and has been linked to certain measurable parameters such as acceleration, pressure, and shear strain in the brain. Damage criteria have also been established for impact induced TBI to provide guidelines as to what type and level of external loads would produce head injuries.

Frequent use of improvised explosive devices (IED's) in recent conflicts has increased the occurrence of blast and ballistic induced TBI amongst military personnel. Because of the limitations of conducting blast or ballistic studies on human subjects, computational models are often used as tools to investigate the physical processes causing blast/ballistic induced traumatic brain injury. The fidelity of such models depends on structural details incorporated in the geometric models of skull and brain, the constitutive models used to represent the material behavior, the nature of contact algorithms implemented, and the use of an appropriate measure of injury. In recent years the complexity of head models in terms of geometry has progressively increased (Willinger and Baumgartner, 2001; Takhounts et al., 2003a; Zhang et al., 2009; Chen and Ostoja-Starzewski, 2010). However, constitutive laws used in simulations, especially those for brain, have received very little attention. The mechanical behavior of brain tissues has been well studied in laboratory settings. Inspite of this research, the material models used in published blast induced TBI simulations tend to be oversimplified. Continuum mechanics based approach is often used for representing brain tissue behavior in simulations. The tissue response is additively decomposed into dilatational and deviatoric parts. The dilatational behavior is most often assumed to be linearly elastic (Taylor and Ford, 2009; Ganpule et al., 2011; Zhang et al., 2011). In some simulations complete incompressibility is assumed, and the dilatational model used in simulations is not mentioned (Mendis, 1992). The deviatoric response is commonly modeled using linear elastic (Ganpule et al., 2011), or isotropic hyperelastic (Taylor and Ford, 2009; Nyein et al., 2010; Grujicic et al., 2010; Zhang et al., 2011) constitutive relations. Time dependent material behavior is either ignored (Moore et al., 2009; Grujicic et al., 2011) or represented by linear viscoelastic models (Chafi et al., 2010; Nyein et al., 2010; Ganpule et al., 2011; Zhang et al., 2011). These differences in the material models affect the stress responses obtained in an analysis. This in turn influences the threshold magnitudes of field variables chosen for establishing damage criteria. Furthermore, variations in boundary conditions, amount of explosive used, distance of the subject from the source of the explosion, and the contact algorithms implemented limits the comparability of results amongst different simulations.

The main goal of this Chapter is to develop an improved of finite element head model for predicting the mechanical response of a human head to blast/ballistic loading. The specific objectives are:

a) Evaluating and comparing the performance of different constitutive relations for describing the response of brain tissues to blast/ballistic events.
b) Consolidating results from existing impact and blast induced TBI simulations.
c) Investigating directional sensitivity of a human head to blast loading.

To this end, three different material models have been implemented in simulations. The rest of the article is organized as follows. A detailed description of the geometric and meshed models for a human skull/brain is presented in section 4.2. Sections 4.3 and 4.4 provide a comprehensive account of the constitutive relations selected for comparison. The material relations for skull and cerebrospinal fluid (CSF) are also described. In section 4.5 validation results for the setup of the transient nonlinear dynamics problem using Abaqus/Explicit are given. The main results obtained in this work are presented and discussed in section 4.6.

4.2 Geometric and Meshed Models

The model of the skull-brain assembly used in this paper has a total mass of 2.94 kg, and a volume of 2550 cm^3. The polygonal model (see Fig. 31) used was provided by TurboSquid®. Polygonal modeling (or mesh modeling) is an approach for modeling objects by approximating their surfaces using polygons. Quadrilaterals and triangles are the most common shapes used in such modeling. This mesh cloud (or polygonal model) was uploaded into Solidworks® and converted into a solid model (surface representation) using the Solidworks® functionality of *ScanTo3D*. Figure 32 shows the resultant solid model of skull and brain. The brain model includes the main brain (cerebrum), small brain (cerebellum), colossal commissure (corpus callosum), pituitary glands (glandula pituitaria), brainstem (truncus encephali), and cerebrospinal fluid (liquor cerebrospinalis). The brain model approximately weighs 1.46 kg, and has a volume of 1410 cm^3. The adult human brain weighs around 1.5 kg with a volume of around 1410 cm^3 (Thompson, 2000). This solid model was then meshed using the general purpose pre-processing program HyperMesh® (Altair Engineering Inc, Troy, Michigan). The entire assembly is discretized using quadratic ten-node tetrahedral solid elements (the C3D10M element in ABAQUS/Explicit®). To study mesh convergence three different mesh models were created consisting of 452483, 552162, and 647936 elements respectively. The use of these three mesh led to somewhat different numerical results. The mesh model with 552162 elements was found to be a good compromise between accuracy and computational efficiency for capturing the shock wave phenomenon (e.g., Brands, 2002). For such a mesh, a typical element length of 4.5 mm was used for the skull, 3 mm for the CSF, and 1 to 3 mm for the brain components. Figure 33 shows the meshed geometry. It can be seen from Fig. 33 that convolutions of the cerebral cortex (surface of the cerebrum) are well captured by the selected mesh size. The CSF is modeled as a solid body with water-like properties. The finite element model in the simulations is oriented in such a way that the positive *x*-axis points forward, *y*-axis points from left to right, and *z*-axis upward. In addition, local orientations have been defined in the finite element model for parts considered as transversely isotropic with the preferred direction along the local *x*-axis. The blast simulations are carried out using ABAQUS/Explicit®. The air blast wave is generated using the conventional weapons (CONWEP®) module. The CONWEP® functionality allows the modeling of incident wave loading in air without having to explicitly model the Eulerian domain.

Two air-blast wave cases are considered in this paper:

a) An air-blast wave characterized by a 0.66 MPa peak overpressure that corresponds to 0.85 kg of trinitrotoluene (TNT) at a distance of 1.06 m from the head.

b) An air-blast wave associated with a peak overpressure of 0.5268 MPa. This is equivalent to a free – air explosion of 0.0698 kg of TNT at a standoff distance of 0.6 m.

The effects of the constitutive models for the brain are investigated for the frontal blast loading case (a), while brain tissue response to frontal and lateral blasts are studied using case (b). A typical blast simulation took 25 hours using 6-8 processors of the Texas A&M Supercomputing Facility *EOS IBM iDataplex Cluster* for the blast event with a duration of 1 ms for the mesh model with 552162 quadratic tetrahedral elements.

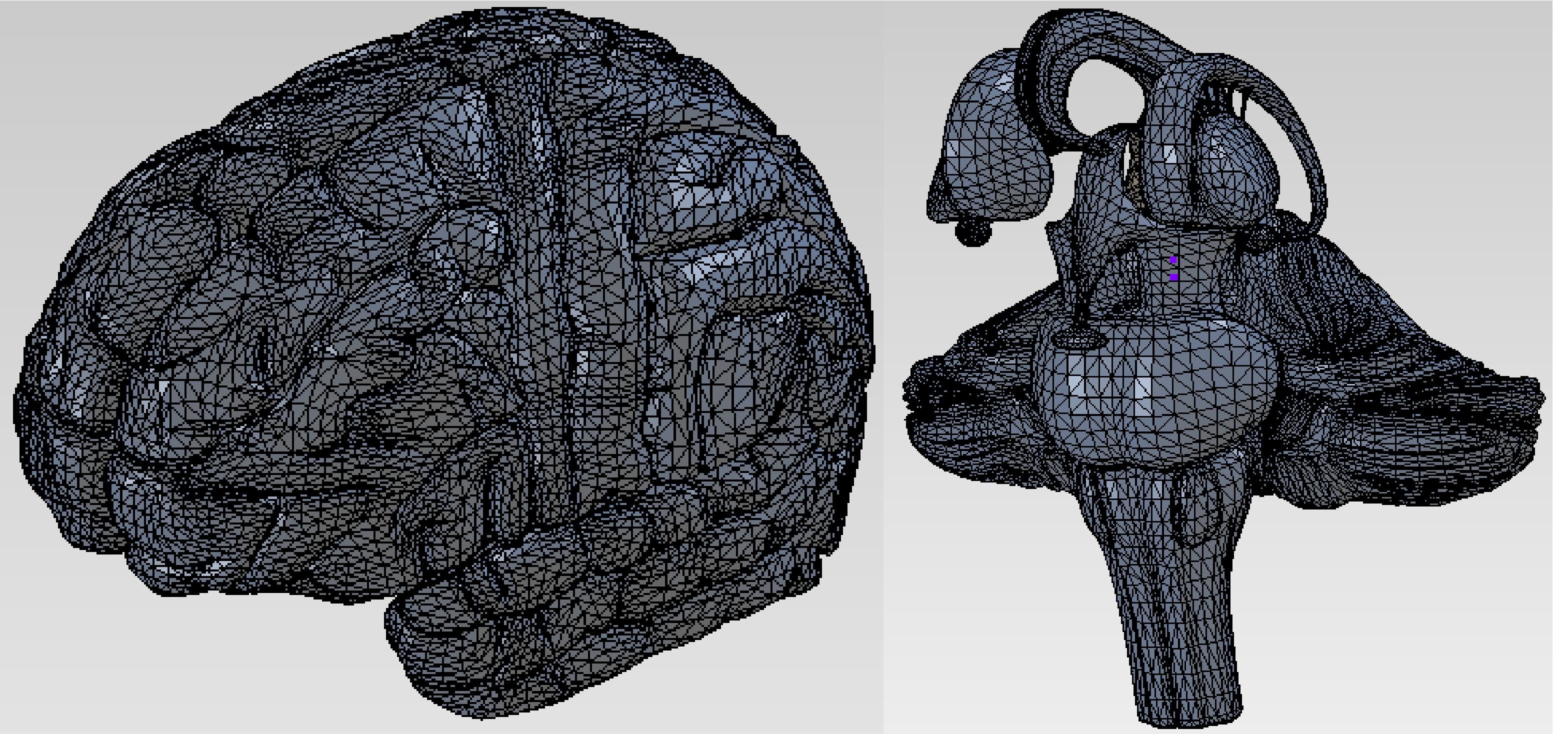

Figure 31. Polygonal model for human brain.

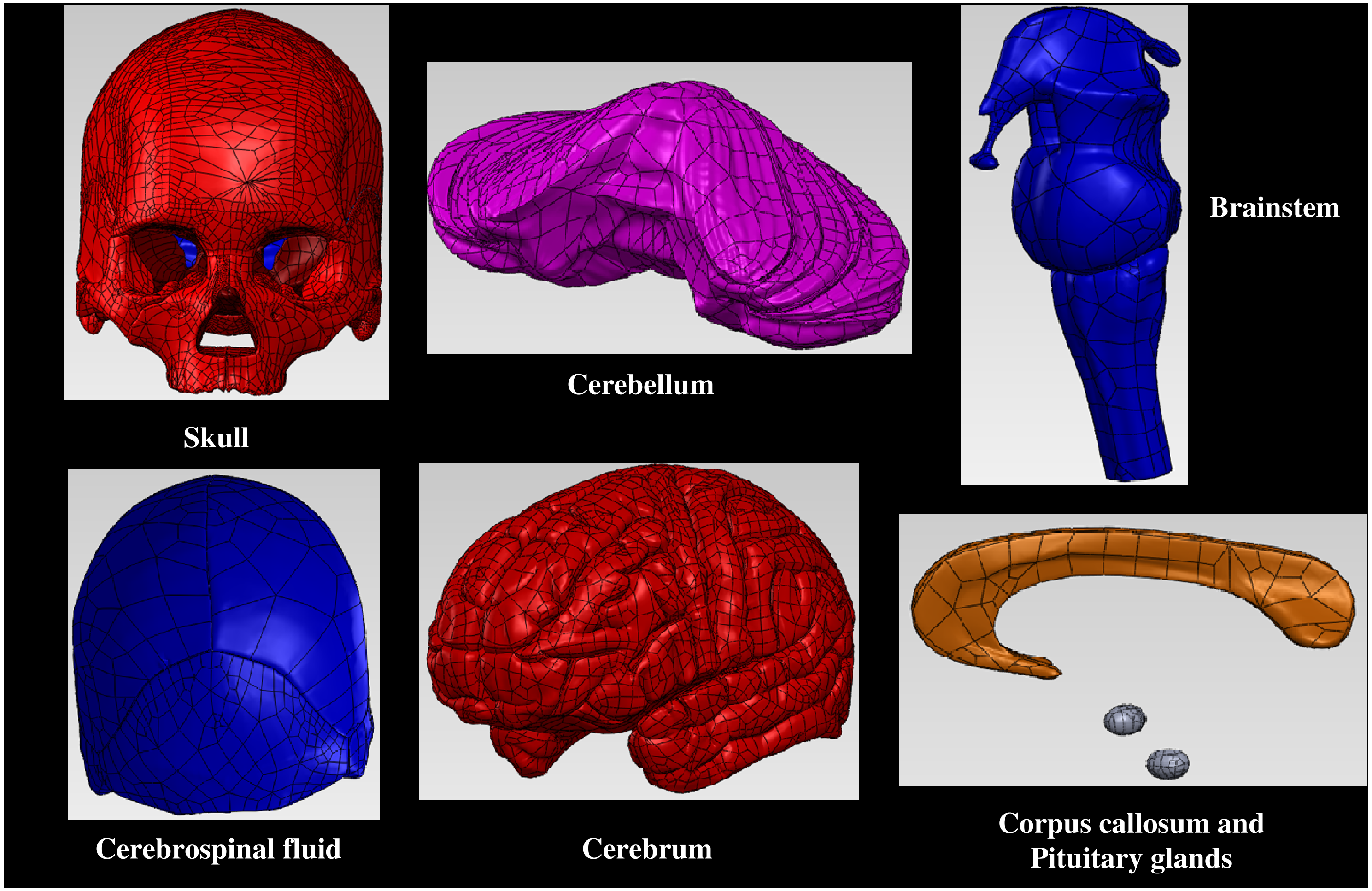

Figure 32. Surface model for skull and various parts of a human brain generated from polygonal model.

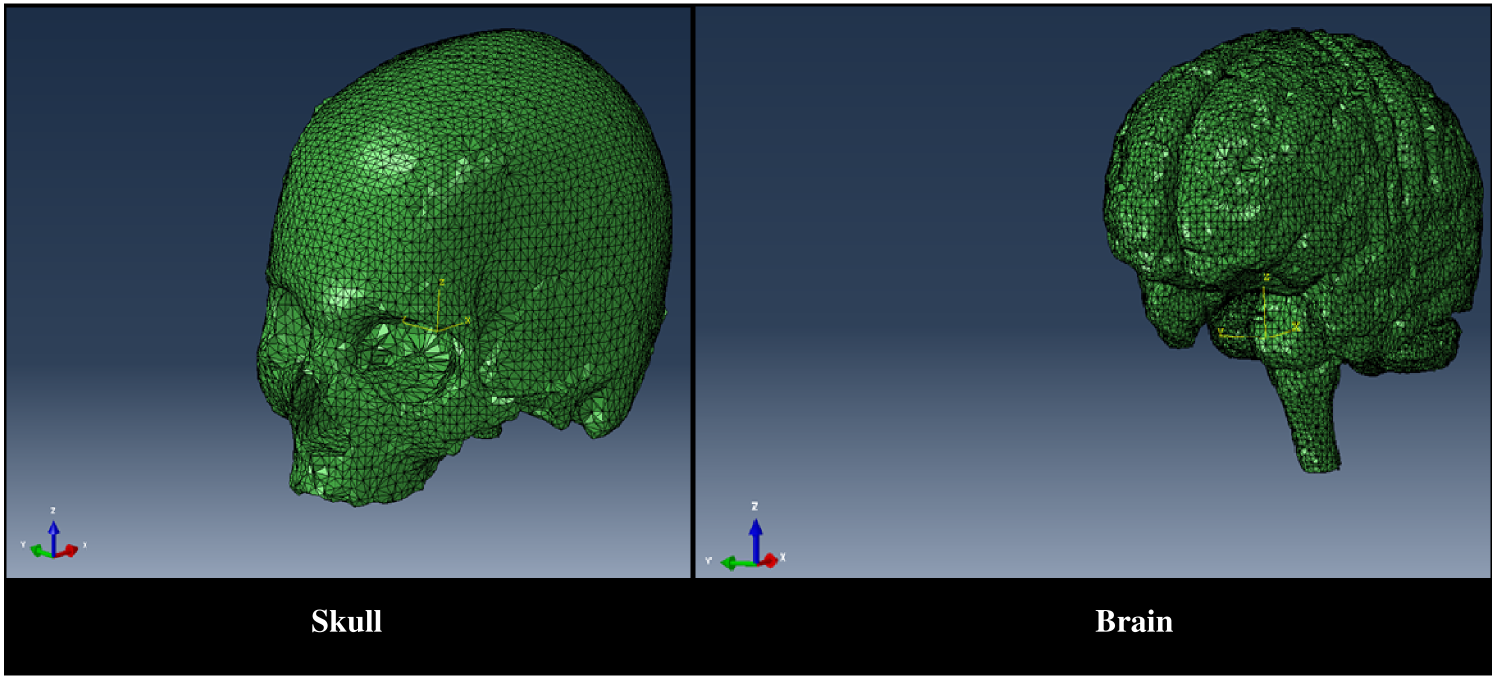

Figure 33. Finite element mesh of a human head.

4.3 Material Models for Skull and CSF

Modeling of the response of a human head to air blast requires the knowledge of the constitutive behavior of various parts of the human brain. Most materials behave quite differently in bulk and under shear. Therefore, it is beneficial to split the deformation of a material locally into volumetric (or dilatational) response and the isochoric (or distortional) responses. A dilatational model defines the pressure – volume (density) response of the material. A strength model is used to define the deviatoric (shape changing) response of the material. Strength models can also be modified to include short term or long term memory effects.

The skull of a human brain is a bony structure and has higher hydrostatic and deviatoric stiffness values compared to other brain tissue materials. The volumetric response of the skull can be described using the linear Hogoniot equation of state (EOS) (e.g., Constantinescu et al., 2011) The most common form of the EOS is the Mie-Gruneisen equation of state (EOS) is as below (Constantinescu et al., 2011):

$$p = \frac{\rho_0 c_0^2 \eta}{(1 - s\eta)^2}\left(1 - \frac{\Gamma_0 \eta}{2}\right) + \Gamma_0 \rho_0 E_m \tag{4.1}$$

where p is the current pressure, E_m is the internal energy per unit mass of the fluid, , Γ_0 is a material constant, ρ_0 is the initial density, η is the nominal volumetric strain and c_0 and s are two material constants which are involved in the following relation:

$$U_s = c_0 + sU_p \tag{4.2}$$

where U_s is the shock velocity and U_p is the particle velocity (Meyers, 1994). The deviatoric response for the skull is modeled as linearly elastic, which satisfies the stress strain relation

$$\boldsymbol{S} = 2G\boldsymbol{e}, \tag{4.3}$$

where **S** is the deviatoric stress, **e** is the deviatoric elastic strain, and G is the shear modulus. The values of Γ_0, s, ρ_0, c_0, and Poisson's ratio (v) for the skull are listed in Table 12.

Table 12 Material parameters for the skull (Chafi et al., 2010).

Material	**Density (kg/m^3)**	**K (GPa)**	**G (GPa)**	**E (GPa)**	**v**	**c_0 (m/s)**	**Γ_0**	**s**
Skull	1800	8.928	6.1475	15	0.22	1850	0	0.94

CSF is a clear, colorless liquid that occupies the subarachnoid space and the ventricular system around the brain and spinal cord. It acts as a shock absorber for the cortex, provides a chemically stable environment, distributes nutrients, and removes waste from the nervous tissue (Thompson, 2000). CSF is a biological fluid with Newtonian characteristics (Ommaya, 1968) and viscosity (also density) similar to that of water. The shock response of the CSF is implemented using linear Hugoniot EOS (given in Eq. (4.1)), with parameters being those of water. The strength model for the CSF is defined using the classical Newtonian fluid model given by

$$\boldsymbol{\tau} = 2\kappa\dot{\boldsymbol{\gamma}} \tag{4.4}$$

In the above equation, $\boldsymbol{\tau}$ is the deviatoric stress, κ is the viscosity, and $\dot{\boldsymbol{\gamma}}$ is the rate of deformation tensor. The material parameters for the CSF are listed in Table 13.

Table 13 Material constants for CSF (Constantinescu et al., 2011).

Material	Density (kg/m^3)	K (GPa)	κ kg/ms	c_0 (m/s)	Γ_0	s
CSF	1000	2.19	0.001	1425	6.15	1.75

4.4 Material Models for Brain Tissue

Brain is a very complex organ involving many sub-structures. The head model considered in this study includes the following seven sections: cerebrum (main brain), cerebellum (small brain), brainstem, cerebrospinal fluid (CSF), corpus callosum, pituitary glands, and skull (see Fig. 32). The cerebral cortex is the outer layer of the brain (Thompson, 2000). It covers the cerebellum and cerebrum. Cerebral cortex is a sheet of neural tissue, and is called gray matter (because of its gray color). The inner layer of the brain is made of a different type of nerve fibers called white matter (Thompson, 2000). The cerebrum is divided into left and right hemispheres, which are connected by a mass of nerve fibers known as the corpus callosum. The corpus callosum is the largest white matter structure in the brain. Previously, brain tissue was hypothesized as an isotropic material. However experiments have shown that while gray matter has an isotropic structure, white matter has a transversely isotropic nature (Prange and Margulies, 2002) because of the oriented neural tracts. The brainstem has also been found to be a transversely isotropic material (Arbogast and Margulies, 1999).

Understanding how the loading and kinematic boundary conditions applied to the head (skull) induce the stress response of the tissue is challenging because of the interplay among a number of factors. In this paper, three different constitutive models are considered to represent mechanical responses of brain tissues.

4.4.1 Material Set 1 (MS 1) – Linearly Elastic Material Model

For this material set, the volumetric response of the brain tissue is modeled using the linear Hogoniot EOS given in Eq. (4.1). The deviatoric portion of the tissue response has is modeled as linearly elastic using Eq. (4.3). Time independent deviatoric deformation has been assumed by Grujicic et al., (2010 ,2011) in their simulations of blast-induced TBI. This can justified by considering the fact that instantaneous to long-term shear modulus relaxation time is on the order of hundreds of milliseconds, which is several orders of magnitude longer than the blast wave- human head interaction time. Thus, time - dependent deviatoric deformations are considered to play a secondary role in the early time response of the head to a blast wave, and can therefore be ignored. For this material set the brain tissue is considered homogeneous. The material parameters describing this constitutive model are provided in Table 14.

Table 14 EOS and strength model parameters for material set 1(Grujicic et al., 2010; Taylor and Ford, 2007)

Material	**Density (kg/m^3)**	***G* (KPa)**	**c_0 (m/s)**	**Γ_0**	***s***
Brain Tissue	1040	22.53	1510	1.41	1

4.4.2 Material Set 2 (MS 2) - Isotropic Hyperelastic and Linearly Viscoelastic Material Model

For Material Set 2 (*MS 2*), the compressible Mooney – Rivlin model was used to represent the hyper-elastic constitutive behavior of the brain. The strain energy density function for the Mooney – Rivlin material is defined as (Chafi et al., 2010):

$$W = C_{10}(I_1 - 3) + C_{01}\left(I_2 - 3\right) + \frac{1}{D_1}\left(J - 1\right)^2 \tag{4.5}$$

where I_1, I_2 are the first and second invariants of the left Cauchy-Green deformation tensor **B**, J (= det **F**) is the Jacobian, and C_{10}, C_{01}, and D_1 are three constants.

The time dependent deviatoric deformations are described using linear viscoelasticity. The shear viscoelastic behavior is defined by a second order Prony series expansion of the dimensionless relaxation modulus as (Chafi et al., 2010):

$$g_R(t) = \frac{G_R(t)}{G_0} = 1 - \sum_{i=1}^{N} g_i\left(1 - e^{-t/\tau_i}\right) \tag{4.6}$$

where G_R(t) is the long term shear relaxation modulus, G_0 is the instantaneous shear relaxation modulus. As in Material Set 1 all parts of the brain tissue are represented by the same material parameters. The material constants in Eqs. (4.5) and (4.6) are listed in Table 15. Material Set 2 has been widely used (e.g., Mendis, 1992; Zhang et al., 2004; Taylor and Ford, 2009; Chafi et al., 2010; Chen and Ostoja-Starzewski, 2010; Nyein et al., 2010) for computational modeling of brain trauma.

Both material set 1 and material set 2 are available in commercial finite element softwares like ABAQUS/Explicit®**.**

Table 15 Material constants for Material Set *2* (Mendis, 1992)

Material	C_{10} (Pa)	C_{01} (Pa)	$1/D_1$ (GPa)	g_1	g_2	τ_1 s^{-1}	τ_2 s^{-1}	Density (kg/m^3)
Brain	3102.5	3447.2	1.095	0.52826	0.3019	0.008	0.1499	1040

4.4.3 Material Set 3 (MS 3) - Anisotropic Hyper-elastic and Viscous Material Model

Following analyses carried out in Chapter 3 the strength model of the brain tissue is defined using a self-developed transversely isotropic viscous hyperelastic model. Strain rate has is regarded as an explicit variable. We briefly describe this model here. The deformation gradient tensor **F** and the right Cauchy-Green deformation tensor **C** (=$\mathbf{F}^T\mathbf{F}$) can be multiplicatively decomposed into a volume-changing and a volume-preserving part as follows (e.g., Holzapfel, 2000):

$$\begin{aligned} \mathbf{F} &= \left(J^{1/3}\right)\overline{\mathbf{F}} \\ \mathbf{C} &= \left(J^{2/3}\right)\overline{\mathbf{F}}^{\mathrm{T}}\overline{\mathbf{F}} = \left(J^{2/3}\right)\overline{\mathbf{C}} \end{aligned} \tag{4.7}$$

where **F** is the deformation gradient tensor, **C** is the right Cauchy – Green deformation tensor, and $\overline{\boldsymbol{F}}$ and $\overline{\boldsymbol{C}} = \overline{\boldsymbol{F}}^T\overline{\boldsymbol{F}}$ are distortional parts, which are called modified **F** and **C**. Clearly it follows from Eq. (4.7) that $\det\overline{\mathbf{F}} = \left(J^{-1/3}\right)^3 \det\mathbf{F} = 1, \det\overline{\boldsymbol{C}} = \left(J^{-2/3}\right)^3 \det\mathbf{C} =$ 1, and

$$\overline{\lambda}_i = \frac{1}{J^{1/3}}\lambda_{\mathrm{i}} \tag{4.8}$$

where λ_i are the principal stretches associated with **F** and $\overline{\lambda}_i$ are the principal stretches for the distortional deformations associated with $\overline{\mathbf{F}}$.

The strain energy density function can be written as:

$$W(\mathbf{C},\dot{\mathbf{C}}) = W_{vol}(J) + W_{iso}(\overline{\mathbf{C}},\dot{\mathbf{C}}), \tag{4.9}$$

where W_{vol} is the part of the strain energy density function describing the volumetric response of the material, W_{iso} is the part of the strain energy density function describing the isochoric response of the material, and $\dot{\mathbf{C}}$ is the tensor defining the total material time derivative of **C.**

This leads to an additive decomposition of the Second Piola-Kirchhoff stress **S** into a volumetric part $\mathbf{S}_{vol}$ and an and isochoric part $\mathbf{S}_{iso}$ as:

$$\mathbf{S} = \mathbf{S}_{vol} + \mathbf{S}_{iso}, \tag{4.10}$$

where:

$$\mathbf{S}_{vol} = JP\mathbf{C}^{-1},\ \mathbf{S}_{iso} = J^{-2/3}Dev\overline{\mathbf{S}} \tag{4.11}$$

with

$$P = \frac{dW_{vol}(J)}{dJ},\ \overline{\mathbf{S}} = 2\frac{\partial W_{iso}(\overline{\mathbf{C}})}{\partial \overline{\mathbf{C}}}, \tag{4.12}$$

with P as the hydrostatic pressure, and $\overline{\mathbf{S}}$ as the modified (fictitious) second P-K stress and

$$Dev(\overline{\mathbf{S}}) = \left(\mathbf{I}_4 - \frac{1}{3}\mathbf{C}^{-1} \otimes \mathbf{C}\right) : \overline{\mathbf{S}} = \overline{\mathbf{S}} - (1/3)\left[\mathbf{C} : \overline{\mathbf{S}}\right]\mathbf{C}^{-1} \tag{4.13}$$

as the deviatoric operator in the Lagrangian description where $\mathbf{I}_4$ is the fourth-order identity tensor.

The incompressible material model developed in Chapter 3 is used to describe the isochoric response of the compressible brain tissue with short-term memory effects. The isochoric stress $\mathbf{S}_{iso} = J^{-2/3}\left(\overline{\mathbf{S}} - p\mathbf{C}^{-1}\right)$ can be expressed as,

$$\mathbf{S}_{iso}(t) = \underbrace{\mathbf{S}_{isoe}(\mathbf{C}(t))}_{\substack{Equilibrium \\ response}} + \underbrace{\mathbf{S}_{isov}(\dot{\mathbf{C}}(t);\mathbf{C}(t))}_{\substack{Short-term \\ memory\ response}} - p\mathbf{C}^{-1}, \tag{4.14}$$

where

$$\mathbf{S}_{isoe} = 2\frac{\partial W_{isoe}}{\partial \mathbf{C}}, \quad \mathbf{S}_{isov} = 2\frac{\partial W_{isov}}{\partial \dot{\mathbf{C}}}, \tag{4.15a,b}$$

are, respectively, the elastic and viscous parts of the isochoric stress tensor.

Based on the strain energy density function proposed in Chapter 3, the total isochoric stress is given as,

$$\begin{aligned} \mathbf{S} &= 2\frac{\partial W_{isoe}(\mathbf{C},\dot{\mathbf{C}})}{\partial \mathbf{C}} + 2\frac{\partial W_{isov}(\mathbf{C},\dot{\mathbf{C}})}{\partial \dot{\mathbf{C}}} \\ W_{isoe}(\mathbf{C}) &= \frac{\mu}{2}(I_1 - 3) + \mu_1(K_4 - 7)^q \\ W_{isov}(\dot{\boldsymbol{C}}) &= \frac{1}{2}\mu_2 J_2 (I_1 - 3)^{n_1} + \mu_3 J_5 (K_4 - 2)^{n_2} \end{aligned} \tag{4.16a,b,c}$$

where,

$$\begin{aligned} K_4 &= I_2 + 2I_1 I_4 - 2I_5 \\ J_2 &= \frac{1}{2} tr\left(\dot{\boldsymbol{C}}^2\right) \\ J_5 &= \left(\boldsymbol{a}_0 \otimes \boldsymbol{a}_0\right) : \dot{\boldsymbol{C}}^2 \end{aligned} \tag{4.17}$$

This strength model is described by 4 material parameters μ, μ_1, μ_2, and μ_3 and three exponents q, n_1 ,n_2, which can be determined from fitting experimental data. As the brain tissue exhibits different behaviors in tension and shear, separate parameters are obtained for each loading type. For Material Set 3 the brain tissue is considered as inhomogeneous for the quasi-static response. The material parameters used for different structures are listed in Tables 16 and 17.

Table 16 Parameters of the brain tissue for the quasi-static response (0.01/s) in tension and shear.

Constants(Model II)	**Quasi-static tensile response**	**Quasi-static shear response**	**Structure**
μ	279.41 Pa	359.74 Pa	Cerebrum
μ_1	0.3315 Pa	0 Pa	
q	6.7	1	
μ	279.41 Pa	359.74 Pa	Cerebellum
μ_1	0 Pa	0 Pa	
q	0	0	
μ	558.82 Pa	719.48 Pa	Brainstem
μ_1	0.6315 Pa	0 Pa	
q	6.7	1	
μ	307.351 Pa	395.714 Pa	Corpus Callosum, Pituitary Glands
μ_1	0.36465 Pa	0 Pa	
q	6.7	1	

Table 17 Parameters representing brain tissue viscous response in tension and shear.

Constants(Model II)	**Viscous tensile response**	**Viscous shear response**
μ_2	2260.9625 Pa	161.44875 Pa
μ_3	60.9 Pa	15395 Pa
n_1	1	1
n_2	0.95	0.6

For the Material Set *3* the volumetric response (*P*) is represented by the Tait EOS. The Tait EOS is commonly used to model fluids under large pressure variations, which is the case for blast/ballistic loading. The pressure *P* is given as (e.g. Moore et al., 2009):

$$P = B\left[J^{-(\Gamma_0+1)} - 1 \right] \tag{4.18}$$

where *B* and Γ_0 are constants. The value of Γ_0 is taken to be 6.15, which is the value for water. The constant *B* is computed using the relation,

$$B = \left(\frac{K}{\Gamma_0 - 1} \right) \tag{4.19}$$

where *K* is taken as 2.19 GPa, which is the bulk modulus of the brain tissue (Stalnaker, 1969).

A VUMAT code is compiled to implement the Material Set 3 in ABAQUS/Explicit. Table 18 summarizes all the constitutive relations used in this study.

Table 18 Summary of the material models used for blast simulations.

Name	**Deviatoric Relation**	**Time Dependent Relation**	**Volumetric Relation**
MS 1	Linear elastic	Ignored	Linear elastic
MS 2	$W_{elastic} = C_{10}(I_1 - 3) + C_{01}\left(I_2 - 3\right)$	$g_R(t) = \dfrac{G_R(t)}{G_0} = 1 - \sum_{i=1}^{N} g_i\left(1 - e^{-t/\tau_i}\right)$	$W_{vol} = \dfrac{1}{D_1}\left(J - 1\right)^2$
MS 3	$W_{isoe} = \dfrac{\mu}{2}(I_1 - 3) + \mu_1(K_4 - 7)^q$	$W_{isov} = \dfrac{1}{2}\mu_2 J_2(I_1 - 3)^{n_1} + \mu_3 J_5(K_4 - 7)^{n_2}$	$P = B\left[J^{-(\Gamma_0+1)} - 1\right]$

4.5 Validation of Finite Element Model Setup

Neuberger et al., (2007) studied the dynamic behavior of blast loaded rolled homogeneous Armor (RHA) circular steel plates subjected to TNT air blast loading. In their experiment, the target plate was supported between two thick armor steel plates. The spherical TNT charges were hung in air at a specified distance from the plate surface. The charges were ignited from the center, and the maximum deflection at the plate center was measured using a custom-made comb-like device. To validate our model setup for simulating air blast loading, a finite element analysis of the experiment of Neuberger et al., (2007) is performed using ABAQUS/Explicit®. In order to represent the dynamic mechanical behavior of the RHA plates, Johnson – Cook (J-C) constitutive model was implemented. The J-C model is given by (e.g. Neuberger et al., 2007):

$$\sigma_y = \left(A + B_1 \varepsilon_p^n\right)\left(1 + c \ln \dot{\varepsilon}\right)\left(1 - T^m\right) \tag{4.20}$$

where, A, B_1, n, c, and m are material constants, whose values are listed in Table 19, ε_p is the effective plastic strain, $\dot{\varepsilon}$ is the effective plastic strain rate for the RHA plates normalized by a reference strain rate $\dot{\varepsilon}_0$ (with $\dot{\varepsilon}_0$ = 1/s in this case) and T is the non-dimensional temperature given by,

$$T = \left(T' - T'_{room}\right) / \left(T'_{melt} - T'_{room}\right) \tag{4.21}$$

where T' is the current material temperature, T'_{room} is the room temperature, and T'_{melt} is the melting temperature of the material. The blast loading was defined using the CONWEP® function in Abaqus/Explicit®. By using the CONWEP® function, both air and surface blasts can be simulated. For CONWEP air blast loading, the explosive charge is not in contact with the ground surface. It is assumed that the observer is close to the source of explosion, and will be subjected to the incident wave loading only, with no interaction between the incident waves and the waves reflected from the ground. In surface blast loading, the explosive charge is located on the ground. As a result, the incident and the reflected waves merge instantly. For ideal (rigid) reflecting surface, characteristics of the reflected waves such as velocity, acceleration, and overpressure are assumed to be the same as that of incident waves. However, because of instant merging of the reflected and incident waves the energy yield for the surface blast is assumed to be twice as large as air burst for the same amount of explosive.

Table 19 Material parameters for the J-C model (Neuberger et al., 2007).

Material	***A* (MPa)**	**B_1 (MPa)**	***n***	***c***	***m***
RHA plate	1000	500	0.26	0.014	1

Two different boundary conditions were used for simulations – free and fixed. For case 1(see Table 20) the following parameters were taken: plate thickness t = 0.05m, plate diameter D = 2m, charge weight W = 50 kg of TNT, and distance from the charge center to the plate surface R = 0.5 m. Figure 34(a) shows the normalized mid-point deflection changing with time predicted by the current model. In Figure 34(b) the results of Neuberger et al. (2007) are displayed. Figures 35(a) and 35(b) show normalized effective stress predicted by the current model and its comparison with that provided in Neuberger et al. (2007). The normalized midpoint deflection values for the other cases are listed in Table 20. From Table 20 and the Figs. 34 and 35 it is seen that the experimental data (Neuberger et al., 2007) and predicted results by the current model are in good agreement for plate under air blast loading. This agreement validates numerical algorithm and model setup in ABAQUS/Explicit®. It can also be seen from Table 20 that the CONWEP® surface blast values for the normalized midpoint deflection are much higher than the experimental values. Hence, for further simulations of the skull/brain assembly the CONWEP® air blast function is used. The CONWEP® air burst module in ABAQUS/Explicit® does permit specification of the distance of the explosive charge from the ground surface. It is assumed that the charge is located far enough above the ground so as to avoid interactions between incident and reflected waves.

Table 20 Comparison of the experimental results of Neuberger et al. (2007) and the computational results in the present study.

t (m)	D (m)	W (kg, TNT)	R (m)	δ/t Experimental	δ/t CONWEP Air Blast	δ/t CONWEP Surface Blast
0.05	2	50	0.5	1.84	1.837	4.05158
0.04	2	30	0.4	2.7	2.788	5.1872
0.01	0.5	0.468	0.1	2.60	2.45	4.41
0.04	2	70	0.26	7.45	7.38	12.99
0.02	1	8.75	0.13	8.25	7.92	12.56
0.01	0.5	1.094	0.065	7.45	7.21948	12.4418

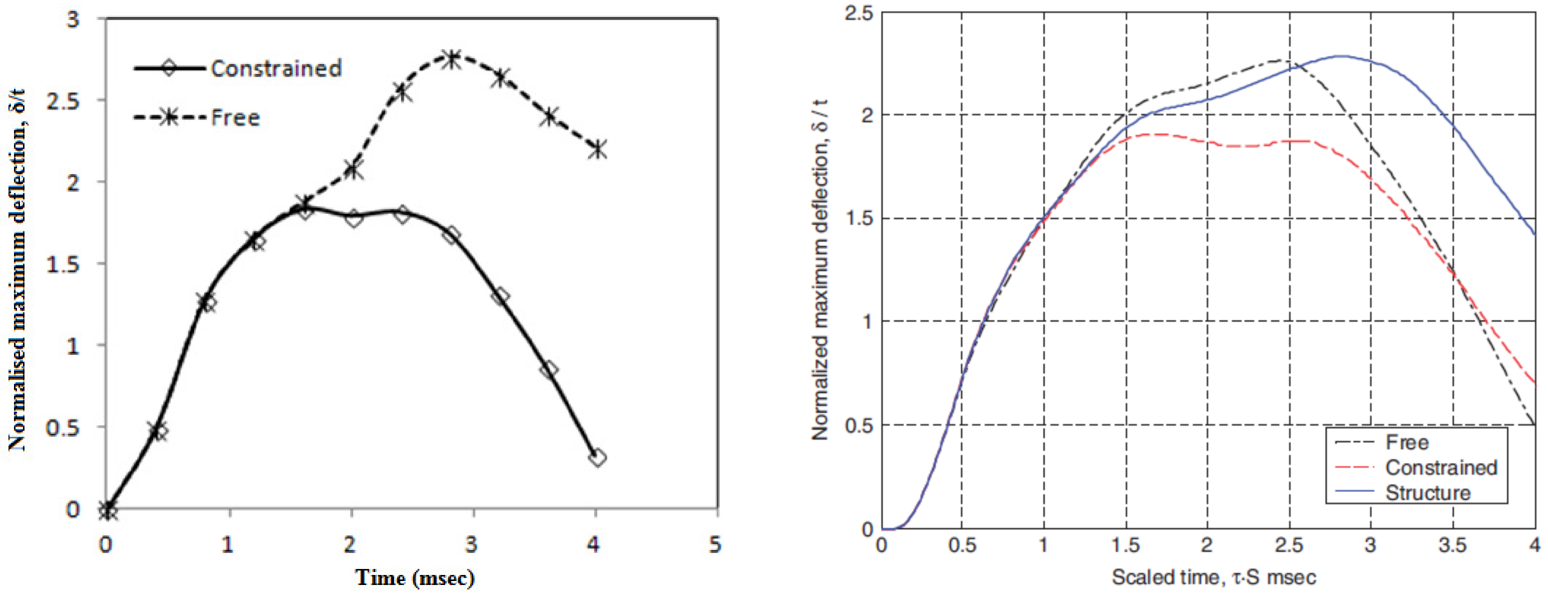

(a) (b)

Figure 34. Midpoint normalised deflection vs. time under free and constrained boundary conditions: a) the curent simulation results b) experimental results of Neuberger et al. (2007)

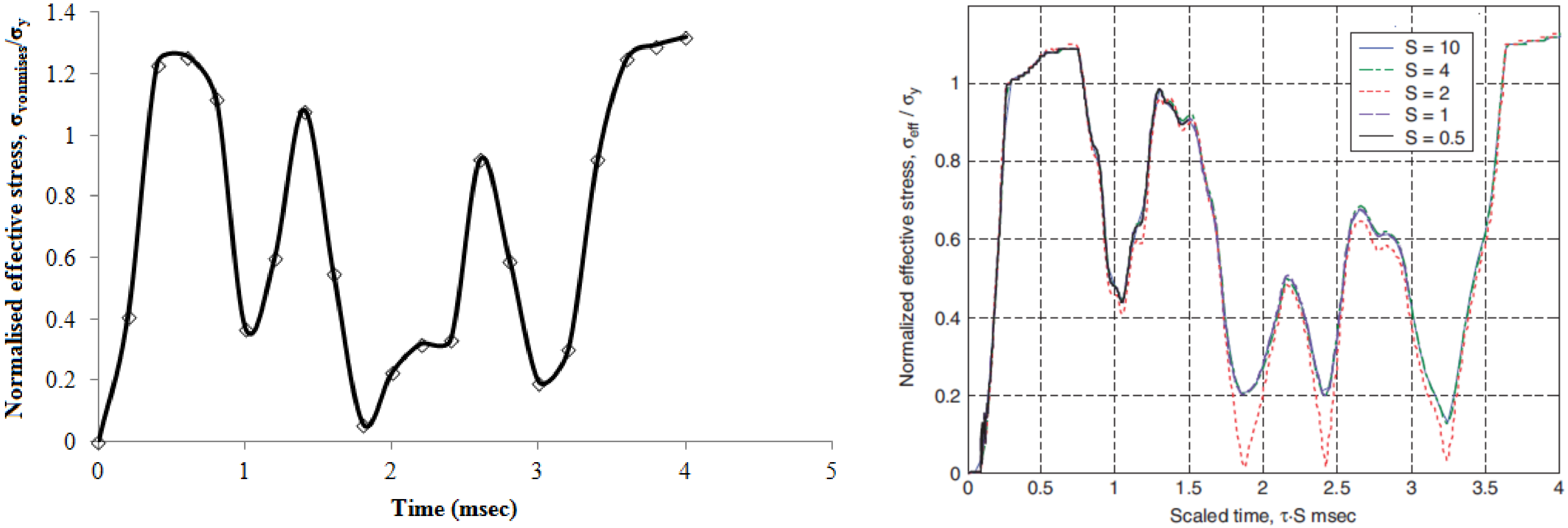

(a) (b)

Figure 35. Normalized stresses vs. time under constrained boundary conditions: a) the curent simulation results b) experimental results of Neuberger et al. (2007)

4.6 Numerical Results and Discussions

In this section, the main simulation results obtained in this study are presented and discussed. All the simulations were run to a time of 1 millisecond in order to study the early time response of the head. The most common types of non-penetrating traumatic brain injury are diffuse axonal injury, contusion and subdural hemorrhage (Taber et al., 2006). Diffuse axonal injuries are caused by shearing, stretching, and/or rotational forces pulling on axons and small vessels. Contusion occurs if the brain undergoes large relative motion with respect to the skull leading to brain – skull collision. This can cause bruising of brain parenchyma. Subdural hemorrhage occurs because of inertia difference between the skull and brain. If the surface layers of the brain undergo severe distortions it can result in tearing of tributary surface veins. In line with these observations, the following mechanical quantities are examined: the temporal and spatial distributions of intracranial pressure, principal stress, von Mises stress, maximum principal strain, and maximum shear strain.

4.6.1 Dilatational Response

The pressure time history for the skull is shown in Figure 36. This graph is obtained for a blast loading of 0.85 kg of TNT at a stand-off distance of 1.06 m, giving a maximum skull front pressure of 18.45 MPa. Figure 37 displays the snapshots of the pressure fields over the frontal bone of the skull. At t = 0.7 ms the blast wave impinges on the frontal bone of the skull, causing an instantaneous rise from atmospheric pressure to a peak overpressure (see Figure 36). As the shock front expands, the pressure decays and the negative pressure (volumetric tension) phase occurs at t = 0.9 ms.

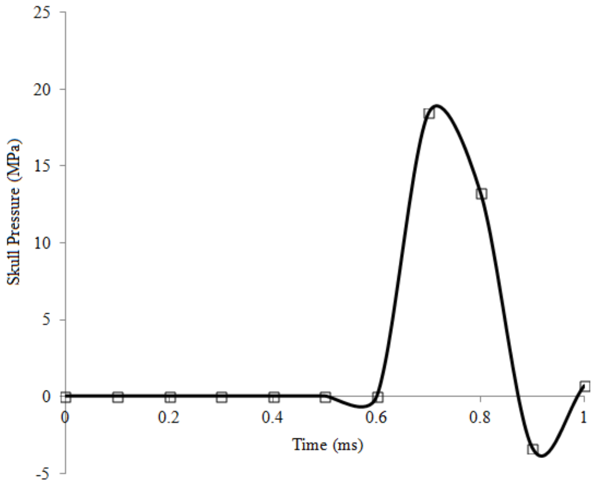

Figure 36. Pressure time history of the skull in response to frontal blast loading of 0.85 kg TNT at distance of 1.06 m distance.

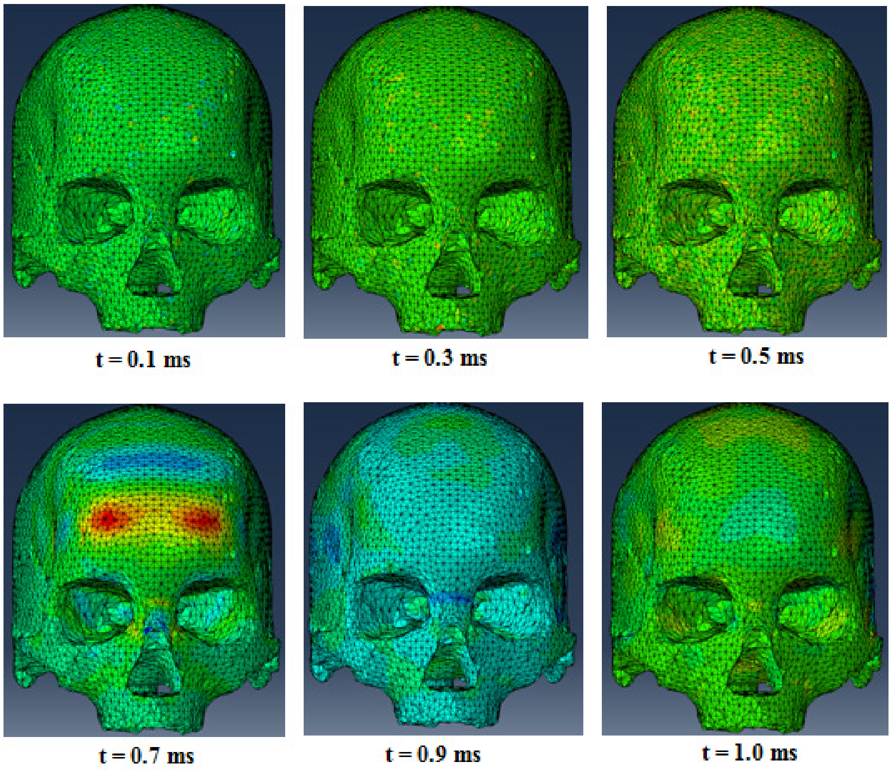

Figure 37. Spatial distribution of blast pressure over the frontal bone of the skull. Red spots are regions of positive pressure, while blue spots are regions of negative pressure.

The negative pressure phase is longer in duration than the positive phase, and is usually less important in design of blast resistant structures. The duration of the positive phase experienced by a structure can be measured in milliseconds (about 0.1 ms in this case) and can change, depending on the nature of explosive, amount of the explosive, and the distance of the structure from the point of detonation. Figures 38a and 38b show the temporal pressure profiles for the brain tissue at coup and contrecoup sites respectively. The TAIT EOS (the Material Set 3) generates highest amounts of coup and contrecoup pressures ranging from −246.8 to 443.5 KPa. Pressure values for the Material Set 2 range from −78.71 to 352.5 KPa, while those for the Material Set 1 fall within −272.5 to 88.8 KPa. The TAIT EOS produces the highest fluctuations in the pressure field with occasional spikes resulting from the interaction of the waves reflected from the inner surface of the skull to the intracranial cavity (see Fig. 40). In Fig. 40 light blue spots are regions of positive pressure, while dark areas are regions of negative pressure. The pressure response for the Material Set 3 is biphasic in nature on both the coup side and the posterior side. In contrast for the Material Set 1 and the Material Set 2 the pressure response follows a typical coup – contrecoup pattern: positive pressures on the impact site are accompanied by negative pressures on the side opposite to the area of impact. For all the three material sets considered, the pressure becomes negative in some locations attaining values that far exceed the pressure values produced by the negative phase of the blast wave.

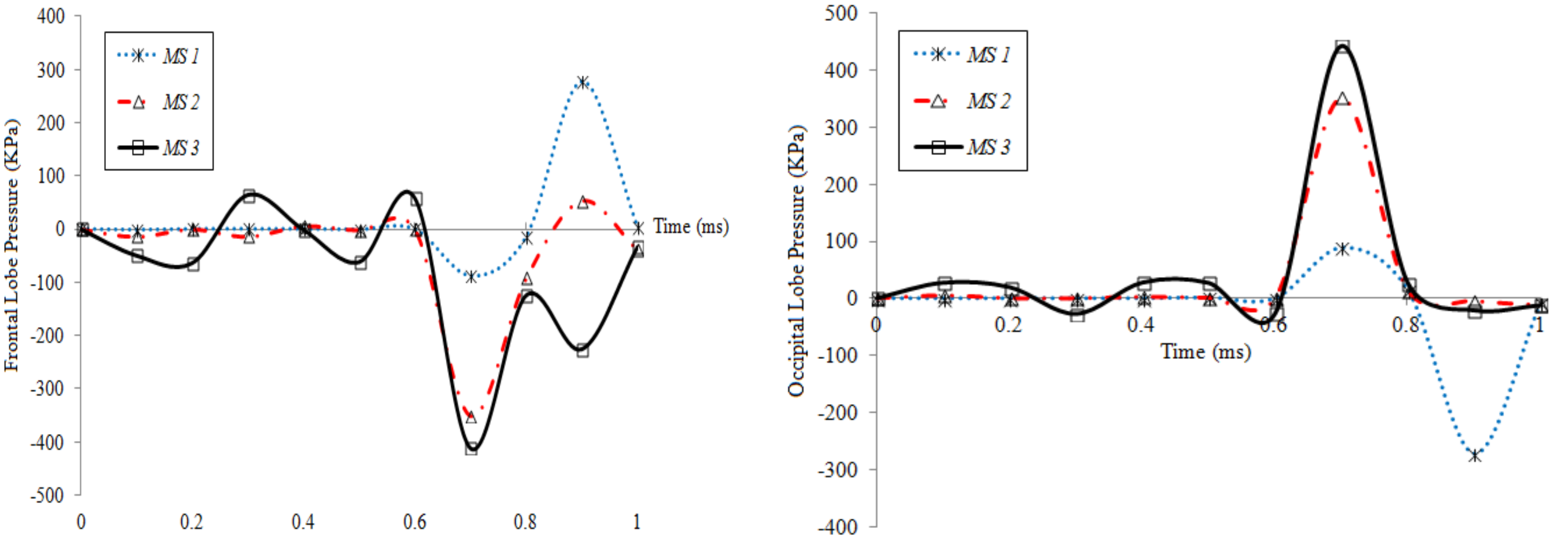

(a) (b)

Figure 38. Pressure response of the cerebrum based on different constitutive relations: a) coup Pressure b) contrecoup pressure

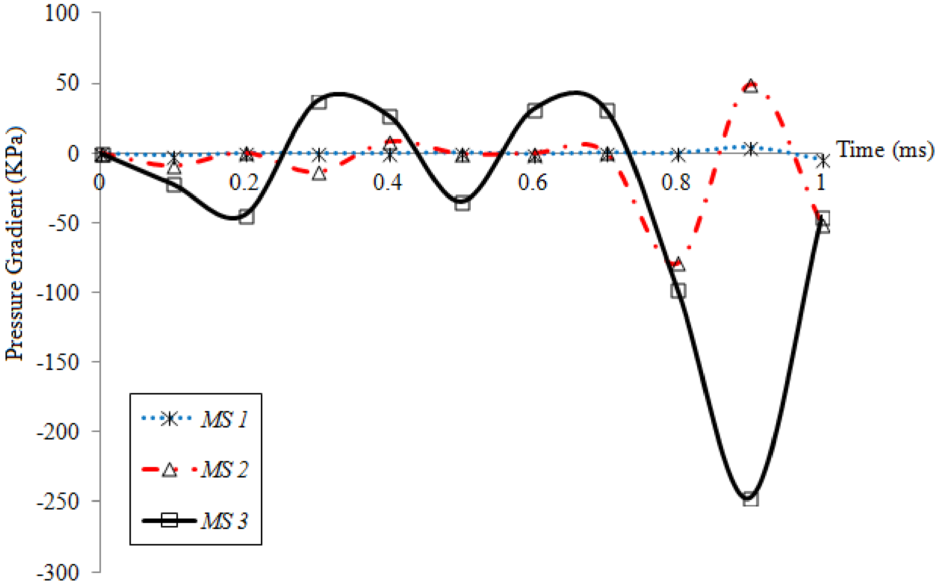

Figure 39. Pressure gradients for the brain in the anterior-posterior direction.

One possible cause of the head injury is the development of pressure gradients upon ingress of pressure the wave into the intracranial cavity. Pressure gradients create shear stresses that result in local deformations of the brain tissue. Figure 39 shows the pressure gradients in the anterior – posterior direction of the brain tissue based on all the three constitutive relations. It can be seen that the Material Set 3 produces very large pressure gradients that fluctuate rapidly as the blast wave undergoes multiple reflection in the intra-cranial cavity. For the Material Set 1 and Material Set 2, only two significant pressure spikes are observed corresponding to the positive and negative (suction) phases of the blast wave over the 1 ms duration.

For blunt trauma injuries the duration of characteristic loading time approximately equals 8 ms (Brands, 2002), which is long compared to the natural period of oscillation of the human head. In such cases the volumetric response of the brain tissue can be explained on the basis of the elastic wave propagation theory. For elastic waves, the pressure and shear wave speeds are related to the bulk and the shear modulus by the equations (e.g., Chen and Ostoja-Starzewski, 2010),

$$c_p = \sqrt{\frac{K + \frac{4}{3}G}{\rho}} \qquad \text{(4.22a,b)}$$

$$c_s = \sqrt{\frac{G}{\rho}}$$

where c_p is the pressure wave velocity, c_s is the shear wave velocity, K is the bulk modulus of material, G is the shear modulus, and ρ is the density of the material. Typically for soft tissues $c_p = 1450$ m/s, while $c_s = 6.3$ m/s (Chen and Ostoja-Starzewski, 2010). Because of very high pressure wave velocities blunt trauma is typically assumed to be a quasi-static event rather than a dynamic one (Brands, 2002; Chen and Ostoja-Starzewski, 2010). Therefore, the volumetric response of the brain tissue for long duration impacts is considered to be independent of the material constitutive relation (Bradshaw and Morfey, 2001; Brands, 2002).

However, the situation is different for blast and ballistic loading. The interaction of a detonating explosive with a material in contact with it (or in the proximity) is complex and involves detonation waves, shock waves, expanding gases, and their interrelationships. When a detonation front encounters a structure, the pressure pulse is transferred to the structure. Shock wave propagation in a material is described by five variables: pressure, particle velocity, shock velocity, specific volume, density, and energy (Meyers, 1994). The equations of conservation of the mass, momentum, and energy give three relations amongst these five variables. An additional fourth equation is needed to describe all the parameters in terms of one parameters (out of the five). This fourth equation is the equation of state (EOS). Some brain injury simulations in the literature assumed the brain tissue volumetric behavior as linearly elastic as done in Material Set 1 for the current simulations (e.g., Ganpule et al., 2011) or use a compressible material with high bulk modulus for representing brain tissue volumetric behavior as done in Material Set 2 (e.g., Chafi et al., 2010; Zhang et al., 2011). However, as can be seen from Figures 38 this leads to underestimation of "shock pressures" compared to the non-linear Tait EOS (the Material Set 3). Also, brain tissue volumetric response is similar to water. Therefore, rather than the actual pressure magnitudes, rapid pressure fluctuations and steep pressure gradients generate high dynamic stresses in the intra-cranial cavity. As can be seen from Fig. 39 the non-linear Tait EOS generates the higher pressure gradients compared to Material Sets 1 and 2. Such assumptions or simplifications about the dilatational response of the brain tissue can lead to artificial attenuation of shock waves and uniform pressure gradients (see Figs. 40 and 41). The bulk modulus of the brain tissue is considered to be similar to that of water. This value was calculated to be approximately 2 GPa by Stalnaker (1969), 2.10 GPa by McElhaney et al. (1976), while Lin et al. (1997) measured the values of 2.28 GPa for the lamb brain gray matter, and 2.41 GPa for the white matter. The most common value used for impact simulations is 2.19 GPa. However, El Sayed et al.(2008) used a much smaller value of 2.19 MPa for impact simulations, while Zhang et al. (2001) reported that the reduction of bulk modulus by an order of magnitude had no significant effect on the model response.

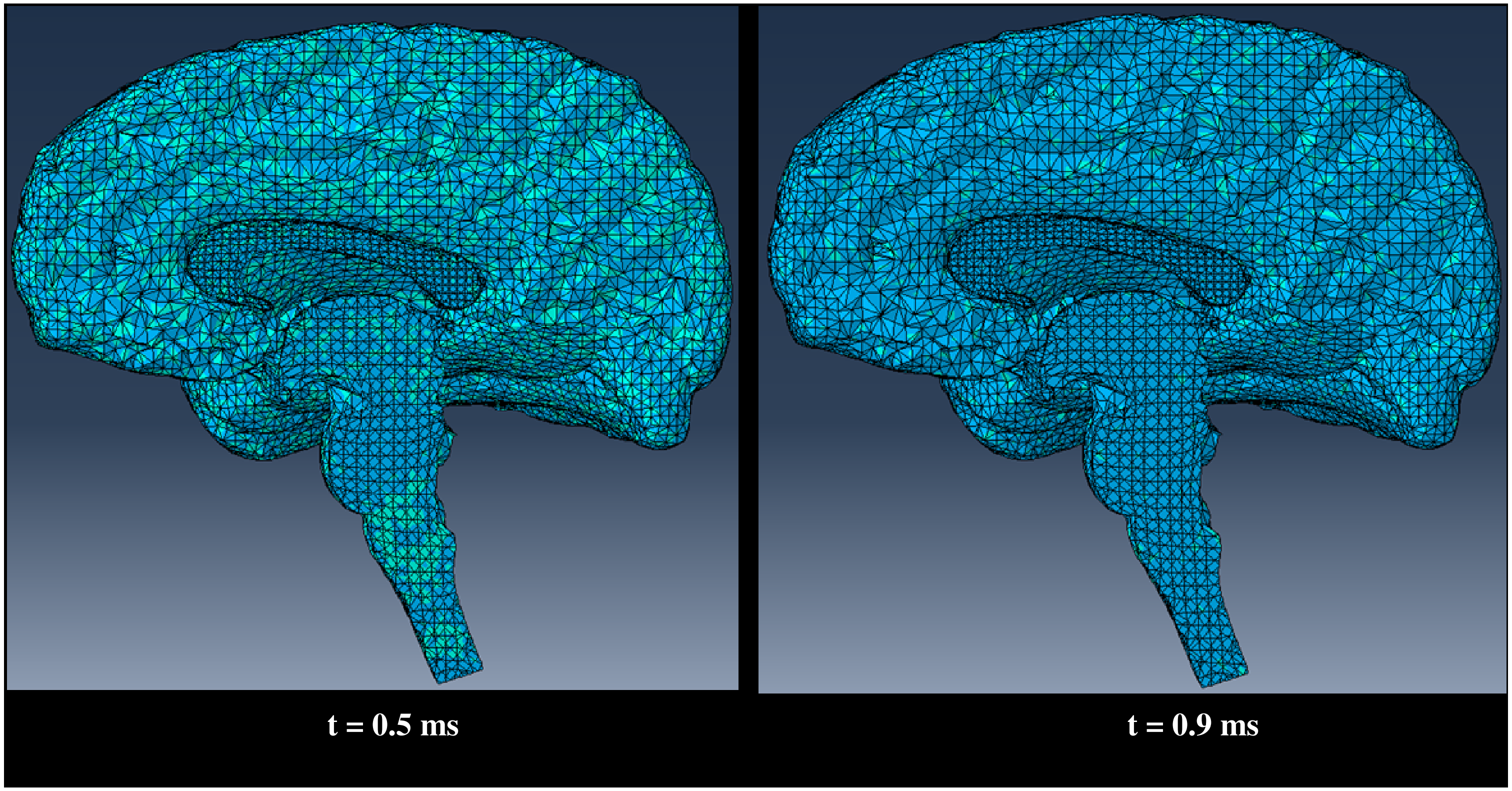

Figure 40. Pressure distribution predicted using the TAIT EOS at the mid-saggital section of the brain.

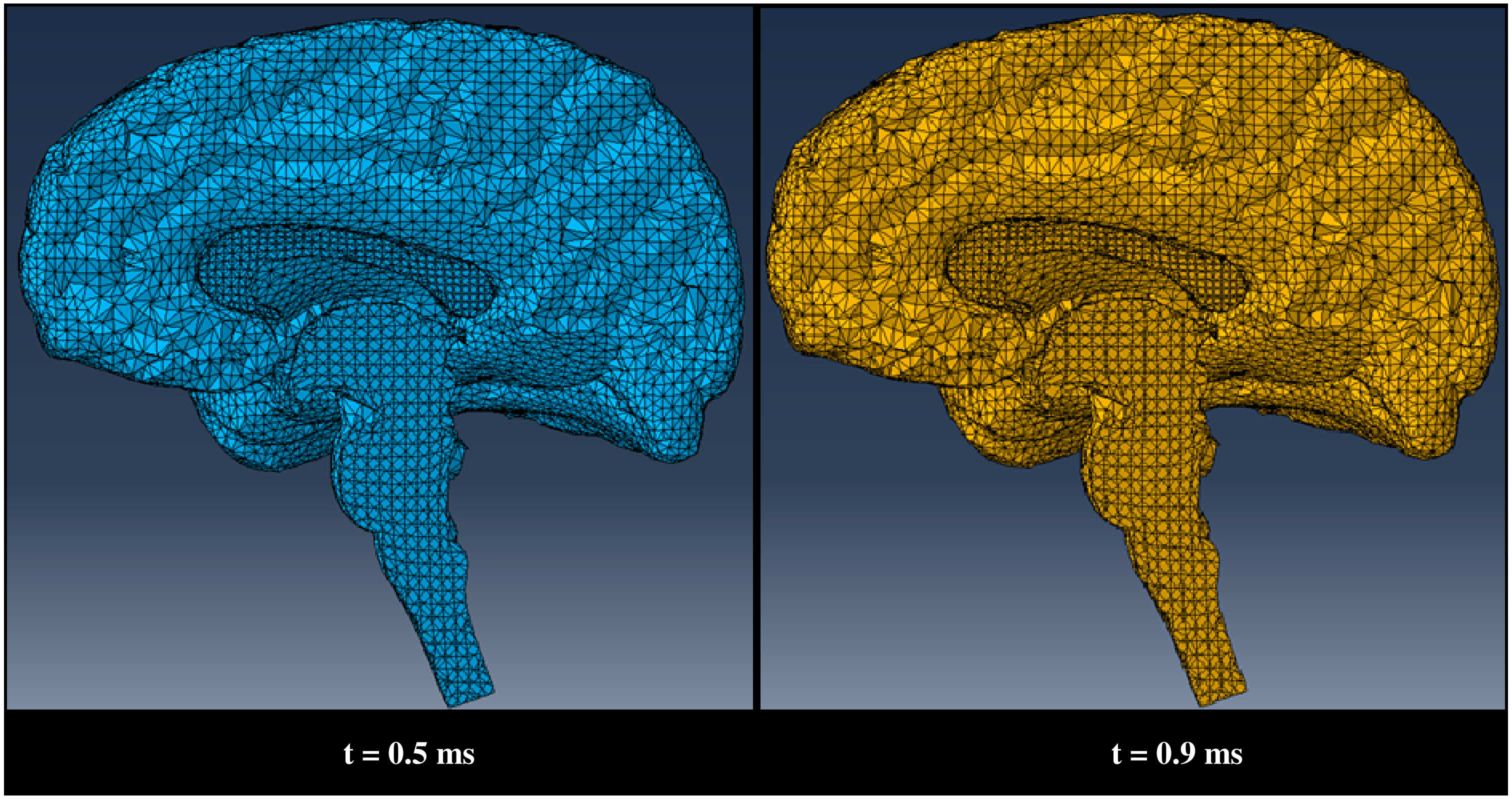

Figure 41. Intracranial pressure distribution based on compressible Mooney-Rivlin constitutive relation (the *MS 2*) at the mid-saggital section of the brain.

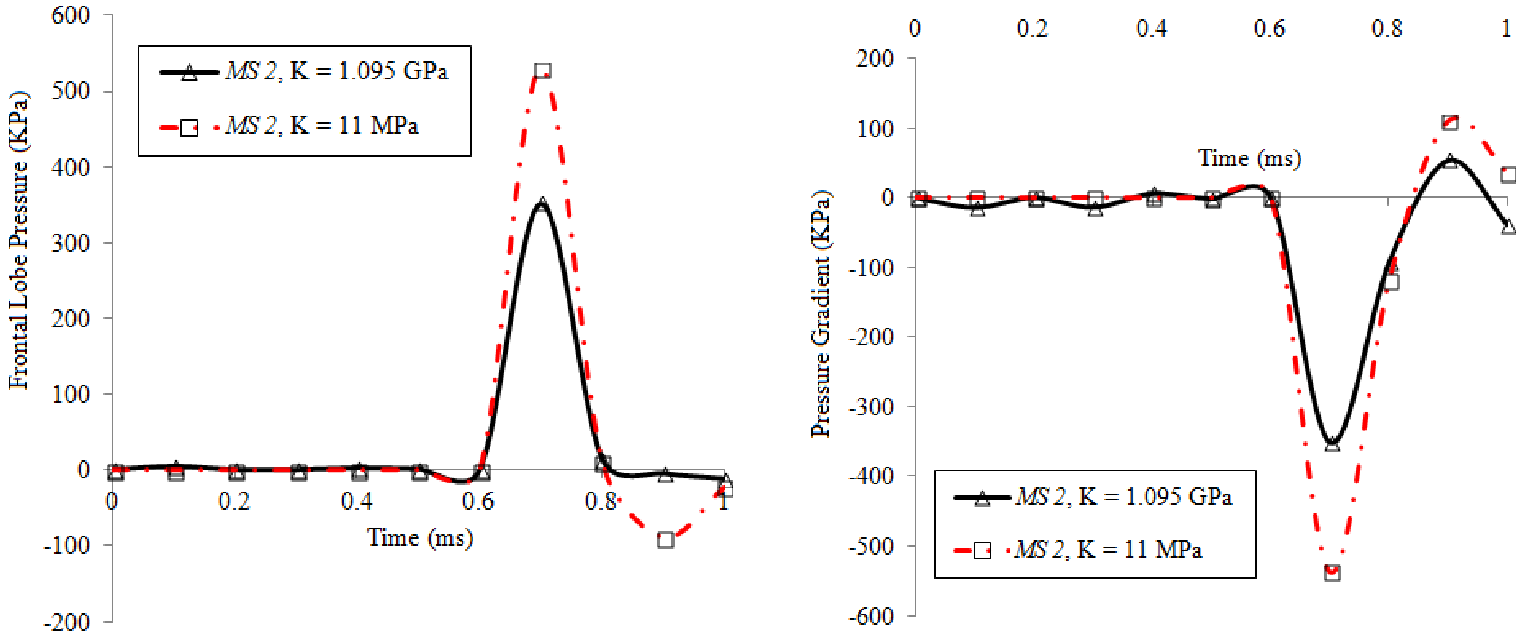

Figure 42. Effect of change in bulk modulus on brain tissue volumetric response a) coup Pressure b) contrecoup pressure

For the explicit dynamic analysis procedure commonly used to solve blast or impact problems, the stable time increment size can be approximated by the following formula (e.g., Brands, 2002):

$$\Delta t \approx \frac{L_{\min}}{c_p} \tag{4.23}$$

where $L_{\min}$ is the smallest element dimension in mesh, and c_p is the dilatational wave speed (see Eq. 4.22a). From Eqs. (4.22) and (4.23) it is clear that for sufficiently fine meshes, higher values of the bulk modulus require excessively small time increments, thus increasing the computational time and the cost. In our simulations it is observed that for a mesh of 552162 elements, a bulk modulus of 11 MPa requires a timestep of 15.5 nano-seconds, while a bulk modulus of 2.19 GPa requires 6 nano-seconds. Figure 14 and Table 21 show the effect of changing (reducing) the bulk modulus on the blast response of the brain tissue. From Fig. 42 it can be seen that even though the response is qualitatively the same for different values of *K*, lowering the dilatational modulus increases the intra-cranial peak pressure and pressure gradient by approximately 50%. It also has an effect on the deviatoric response (see Table 21) causing an 80% increase in the shear and von Mises stress values. Even though the volumetric and the deviatoric responses are decoupled, change in the bulk modulus is seen to affect the deviatoric response possibly because of the change in the pressure gradients. Therefore, unlike longer duration impacts (blunt trauma), the blast response of the brain tissue is sensitive to changes in the bulk modulus. It is advisable to use the value of 2.19 GPa for the bulk modulus in simulations despite high computational costs.

Table 21 Effect of change in bulk modulus on deviatoric stress values in brain tissue

Brain Tissue	Peak Values	
	MS 2	*MS 2-smaller bulk modulus*
Bulk Modulus (MPa)	1100	11
$\sigma_{\text{principal}}$ (KPa)	−85.3 to 59.4	−52.2 to 27.84
$\varepsilon_{\text{principal}}$	0.0361	0.0638
τ (KPa)	−1.07 to 3.18	−5.58 to 5.77
$\tau_{\text{von Mises}}$ (KPa)	8.24	15.14
p (KPa)	−78.71 to 352.5	−109.3 to 529
γ	−0.00196 to 0.0392	−0.00995 to 0.0753

4.6.2 Deviatoric Response

The deviatoric responses of the brain tissue predicted by using different material sets are shown in Figure 44. It should be noted that the time history as shown in figures 36, 38, 39, and 44 displays the temporal variation of peak quantities. Peak intracranial pressure values are observed at the coup and contre-coup sites in the cerebrum, while peak principal and von Mises stress values are found to occur in the brainstem and corpus callosum regions. Table 22 shows the field values based on three material sets. The principal stress and von Mises stress values obtained using the rate dependent viscous model (the Material Set 3) are considerably higher than the other two material sets (Material Set 1 and Material Set 2). Ignoring the time dependent deviatoric deformation (the Material Set 1) generates higher stresses compared to the linear viscoelastic model (Material Set 2). Intra-cranial shear stress magnitudes are substantially lower than the principal stress and von Mises stress levels. Because of the short duration of the shock loading, the principal strain and shear strain are found to be very small. The values up to 0.2 for the principal strain, and 0.2 for the shear strain are obtained for Material Set 1, while least values (see Table 22) were obtained using the Material Set 2.

Explicit modeling of the rate effects and the inclusion of anisotropy have important implications for prediction of BTBI based on damage criteria. For a blast loading of a 0.85 kg of TNT at stand-off distance of 1.06 m, the Material Set 3 predicts failure by the von Mises stress criterion (Shreiber et al., 1997; Kleiven, 2008), the intra cranial pressure criterion (Ward et al., 1980; Zhang et al., 2004), and the strain-strain rate criterion (Viano and Lovsund, 1999; Morrison et al., 2003; Kleiven, 2008). The Material Set 2 and Material Set 1 do not predict failure at all.

Thus the anisotropic viscous hyperelastic constitutive relation gives the stiffest deviatoric response that is for same amount of explosive and the same detonation distance it generates the highest stresses. This stiffer response is due to explicit dependence on the loading rate. The isotropic hyperelastic (Mooney Rivlin or neo-Hookean) linear viscoelastic relation (the Material Set 2) is most often used for BTBI simulations as it is readily available in commercial finite element packages. However, the time scale parameter values for viscoelastic models are two orders of magnitude higher than the duration of a blast. Thus, viscoelastic models only provide the decaying response of soft tissues – either relaxation or creep. Under loading conditions applicable to blast induced TBI, the brain tissue is subjected to a wide range of strain rates and rapid changes in the loading rate of loading. Experiments on brain tissue have also shown that strain rate effects are prominent in brain tissue response to loading (Donnelly and Medige, 1997; LaPlaca et al., 2005; Elkin and Morrison, 2007).

Diffuse axonal injuries (DAI) are caused by elongation of axons (axonal strain) or blood vessels and are characterized by white mater lesions (Mendis, 1992). Corpus callosum (see Fig. 43) is the largest white matter structure in the brain, and connects the left and the right cerebral hemisphere. Under rotational accelerations the corpus callosum is especially susceptible to lesions and hematomas (Mendis, 1992). The intensity of DAI is found to be proportional to the lesions in the corpus callosum region.

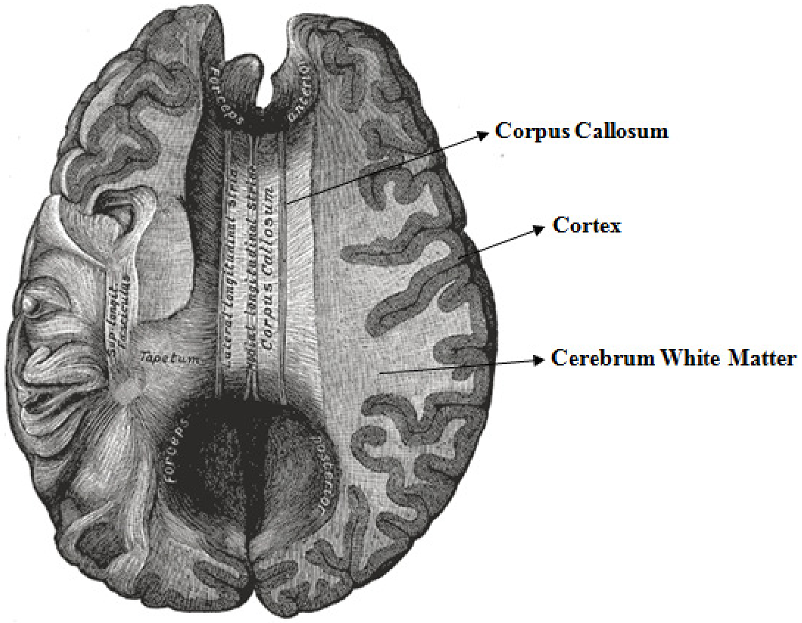

Figure 43. Orientation of axonal fibers in corpus callosum (Gray, 1858)

The axonal bundles in the corpus callosum and white matter of the cerebrum are oriented in the lateral direction (see Fig 43). The axonal strain produced in the corpus callosum might also extend into the cerebrum white mater region to cause DAI. In order to accurately model the progression and location of DAI in computational models it is necessary to measure the axonal strain (normal strain in same direction as axons). Hence it is important to consider the orientation (transversely isotropic) of the axonal bundles in white matter region.

Table 22 Dilatational and deviatoric peak response limits for the selected material models.

Brain Tissue	**Peak Values**		
	MS 1	***MS 2***	***MS 3***
Bulk Modulus (GPa)	2.19	2.19	2.19
$\sigma_{principal}$ (KPa)	–94.1 to 144.3	–85.3 to 59.4	–390.5 to 374.1
$\varepsilon_{principal}$	0.1955	0.0361	0.04971
τ (KPa)	–0.2 to 0.37	–1.07 to 3.18	–0.1306 to 2.118
$\tau_{von\ Mises}$ (KPa)	11.8	8.24	142.5
p (KPa)	–272.5 to 88.8	–78.71 to 352.5	–246.8 to 443.5
σ_{xx} (KPa)	–100 to 138.1	–98.23 to 46.27	–392 to 373.2
σ_{yy} (KPa)	–104.2 to 133.	–91.52 to 41.4	–391 to 374
ε_{xx}	–0.163 to 0.118	–0.00627 to 0.0162	–0.0158 to 0.00970
ε_{yy}	–0.0367 to 0.0209	–0.00852 to 0.00342	–0.00684 to 0.0438
γ	–0.0543 to 0.2017	–0.00196 to 0.0392	–0.04124 to 0.01733
strain rate (/s)	8378	412.8	1655

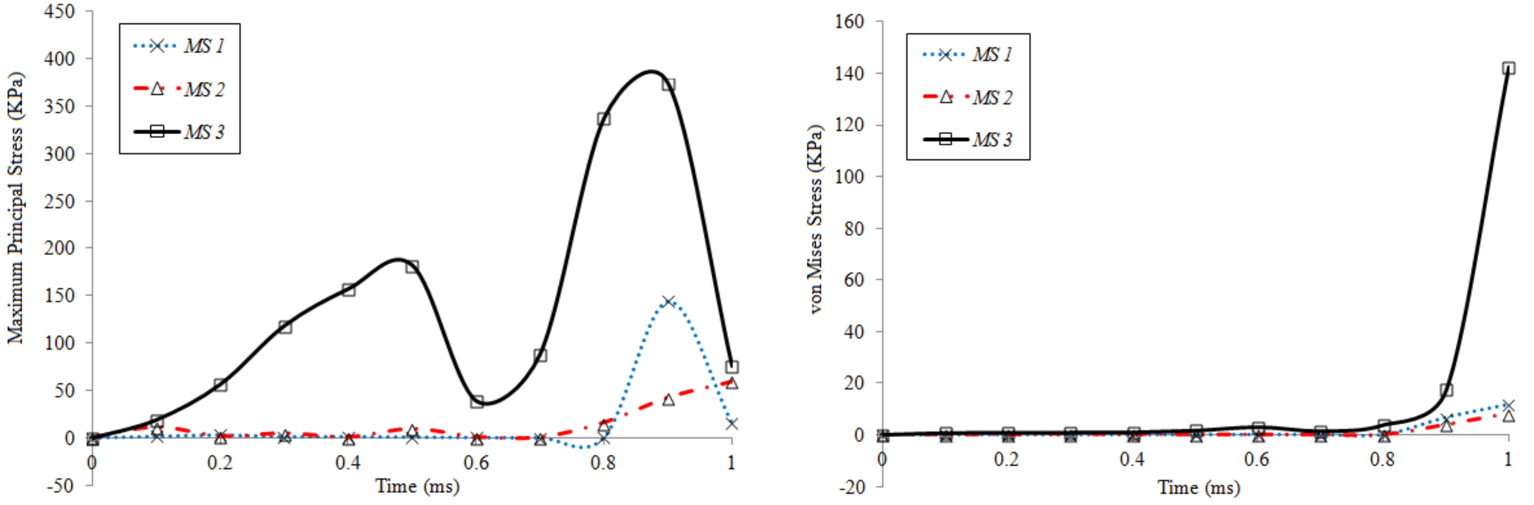

(a) (b)

Figure 44. Deviatoric responses based on different constitutive relations: a) maximum principal stress b) von Mises stress

4.6.3 *Lateral and Frontal Blasts*

In this sub-section the differences in the brain response to lateral and frontal blasts are studied. The simulations are carried out for a blast loading of 0.0698 kg of TNT at a stand-off distance of 0.6 m using the Material Set 2. For the lateral detonation, the blast was directed at the right (from the perspective of an observer facing the subject) temporal region of the skull.

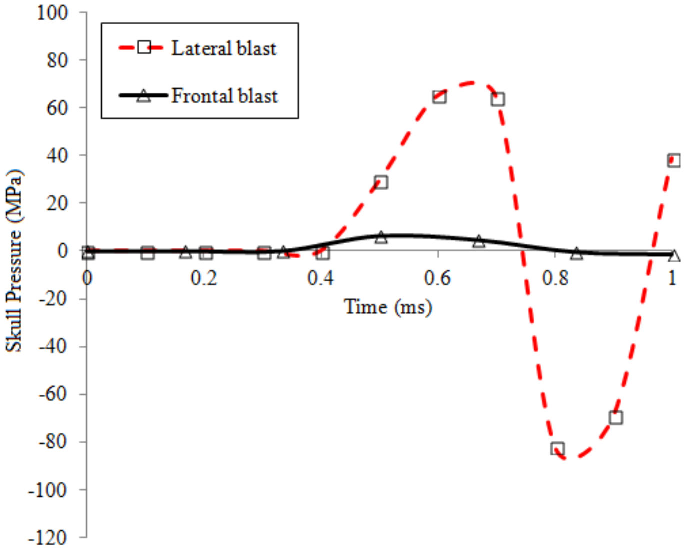

Figure 45. Skull pressure response for frontal and lateral blasts.

The lateral blast generates substantially higher skull pressures compared to the frontal detonation as shown in Fig. 45.The maximum skull deflection for the frontal blast at the point of impact is about 0.30171 mm at t = 0.7 ms (see Fig. 46a). The corresponding deflection in the CSF (modeled as a solid body) is around 1.1 mm (see Fig. 46b), and in the cerebrum is 0.07218 mm (see Fig. 46c).For a lateral blast, the maximum skull deflection is 3.71 mm at t = 0.7 ms (see Fig. 47a). The corresponding deflections in CSF and cerebrum is 2.569 mm and 0.55mm (see Figs. 47b and 47c). For the lateral blast loading the skull deflection has increased about 10 times compared to frontal loading, while the brain deflection has increased around 7 times. Therefore, a lateral blast has a higher possibility of contusion type of injuries (see Figs. 46c and 47c). The pressure spikes in the intracranial cavity associated with the positive pulse of the blast wave are much higher for the lateral blast than the frontal detonation (see Fig. 48). The pressure gradients in the lateral direction are stronger than in the anterior – posterior direction. Figure 48 also shows the deviatoric stress envelopes for both the blast loading cases. One can observe that markedly higher shear and von Mises are induced for the lateral blast loading. The shear strain values under the lateral blast loading are up to 5 times higher than those predicted under the frontal detonation. For both types of blasts, the highest shear and von Mises stresses predicted by the current model are in the brainstem and the corpus callosum region.

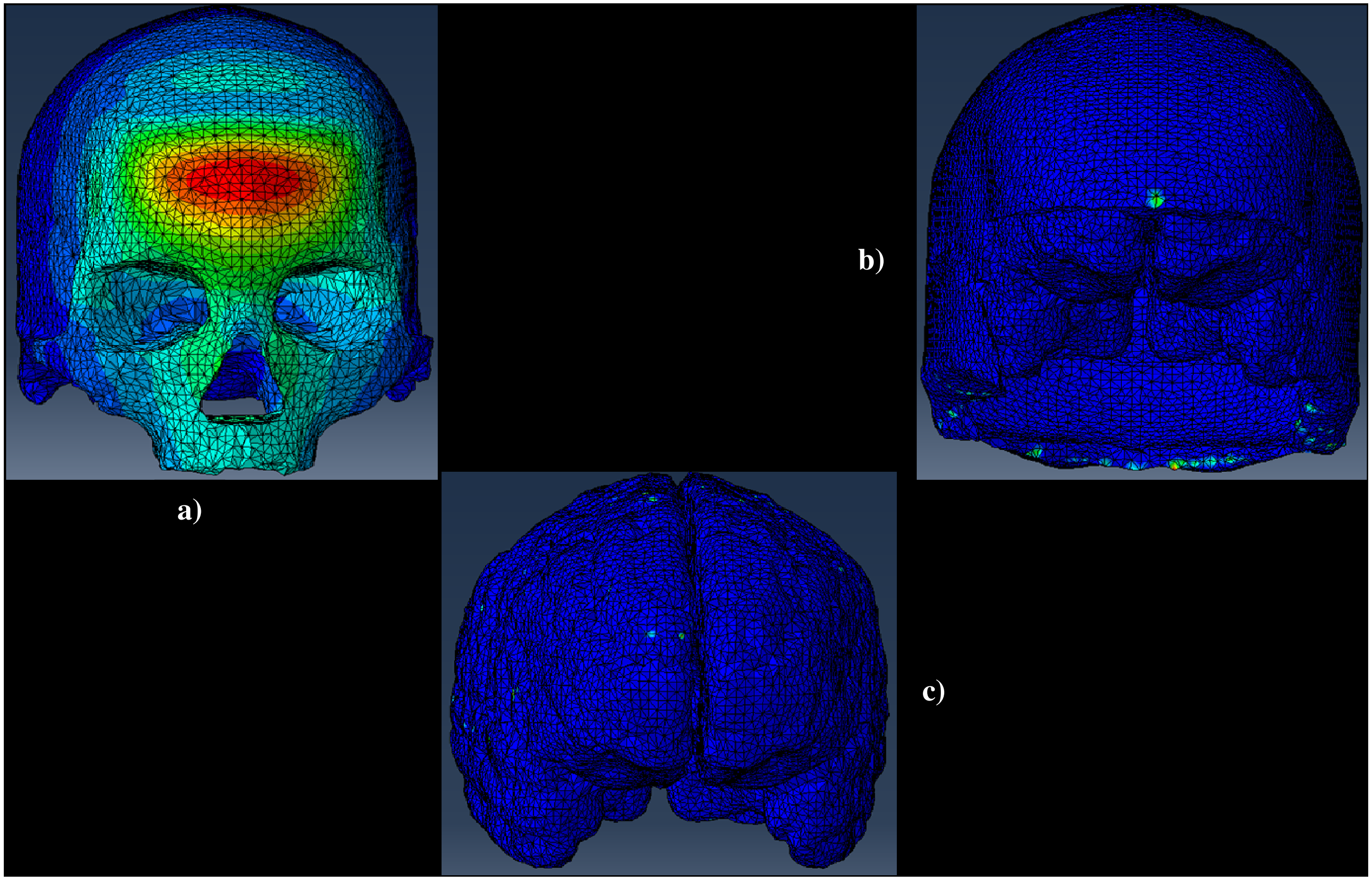

Figure 46. Maximum deflections under the frontal blast loading: a) skull deflection of 0.30 mm, b) CSF deflection of 1.1 mm, c) cerebrum deflection of 0.07218 mm with no contusion type injuries.

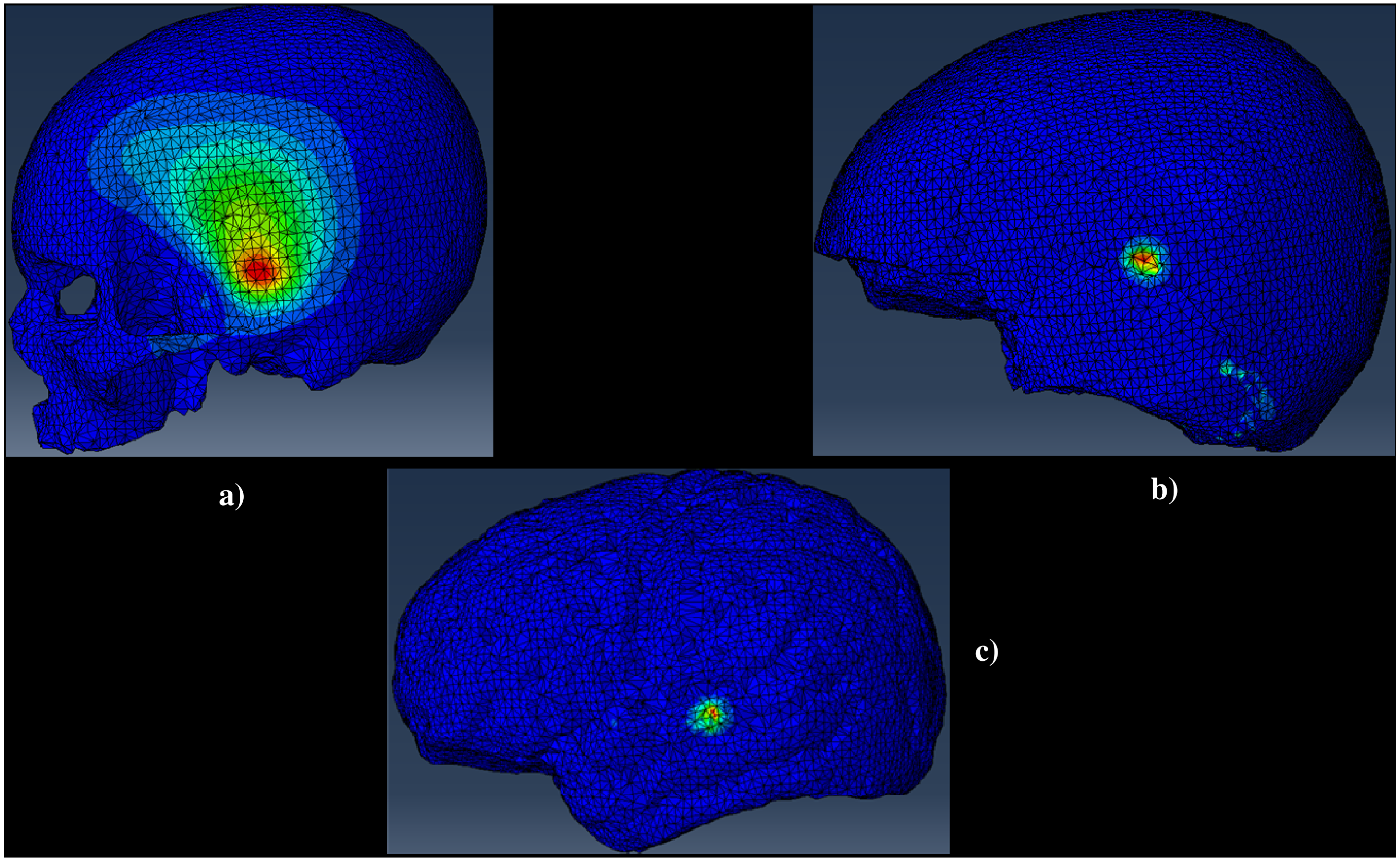

Figure 47. Maximum deflections under the lateral blast loading: a) skull deflection of 3.71 mm, b) CSF deflection of 2.569 mm, c) contusion type injury on the cerebrum.

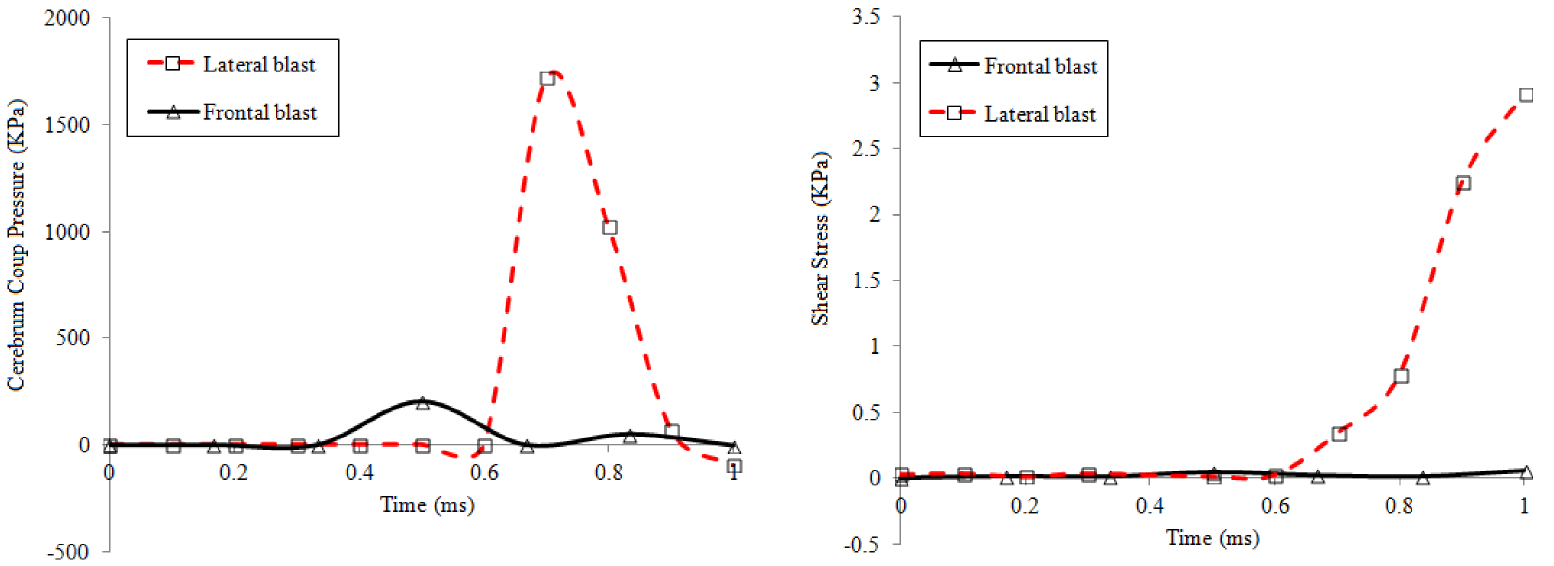

(a) (b)

Figure 48. Comparative response of the brain tissue for frontal and lateral blasts: a) CSF/Cerebrum pressure; b) Brainstem shear stress.

The geometry of the human head and the inhomogeneity of the skull bones can be one possible explanation for the difference in the skull deformation induced by lateral and frontal blasts respectively. The anterior – posterior span of the human skull is approximately 212 mm, compared to a width (left- right temporal span) of about 150 mm. This longer length from the front to the back of the head provides a greater surface area for the blast wave in the lateral detonation. The frontal blast predominantly exerts linear translation on the human head, while the lateral detonation exerts greater angular accelerations. The deviatoric and dilatational response of the brain tissue is related to the head motion and skull deformation. Higher skull flexure under the lateral blast loading produces higher mechanical loads in the brain. The inability of the human brain to rotate freely under angular accelerations would cause high deviatoric stresses and strains for the lateral blast loading, as observed in the current simulations.

CHAPTER V

MODELING OF THE EFFECTIVENESS OF COMBAT HELMETS AGAINST NON-PENETRATING TRAUMATIC BRAIN INJURIES INDUCED BY BLAST AND BALLISTIC IMPACT

5.1 Introduction

Helmets have been used for head protection for centuries. A comprehensive review on the development of combat helmets since World War II has been provided in Chapter 1. Two helmet designs are currently being used by the U.S. Army. The first one is the Advanced Combat Helmet (ACH), which has been in use since 2003. The ACH is made from a Kevlar® K129 fiber/ Phenolic resin composite material and has a higher ballistic and impact protection capability than the previous (PASGT) helmet at a lighter weight. In order to further reduce the helmet weight, the Enhanced Combat Helmet (ECH) has been under development since 2007 for the U.S. Army. The ECH makes use of the Dyneema® HB80 unidirectional composite material and has been fielded on a trial basis. Ballistic protection has been the primary function of a combat helmet. The performance of a combat helmet has always been measured in terms of its ability to defeat a bullet travelling at certain velocity, thus preventing penetrating trauma to the user. Modern combat helmets have been quite successful in preventing penetrating traumatic brain injuries.

However frequent use of improvised explosive devices, increase in available energy of bullets, and reduction in weight of the combat helmets have exacerbated occurrence of non-penetrating traumatic brain injuries. Blast-induced traumatic brain injury is one such non-penetrating TBI caused by ingress and reflection of blast-induced shock-waves in the intra-cranial cavity (see Chapter 2). Ballistic impact induced behind helmet blunt trauma (Cannon, 2001; Prat et al., 2012) is another type of non-penetrating injury resulting from projectile impacts on combat helmets. Although the combat helmet may stop the projectile, part of the energy of the projectile absorbed by the helmet shell is transferred to the skull and intracranial cavity because of rapid deformations of the helmet shell. If this energy transferred to the brain tissue is sufficiently large enough it may lead to non-penetrating type of TBI's.

The main objective of this chapter is to evaluate the effectiveness of current combat helmets (ACH and ECH) in preventing non-penetrating TBI for both blast and ballistic events. The constitutive relation previously proposed in Chapter 3 will be employed here to understand how a helmeted head responds to transient dynamic loading. In section 5.2 the geometric and finite element models are described. The material relations for helmet shell and foam pads are discussed in section 5.3. In sections 5.4 and 5.6 the observations for blast and ballistic impact simulations are presented respectively, while behind helmet blunt trauma for the ACH is studied in section 5.7.

5.2 Geometric and Meshed Models

The geometric model of the human head developed in Chapter 4 is combined with a combat helmet CAD model and meshed using the general purpose pre-processing program HyperMesh® (Altair Engineering Inc, Troy, Michigan). The combat helmet model consists of a helmet shell and seven foam pads. The helmet is fitted such that the crown pad just touched the top of the head and the front rim was no more than 0.5'' above the eyebrows (Operators Manual for the ACH). The skull-CSF-brain assembly and the helmet pads are discretized using quadratic ten node tetrahedral solid elements (the C3D10M element in ABAQUS/Explicit®) while the helmet shell was meshed using 8 node linear hexahedral elements (the C3D8 element in ABAQUS/Explicit®). The head-helmet FE model has a total of 1032905 elements including 997747 quadratic tetrahedral elements and 35158 linear hexahedral elements. The use of finer meshes for the helmet shell (90000 elements) did not show much difference in the numerical values of key field quantities. The helmet components and a typical finite element mesh used in the current simulations are displayed in Fig. 49.

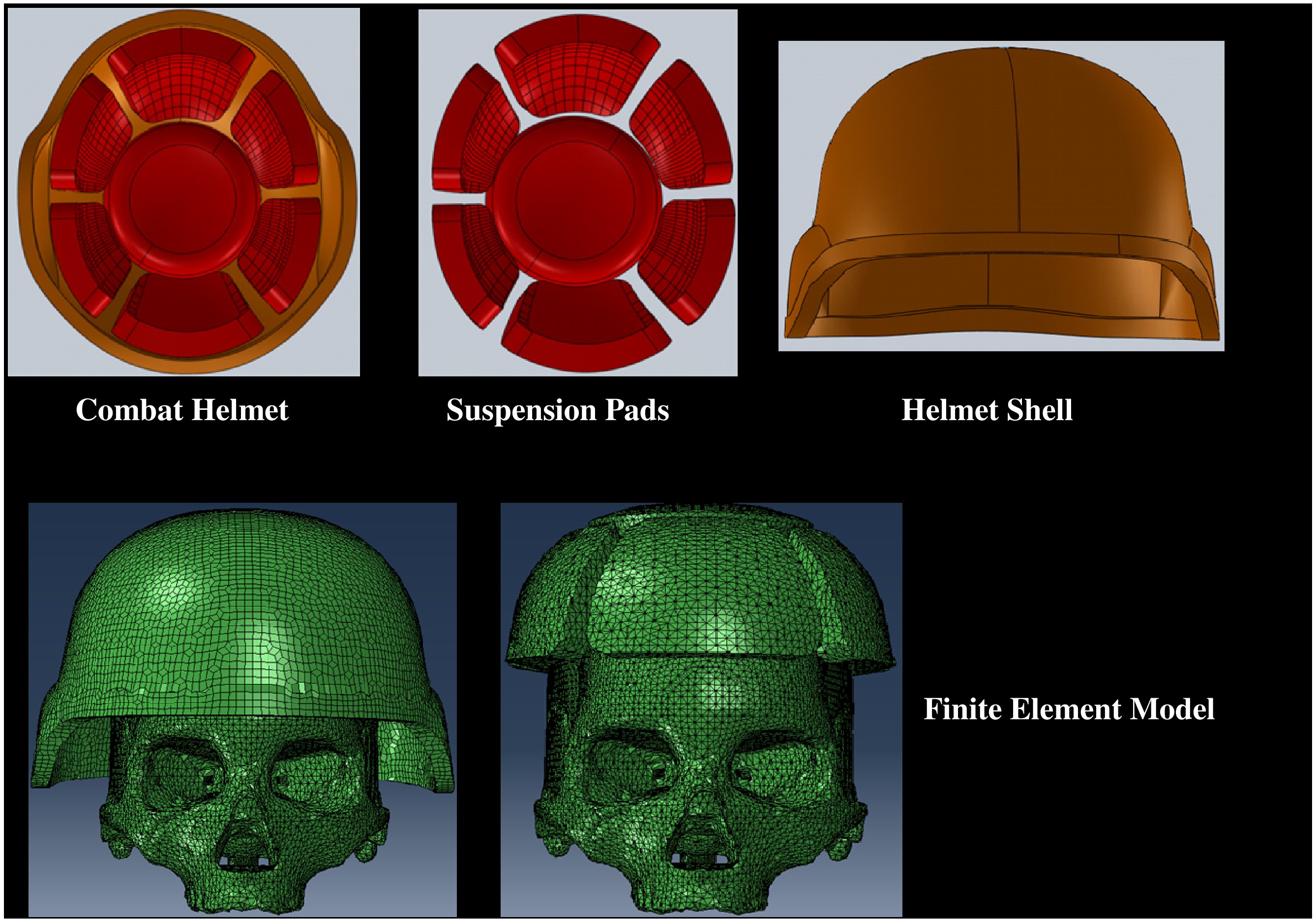

Figure 49. Geometric model and finite element meshes of a head-helmet assembly.

5.3 Material Models

5.3.1 Material Model for Helmet Shell

The ACH shell is made from Kevlar® K129 fiber/Phenolic resin composite material while the ECH shell is made from Dyneema® HB80 unidirectional composite. Following the model presented in Tham et al. (2008) the volumetric response of the combat helmet shell is modeled using an orthotropic EOS, in which the pressure (*P*) is defined by

$$\begin{aligned} P = & -\frac{1}{9}\left[C_{11} + C_{22} + C_{33} + 2\left(C_{12} + C_{23} + C_{31}\right)\right]\varepsilon_{vol} \\ & + K\varepsilon_{vol}^{2} - \frac{1}{3}\left(C_{11} + C_{12} + C_{13}\right)\varepsilon_{11dev} \\ & - \frac{1}{3}\left(C_{21} + C_{22} + C_{23}\right)\varepsilon_{22dev} \\ & - \frac{1}{3}\left(C_{31} + C_{32} + C_{33}\right)\varepsilon_{33dev} \end{aligned} \tag{5.1}$$

where ε_{vol} is the volumetric strain (with $\varepsilon_{vol} = \varepsilon_{11} + \varepsilon_{22} + \varepsilon_{33}$) , C_{ij} are the components of the elastic stiffness matrix, *K* is the bulk modulus, and the last three terms represent the contributions of the deviatoric components of the strain $(\varepsilon_{ij})_{dev}$ to the pressure. For an isotropic material, the deviatoric strain terms are zero. The orthotropic strength model for the helmet shell is defined using generalized Hooke’s law as

$$\begin{bmatrix} \sigma_{11dev} \\ \sigma_{22dev} \\ \sigma_{33dev} \\ \sigma_{23dev} \\ \sigma_{31dev} \\ \sigma_{12dev} \end{bmatrix} = \begin{bmatrix} C_{11} & C_{12} & C_{13} & 0 & 0 & 0 \\ C_{21} & C_{22} & C_{23} & 0 & 0 & 0 \\ C_{31} & C_{32} & C_{33} & 0 & 0 & 0 \\ 0 & 0 & 0 & C_{44} & 0 & 0 \\ 0 & 0 & 0 & 0 & C_{55} & 0 \\ 0 & 0 & 0 & 0 & 0 & C_{66} \end{bmatrix} \begin{bmatrix} \varepsilon_{11dev} \\ \varepsilon_{22dev} \\ \varepsilon_{33dev} \\ \varepsilon_{23dev} \\ \varepsilon_{31dev} \\ \varepsilon_{12dev} \end{bmatrix}. \tag{5.2}$$

The components of the elasticity stiffness matrix, C_{ij}, can be expressed in terms of the engineering constants (E_{ij}, v_{ij}) (e.g., Jones, 1999; Gao, 2001). The model parameters for the helmet shell are provided in Table 23, where E is the Young's modulus, v is Poisson's ratio, G is the shear modulus, ρ is the density, and K is the bulk modulus. The material properties for the ECH listed in Table 23 are provided by DSM Dyneema®.

Table 23 Material parameters for the ACH (Lee and Gong, 2010) and the ECH.

Combat Helmet	**E_{11} (GPa)**	**E_{22} (GPa)**	**E_{33} (GPa)**	**v_{21}**	**v_{23}/v_{31}**	**G_{12} (GPa)**	**G_{23}/G_{31} (GPa)**	**ρ (kg/m^3)**	**K (GPa)**
ACH	18.5	18.5	6	0.25	0.33	0.77	2.715	1230	50
ECH	60	60	5.5	0.1	0.2	5	5	980	50

It has been verified that the values of the material parameters given in Table 23 satisfy the following conditions (Lai et al. 2010):

$$\det\begin{bmatrix} C_{11} & C_{12} \\ C_{21} & C_{22} \end{bmatrix} > 0, \quad \det\begin{bmatrix} C_{11} & C_{13} \\ C_{31} & C_{33} \end{bmatrix} > 0,$$

$$\det\begin{bmatrix} C_{22} & C_{23} \\ C_{32} & C_{33} \end{bmatrix} > 0, \quad \det[\boldsymbol{C}] > 0. \tag{5.3}$$

These conditions ensure that the stiffness matrix is positive definite for an elastic material (Lai et al., 2010).

5.3.2 Damage Model for Helmet Shell (Ballistic Impact)

Ballistic impact on a composite structure is a complex process involving different damage and energy absorption mechanisms. Some of the possible energy absorption mechanisms that have been identified (Naik and Shrirao, 2004) are cone formation on the back face of the target, primary and secondary yarn breakage, inter-ply delamination, matrix cracking, formation of shear plugs, and fabric-projectile friction. In the current simulations a progressive damage model has been is implemented in four stages: damage initiation, damage evolution, material degradation, and element deletion. Damage initiation is the onset of degradation at a material point. Hashin's (1980) failure criterion is adopted as the damage initiation criterion for primary and secondary yarns. Hashin's (1980) failure criterion considers four different failure modes: fiber tension (*FT*), fiber compression (*FC*), matrix compression (*MC*), and matrix tension (*MT*). For the current ballistic impact simulations, fiber and matrix failures in compression are not considered as a criterion for element deletion because the fibers continue to resist the projectile as long as tensile failure does not occur. The failure indices for *FT* and *MT* are defined as follows:

First failure index: Tensile fiber mode in X (or "1") direction for $\sigma_{11dev} > 0$,

$$\phi_{11FT} = \left(\frac{\sigma_{11}}{X_{11}^{T}} \right)^2 + \left(\frac{\tau_{12}}{X_{12}^{S}} \right)^2 + \left(\frac{\tau_{13}}{X_{13}^{S}} \right)^2 \geq 1 \qquad (5.4)$$

Second failure index: Tensile fiber mode in Y (or "2") direction for $\sigma_{22dev} > 0$,

$$\phi_{22FT} = \left(\frac{\sigma_{22}}{X_{22}^{T}}\right)^2 + \left(\frac{\tau_{12}}{X_{12}^{S}}\right)^2 + \left(\frac{\tau_{23}}{X_{23}^{S}}\right)^2 \geq 1 \tag{5.5}$$

Third failure index: Tensile matrix mode in Z (or "3") direction for $\sigma_{33dev} > 0$,

$$\phi_{33MT} = \left(\frac{\sigma_{33}}{X_{33}^{T}}\right)^2 + \left(\frac{\tau_{12}}{X_{12}^{S}}\right)^2 + \left(\frac{\tau_{23}}{X_{23}^{S}}\right)^2 + \left(\frac{\tau_{13}}{X_{13}^{S}}\right)^2 \geq 1. \tag{5.6}$$

In the above expressions, $\left(\phi_{ij}\right)_I$ are the failure indices in the direction *ij* for the failure mode *I,* X_{11}^{T} and X_{22}^{T} denote respectively, the in plane tensile strengths in the 11 and 22 directions, while X_{ij}^{S} are the shear strengths. Damage initiation (i.e. onset of material degradation) is assumed any of the failure indices in Eqs. (5.4)-(5.6) becomes equal to or greater than one. After the initiation of damage, the numerical solution greatly depends on the mesh refinement (element size). In order to reduce this mesh dependence, crack band models have been developed (Bazant and Oh, 1983; Fang et al., 2011; Lapczyk and Hurtado, 2007; Maimi et al., 2007) to establish damage indicators, which depend on the characteristic element length used in the finite element mesh. In this study, the crack band theory developed by Maimi et al., (2007) is adopted as the damage evolution model for the helmet shell. The damage evolution equation for each failure mode is expressed as follows (e.g. Fang et al., 2011):

$$d_{ijI} = \frac{Y_{ijI}^{initial}\left(Y_{ijI}^{final} - Y_{ijI}\right)}{Y_{ijI}\left(Y_{ijI}^{final} - Y_{ijI}^{initial}\right)}, \tag{5.7}$$

where d_{ij} is the damage indicator , Y_{ij} is the equivalent displacement at a material point, $Y_{ij}^{initial}$ is the damage initiation equivalent displacement, and Y_{ij}^{final} is the full damage equivalent displacement, for the failure mode "*I*". For the failure indices defined in Eqs. (5.4) – (5.6), Y_{ijI} can be determined as:

$$Y_{11FT} = l\sqrt{\left(\left(\frac{\varepsilon_{11dev} + \left|\varepsilon_{11dev}\right|}{2}\right)^2 + \varepsilon_{12dev}^2 + \varepsilon_{31dev}^2\right)}, \tag{5.8}$$

$$Y_{22FT} = l\sqrt{\left(\left(\frac{\varepsilon_{22dev} + \left|\varepsilon_{22dev}\right|}{2}\right)^2 + \varepsilon_{12dev}^2 + \varepsilon_{23dev}^2\right)}, \tag{5.9}$$

$$Y_{33MT} = l\sqrt{\left(\left(\frac{\varepsilon_{33dev} + \left|\varepsilon_{33dev}\right|}{2}\right)^2 + \varepsilon_{23dev}^2 + \varepsilon_{31dev}^2\right)}, \tag{5.10}$$

where *l* is the characteristic length of an element in the finite element mesh. $Y_{ijI}^{initial}$ and Y_{ijI}^{final} in Eq. (5.7) are evaluated as

$$Y_{ijI}^{initial} = \frac{Y_{ijI}}{\sqrt{\phi_{ijI}}}, \quad Y_{ijI}^{final} = \varepsilon_{I,f}\, l, \tag{5.11a,b}$$

where $\varepsilon_{I,f}$ is the failure strain for the mode "*I*". After the initiation of damage the response of the material is computed from the damaged stiffness matrix, which is given by,

$$C(d)=\begin{bmatrix} D_{11}^2C_{11} & D_{11}D_{22}C_{12} & D_{11}D_{33}C_{13} & 0 & 0 & 0 \\ & D_{22}^2C_{22} & D_{22}D_{33}C_{23} & 0 & 0 & 0 \\ & & D_{33}^2C_{33} & 0 & 0 & 0 \\ & & & D_{12}C_{44} & 0 & 0 \\ & sym & & & D_{31}C_{55} & 0 \\ & & & & & D_{23}C_{66} \end{bmatrix}, \tag{5.12}$$

where C_{ij} are components of undamaged stiffness matrix, and,

$$D_{11}=\left(1-d_{11FT}\right), \tag{5.13}$$

$$D_{22}=\left(1-d_{22FT}\right), \tag{5.14}$$

$$D_{33}=\left(1-d_{33FT}\right), \tag{5.15}$$

$$D_{12}=\left(\frac{2*\left(1-d_{11FT}\right)*\left(1-d_{22FT}\right)}{2-d_{11FT}-d_{22FT}}\right)^2, \tag{5.16}$$

$$D_{23}=\left(\frac{2*\left(1-d_{22FT}\right)*\left(1-d_{33FT}\right)}{2-d_{22FT}-d_{33FT}}\right)^2, \tag{5.17}$$

$$D_{31}=\left(\frac{2*\left(1-d_{33FT}\right)*\left(1-d_{11FT}\right)}{2-d_{33FT}-d_{11FT}}\right)^2 \tag{5.18}$$

are the material degradation constants.

When any of the damage indicators d_{11FT}, d_{22FT} and d_{33FT} becomes equal to or greater than one, the corresponding element is deleted from the finite element mesh. The failure properties of the ACH and ECH have been listed in Table 24. The failure properties for the ECH listed in Table 24 are provided by DSM Dyneema®**.**

Table 24 Failure properties for the ACH (Lee and Gong, 2010) and the ECH.

Properties	**Combat Helmets**	
	ACH	**ECH**
X_{11}^{T} (MPa)	555	1200
X_{11}^{C} (MPa)	555	25
X_{22}^{T} (MPa)	555	1200
X_{22}^{C} (MPa)	555	25
X_{33}^{T} (MPa)	1050	8.3
X_{33}^{C} (MPa)	1050	1500
X_{12}^{S} (MPa)	77	43
X_{13}^{S} (MPa)	1060	9
X_{23}^{S} (MPa)	1086	9
$\varepsilon_{I,f}$	1.9	2.6

5.3.3 Material Model for the Helmet Foam Pads

The current ACH/ECH padding system uses Zorbium® Action Pad (ZAP™) NSN System manufactured by Team Wendy, which is a polyurethane based foam material (Zhang et al., 2011). The foam material was modeled using the Ogden hyperfoam model (Ogden, 1972) described by the following strain energy density function:

$$W = \sum_{i=1}^{N} \frac{2\mu_i}{\alpha_i^2} \left[\lambda_1^{\alpha_i} + \lambda_2^{\alpha_i} + \lambda_3^{\alpha_i} - 3 + \frac{1}{\beta_i} \left(\left(J^{el} \right)^{-\alpha_i \beta_i} - 1 \right) \right] \tag{5.19}$$

where N is the number of terms used in data fiting, μ_i, α_i, and β_i are material parameters, λ_j (j = 1 ,2, 3) are the principal stretches, and J^{el} is the determinant of the deformation gradient tensor. In the current simulations, N = 2 is used, and the relevant material constants are provided in Table 25.

Table 25 Material constants for the Ogden hyperfoam model (Briody et al., 2011; Grujicic et al., 2010).

N	***μ (Pa)***	***α***	***β***
1	12740.4	7.2810	0
2	2.7459	−5.7311	0

The time dependent deviatoric response of the polyurethane foam is represented using eight parameter Prony series expansion of the dimensionless shear modulus $g_R(t)$ as

$$g_R(t) = \frac{G_R(t)}{G_0} = 1 - \sum_{i=1}^{N} g_i \left(1 - e^{-t/\tau_i}\right), \tag{5.20}$$

In Eq. (5.20), N is the number of terms, g_i is the relaxation modulus, τ_i is the relaxation time, $G_R(t)$ is the "long term shear relaxation modulus", and G_0 is the instantaneous shear relaxation modulus. The Prony series parameters for Eq. (5.20) are given in Table 26.

Table 26 Prony series parameters (Briody et al., 2011).

N	g_i	τ_i
1	6.17×10^{-4}	1.01×10^{-3}
2	-1.27×10^{-3}	1.89×10^{-3}
3	8.99×10^{-2}	0.2928
4	1.15×10^{-1}	4.7441
5	8.30×10^{-2}	55.234
6	7.72×10^{-2}	629.87
7	6.86×10^{-2}	8656
8	-3.01×10^{-2}	1.74×10^{8}

5.4 BTBI Mitigation Performance of Combat Helmets

5.4.1 Results and Observations

The effectiveness of current combat helmets to attenuate the effects of shock waves on the human head following a blast is evaluated in this section. The simulations are carried out for a blast with an overpressure of 5.2 atm (lung injury threshold), which is equivalent to a free air explosion of 0.0698 kg TNT at a stand-off distance of 0.6 m. The blast wave is incident on the right (from the perspective of an observer facing the subject) temporal region of the skull. In order to mimic the skull-spinal cord joint the nodes at the bottom of the brainstem have been kinematically constrained to allow only rotation.

The most obvious effect of the helmet is to prevent direct impact of the air-borne blast wave on the surface of the skull. For a helmet protected head, the skull is loaded indirectly through the foam pads. This limits the magnitude of the blast overpressure (and underpressure) transmitted to the skull surface (see Fig. 50(a)).

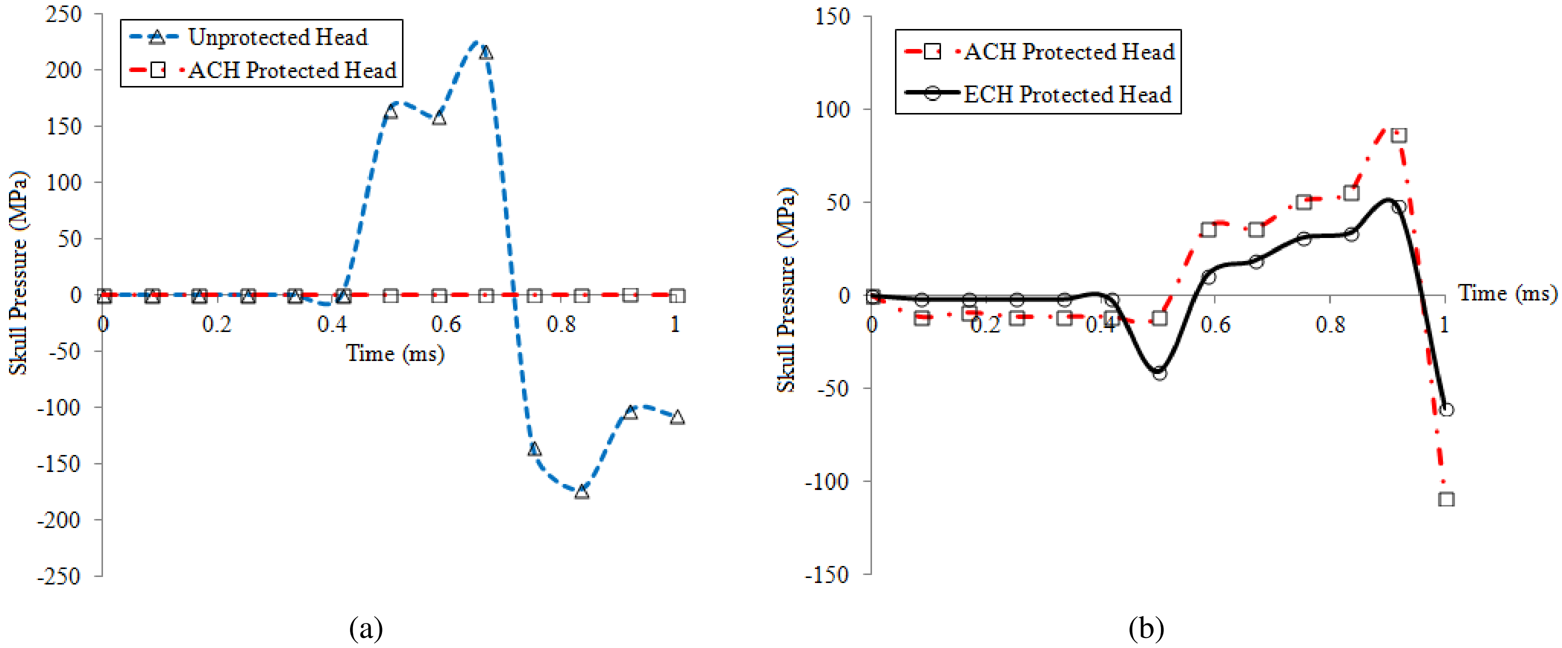

Figure 50. Progression of blast wave as it interacts with the skull: a) helmet protected and unprotected head; b) ECH and ACH

The maximum skull pressure observed on the coup side for an unprotected head is 217.1 MPa at t = 0.66 ms, while the maximum negative pressure (hydrostatic tension) magnitude is −173.8 MPa at t = 0.83 ms. In contrast, for an ACH protected head, the maximum skull pressure is limited to 0.09278 MPa at t = 0.91 ms, while the maximum negative pressure is −0.00124 MPa at t = 0.8333 ms. The use of the ECH is associated with a greater reduction in the pressure loading experienced by the skull relative to the ACH (see Fig. 50(b)). As shown in Fig. 50(b), the peak positive pressure experienced by an ACH protected skull is almost twice as large as the peak positive pressure experienced by an ECH protected skull. The reduction of the skull pressure for a helmet protected head results in a much lower skull deformation and rapid damping of the skull oscillations. This can be seen in Figs. 51 and 52. For an unprotected head, the maximum skull deformation ranges from −5.514 mm to 1.3 mm. In contrast, an ACH protected skull deforms only about 0.01776 mm, which remains more or less constant in the duration of the current simulations (1 ms). This observation is in contrast to what has been reported for frontal explosions, wherein the skull front pressure and deformation increase for a helmet protected head (Nyein et al., 2010).

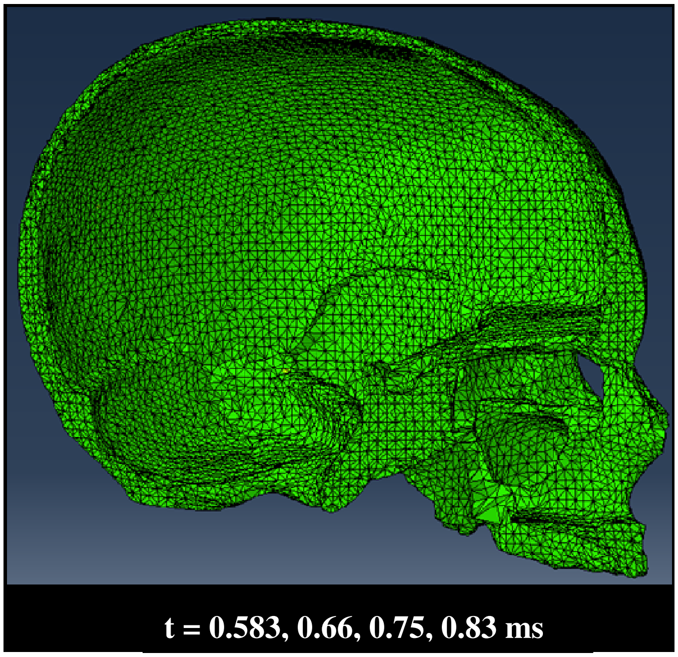

Figure 51. Uniform deformation on the inner surface of the skull for a helmet protected head at different times.

Figs. 53(a) and 53(b) show the particle velocity and acceleration profiles in the brain. It can be seen that the presence of the helmet results in increase in the velocity and acceleration transferred to the brain. This increase is smaller for the ECH protected head than for the ACH protected head. The change in the velocity is an indication of the impulse (i.e., the area under pressure time curve) transmitted to the brain. Therefore, the specific impulse transmitted to the brain is much higher in a helmeted head than in an unprotected head. This is due to the extra amount of impulse transmitted through the helmet shell and foam pads and an increase in the overall weight supported by the neck.

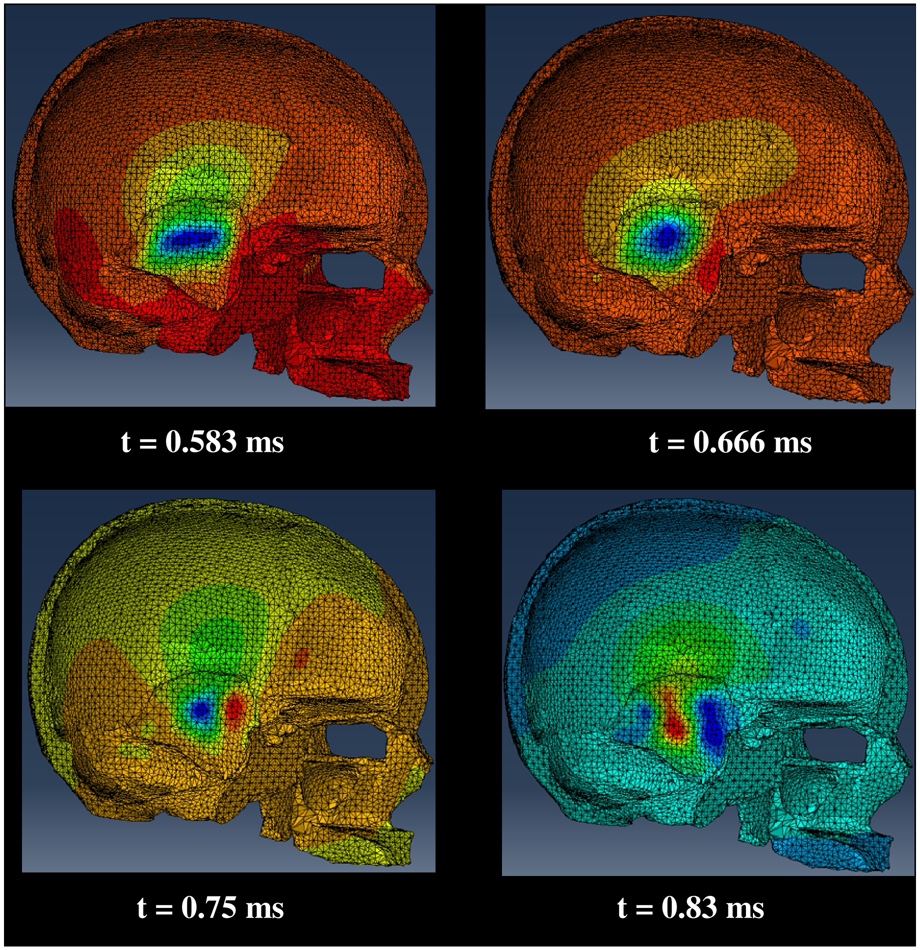

Figure 52. Rapid oscillations of the inner surface of the skull for an unprotected head at different times. Blue regions indicate the inward deformation, and red spots are for the outward deformation

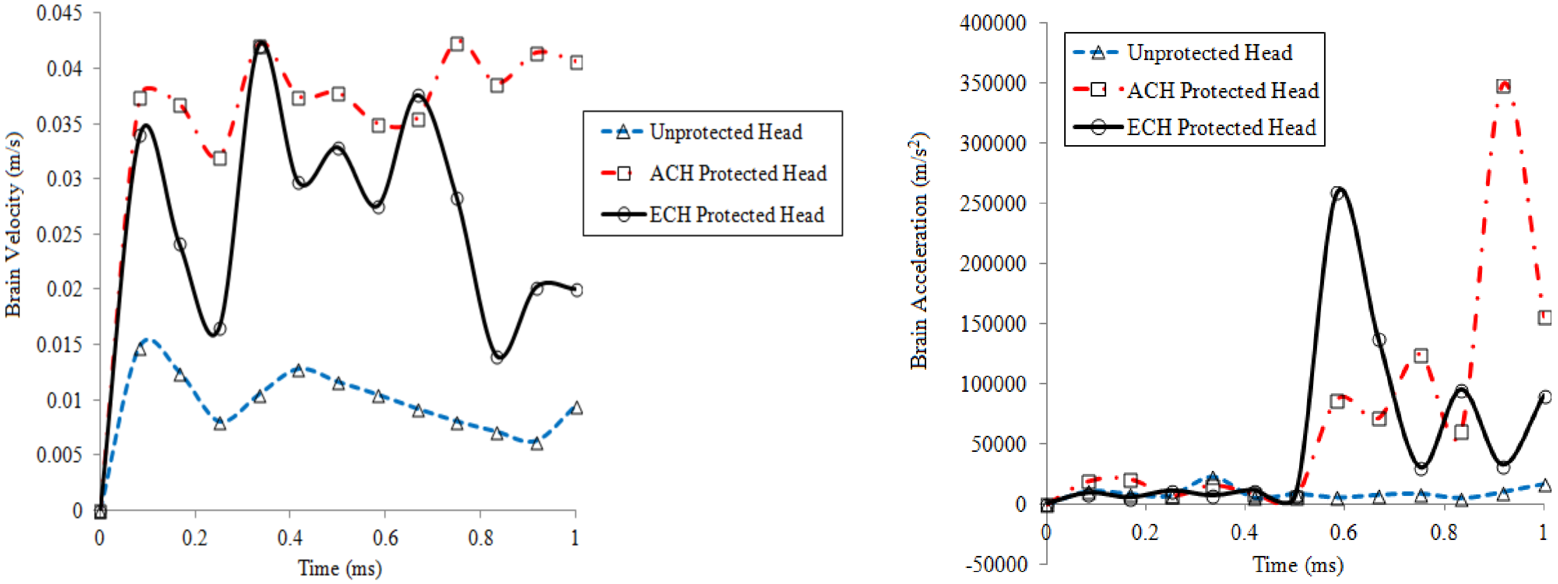

(a)

(b)

Figure 53. Particle velocity (a) and acceleration (b) profiles in the brain

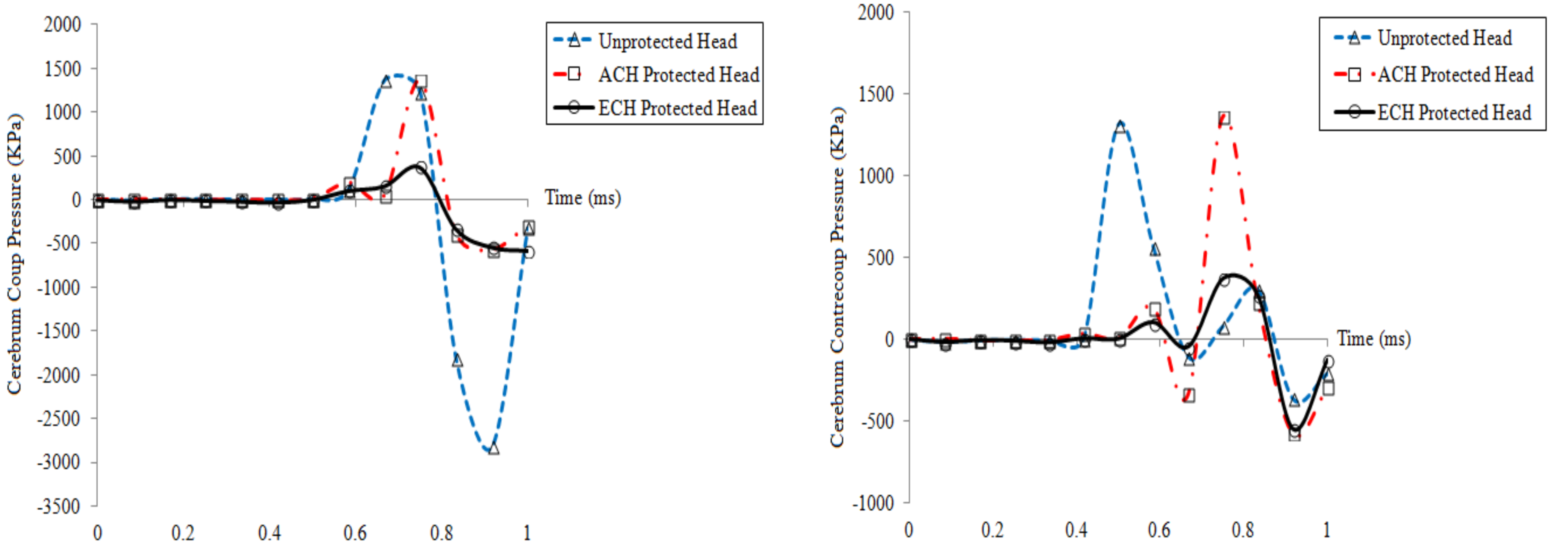

(a) (b)

Figure 54. Pressure-time histories predicted for the main brain at the cerebrum/CSF interface: (a) coup pressure b) contrecoup pressure.

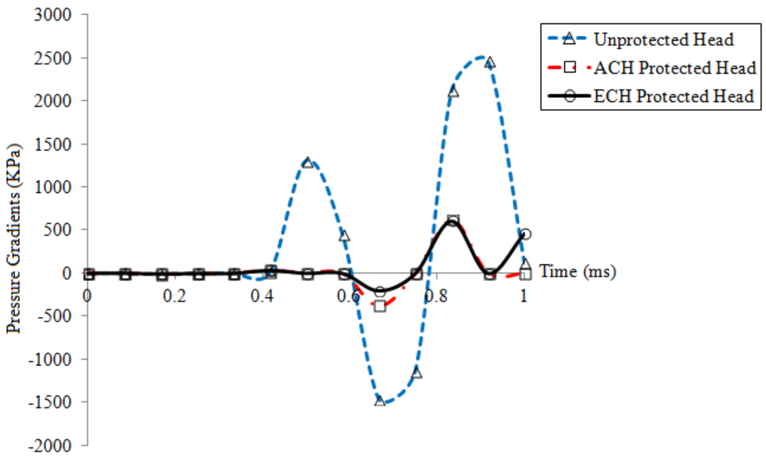

Figure 55. Pressure gradients histories predicted for the main brain at the cerebrum/CSF interface.

Although the specific impulse transmitted to the brain is higher for the helmet head, the presence of the helmet is seen to cause a reduction in the magnitude of the intracranial pressures on the coup side of the main brain (see Fig. 54(a)). The helmet also delays the arrival of the blast wave into the intracranial cavity. The ACH only slightly reduces the magnitudes of positive pressure peaks, while the mitigating effect of the ECH is more pronounced. It can also be seen from Fig. 54(a) that the presence of the helmet avoids the underpressure (i.e., large negative pressures) in the CSF. For an unprotected head the CSF experiences a peak negative pressure of −2828 KPa, which reduces to −575.6 KPa for an ACH protected head and −550.2 KPa for an ECH protected head. Large negative pressures observed at the coup site for an unprotected head can lead to fluid cavitation in the CSF (Hardy et al., 1993). This is shown in Fig. 57, where increasing distortion of the elements of the CSF can be seen clearly. This element distortion is not observed in the

CSF at the coup site for a helmet protected head (see Fig. 56). Thus the presence of the helmet (ACH or ECH) helps in avoiding head injuries of the fluid cavitation type.

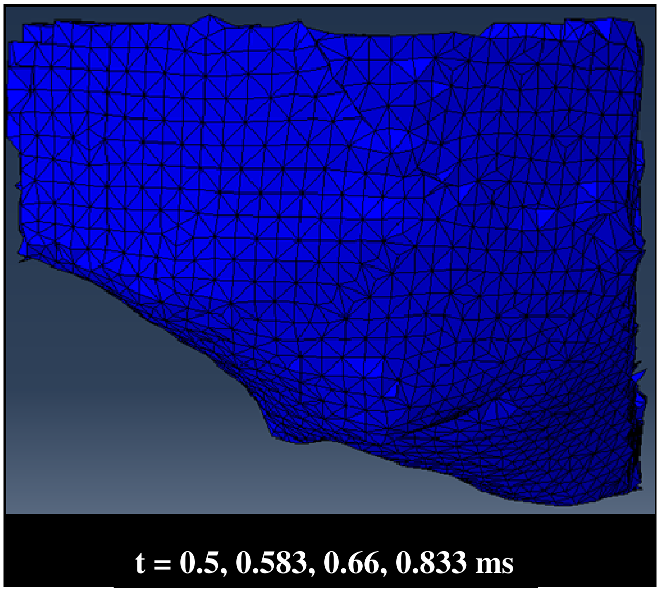

Figure 56. Absence of the fluid cavitation on the coup side in the CSF for a helmet protected head

In contrast to the dilatational response at the coup site, the negative pressure magnitudes at the contrecoup site do not show any significant difference between the helmet protected head and the unprotected head (see Fig. 54(b)). The maximum overpressure and underpressure values at the contrecoup site for the unprotected head are 1311 KPa (at t = 0.75 ms) and −361.7 KPa (at t = 0.91667), respectively. The corresponding values for the ACH protected head are 1362 KPa (at t = 0.75 ms) and −575.6 KPa (at t = 0.66 ms), while for an ECH protected head the pressure values ranged from 370.8 KPa to −550.2 KPa. For the unprotected head, strong pressure gradients are developed in the brain (CSF/cerebrum) in contrast to a helmet protected head (see Fig. 55).

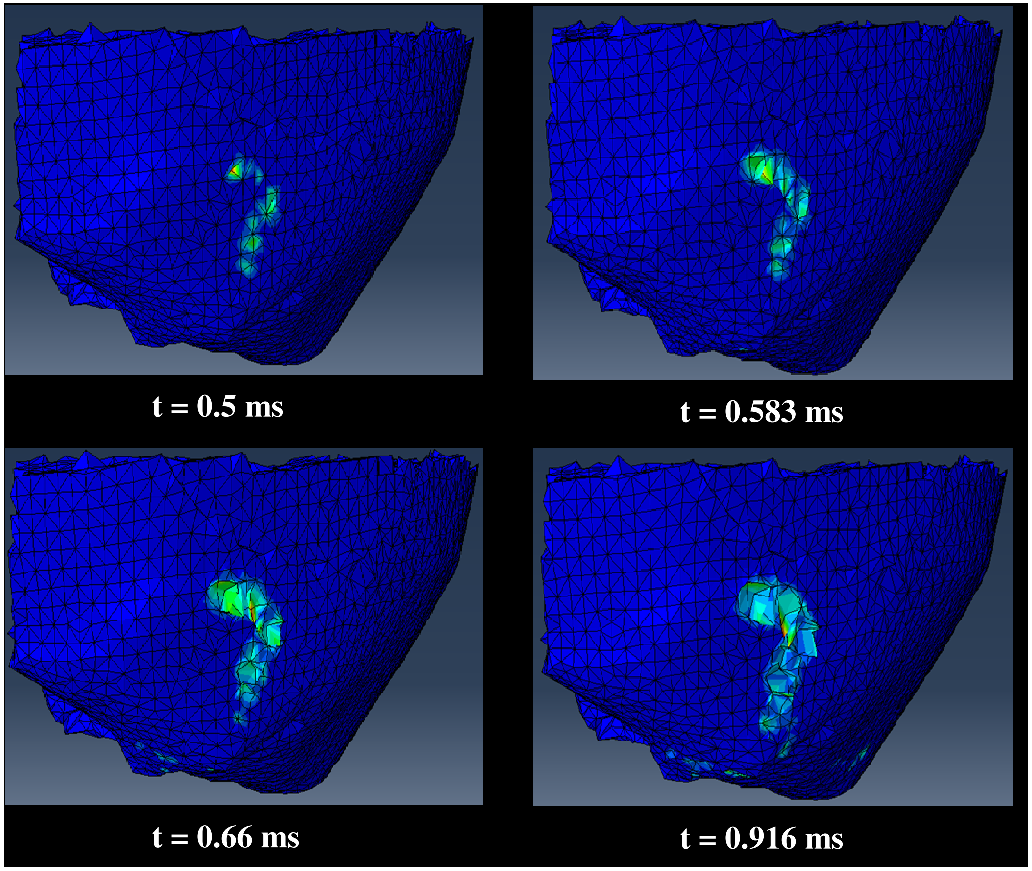

Figure 57. Fluid cavitation damage observed on the coup side in the CSF for an unprotected head

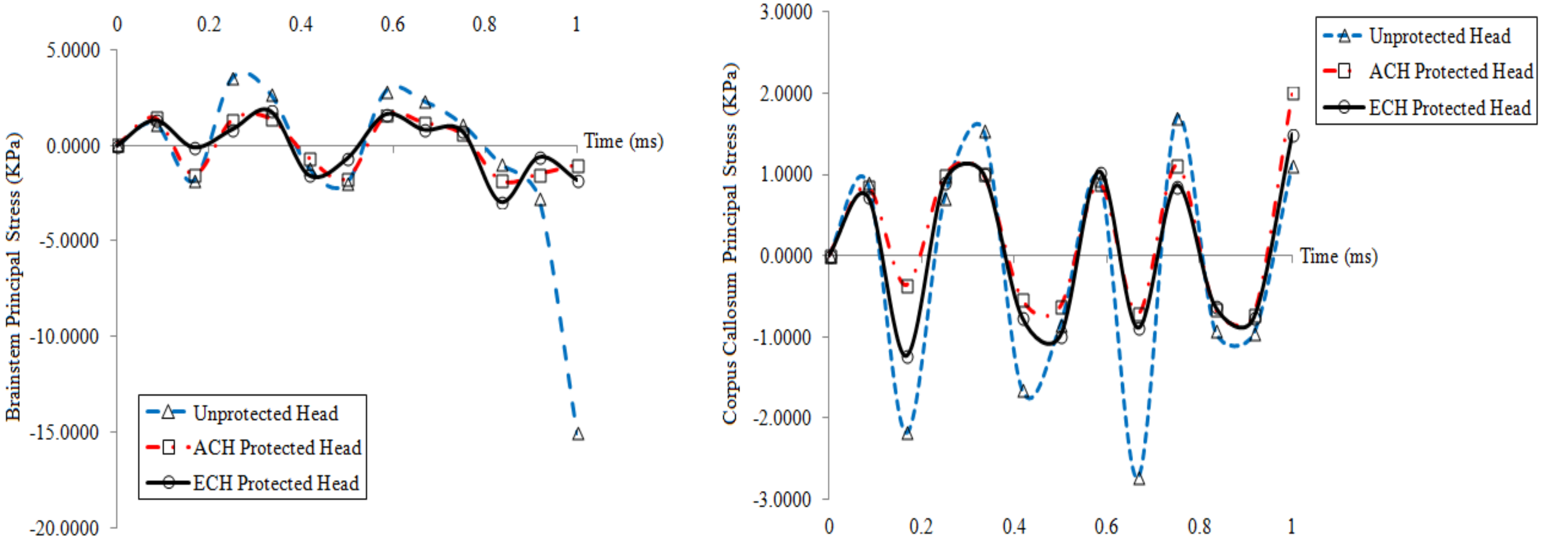

(a) (b)

Figure 58. Temporal evolution of principal stresses: (a) brainstem and (b) corpus callosum

The maximum values of the deviatoric stress values occur in the brainstem, which is followed by the corpus callosum region (see Table 27 and Fig. 58) for all the three cases studied. The values of the shear stress are two orders of magnitude lower than the values of the principal and von Mises stresses. The peak values of the deviatoric stress in the brainstem reduce for the helmet protected head (see Table 27). The principal stress envelopes for the corpus callosum are shown in Fig. 58(b). It can be seen that the helmet does not significantly mitigate the stresses in the corpus callosum region. On the contrary, at t = 1 ms the magnitude of the shear and von Mises stresses in the corpus callosum are higher in a helmet protected head (ACH or ECH) than in the unprotected head. The increases in the peak values of shear and von Mises peak stresses are higher in the ACH protected head than in the ECH protected head (see Table 27). There is also a probability that the magnitude of the deviatoric stresses will continue to increase 1 ms (the simulation period used here) after the blast takes place.

5.5 Discussions

The observations in this subsection suggest that for a lateral blast the presence of the combat helmet provides mixed results in mitigating the blast effects on the brain tissue. For a helmet protected head the blast waves do not directly impact the skull resulting in reduction of the skull deformation and oscillation of the skull and in the amplitude of the pressure waves entering the intracranial cavity. This reduces the pressure fluctuations in the intracranial cavity at the coup site thereby mitigating the of brain collision with the skull and the fluid cavitation.

Table 27 Peak values of the intracranial deviatoric stress

Region	**Unprotected Head**		**Head with ACH**		**Head with ECH**	
	Shear Stress (Pa)	von Mises Stress (Pa)	Shear Stress (Pa)	von Mises Stress (Pa	Shear Stress (Pa)	von Mises Stress (Pa)
Brainstem	−927.1 to 2163	26410	−1.34 to 1.34	79.1	−1.09 to 2.674	50.26
Corpus Callosum	−2.56 to 1.621	48.49	−2.89 to 6.335	140	−3.60 to 4.384	95.7

However, at the contrecoup site the pressure response is more likely to be associated with wave reflections from the inner surface of the skull. As a reflected wave possesses a greater strength than an incident wave, this might explain the negligible reduction in the pressure values at the contrecoup site. The ECH was found to be more efficient in mitigating the effects of a blast wave on the human head than the ACH. Figures 59 and 60 show the spatial distribution of pressure in the helmet shell for the ECH and ACH, respectively. The early time response of the ACH shell displays fewer variations in the spatial pressure distribution (see Fig. 60), while large bands of high negative and positive pressures are seen to develop in the ECH (Fig. 59). The maximum positive pressure (red color bands in Fig. 59) in the ECH is found to peak at a post blast time of 0.58 ms with a value of 16.43 MPa, while the maximum negative pressure (blue color bands in Fig. 59) of −15.8 MPa occurs at t = 1 ms after the blast. The corresponding pressure limits for the ACH shell are −6.6 MPa (at t = 0.91 ms) to 12.69 MPa (at t = 0.5833 ms). When a blast wave interacts with a structure it delivers the blast energy into the structure. The nature and extent of the deformation of the structure depends on the strength of the blast wave and properties of the structure. The ECH is made from the Dyneema$^{®}$ HB80 unidirectional composite, which is lighter but stiffer (see Table 23) than the Kevlar$^{®}$ fiber Phenolic resin composite used to make the ACH. Because of its higher stiffness the ECH can reach stress levels higher than the ACH, and owing to its lighter weight the ECH can react faster to pressure variations than the ACH. These allow the ECH shell to absorb a higher amount of blast loading than to the ACH shell thereby reducing the intensity of a blast wave transferred to the skull (and subsequently to the intracranial cavity) through the foam padding system (see fig. 50(b)).

The brainstem and corpus callosum are stiffer than the main brain, leading to higher values of the deviatoric stress components. The presence of the helmet lowers the deviatoric stress in the brainstem. However, an opposite trend is observed in the corpus callosum region for both the ECH and ACH protected heads. The corpus callosum forms a link between the left and right cerebral hemispheres. Rotational acceleration in lateral direction is conducive to axonal stretching in the white matter region of the cerebrum via the corpus callosum (Mendis, 1992). Therefore, the corpus callosum is more susceptible to diffuse axonal injuries, which are induced by acceleration and deceleration forces acting on the brain. As can be seen in Fig. 54(b) the rotational acceleration for an helmet protected head is higher than that for an unprotected head. This might be a probable cause for the increase in shear stresses that has been observed in the corpus callosum region for a helmet protected head as compared to an unprotected head. This increase is less for a head protected by an ECH, which is lighter than an ACH. Based on the findings presented herein it can be said that for a lateral blast the intracranial wave reflection and the head/helmet weight control the levels of the deviatoric stress and pressure generated inside the brain. Several causes have been identified for BTBI. The primary blast injury is induced by ingress of the blast wave into the intracranial cavity. The secondary blast injuries are caused by flying debris, and the tertiary blast injuries are predominantly caused due to the rotational acceleration exerted on the skull and brain by the blast wind. The ECH provides a better protection against the primary, secondary and tertiary blast injuries than the ACH. The helmet development so far has been mainly focused on modifying to the helmet shell (e.g., using new materials or face shield). In addition to these improvements, research on the role of foam pads in shock wave absorption and on the development of new materials for foam pads that can further reduce the strength of blast waves entering the intracranial cavity should help in enhancing the blast impact mitigation capabilities of combat helmets.

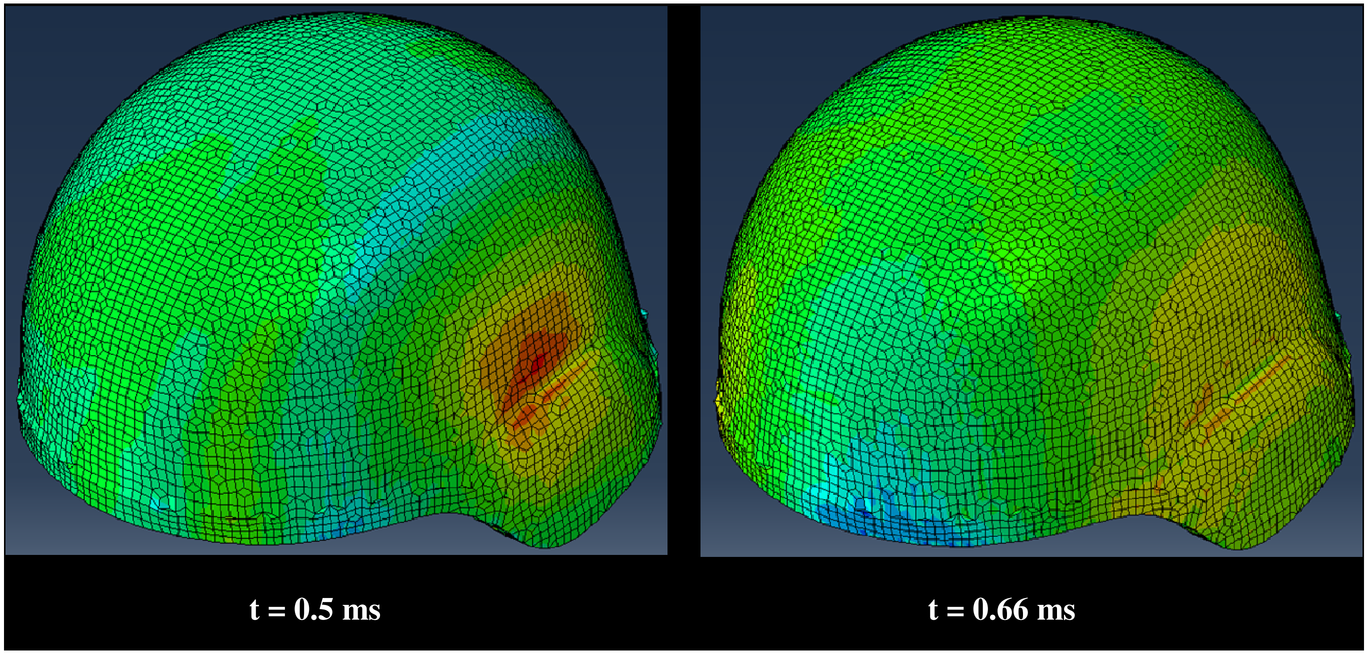

Figure 59. High positive (red/orange bands) and negative (blue bands) pressure regions developed in the ECH shell. The pressure values range from −15.48 MPa to 16.43 MPa.

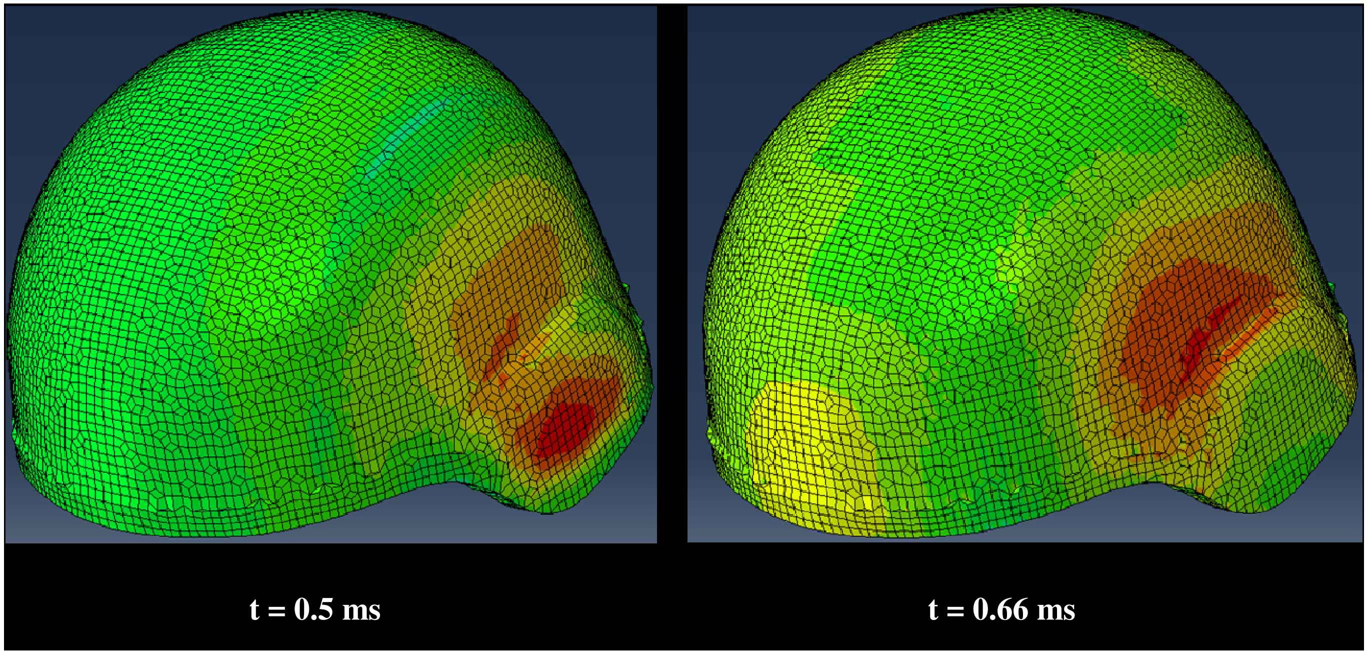

Figure 60. Pressure distribution in the ACH shell. The pressure values range from –6.6 MPa to 12.60 MPa.

5.6 Ballistic Impact

5.6.1 Experimental Validation

Ballistic impact induced behind helmet blunt trauma occurs as a result of rapid deformations of the combat helmet shell subjected to a projectile impact. In this section the helmet shell deformation for two different projectiles and two different helmet shell materials are evaluated.

5.6.1.1 Ballistic Impact of a Spherical Steel Projectile on the ACH

Experiments involving frontal and lateral ballistic impacts of a spherical steel projectile on an ACH were performed by Tan et al. (2012). In these tests, the ACH with an interior foam cushioning system was placed on a Hybrid III headform. The projectiles used were 14.2 mm diameter spherical steel balls. A ballistic gas gun was used to launch these projectiles to strike the front and left side of the helmet at velocities of 205 m/s and 220 m/s respectively. These shooting tests are simulated in our study in order to ascertain the accuracy of our finite element predictions. For the purpose of validation, the skull was assumed to be made of magnesium alloy as specified by the National Institute of Justice Standard for ballistic testing of combat helmets (NILECJ-STD-0106.00) with a Young's modulus 45 GPa, and a Poisson's ratio of 0.35. Table 28 provides a comparison of the current simulation results with the shooting test data of Tan et al. (2012). It is seen that the simulation values for the rebound velocity of the projectile, energy absorbed by the helmet, and dynamic deflection radius correlate well with the experimental results.

Table 28 Comparison of the simulation results with the experimental data of Tan et al. (2012).

Measured Quantity	Frontal Impact at 205 m/s		Lateral Impact at 220 m/s	
	Experimental data	Current simulation results	Experimental data	Current simulation results
Rebound velocity of projectile (m/s)	15	15.11	10	14.33
Energy absorbed by helmet (J)	248.4	248.69	288.6	286.758
Dynamic deflection radius (mm)	21.5	19.453	32.3	34.43
Helmet dent depth (mm)	12.6	9.364	13.1	10.68
Permanent dent region diameter	46	44.534	42	22.772

5.6.1.2 Ballistic Impact of a Full Metal Jacket Bullet (FMJ) on the ACH and ECH

The NIJ Standard for Ballistic Helmets (NILECJ – STD – 0106.00) specifies a 9mm full metal jacket bullet (FMJ) with velocities of 358±15 m/s for high velocity ballistic testing of combat helmets. The FMJ bullet consists of a soft core enclosed in a hard metal shell. Ballistic tests using the FMJ bullets were performed by Hisley et al. (2011). In their experiments the helmet was mounted on a skull fixture (of thickness 6.8mm) and a total of fifteen 9 mm shots were fired at the front, back, and crown locations of the helmet. Helmets of different sizes (large, X-large) with standoff distances of 12.7mm and 19.1mm, respectively were used for the experiments. The bullet velocities were in the range of 370±15 m/s. However, the type of helmet used

(ECH or ACH), kind of helmet padding system, and helmet shell thickness has were not provided in Hisley et al. (2011). The current simulations results for the FMJ bullet strike are compared with the experimental data of Hisley et al. (2011). In the simulations the skull (of thickness 8.09 mm) is taken to be made of a magnesium alloy (with its material properties provided in Section 5.6.1.1) and the helmet standoff distance is 19.9 mm. The FMJ bullet consists of two parts – a brass cartridge surrounding a lead core. The average helmet shell thickness is 8.85 mm and a seven foam padding system (shown in Fig. 49) is used.

Table 29 Comparison between the current simulation results and the experiment data of Hisley et al. (2011).

Measured Quantity	Right impact at 377.6 m/s		
	Experimental Results	Simulation results	
		ACH	ECH
Skull Thickness (mm)	6.8	8.09	8.09
Helmet standoff distance (mm)	19.1	19.9	19.9
Helmet size	Large	Large	Large
Shell thickness	Not mentioned	8.85	8.85
Maximum helmet shell velocity at time of impact (m/s)	167.7	167.2	111.8
Rebound velocity of the projectile	-	83.72	52.92
Dent depth impact (mm)	≈10	9.803	9.77

Table 29 continued

Measured Quantity	Right impact at 377.6 m/s		
	Experimental Results	Simulation results	
		ACH	ECH
Maximum Helmet back face deformation (mm)	38.3	18.27	11.64
Diameter of dent (mm)	43	41.06	114.76

A comparison of the FE results for the right lateral impact and the experimental measurements (of test number 18) from Hisley et al. (2011) is given in Table 29. Fig. 61 shows the helmet shell velocity vs. time and the deformation vs. time graphs for the right lateral impact. It is seen from Fig. 61 that the simulation results for the ACH correlates well with the graph shown in Hisley et al. (2011). The back face deformation (BFD) of the helmet shell is shown in Figs. 64 and 65. The shape of the deformed helmet shell matches well with the experimental observation of Hisley et al. (2011). For the ACH the calculated values of the maximum shell velocity at the time of impact, diameter of dent, and helmet BFD at the time of impact show good agreement with the experimental results. The results for the front FMJ bullet impact are provided in Table 30 and Fig. 62. These results are qualitatively similar to their counterparts for the right lateral impact presented above.

The simulations underestimate the maximum helmet deformation at the point of impact. This trend can also be seen in the simulation results of Tan et al. (2012) for a spherical projectile. However, the peak helmet shell velocity occurs just after initial impact, as can be seen from Figs. 61 and 62. Therefore, the most important period when the probability of ballistic impact induced behind helmet blunt trauma is highest is right after the initial impact. The velocity and kinetic energy decrease well before the maximum helmet shell deformation is reached (at about 0.15 ms). As a result there is a very small possibility of occurrence of additional injury after the maximum deformation. This has also been noted by Hisley et al. (2011) based on the velocity vs. time and energy vs. time graphs obtained from their experiments. Good correlation between the numerical and experimental values of the immediate post impact velocity, diameter of dent and helmet shell BFD for the ACH demonstrate that the FE model can give reasonable predictions regarding the amount of energy (or force) transmitted to the head that might cause ballistic impact induced behind helmet blunt trauma.

Table 30 Simulation results for the front impact.

Measured Quantity	Simulation results for the front impact at 377.6 m/s	
	ACH	ECH
Maximum helmet shell velocity at time of impact (m/s)	148.8	94.27
Helmet shell velocity at maximum back face deformation (m/s)	85.74	58.79
Rebound velocity of the projectile	105.6	93.61
Dent depth at time of impact (mm)	13.13	13.05
Maximum Helmet back face deformation (mm)	14.32	10.33
Diameter of dent (mm)	41.98	156.48

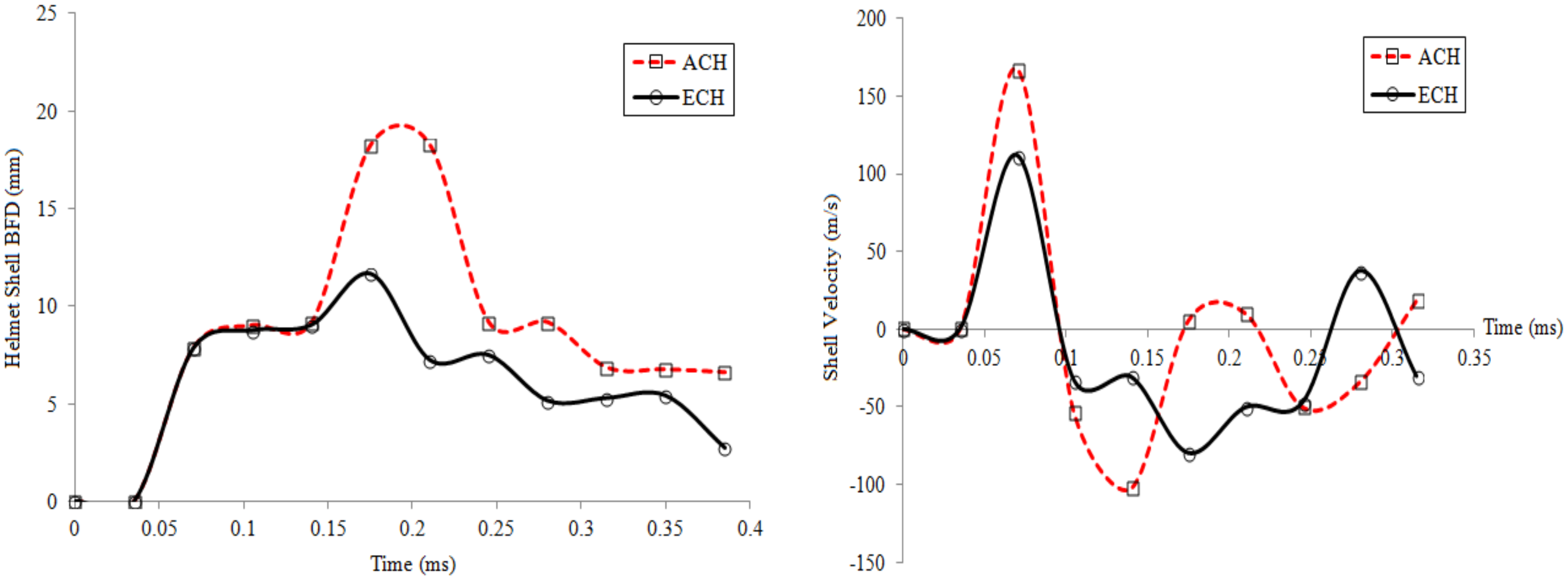

(a) (b)

Figure 61. Helmet shell deformation and velocity time history for the right lateral ballistic impact

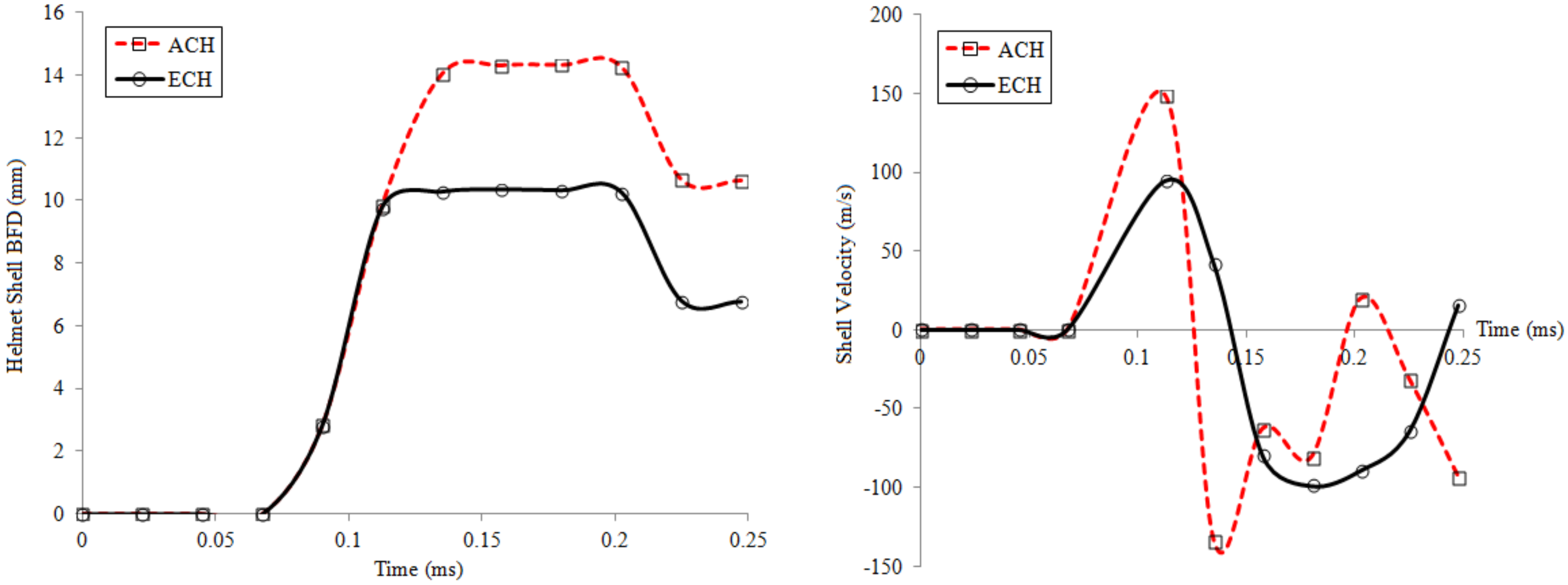

(a) (b)

Figure 62. Helmet shell deformation and velocity time histories for the front ballistic impact.

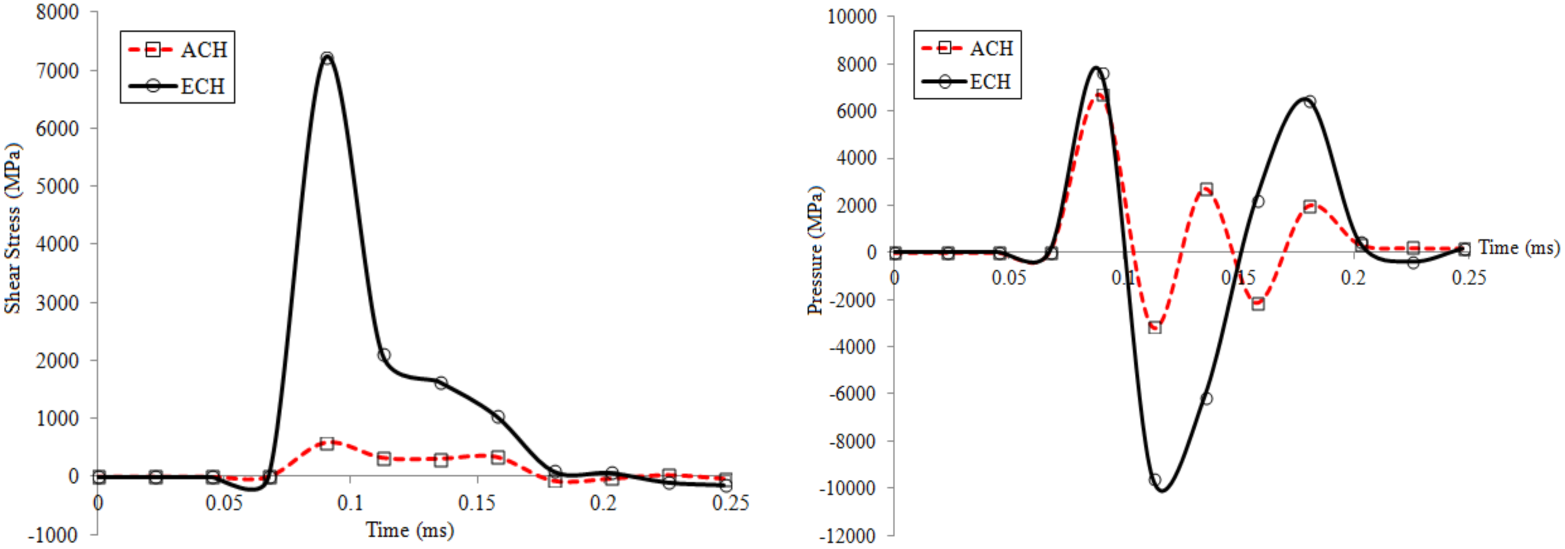

Figure 63. Shear stress and pressure time envelopes for the helmet shell for the front ballistic impact.

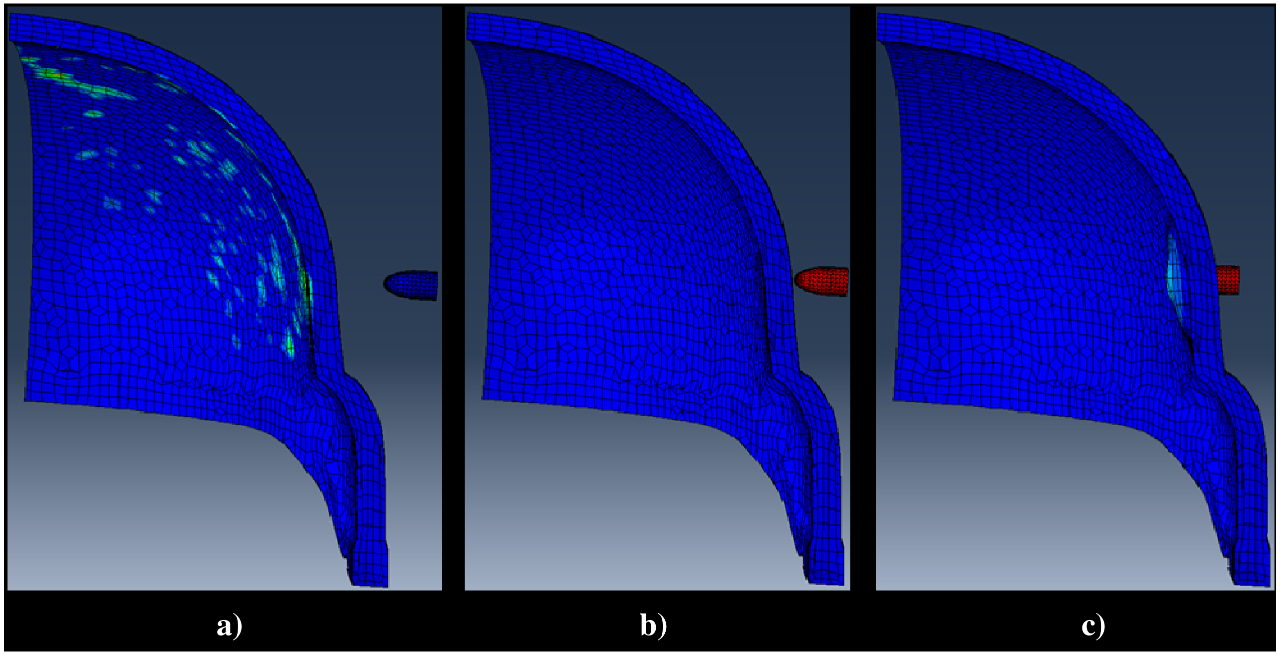

Figure 64. Helmet shell BFD for the FMJ bullet strike at 377.6 m/s at three post impact times: a) 0 ms, b) 0.035 ms, c) 0.07 ms

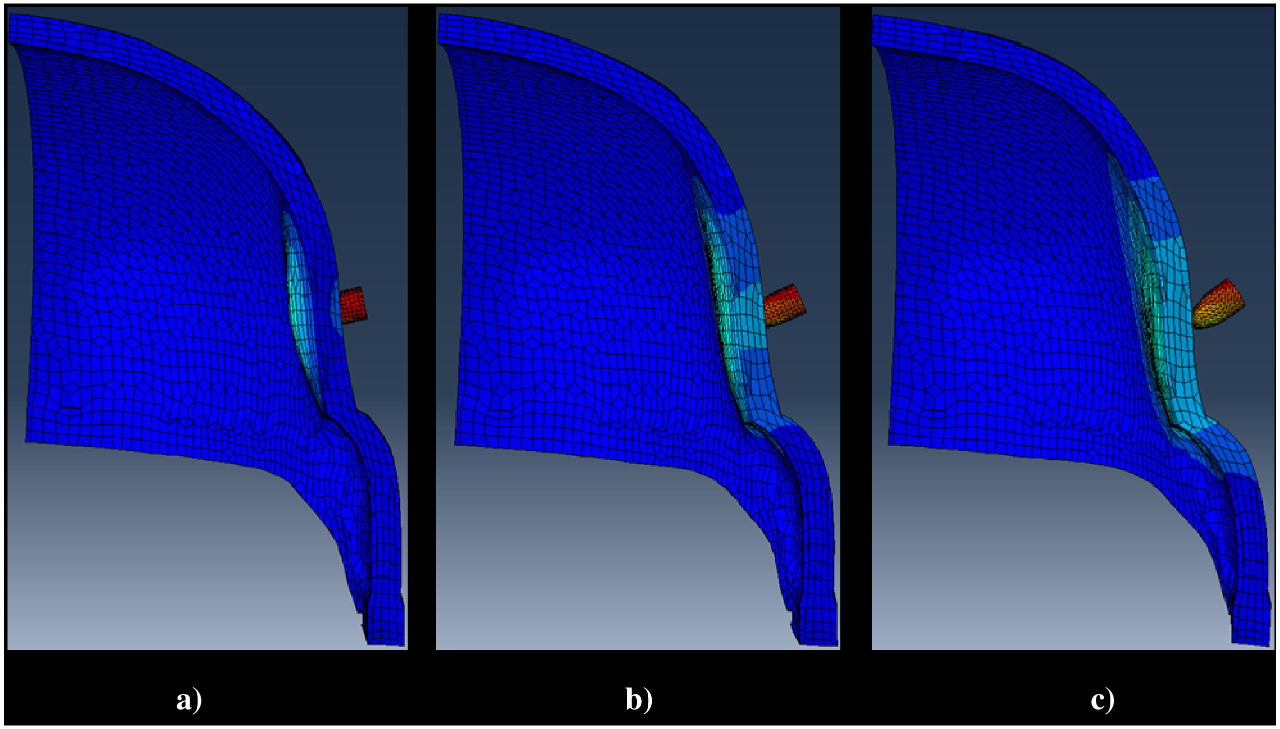

Figure 65. Helmet shell BFD for the FMJ bullet strike at 377.6 m/s at three post impact times: a) 0.1 ms, b) 0.14 ms and c) 0.175 ms.

The finite element simulation results for the ECH show some differences from those for the ACH. The damaged area for the ECH as calculated from the diameter of dent (see Tables 29 and 30) is much larger than the ACH. Based on the rebound velocities of the projectile (see Table 29 and 30) it can be said that the ECH absorbs more of the projectile energy than the ACH, but has a smaller back face deformation (BFD). This difference in response to the high velocity impact is related to the change in material of the helmet shell. As mentioned earlier some of the mechanisms that absorb the energy of the projectile are tensile straining (and failure) of the primary yarns, deformations of the secondary yarns, and matrix cracking and delamination (Naik and Shrirao, 2004). The ECH shell is made from the Dyneema® HB80 unidirectional composite, which has a very soft matrix compared to that of the Kevlar® fiber/Phenolic-resin composite used to make the ACH shell (see Table 23).Therefore, matrix cracking and delamination occur at much lower values for the ECH leading to an increase in the damaged area. Even after the matrix fails the UHMWPE fibers in the Dyneema® HB80 composite continue to resist loads. The Dyneema® fibers have a higher tensile stiffness (and failure strength) than Kevlar® K129 fibers (see Table 23 and 24). As a result, the ECH shell absorbs more energy and yet has a smaller BFD than the ACH. The results presented in this subsection have shown that the ECH can offer better protection against ballistic impact induced behind helmet blunt trauma than ACH. In order to have a better understanding of this observation, the pressure and stress histories for the helmet shell are extracted and compared for both the ECH and ACH. These curves for the front impact are displayed in Fig. 63. The trends for the lateral impact are similar, and the corresponding curves are therefore not presented here. It can be seen from Fig. 63 that the shear stress and pressure in the ECH shell are higher than those in ACH shell. Therefore, the lighter and stiffer ECH absorbs more energy of the projectile but dissipates it in the form of higher stress and pressure variations. This can be one possible explanation for the increase in the energy absorption but reduction in the BFD for the ECH.

5.7 Behind Helmet Blunt Trauma for the ACH

Figure 66 shows snapshots of the ballistic impact event. The FMJ bullet travelling at 365 m/s impacts the helmet shell at 0.075 milliseconds. The actual impact event lasts about 0.075 ms, and the bullet rebounds at 0.15 milliseconds with a rebound velocity of 61.61 m/s. The total energy delivered to the helmet shell was 517.716 J. The projectile impact transmits a strong pressure wave to the skull at t = 0.175 milliseconds. The maximum overpressure in the skull at this time is 31.51 MPa. The rapid deformation of the helmet shell and compression of the polyurethane pads causes the front of the helmet shell to impact the skull at t = 0.25 milliseconds (see Fig. 66). This blunt impact generates secondary pressure waves in the skull that are of higher intensity than the waves generated by the projectile impact. The peak pressure in the skull reaches its maximum value of 380.2 MPa at t = 0.25 milliseconds (see Fig. 67). The temporal evolution of the von Mises stress in the skull is qualitatively similar to the pressure versus time curve with a peak value of 674.6 MPa occurring at t = 0.25 ms (see Fig. 67).

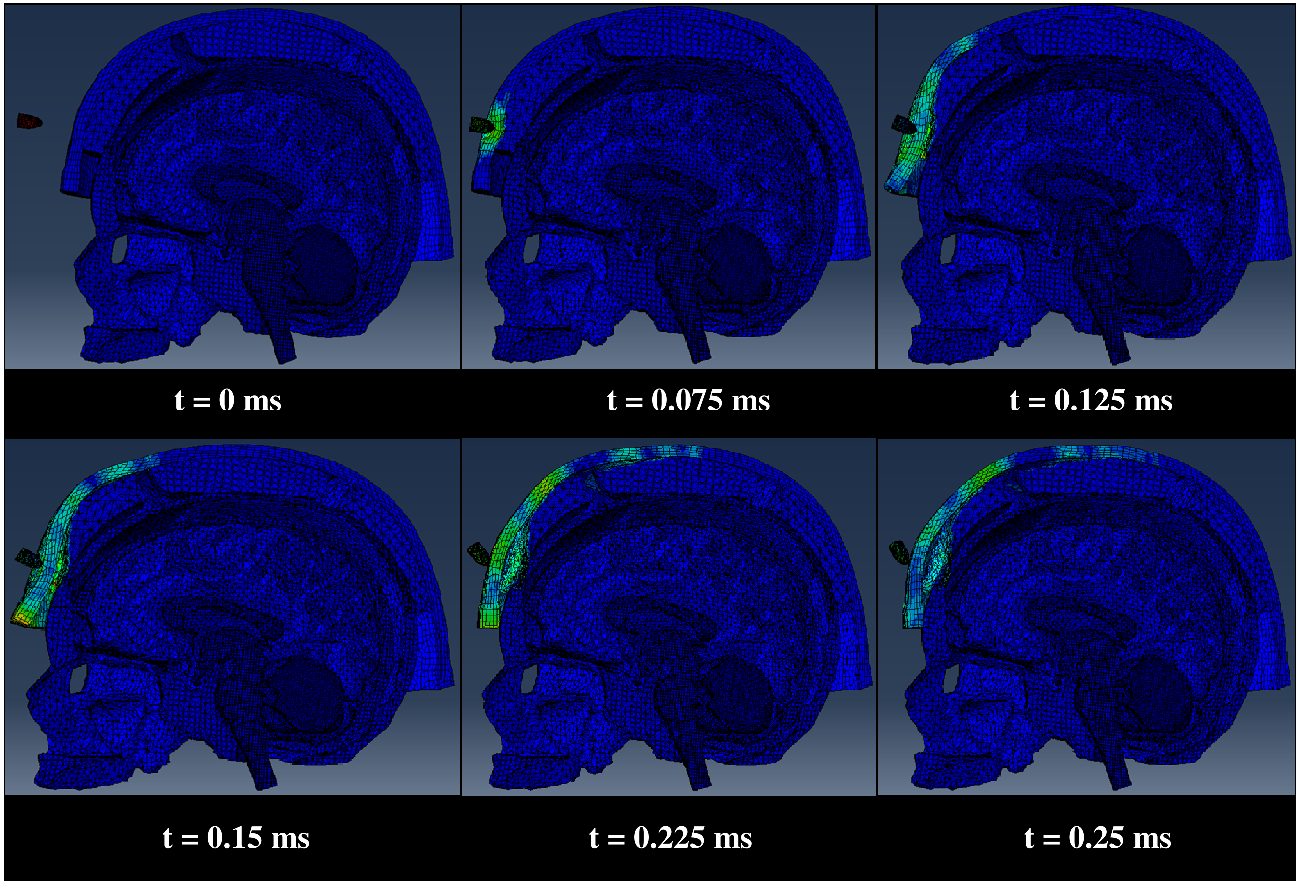

Figure 66. Ballistic impact of the FMJ bullet with head/helmet assembly.

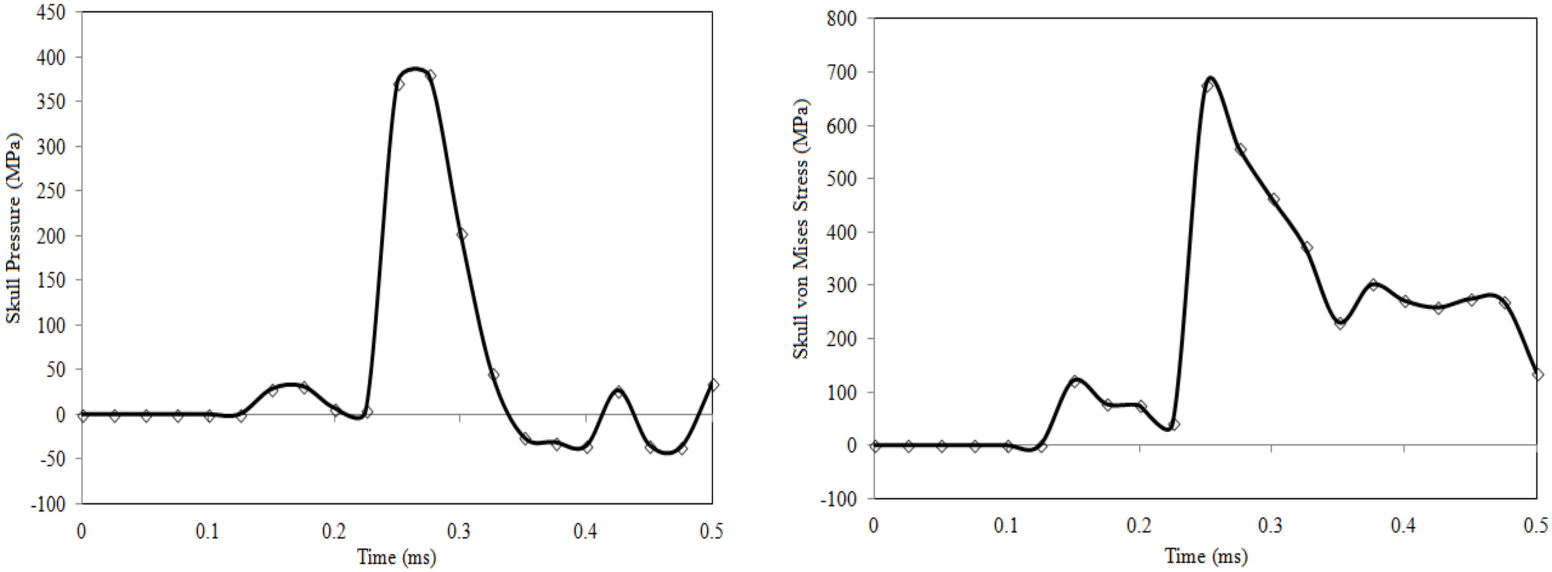

Figure 67. Pressure and von Mises stress profiles for the skull.

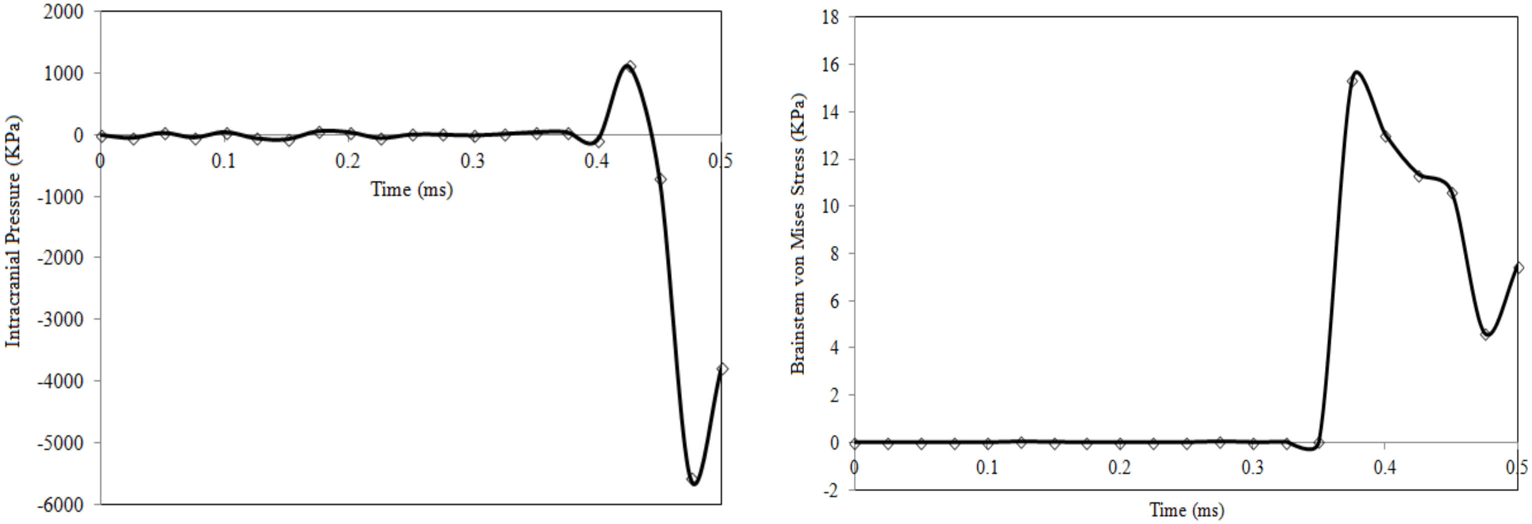

a) b)

Figure 68. Temporal evolution of the pressure and stress in the intracranial cavity: a) the cerebrum/CSF pressure; b) the von Mises stress in the brainstem.

Stress thresholds for skull fracture have been obtained in McElhaney et al. (1970), Robbins and Wood (1969), and Wood (1971). According to these studies, the tensile strength for the skull bone is between 48 – 128 MPa, and the compressive strength is between 32 – 74 MPa. Comparing the results from the present study to these values it can be said that the actual ballistic impact and helmet shell deformation do not induce skull fractures. However, the secondary blunt impact between the shell and the skull (occurring at $t = 0.25$ ms) is likely to induce skull fracture.

The peak intracranial pressure occurs at the CSF-cerebrum interface directly underneath the point of impact and decreases away from point of impact. In the finite element simulations a high stress (pressure) concentration is seen at places where tissue damage has occurred. Damage criteria are useful for predicting the probability of TBI under mechanical loading. The currently used injury criterion is the head injury criterion (HIC) adopted by the National Highway Traffic Safety Administration (NHTSA) based on the work of Gadd (1966). The HIC is an empirical criterion mainly used in the automobile industry and is based on the probability of injury due to a global translational head acceleration. The HIC criterion does not take into account the intracranial mechanical response and hence cannot distinguish between various types of traumatic brain injuries. In the past decade, many 3-D finite element based head models have been used to develop injury criteria for the brain. Various injury criteria based on stress, strain, strain rate, intra-cranial pressure gradient, and type of explosives are summarized in Chapter 2. The criterion developed by Ward (1980) uses the intracranial pressure values as an indicator for brain contusion type injuries. The intracranial pressure values obtained in the current simulations at the cerebrum/CSF interface (see Fig. 68(a)) exceed the threshold for brain injury. Therefore, there is a possibility of brain contusion injury for a FMJ bullet frontal impact on an ACH. However, the peak deviatoric stress (strain) values in the brainstem and corpus callosum (see Fig 68(b)) do not exceed the thresholds for diffuse axonal injuries. Even though the probability of occurrence of contusion type injuries can be predicted with some degree of confidence, it is difficult to quantify the extent and severity of brain injury based on this effort alone.

CHAPTER VI

SUMMARY AND CONCLUSIONS

6.1 Summary and Conclusions

A transversely isotropic visco-hyperelastic constitutive model is provided for soft tissues based on continuum mechanics. A new form of the strain energy density function based on five invariants of the right Cauchy-Green deformation tensor **C** is proposed to model quasi-static responses, and a rate-dependent viscous potential involving two invariants of $\dot{\mathbf{C}}$ (the total material time derivative of **C)** additionally is suggested to account for short-term memory effects. The predicted stress responses by the newly proposed constitutive model compare well with available experimental data for porcine and human brain tissues at different strain rates and under multiple loading conditions. The model can be applied to other soft tissues by using different values of material and fitting parameters. The elasticity and viscosity tensors are explicitly derived using the general form of the strain energy density function of the five invariants of **C** and the viscous potential of the first five invariants of $\dot{\mathbf{C}}$, which can be directly used in finite element simulations of blast-induced traumatic brain injury.

Using this constitutive relation a finite element model is established to study non-penetrating traumatic brain injuries. The geometric model of human head consists of the skull and several intra-cranial brain sections. The effects of the constitutive models and blast direction on the finite element simulations of BTBI are investigated. Further, this human head model is combined with a geometric model of combat helmet and the effectiveness of combat helmets on the propagation of pressure/stress waves within the brain tissue following blast and ballistic impacts is investigated. Blast and ballistic impact simulations have been validated against available experimental data. Two helmet designs are considered: the Advanced Combat Helmet, which is the current helmet of the U.S. Army and the Enhanced Combat Helmet, which is under development since 2007. Based on the simulation results obtained in this work, the following conclusions are derived:

- In a blunt impact (such as traffic accidents or a sports collision) the head experiences a quasi-static load. The pressure varies very slowly, has a long rise time, and can be approximated by an average constant value. In such a case, choosing a different constitutive relation for the volumetric response or reducing values of the bulk modulus has very little effect on the intracranial pressure response. As strain rate effects are negligible, hyper-viscoelastic models can be used to capture the deviatoric and decaying responses of the tissue.
- Blast and ballistic impacts involve interactions between detonation waves and shock waves. Shock waves are defined by abrupt changes in the characteristics of the medium such as pressure, velocity, density, and loading rate. The meshing and material modeling requirements for shock waves are higher than modeling a structural dynamic quasi-static event like blunt impact.
- Unlike blunt impacts, the volumetric response of the brain tissue to blast events is sensitive to change in the constitutive relations and the values of bulk modulus.

A non-linear EOS is essential to describe the shock response of the brain tissue. Simplifying assumptions can save computational cost, but they underestimate pressure and strain gradients.

- Including the strain rate effects (short-term memory) leads to deviatoric response that is substantially stiffer than that predicted using a linear elastic or hyper-viscoelastic material relation. A linear elastic model generates higher stresses than a hyper-viscoelastic one.
- Inclusion of anisotropy in the constitutive relation can have an effect on the nature and location of injury.
- Brain tissue constitutive relations validated against low velocity impact experiments (cadaver impact experiments) may not necessarily provide accurate results for shock wave dominated events. In the absence of experimental data for validating BTBI simulations, numerical modelers can do little more than ensure that the constitutive relations implemented are accurate.
- Localized skull deformations, coup and contrecoup pressures, and deviatoric stresses are larger under a lateral blast than those under a frontal blast.
- For a lateral blast loading the presence of the combat helmet significantly reduces the skull deformation and oscillation. The helmet decreases the underpressure in the CSF on the coup side by absorbing some of the incident blast loading. Thus, the combat helmets provide some degrees of protection against contusion and fluid cavitation. In contrast to the dilatational response at the coup site, the negative pressure magnitudes at the contrecoup site do not

show any significant difference between a helmet protected head and an unprotected head under blast loading.

- For a blast impact the velocity and acceleration transferred to the brain is higher for a helmet protected head than for an unprotected head.
- The deviatoric stress values in the brainstem region are smaller in a helmet protected head than in an unprotected head. However, the presence of a helmet is seen to cause an increase in the shear and von Mises stress values in the corpus callosum region. This increase is smaller for the ECH than for the ACH.
- The Dyneema® HB80 unidirectional composite based ECH provides higher protection against BTBI than the Kevlar® fiber/Phenolic-resin based ACH. The ECH is lighter but stiffer than the ACH and is able to absorb larger amount of blast loading.
- For a FMJ bullet ballistic impact, the ECH absorbs more of the projectile energy than the ACH, but has a smaller back face deformation (BFD) and a smaller helmet shell velocity. As a result, the ECH reduces the risk of ballistic impact induced behind armor blunt trauma injuries even though it is lighter than the ACH.
- A FMJ bullet front impact at 365 m/s on an ACH is likely to cause skull fracture and brain contusion. However, the peak deviatoric stress (strain) values are not large enough to cause any permanent damage in the white matter regions or the brainstem.

- In addition to developing new materials for the helmet shell, research into the behavior of foam pad material under blast or ballistic loading can help in mitigating non-penetrating TBI's.

REFERENCES

Aare, M. and Kleiven, S. (2005). “Evaluation of head response to ballistic helmet impacts using the finite element method.” International Journal of Impact Engineering **34** (3): 596-608.

Anderson, R. W. G., Brown, C. J., Blumbergs, P. C., Scott, G., Finney, J. W., Jones, N. R. and Mclean, A. J. (1999). “Mechanisms of axonal injury:an experimental and numerical study of a sheep model of head impact.” Proceedings of the 1999 International Conference on the Biomechanics of Impact. International Research Council on the Biokinetics of Impact (IRCOBI), Sitges, Spain, September 23-24, 1999.

Arbogast, K. B. and Margulies, S. S. (1999). "A fiber-reinforced composite model of the viscoelastic behavior of the brainstem in shear." Journal of Biomechanics **32** (8): 865-870.

Bain, A. C. and Meaney, D. F. (1998). “Tissue level thresholds for axonal damage in an experimental model of central nervous systems white matter injury.” Journal of Biomechanical Engineering **122** (6): 615-622.

Balzani, D., Neff, P., Schroder, J. and Holzapfel, G. A. (2006). “A polyconvex framework for soft biological tissues. Adjustment to experimental data.” International Journal of Solids and Structures **43**: 6052-6070.

Bass, E. C., Ashford, F. A., Segal, M. R. and Lotz, J. C. (2004). "Biaxial testing of human annulus fibrosus and its implications for a constitutive formulation." Annals of Biomedical Engineering **32**: 1231-1242.

Bazant, Z. P. and Oh, B. H. (1983). "Crack band theory for fracture of concrete." Materials and Structures **16**(3): 155-177.

Bazhenov, S. (1997). “Dissipation of energy by bulletproof aramid fabric.” Journal of Materials Science **32** (15): 4167-4173.

Bilisik, A. K. and Turhan, Y. (2009). “Multidirectional stitched layered aramid woven fabric structures and their experimental characterization of ballistic performance.” Textile Research Journal **79** (14): 1331-1343.

Boehler, J. P. (1987). *“Application of Tensor Functions in Solid Mechanics.”* Springer - Verlag, Vienna, Austria.

Bowen, I. G., Fletcher, E. R. and Richmond, D. R. (1968). “Estimate of Man’s Tolerance to the Direct Effects of Air Blast.” Technical Report DASA 2113, Defense Atomic Support Agency, Washington, D.C.

Bradshaw, D. R. S. and Morfey, C. L. (2001). “Pressure and shear responses in brain injury models.” The 17th International Technical Conference on the Enhanced Safety Vehicles (ESV), June 4-7, 2001, Amsterdam, The Netherlands.7 pages.

Brands, D. W. A. (2002). “Predicting Brain Mechanics During Closed Head Impact - Numerical and Constitutive Aspects.” Ph.D. dissertation,Eindhoven University of Technology, Eindhoven, Netherlands.

Briody, C., Duignan, B. and Jerrams, S. (2011). Testing, modelling and validation of numerical model capable of predicting stress fields throughout polyurethane foam. ECCMR, 7th European Conference on Constitutive models for Rubber,20-23 September, 2011. Dublin,Ireland.

Cannon, L. (2001). “Behind armour blunt trauma - an emerging problem.” Journal of the Royal Army Medical Corps **147**, 87-96.

Carey, M. E., Herz, M., Corner, B., McEntire, J., Malabarba, D., Paquette, S. and Sampson, J. B. (2000). “Ballistic helmets and aspects of their design.” Neurosurgery **47** (3): 678-689.

Carroll, A. W. and Soderstrom, C. A. (1978). “A new nonpenetrating ballistic injury.” Annals of Surgery **188**, 753-757.

Cernak, I. and Haeusslein, L. J. N. (2010). “Traumatic brain injury: an overview of pathobiology with emphasis on military populations.” Journal of Cerebral Blood Flow and Metabolism **30** (2): 255-266.

Chafi, M. S., Karami, G. and Ziejewski, M. (2009). “Biomechanical assesssment of brain dynamic responses due to blast pressure waves.” Annals of Biomedical Engineering **38** (2): 490-504.

Chatelin, S., Deck, C. and Willinger, R. (2012). “An anisotropic viscous hyperelastic constitutive law for brain material finite-element modeling.” Journal of Biorheology (published on-line) DOI: 10.1007/s12573-012-0055-6.

Chatelin, S., Constantinesco, A. and Willinger, R. (2010). “Fifty years of brain tissue mechanical testing: From in vitro to in vivo investigations.” Biorheology **47**: 255-276.

Chen, Y. and Ostoja-Starzewski, M. (2010). “MRI-based finite element modeling of head trauma:spherically focusing shear waves.” Acta Mechanica **213** (1-2): 155-167.

Cheng, K. C. and Chen, Y. L. (2010). “Ballistic-proof effects of various woven constructions.” Fibers and Textiles in Eastern Europe **18** (6): 63-67.

Ciarletta, P., Izzo, I., Micera, S. and Tendick, F. (2010). "Stiffening by fiber reinforcement in soft materials:A hyperelastic theory at large strains and its application." Journal of the Mechanical Behavior of Biomedical Materials **4**: 1359-1368.

Claessens, M., Sauren, F. and Wismans, J. (1997). “Modeling of Human Head under impact conditions.” Proceedings of the 41st STAPP Car Crash Conference, Lake Buena Vista, Florida, November 13-14, 1997. SAE Paper No. 973338.

Clayton, E. H., Genin, G. M. and Bayly, P. V. (2012). “Transmission, attenuation and reflection of shear waves in the human brain.” Journal of the Royal Society Interface **9**: 2899-2910.

Coleman, B. D. and Noll, W. (1963). "The thermodynamics of elastic materials with heat conduction and viscosity." Archive for Rational Mechanics and Analysis**13**: 167-178.

Constantinescu, A., Aboulghit El Malki, A., Neme, A. and Rigo, P. (2011). "Numerical and experimental studies of simple geometries in slamming." International Journal of Offshore and Polar Engineering **21**(3): 9 pages.

Criscione, J. C., Douglas, A. S. and Hunter, W. C. (2001). "Physically based strain invariant set for materials exhibiting transversely isotropic behavior." Journal of the Mechanics and Physics of Solids **49**: 871-897.

Czechowski, L., Jankowski, J. and Kubiak, T. (2012). “Experimental tests of a property of composite material assigned for ballistic products.” Fibers and Textiles in Eastern Europe **20** (3): 61-66.

Darvish, K. K. and Crandall, J. F. (2001). “Nonlinear viscoelastic effects in oscillatory shear deformation of brain tissue.” Medical Engineering and Physics **23**: 633-645.

David, N. V., Gao, X.-L. and Zheng, J. Q. (2012). “Creep of a Twaron®/natural rubber composite.” Mechanics of Advanced Materials and Structures (in press) (DOI: 10.1080/15376494.2012.676719).

David, N. V., Gao, X.-L. and Zheng, J. Q. (2011). “Stress relaxation of a Twaron®/ natural rubber composite.” ASME Journal of Engineering Materials and Technology **134** (3), 011001-1~9.

David, N. V., Gao, X.-L. and Zheng, J. Q. (2010). “Constitutive behavior of a Twaron®/natural rubber composite.” Mechanics of Advanced Materials and Structures **17** (4), 246-259.

David, N. V., Gao, X.-L. and Zheng, J. Q. (2009a). “Ballistic resistant body armor: contemporary and prospective materials and related protection mechanisms.” Applied Mechanics Reviews **62**(5): 050802-1~20.

David, N. V., Gao, X.-L. and Zheng, J. Q. (2009b). “Modeling of viscoelastic behavior of ballistic fabrics at low and high strain rates.” International Journal for Multiscale Computational Engineering **7** (4), 295-308.

Destrade, M., Gilchrist, M. D., Prikazchikov, D. A. and Saccomandi, G. (2008). "Surface instability of sheared soft tissues." Journal of Biomechanical Engineering**130**: 061007.

Ding, H.-J., Chen, W. Q. and Zhang, L.(2006). “*Elasticity of Transversely Isotropic Materials*.” Springer, Dordrecht, The Netherlands.

Dokos, S., Smaill, B. H., Young, A. A. and LeGrice, I. J. (2002). "Shear properties of passive ventricular myocardium." American Journal of Physiology, Heart and Circulatory Physiology **283**: H2650 - H2659.

Dokos, S., LeGrice, I. J., Smaill, B. H., Kar, J. and Young, A. A. (2000). "A triaxial measurement shear-test device for soft biological tissues." Journal of Biomechanical Engineering **122**: 471-478.

Donnelly, B. R. and Medige, J. (1997). “Shear properties of human brain tissue.” Journal of Biomechanical Engineering **119** (4): 423-432.

Dorfmann, A. L., Woods, W. A. J. and Trimmer, B. A. (2007). “Muscle performance in a soft-bodied terrestrial crawler:constitutive modelling of strain-rate depedency.” Journal of the Royal Society Interface **5** (20): 349-362.

El Sayed, T., Mota, A., Fraternali, F. and Ortiz, M. (2008). “Biomechanics of traumatic brain injury.” Computer Methods in Applied Mechanics and Engineering **197** (51-52): 4692-4701.

Elkin, B. S. and Morrison, B. (2007). "Region-specific tolerance criteria for the living brain." Stapp Car Crash Journal **51** (2007): 127-138.

Fallenstein, G. T. and Hulce, V. D. (1969). “Dynamic mechanical properties of human brain tissue.” Journal of Biomechanics **2**: 217-226.

Fang, G., Liang, J., Lu, Q., Wang, B. and Wang, Y. (2011). "Investigation on the compressive properties of the three dimensional four-directional braided composites." Composite Structures **93** (2011): 392-405.

Faur-Csukat, G. (2006). “A study on the ballistic performance of composites.” Advanced Polymer Composites and Technologies **239** (1): 217-226.

Fung, Y. C., Fronek, K. and Patitucci, P. (1979). "Pseudoelasticity of arteries and choice of its mathematical expression." The American Journal of Physiology **237**: H620-H631.

Fung, Y. C. (1967). “Elasticity of soft tissues in simple elongation.” American Journal of Physiology **213** (6): 1532-1544.

Gadd, C. W. (1966). “Use of weighted-impulse criterion for estimating injury hazard.” Proceedings of the 10th STAPP Car Crash Conference, Alamogordo, New Mexico, November 8-9, 1966. SAE Paper No. 660793.

Ganpule, S., Gu, L., Alai, A. and Chandra, N. (2011). “Role of helmet in the mechanics of shock wave propogation under blast loading conditions.” Computer Methods in Biomechanics and Biomedical Engineering **10**: 1-12.

Ganpule, S., Gu, L. and Chandra, N. (2010). “MRI-based three dimensional modeling of blast traumatic brain injury (bTBI).” Proceedings of the ASME 2010 International Mechanical Engineering Congress and Exposition, Vancouver, Canada, November 12-18, 2010. Paper # IMECE2010-39428.

Gao, X.-L. and Mao, C. L. (2013). Solution of the contact problem of a rigid conical frustum indenting a transversely isotropic elastic half-space. ASME Journal of Applied Mechanics(in press) (DOI: 10.1115/1.4025140)

Gao, X. –L. (2001). “Two displacement methods for in-plane deformations of orhtotropic linear elastic materials.” Z. angew. Math. Phys. 52 : 810-822.

Gao, X.-L. and Mall, S. (2000). “A two-dimensional rule-of-mixtures micromechanics model for woven fabric composites.” ASTM Journal of Composites Technology and Research **22**: 60-70.

Gefen , A., Gefen, N., Zhu, Q. L., Raghupati, R. and Margulies , S. S. (2003). “Age-depedent changes in material properties of the brain and brain case of the rat.” Journal of Neurotrauma **20**: 1163-1177.

Goel, R. (2011). “Study of an Advanced Helmet Liner Concept to Reduce TBI:Experiments and Simulation using Sandwich Structures.” Master's thesis, Massachusetts Institute of Technology, Cambridge. 104 pages.

Gogineni, S., Gao, X.-L., David, N. V. and Zheng, J. Q. (2012). “Ballistic impact of Twaron CT709® plain weave fabrics.” Mechanics of Advanced Materials and Structures **19** (6): 441-452.

Gray, H. (1858). "*Anatomy Descriptive and Surgical.*" John W. Parker and Son, London, England.

Green, A. E. and Naghdi, P. M. (1971). "Some remarks on elastic-pastic deformation at finite strain." International Journal Engineering Science **9**: 1219-1229.

Grujicic, M., Bell, W. C., Pandurangan, B. and Glomski, P. S. (2010a). "Fluid/Structure interaction computational investigation of blast-wave mitigation efficacy of the Advanced Combat Helmet." Journal of Materials Engineering and Performance **20** (6): 877-893.

Grujicic, M., Bell, W. C., Pandurangan, B. and He, T. (2010b). "Blast-wave impact-mitigation capability of polyurea when used as helmet suspension-pad material." Materials and Design **31** (9): 4050-4065.

Grujicic, M., Arakere, G. and He, T. (2009). "Material-modeling and structural mechanics aspects of the traumatic brain injury problem." Multidiscipline Modeling in Materials and Structures **6** (3): 335-363.

Guo, Z. Y., Peng, X. Q. and Moran, B. (2007). "Large deformation response of a hyperelastic fibre reinforced composite:Theoretical model and numerical validation." Composites Part A - Applied Science and Manufacturing **38**: 1842-1851.

Guo, Z. Y., Peng, X. Q. and Moran, B. (2006). "A composites-based hyperelastic constitutive model with fiber matrix shear interaction for the human annulus fibrosus." Journal of the Mechanics and Physics of Solids **54**: 1952-1971.

Gurtin, M.E., Fried, E. and Anand, L. (2010). "*The Mechanics and Thermodynamics of Continua."*Cambridge University Press. New York,USA.

Hardy, W. N., Mason, M. J., Foster, C. D., Shah, C. S., Kopacz, J. M., King, H. Y., King, A. I., Bishop, J., Bey, M., Anderst, W. and Tashman, S. (2007). "A study of response of the human cadaver head to impact." Stapp Car Crash Journal **51** (2007): 17-80.

Hardy, W. N., Khalil, T. B. and King, A. I. (1993). "Literature review of head injury biomechanics." International Journal of Impact Engineering **15** (4): 561-586.

Hashin, Z. (1980). "Failure criteria for unidirectional fiber composites." Journal of Applied Mechanics **47** (2): 329-334.

Hearle, J. W. S. (2001). "*High Performance Fibers."* Woodhead Publishing, Cambridge, England.

Hisley, D. M., Gurganus, J. C. and Drysdale, A. W. (2011). “Experimental methodology using digital image correlation to assess ballistic helmet blunt trauma.” ASME Journal of Applied Mechanics **78**: 051022-1~7.

Holzapfel, G. A. and Ogden, R. W. (2010). "Constitutive modelling of arteries." Proceedings of the Royal Society A **466**: 1551-1597.

Holzapfel, G.A. and Ogden, R.W. (2009). "Constitutive modeling of passive myocardium: a structurally based framework for material characterization." Philosophical Transactions of the Royal Society of London, Series A **367**: 3445-3475.

Holzapfel, G. A. (2000). “*Nonlinear Solid Mechanics:A Continuum Approach for Engineering.”* John Wiley & Sons Ltd., West Sussex, England

Holzapfel, G. A., Gasser, T. C. and Ogden, R. W. (2000). "A new constitutive framework for arterial wall mechanics and a comparative study of material models." Journal of Elasticity **61**: 1-48.

Horgan, C. O. and Murphy, J. G. (2011). "Simple shearing of soft biological tissues." Proceedings of the Royal Society A **467**: 760-777.

Horgan, C. O. and Saccomandi, G. (2005). "A new constitutive theory for fiber-reinforced incompressible nonlinearly elastic solids." Journal of the Mechanics and Physics of Solids **53**: 1985-2015.

Hrapko, M., van Dommelen, J. A. W., Peters, G. W. M. and Wismans, J. S. H. M. (2009). “On the consequences of non linear constitutive modelling of brain tissue for injury prediction with numerical head models.” International Journal of Crashworthiness **14** (3): 245-257.

Hrapko, M., van Dommelen, J. A. W., Peters, G. W. M. and Wismans, J. S. H. M. (2008). “Characterisation of the mechanical behaviour of brain tissue in compression and shear.” Biorheology **45**(6): 663-676.

Humphrey, J. D. (2003). "Review Paper: Continuum biomechanics of soft biological tissues." Proceedings of the Royal Society A **459**: 3-46.

Ivins, B. J., Schwab, K. A., Crowley, J. S., McEntire, J., Trumble, C. C., Brown, F. H. and Waarden, D. L. (2007). “How Satisfied are soldiers with their ballistic helmets? A comparison of soldiers’ opinions about the Advanced Combat Helmet and the Personal Armor System for ground troops helmet.” Military Medicine **172** (6): 586-591.

Jason, A. M. (2010). “Facial Protective Devices for Blast-Induced Traumatic Brain Injury Mitigation.” Master's thesis, Massachusetts Institute of Technology, Cambridge. 77 pages.

Jones, R.M. (1999). “*Mechanics of Composite Materials*”, 2nd edition, Taylor and Francis, New York.

Keyak, J. H., Meagher, J. M., Skinner, H. B. and Mote, C. D. (1990). “Automated three-dimensional finite element modelling of bone: a new method.” Journal of Biomedical Engineering **12** (5): 389-397.

Kleiven, S. (2008). “Biomechanics and thresholds for MTBI in humans”. Proceedings of the International Brain Injury Associataion's Seventh World Congress, Lisbon, Portugal, April 9-12, 2008.

Kleiven, S. and Hardy, W. N. (2002). "Correlation of an FE Model of the human head with local brain motion - Consequences for injury prediction." Stapp Car Crash Journal **46** (2002): 123-144.

Lai, M.W., Rubin, D. and Krempl E. (2010). “*Introduction To Continuum Mechanics*”, 4th edition, Butterworth - Heinemann, New York.

Laible, R. C. (1980). “*Ballistic Materials and Penetration Mechanics*.” Elsevier, Amsterdam.

LaPlaca, M. C., Cullen, D. K., McLoughlin, J. J. and Cargill, R. S. N. (2005). "High rate shear strain of three-dimensional neural cell culures:a new in vitro traumatic brain injury model." Journal of Biomechanics **38** (5): 1093-1105.

Lapczyk, I. and Hurtado, J. A. (2007). "Progressive damage modeling in fiber-reinforced materials." Composites Part A: Applied Science and Manufacturing **38** (11): 2333-2341.

Lee, E. H. (1969). “Elastic-plastic deformation at finite strains.” ASME Journal of Applied Mechanics **38**: 1-6.

Lee, H. P. and Gong, S. W. (2010). "Finite element analysis for the evaluation of protective functions of helmets against ballistic impact." Computer Methods in Biomechanics and Biomedical Engineering **13** (5): 537-550.

Limbert, G. and Middleton, J. (2004). "A transversely isotropic viscohyperelastic material. Application to the modeling of biological soft connective tissues." International Journal of Solids and Structures **41** (2004): 4237-4260.

Lin, S., Shieh, S. and Grimm, M. (1997). “Ultrasonic measurements of brain tissue properties.” Proceedings of the 7th Injury Prevention through Biomechanics Symposium, Detroit, Michigan,8-9 May, 1997. pages 27-31.

Lu, J. and Zhang, L. (2005). “Physically motivated invariant formulation for transversely isotropic hyperelasticity.” International Journal of Solids and Structures **42**: 6015-6031.

Lu, Y. T., Zhu, H. X., Richmond, S. and Middleton, J. (2012). "Numerical modelling of the fibre-matrix interaction in biaxial loading for hyperelastic soft tissue models." International Jounal for Numerical Methods in Biomedical Engineering **28**: 401-411.

Maimi, P., Camanho, P. P., Mayugo, J. A. and Davila, C. G. (2007). "A continuum damage model for composite laminates: Part II - Computational implementation and validation." Mechanics of Materials **39** (10): 909-919.

Marjoux, D., Baumgartner, D., Deck, C. and Willinger, R. (2006). “Head injury prediction capability of the HIC, HIP, SIMon, and ULP criteria.” Accidend Analysis and Prevention **40**: 1135-1148.

McElhaney, J. H., Roberts, V. L. and Hilyard, J. F. (1976). “Handbook of Human Tolerance.” Japan Automobile Research Institute. 143 pages.

McElhaney, J. H., Fogle, J. L., Melvin, J. W., Haynes, R. L., Roberts, V. L. and Alem, N. M. (1970). "Mechanical properties of cranial bone." Journal of Biomechanics **3**: 495-511.

Mendis, K. (1992). “Finite Element Modeling of the Brain to Establish Diffuse Axonal Injury Criteria.” Ph.D. dissertation,The Ohio State University, Columbus, OH.

Merodio, J. and Ogden, R. W. (2004). "Mechanical response of fiber-reinforced incompressible non-linearly elastic solids." International Journal of Non-linear Mechanics **40** (2-3): 213-227.

Merodio, J. and Ogden, R. W. (2003). "Instabilities and loss of ellipticity in fiber-reinforced compressible non-linearly elastic solids under plane deformation." International Journal of Solids and Structures **40** (18): 4707-4727.

Merodio, J. and Ogden, R. W. (2002). "A Note on strong ellipticity for transversely isotropic linearly elastic solids." The Quarterly Journal of Mechanics and Applied Mathematics **56** (4): 589-591.

Meyers, M. A. (1994). *“Dynamic Behavior of Materials.”* John Wiley & Sons, Inc. New York,USA.

Moore, D. F., Jerusalem, A., Nyein, M., Noels, L., Jaffee, M. S. and Radovitzky, R. A. (2009). “Computational biology - Modeling primary blast effects on the central nervous system.” NeuroImage **47** (Supplement 2): T10-T20.

Morrison, B., Cater, H. L., Wang, C. B., Thomas, F. C., Hung, C. T., Ateshian, G. A. and Sundstrom, L. E. (2003). “A tissue level tolerance criterion for living brain developed with an In-Vitro model of Traumatic Mechanical Loading.” Stapp Car Crash Journal **47**: 93-105.

Moss, W. C., King, M. J. and Blackman, E. G. (2009). “Skull flexure from blast waves:A mechanism for brain injury with implications for helmet design.” Physical Review Letters **103**: 108702-1~4.

Mylvaganam, K. and Zhang, L. C. (2007). “Ballistic resistance capacity of carbon nanotubes.” Nanotechnology **18** (47): 5701-5704.

Naik, N. K. and Shrirao, P. (2004). “Composite structures under ballistic impact.” Composite Structures **66** (1-4): 579-590.

Neuberger, A., Peles, S. and Rittel, D. (2007). "Scaling the response of circular plates subjected to large and close-range spherical explosions. Part I: Air-blast loading." International Journal of Impact Engineering **34** (2007): 859-873.

Newman, J. A., Shewchenko, N. and Welbourne, E. (2000). “A new biomechanical head injury assessment function:the maximum power index.” Proceedings of the 44th STAPP Car Crash Conference, Atlanta, Georgia, November 6-8, 2000. SAE Paper No. 2000-01-SC16.

Nicolle, S., Lounis, M. and Willinger, R. (2004). “Shear properties of brain tissue over a frequency range relevant for automotive impact situations:new experimental results.” Stapp Car Crash Journal **48**: 239-258.

Nilakantan, G., Keefe, M., Wetzel, E. D., Bogetti, T. A. and Gillespie, J. W. (2011). “Computational modeling of the probabilistic impact response of flexible fabrics.” Composite Structures **93**: 3163-3174.

Ning, X., Zhu, Q., Lanir, Y. and Margulies, S. S. (2006). "A transversely isotropic viscoelastic constitutive equation for brainstem undergoing finite deformation." Journal of Biomechanical Engineering **128** (6): 925-933.

Nyein, M. K., Jason, A. M., Yu, L., Pita, C. M., Joannopoulos, J. D., Moore, D. F. and Radovitzky, R. A. (2010). “In silico investigation of intracranial blast mitigation with relevance to military traumatic brain injury.” Proceedings of the Natural Academy of Sciences **109** (23): 20703-20708.

Ogden, R. W. (1972). "Large deformation isotropic elasticity: On the correlation of theory and experiment for compressible rubberlike solids." Proceedings of the Royal Society of London. Series A, Mathematical and Physical Sciences **328** (1575): 567-583.

Ommaya, A. K. (1968). "Mechanical properties of tissues of the nervous system." Journal of Biomechanics **1** (1968): 127-138.

Operator's Manual 2008 Advanced Combat Helmet (ACH), Department of the Army ACH-TM10847020410R001,2008, Washington, D.C.

Peng, X. Q., Guo, Z. Y. and Moran, B. (2006). "An anisotropic hyperelastic constitutive model with fiber-matrix shear interaction for the human annulus fibrosus." ASMEJournal of Applied Mechanics **73** (5): 815-824.

Pervin, F. and Chen, W. (2011). "Effect of inter-species, gender, and breeding on the mechanical behavior of brain tissue." NeuroImage **54** (S1): S98-S102.

Pervin, F. and Chen, W. W. (2010). "Dynamic mechanical response of bovine gray matter and white matter brain tissues under compression." Journal of Biomechanics **42** (2009): 731-735.

Pioletti, D. P. and Rakotomanana, L. R. (2000). "Non-linear viscoelastic laws for soft biological tissues." European Journal of Mechanics and Solids **19** (5): 749-759.

Pioletti, D. P. (1997). "Viscoelastic properties of soft tissues: Application to knee ligaments and tendons." Journal of Biomechanics **31** (8): 753-757.

Prange, M. T. and Margulies, S. S. (2002). "Regional,directional, and age-depedent properties of the brain undergoing large deformation." Journal of Biomechanical Engineering **124** (2): 244-252.

Prat, N., Rongieras, F., Sarron, J.-C., Miras, A. and Voiglio, E. (2012). "Contemporary body armor: technical data, injuries, and limits." European Journal of Trauma and Emergency Surgery **38**: 95-105.

Prevost, T. P., Balakrishnan, A., Suresh, S. and Socrate, S. (2011). "Biomechanics of brain tissue." Acta Biomaterialia **7** (1): 83-95.

Qiu, G. Y. and Pence, T. J. (1997). "Remarks on the behavior of simple directionally reinforced incompressible nonlinearly elastic solids." Journal of Elasticity **49** (1): 1-30.

Rashid, B., Destrade, M. and Gilchrist, M. (2012). "Mechanical characterization of brain tissue in compression at dynamic strain rates." Journal of the Mechanical Behavior of Biomedical Materials **10**: 23-38.

Roan, E. and Vemaganti, K. (2010). "Strain rate dependent viscohyperelastic constitutive modeling of bovine liver tissue." Medical and Biological Engineering and Computing **49** (4): 497-506.

Robbins, D. H. and Wood, J. L. (1969). "Determination of mechanical properties of the bones of the skull." Experimental Mechanics **9** (5): 236-240.

Rubin, M. B. and Bodner, S. R. (2001). “A three-dimensional nonlinear model for dissipative response of soft tissue.” International Journal of Solids and Structures **39** (19): 5081-5099.

Sacks, M. S. and Sun, W. (2003). "Multiaxial mechanical behavior of biological materials." Annual review of biomedical engineering **5** (2003): 251-284.

Sarron, J.-C., Caillou, J.-P., Da Cunha, J., Allain, J.-C. and Tramecon, A. (2000). “Consequences of nonpenetrating projectile impact on a protected head: study of rear effects of protections.” Journal of Trauma **49**: 923-929.

Schröder, J. (2010). *“Poly-, Quasi- and Rank-one Convexity in Applied Mechanics.”* Springer-Verlag. Berlin,Germany.

Schröder, J. and Neff, P. (2003). "Invariant formulation of hyperelastic transverse isotropy based on polyconvex free energy functions." International Journal of Solids and Structures **40** (2003): 401-445.

Shafieian, M., Bao, K. and Darvish, K. (2011). “Mechanical properties of brain tissue in strain rates of blast injury.” 37th Annual Northeast Bioengineering Conference, Troy, NY, April 1-3, 2011. DOI 10.1109/NEBC.2011.5778711.

Shafieian, M. and Darvish, K. (2009). Viscoelastic properties of brain tissue under high-rate large deformation. ASME 2009 International Mechanical Engineering Congress and Exposition. November 13-19, 2009, Lake Buena Vista, Florida. Paper no. IMECE2009-11681 83-85.

Shariff, M. H. B. M. (2008). “Nonlinear transversely isotropic elastic solids: an alternative representation.” The Quartly Journal of Mechanics and Applied Mathematics **61** (2): 129-149.

Shreiber, D., Bain, A. and Meaney, D. (1997). “In Vivo thresholds for mechanical injury to the blood-brain barrier.” Proceedings of the 41st Stapp Car Crash Conference. Lake Buena Vista, Florida, November 13-14, 1997. SAE Paper No. 973335.

Shuck, L. Z. and Advani, S. H. (1972). “Rheological response of human brain tissue in shear.” ASME Journal of Basic Engineering **94**: 905-911.

Simonds, J. (2008). “Non-Lethal Weapons Human Effects.” Air Force Research Laboratory, Brooks City-Base, TX. PPT file, 19 pages.

Song, J. W. (1986). “Thermoplastic Composite for Ballistic Application.” Ph.D. dissertation, University of Massachusetts at Lowell. 118 pages.

Spencer, A. J. M. (1972). *“Deformations of Fibre-reinforced Materials.”* Clarendon Press, Oxford.

Spencer, A. J. M. (1971). “*Theory of invariants.”In“Continuum Physics, Vol I.”* Academic Press,New York,USA.

Stalnaker, R. L. (1969). “Mechanical Properties of the Head.” Ph.D. dissertation, West Virginia University, Morgantown.

Steigmann, D. J. (2003). "Frame-invariant polyconvex strain energy functions for some anisotropic solids." Mathematics and Mechanics of Solids **8** (5): 497-506.

Stuhmiller, J. H. (2008). “Blast Injury-Translating Research into Operational Medicine.” Borden Institute, Washington, D.C.

Taber, K.H., Warden, D.L. and Hurley, R.A. (2006). “Blast-related traumatic brain injury: What is known?” The Journal of Neuropsychiatry and Clinical Neurosciences **18** (2):141–145.

Takhounts, E. G., Eppinger, R. H., Campbell , J. Q., Tannous, R. E., Power, E. D. and Shook, L. S. (2003a). “On the development of the SIMon finite element model.” Stapp Car Crash Journal **47**:107-133.

Takhounts, E. G., Crandall, J. F. and Darvish, K. (2003b). “On the importance of nonlinearity of brain tissue under large deformations.” Stapp Car Crash Journal **47**: 79-92.

Tamura, A., Hayashi, S., Nagayama, K. and Matsumoto, T. (2008). "Mechanical characterization of brain tissue in high-rate extension." Journal of Biomechanical Science and Engineering **3** (2): 263-274.

Tamura, A., Hayashi, S., Watanabe, I., Nagayama, K. and Matsumoto, T. (2007). "Mechanical characterization of brain tissue in high-rate compression." Journal of Biomechanical Science and Engineering **2** (3): 115-126.

Tan, L. B., Tse, K. W., Lee, H. P., Tan, V. B. C. and Lim, S. P. (2012). "Performance of an advanced combat helmet with different interior cushioning systems in ballistic impact:Experiments and finite element simulations." International Journal of Impact Engineering **50** (2012): 99-112.

Taylor, P. A. and Ford, C. C. (2009). “Simulation of blast-induced early-time intracranial wave physics leading to traumatic brain injury.” Journal of Biomechanical Engineering **131** (6): 061007-1~11.

Taylor, P. A. and Ford, C. C. (2007). “Simulation of early-time head impact leading to traumatic brain injury.” International NeuroTrauma Letter of the International Brain Injury Association.6 pages.

Teland, J. A. (2010). “Numerical simulation of blast-induced mild traumatic brain injury.” IFMBE Proceedings **31** (Part 2): 350-353.

Tham, C. Y., Tan, V. B. C. and Lee, H. P. (2007). “Ballistic impact of a KEVLAR helmet:Experiment and simulations.” International Journal of Impact Engineering **35**: 304-318.

Thompson, R. F. (2000). “*The Brain: An Introduction to Neuroscience*.” Worth Publishers, Cambridge, England.

Truesdell, C., Noll, W. and Antman, S. S. (2004). “*The Non-Linear Field Theories of Mechanics.”* Springer-Verlag. Berlin,Germany.

Vaishnav, R. N., Young, J. T., Janicki, J. S. and Patel, D. J. (1972). "Nonlinear anisotropic elastic properties of the canine aorta." Biophysics Journal **12** (8): 1008-1027.

Velardi, F., Fraternali, F. and Angelillo, M. (2006). “Anisotropic constitutive equations and experimental tensile behavior of brain tissue.” Biomechanics and Modeling in Mechanobiology **5** (1): 53-61.

Viano, D. C. and Lovsund, P. (1999). “Biomechanics of brain and spinal-cord injury:analysis of neuropathologic and neurophysiologic experiments.” Journal of Crash Prevention and Injury Control **1**: 35-43.

Walsh, S. M., Scott, B. R., Spagnuolo, D. M. and Wolbert, J. P. (2006). “Hybridized thermoplastic aramids:enabling material technology for future force headgear.” U.S. Army Research Laboratory, Aberdeen Proving Ground, MD. 8 pages.

Walsh, S. M., Scott, B. R. and Spagnuolo, D. M. (2005). “The development of a hybrid thermoplastic ballistic material with applications to helmets.” U.S. Army Research Laboratory, Aberdeen Proving Ground, MD. ARL-TR-3700. 19 pages.

Wang, H. C. and Wineman, A. S. (1972). “A mathematical model for the determination of viscoelastic behavior of brain in vivo - II Relaxation Response.” Journal of Biomechanics **5**: 571-580.

Ward, C. C., Chan, M. and Nahum, A. M. (1980). “Intracranial pressure-a brain injury criterion.” Proceedings of the 24th Stapp Car Crash Conference, Troy, Michigan, October 15-17, 1980. SAE Paper No. 801304.

Weiss, J. A., Maker, B. N. and Govindjee, S. (1996). “Finite elememt implementation of incompressible, transversely isotropic hyperelasticity.” Computer Methods in Applied Mechanics and Engineering **135**: 107-128.

Willinger, R. and Baumgartner, D. (2001). “Numerical and physical modelling of the human head under impact-toward new injury criterion.” International Journal of Vehicle Design **32** (1-2): 94-115.

Wood, J. L. (1971). "Dynamic response of human cranial bone." Journal of Biomechanics **4** (1): 1-12.

Wright, R. M. and Ramesh, K. T. (2012). “An axonal strain injury criterion for traumatic brain injury.” Biomechanics and Modeling in Mechanobiology **11** (1-2): 245-260.

Wu, H. C. and Yao, R. F. (1976). "Mechanical behavior of human annulus fibrosis." Journal of Biomechanics **9** (1): 1-7.

Xiong, D. (2004). “Friction and wear properties of UHMWPE composites reinforced with carbon fibers.” Material Letters **59** (2-3): 175-179.

Zemanek, M., Bursa, J. and Detak, M. (2009). "Biaxial tension tests with soft tissues of arterial wall." Engineering MECHANICS **16** (1): 3-11.

Zhang, L., Makwana, R. and Sharma, S. (2011). “Comparison of the head response in blast insult with and without combat helmet.” Research and Technology Organization of NATO Human Factors and Medicine Panel (HFM) Symposium. Halifax,Canada,3-5 October 2011**:** Paper No 33, 18 pages.

Zhang, J., Pintar, F., Yoganandan, N., Gennarelli, T. and Son, S. (2009). "Experimental study of blast induced traumatic brain injury using a physical head model " Stapp Car Crash Journal **53** (2009): 215-227.

Zhang, L., Yang, K. H. and King, A. I. (2004). “A proposed injury threshold for mild traumatic brain injury.” ASME Journal of Biomechanical Engineering **126** (2): 226-236.

Zhang, L., Yang, K. H. and King, A. I. (2001). "Comparison of brain responses between frontal and lateral impacts by finite element modeling." Journal of Neurotrauma **18** (1): 21-30.

Zheng, Q.-S. (1994). "Theory of representations for tensor functions - A unified invariant approach to constitutive equations." Applied Mechanics Reviews**47** (11): 545-587.

Zhurov, A.I., Limbert, G., Aeschlimann, D.P. and Middleton, J. (2007). "A constitutive model for the periodontal ligament as a compressible transversely isotropic visco-hyperelastic tissue." Computer Methods in Biomechanics and Biomedical Engineering **10** (3): 223-235.